AD/A-006 584

INVESTIGATION OF GEAR DYNAMICS SIGNAL ANALYSIS

Michael J. Drosjack, et al

Ohio State University Research Foundation

Prepared for:

Army Air Mobility Research and Development Laboratory

January 1975

UNCLASSIFIED

SECURITY CLASSIFICATION OF THIS PAGE (When Data Entered)

REPORT DOCUMENTATION PAGE		READ INSTRUCTIONS BEFORE COMPLETING FORM
1. REPORT NUMBER USAAMRDL-TR-75-1	2. GOVT ACCESSION NO.	3. RECIPIENT'S CATALOG NUMBER AD/A-006584
4. TITLE (and Subtitle) INVESTIGATION OF GEAR DYNAMICS SIGNAL ANALYSIS		5. TYPE OF REPORT & PERIOD COVERED Final 15 Jul 73 to 15 Sep 74
		6. PERFORMING ORG. REPORT NUMBER
7. AUTHOR(s) Michael J. Drosjack Donald R. Houser Arthur C. Tinney		8. CONTRACT OR GRANT NUMBER(s) DAAJ02-73-C-0103
9. PERFORMING ORGANIZATION NAME AND ADDRESS The Ohio State University Research Foundation 1314 Kinnear Road Columbus, Ohio 43212		10. PROGRAM ELEMENT, PROJECT, TASK AREA & WORK UNIT NUMBERS Task 1F262209AH7604
11. CONTROLLING OFFICE NAME AND ADDRESS Eustis Directorate, U. S. Army Air Mobility Research and Development Laboratory Fort Eustis, Virginia 23604		12. REPORT DATE January 1975 13. NUMBER OF PAGES 189
14. MONITORING AGENCY NAME & ADDRESS(if different from Controlling Office)		15. SECURITY CLASS. (of this report) Unclassified 15a. DECLASSIFICATION/DOWNGRADING SCHEDULE

16. DISTRIBUTION STATEMENT (of this Report)

Approved for public release; distribution unlimited.

17. DISTRIBUTION STATEMENT (of the abstract entered in Block 20, if different from Report)

18. SUPPLEMENTARY NOTES

19. KEY WORDS (Continue on reverse side if necessary and identify by block number)

Gear	Fault Detection	Dynamic Modelling
Gear Dynamics	Gear Tooth Pitting	
Mesh Stiffness	Torsional Dynamics	
Condition Monitoring	Failure Analysis	
Vibration Diagnostics	Power Transmission	

20. ABSTRACT (Continue on reverse side if necessary and identify by block number)

This study was performed to investigate the dynamic effects encountered at the gear mesh as the result of gear tooth surface faults. For this purpose, a torsional dynamic simulation of a geared system was developed which included provisions to account for the effect of pitting on a gear tooth. Tests were performed with gears which were in good condition and with gears containing manufactured faults. Results of the experiments and simulation were compared, and substantial correlation was found between the two. Thus, the capability of the simulation to model a fault on a tooth was substantiated.

DD FORM 1 JAN 73 1473 EDITION OF 1 NOV 65 IS OBSOLETE

UNCLASSIFIED

SECURITY CLASSIFICATION OF THIS PAGE (When Data Entered)

EUSTIS DIRECTORATE POSITION STATEMENT

The Eustis Directorate of the U. S. Army Air Mobility Research and Development Laboratory is conducting a series of efforts directed at advancing the state of the art of vibration signal analysis techniques. These techniques are in support of efforts associated with improving the capability of diagnosing the mechanical condition of Army helicopter power train components.

This contract was awarded to investigate the dynamic effects encountered at the gear mesh due to incipient gear tooth failure modes. Laboratory investigations were conducted using gears from UH-1 helicopters.

The conclusions presented herein are generally agreed with by the Eustis Directorate.

The technical monitor of this contract was Mr. G. William Hogg, Reliability and Maintainability Technical Area, Military Operations Technology Division.

PREFACE

Special thanks go to Messrs. Alexander, Spencer, Hanlon, and Leslie of Speco Division of Kelsey-Hayes for their advice on test stand design and aid in obtaining gear measurements; to Messrs. Laingor, Pattin, and Murphy of Bell Helicopter Company for their aid; and to Mr. T. Genny of USAAVSCOM, St. Louis, Missouri, for his aid in obtaining test stand materials.

TABLE OF CONTENTS

LIST OF ILLUSTRATIONS

LIST OF TABLES

INTRODUCTION

This section includes a discussion of the objectives of the research program, a review of the work performed, and the results obtained. The work was performed by The Ohio State University from 15 July 1973 to 30 June 1974.

OBJECTIVE

The objective of this program was to investigate the dynamic effects encountered at the gear mesh due to incipient gear tooth failure modes. The specific failure mode under study was pitch-line pitting of a gear tooth.

A goal of the study was to develop a dynamic model capable of predicting gear behavior. Experimental data were to be used in verification of the model and the results then applied to possible applications in the evaluation and development of gear diagnostic techniques.

PROGRAM CONDUCT

The program was divided into five tasks:

Task I. Mathematical Formulation
Task II. Model Simulation
Task III. Experimental Studies
Task IV. Model Verification
Task V. Recommendations

During Task I a set of equations, based on analytical considerations, was developed to predict the dynamic response of a geared system both when the system contains all good gears and when gear tooth faults are present. The basic procedure was an analysis of the torsional dynamic response of the system with and without gear tooth faults. A separate formulation was performed to determine gear tooth stiffness functions.

The work of Task II consisted of using the equations developed during Task I to develop a computational procedure for evaluating the geared system's response characteristics. The simulation was performed on The Ohio State IBM System 370/165 digital computer. Programming was performed in FORTRAN and utilized a number of IBM subroutines and subprograms.

A test apparatus was designed and built and experiments were performed in Task III. The test stand utilized a Generator Drive Offset Quill gearbox which is used on the UH-1 helicopter. Faults were manufactured into a total of four gears; experiments were performed on good gears as well as those containing the faults. A number of parameters were monitored during testing, including acceleration at various gearbox positions and dynamic strain of the gear mesh.

The results of the simulation and experiments were compared as part of Task IV. Appropriate adjustments in the model were made as a result of experimental evidence.

Task V consisted of evaluating the results of the simulation with respect to possible applications. These consist of the applicability of the model and modelling procedures to the evaluation and development of diagnostic procedures, as well as further developmental possibilities of the simulation which might prove valuable.

REPORT CONTENTS

The testing equipment is described and a theoretical analysis performed on the test system. Data are presented on time-domain response and frequency-domain response from both experiments and simulation results. The data are presented for both the cases of operation of the system in good condition and also when faults are present. Changes noted as the result of fault introduction are described, and correlation between theory and experiment is discussed.

BACKGROUND

This study was performed to develop a dynamic model of a geared system which incorporates the effects of gear tooth surface faults. The response characteristics of the model could then be used to determine differences between the vibrations generated by good gears and those possessing faults. Once such a capability is available, it may be applied to the development and evaluation of discriminants for use in vibration diagnostic procedures. A model of this sort must, of course, be verified as reliable through correlation with experimental data. However, once such a model is considered valid, variations in the system such as load, speed, fault size, fault position, etc., may be studied without the immediate need for experimental data. This type of result can present both cost and time savings in the development and analysis of diagnostic techniques.

DIAGNOSTIC ANALYSIS

A great deal of interest has been evidenced in the use of vibration diagnostic techniques in conjunction with maintenance procedures. Diagnostic techniques are defined as those which identify the condition of a system from its external signs or symptoms. In the case dealt with in this study, the condition of a power train gear is to be determined by analyzing vibration signals from the power train housing. In actual practice such a procedure eliminates the need for visual inspection of the individual power train component. There has been considerable study of vibration diagnostic procedures as applied to power trains. An overview may be obtained from a report on the subject prepared by Houser and Drosjack.[1] A number of techniques have shown strong promise for application with bearing failures. However, the same statement may not be made with respect to gearing.

In bearing diagnostics, the techniques which have shown the most success analyze in one manner or another the impact which a rolling-element surface fault produces as the fault passes through the interface between two contacting surfaces. This force then excites bearing support structures which produce a measurable "ringing" response as seen in Figure 1. The repetition rate relates to a characteristic frequency which may be determined on the basis of fault position and is readily calculable. The "ringing" frequency is not yet predictable theoretically.

A wide variety of analysis procedures are used in processing the vibration signals. SKF, in the Shock Pulse Meter, uses the wave propagation response to the impact force to "ring" an accelerometer (mounted on the machine structure) at its resonance.[2] The output of this accelerometer is monitored for both peak amplitude and frequency of occurrence of rings. Mechanical Technology Incorporated, with their Bearing "Ring" Analyzer processes the signal as shown in Figure 1.[3] They analyze it for both the amplitude of the "ringing" response and the repetition rate of the impact. General Electric Company uses a simpler analysis in their Impact Index Analyzer,[4] where they calculate the value of the ratio of peak vibration signal to the r.m.s. level. These are just three examples from many analysis techniques. Almost

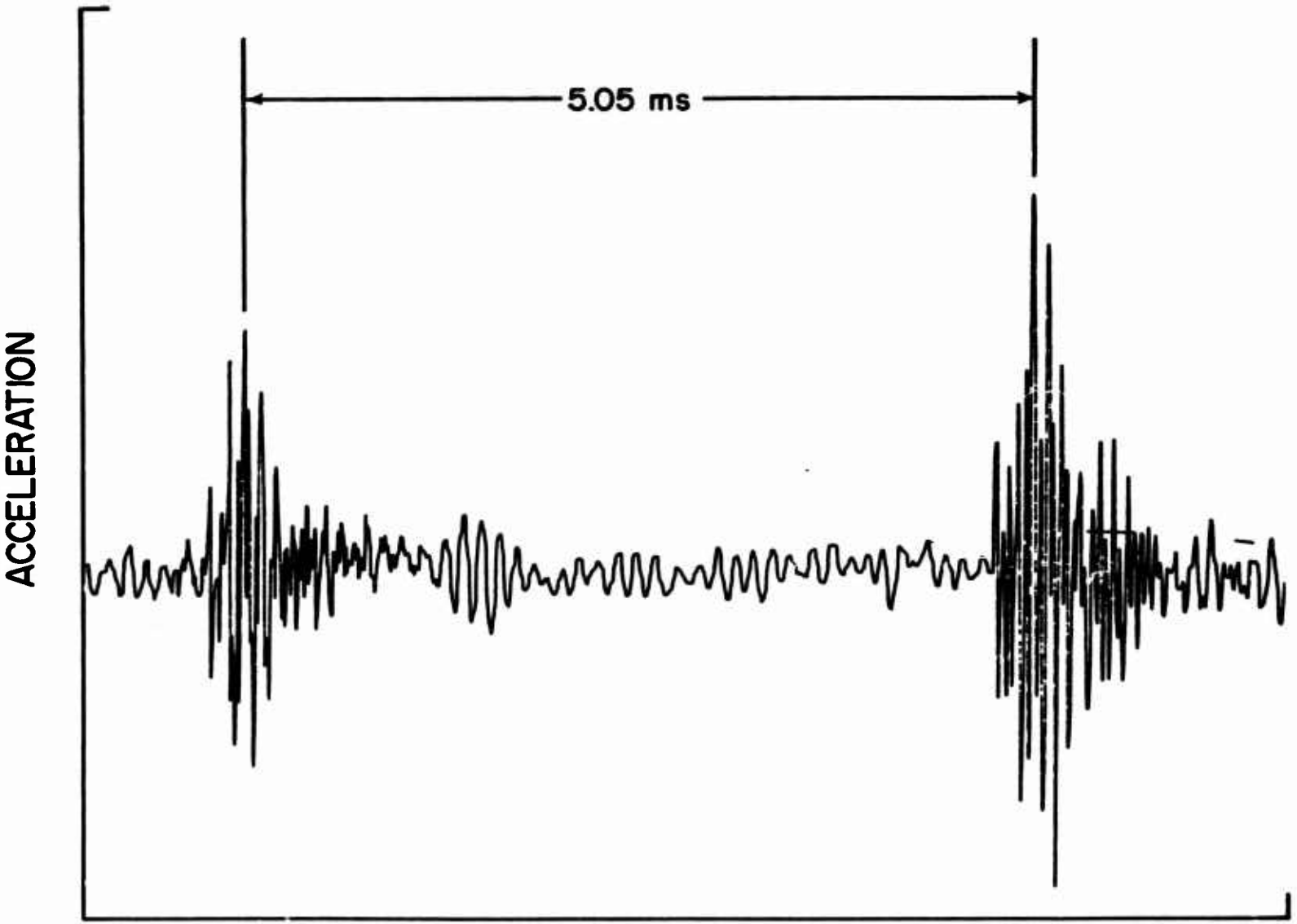

Figure 1. Time Response of Bearing "Ringing" Response for Two Impacts.

all of them, however, in some manner make use of information relating response to the repetition rate of the impact and the effect of fault size, position, and type on amplitudes of bearing force and, hence, vibration that may be expected.

There is much less understanding of the mechanisms encountered in gearing when a fault is present. The dynamic phenomena have not been analyzed to any great extent, and data obtained experimentally are difficult to interpret. A fault may be expected to cause dynamic forces in the gear mesh. However, unless sliprings or telemetry devices are used, this force cannot be monitored. Instead, vibrations on housing structures of the gearbox are usually measured. The characteristics of the transmission path between the gear mesh and the transducer may severely distort the signal and make analysis of it quite difficult.

There have been some gear diagnostic attempts based on the observed changes in the frequency spectrum. Faulty gears typically exhibit more energy at harmonics of the meshing frequency and at sidebands of both the meshing frequency and its harmonics. The interrelationships between position and/or size of these spectrum changes to the fault type and size have not been well understood.

General Electric Company used three ratios as gear condition indicators on their TF-34 Analyzer.[5] They took a ratio in the manner of their Impact Index, a ratio of harmonic content to the amplitude of the gear meshing frequency, and a ratio of side-band content to the fundamental and harmonic content. A joint technique was developed by General Electric and Mechanical Technology Incorporated for monitoring gear wear.[6,7] The ratios of energy at the first, second, and third harmonics to the fundamental gear meshing frequency were formed. Experimental results showed these ratios to increase as the gear wear progressed. Some later work on this technique included preconditioning of the data by time-averaging of the signal at the gear-meshing period or shaft rotational period.[8] Time-averaging adds together blocks of data at intervals of the gear-meshing period. Response which is uncorrelated at this period will cancel itself out, thus allowing the response of the gear to predominate. No widespread application of any of these gear diagnostic techniques has been discovered by the investigators in this study.

One of the primary roadblocks to further development of gear diagnostic techniques has been the lack of analytical results relating gear response to faults. This is not to say that dynamic studies of gearing have not been preformed. There have been a large number or studies performed, but most of these deal with either design procedures of the dynamic effects of manufacturing errors. A listing of work would include study of dynamic loading, mesh stiffnesses, load distributions, gear noise, and geared system response.

GEAR DYNAMIC LOADING

An area where interest has long been evident is the study of acceptable load rating of gear sets. In the nineteenth century a number of theories

yielding wide variations in calculated allowed loads were used. A presentation was made in 1892 by W. Lewis to the Engineers Club of Philadelphia which included the following equation:[9]

$$F_s = \tau_d W P_c Y \qquad (1)$$

where F_s = safe allowable load, lb
τ_d = design stress, lb/in.^{2}
W = facewidth of gear, in.
Y = form factor depending upon tooth shape
P_c = circular pitch, in.

This equation was based on an analysis of the material working stress using simple beam theory. Lewis also felt that gear velocities should be included in the equation. This led to the development of the following equation by Barth:[10]

$$\tau_d = \tau \frac{600}{600 + v} \qquad (2)$$

where τ = safe static stress, lb/in.^{2}
v = pitch-line velocity, ft/min

This modified design stress was then used in Lewis' design equations. It was one of the earliest dynamic increment or derating factors used to account for dynamic loading encountered by normal gear operation.

In 1913, E. Buckingham authored a report of the A.S.M.E. Research Committee on Dynamic Loads[11] which presented the results of work carried on by the committee on the effect of manufacturing errors and pitch-line velocity on the dynamic loads of gears. The equations which were developed are still in use with appropriate modifications.

In the early 1950's, Tuplin presented a more refined analysis for determining the loads due to manufacturing errors.[12] Figure 2 shows the model used in his analysis. The mass (m) represents the equivalent gear inertias, and the stiffness (K) is an average mesh stiffness calculated using a static analysis. The wedge, moving at a velocity V, represents a positive pitch error of size e. Attia published the result of experimental work which used strain gages to record the deflections of gear teeth and the maximum instantaneous tooth loading as the gear teeth passed through the zone of contact at various speeds and static loads.[13] His results showed differences from the predictions of both Buckingham and Tuplin. In 1954, Reswick presented a more sophisticated analysis procedure for determining dynamic loading.[14] In it, he used a parabolic cam to represent tooth

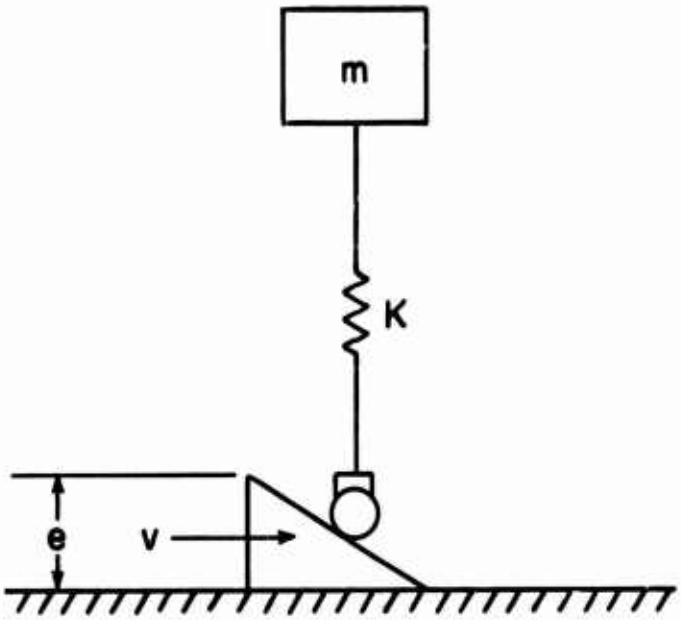

Figure 2. Tuplin's Model for a Gear Tooth With a Pitch Error.

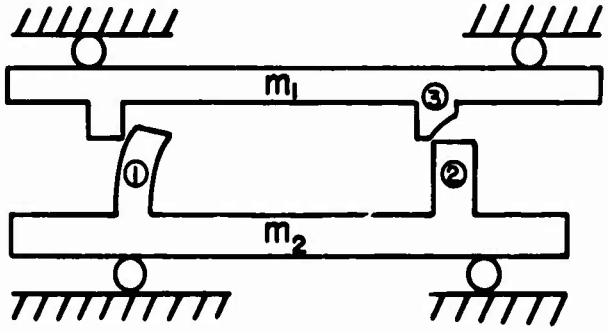

Figure 3. Reswick's Model for a Pair of Teeth With an Error.

errors and allowed the inclusion of the effect of more than one tooth pair. Figure 3 shows the model which was used.

Niemann and Rettig reported the results of a study which experimentally determined the effect of various operating conditions and tooth errors on the dynamic loading and deflection of the gear teeth.[15] Experimental work was performed by Harris to study tooth stresses by photoelastic methods.[16] He concluded that dynamic loading may be attributed to manufacturing errors, parametric excitation due to stiffness variations in the mesh, and backlash effects in the gears. Gregory, Harris, and Munro performed studies which concluded that damping was an important consideration in any analysis.[17] Later work by Munro stated that transients did not die out as quickly as previously considered.[18] For this reason, he suggested that analyses must consider several tooth pairs to be accurate. Richardson performed a comprehensive study of tooth deflection, stress, and loading that included both theoretical development and experimentation;[19] his model is shown in Figure 4.

A planetary geared system was analyzed by Kasuba,[20] who developed a model as shown in Figure 5. The errors were simulated by a displacement strip [S(t)]. He also extended his model to two degrees of freedom. Hahn later extended Kasuba's analysis to include the effect of other system components, including shafting, bearing, and housing.[21]

Houser performed a study of spur and helical gears which led to the development of a semiempirical dynamic loading factor.[22,23] He calculated velocity differences based on pitch errors and performed experimental studies to determine the effects of pitch errors and face-width variations on dynamic tooth loads. Dynamic strains were measured with the use of strain gages mounted in the tooth roots.

Various studies of a nature similar to many previously mentioned have also been performed by a number of Japanese investigators.[24-27]

In the analyses discussed in the above paragraphs, the prime considerations involved either normal gear operation or operation with gears containing manufacturing errors. Most of the work also analyzes only the interaction between one tooth pair or at most two or three tooth pairs. While the information is of some value in studying the effects of tooth surface faults on gear system response, the studies are not adequate to provide the desired predictive capabilities.

MESH STIFFNESS AND TOOTH DEFLECTION ANALYSIS

A number of studies have been performed on gear mesh stiffness functions and deflections under load. This type of information has two uses; i.e., information on torsional resonant response characteristics may be obtained, and the values of deflection may be used to modify teeth for smoother operation under load.

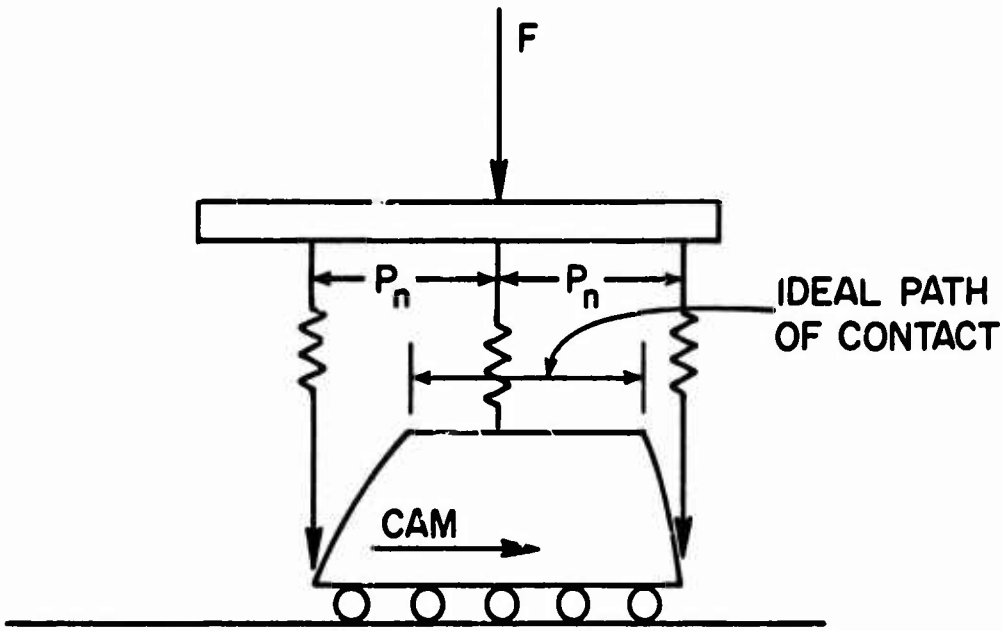

Figure 4. Richardson's Model for Gear Analysis.

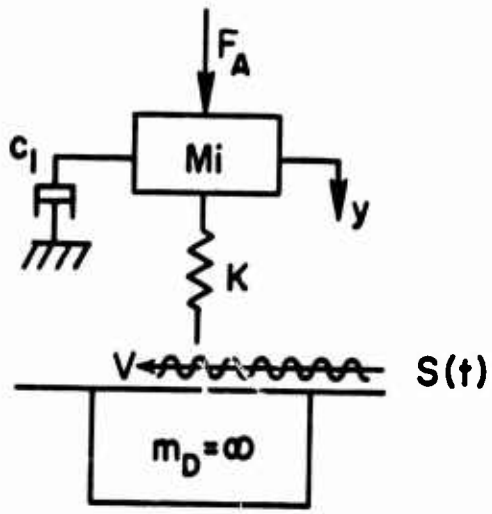

Figure 5. Kasuba's Single-Degree-of-Freedom Model.

Work in this area considers compliance (the inverse of stiffness) as well as stiffness itself. The mesh compliance coefficient (C_M) is defined to be the deflection in inches (measured relative to the base circle of the gear) per pound of force applied along the pressure line per inch of face-width of the gear. Typical values of compliance coefficient versus distance along the line of action are shown in Figure 6.

Load sharing between tooth pairs must also be included when determining total mesh stiffness. In a spur gear pair having a contact ratio between one and two, the load will be carried first by one pair, then by two pairs, then by one pair, etc. This change in loading can cause abrupt variations in the overall mesh stiffness. Meshing is assumed to occur only along the line of action of the gears, and load-sharing occurs on portions of this line which are dependent on the tooth and mesh design parameters, and which may be determined geometrically. When more than one tooth pair is in contact, the tooth pairs are treated as springs in parallel. A second possible analysis procedure which, to the knowledge of the investigators, has not been performed is to model noninvolute action due to errors and tooth deflections. This would move contact off the line of action and would require an iterative computation procedure.

In 1926, Timoshenko and Baud[28] presented an equation for tooth bending deflection which was based on the analysis of a tooth modelled as a trapezoidal beam (see Figure 7). An average value was used for shear deflection, and the equations for contact between two cylinders gave Hertzian deflection values. The equation was:

$$\delta = \delta_B + \delta_S + \delta_H$$

$$= \frac{12P}{E}\frac{\ell^3}{h_o^3}\left[\left(\frac{3}{2} - \frac{a}{2\ell}\right)\left(\frac{a}{\ell} - 1\right) + \ell n \frac{\ell}{a}\right] + \frac{4P(\ell-a)(1-\mu)}{(h+h_o)E}$$

$$+ \frac{2(1-\mu^2)P}{\pi E}\left(\frac{2}{3} + \ell n \frac{4r_g}{b} + \ell n \frac{4r_p}{b}\right) \qquad (3)$$

where

δ = total deflection
δ_B = bending deflection
δ_S = shear deflection
δ_H = Hertzian deflection
r_g, r_p = radius of curvature of contacting involute surfaces at contact
b = width of contact strip

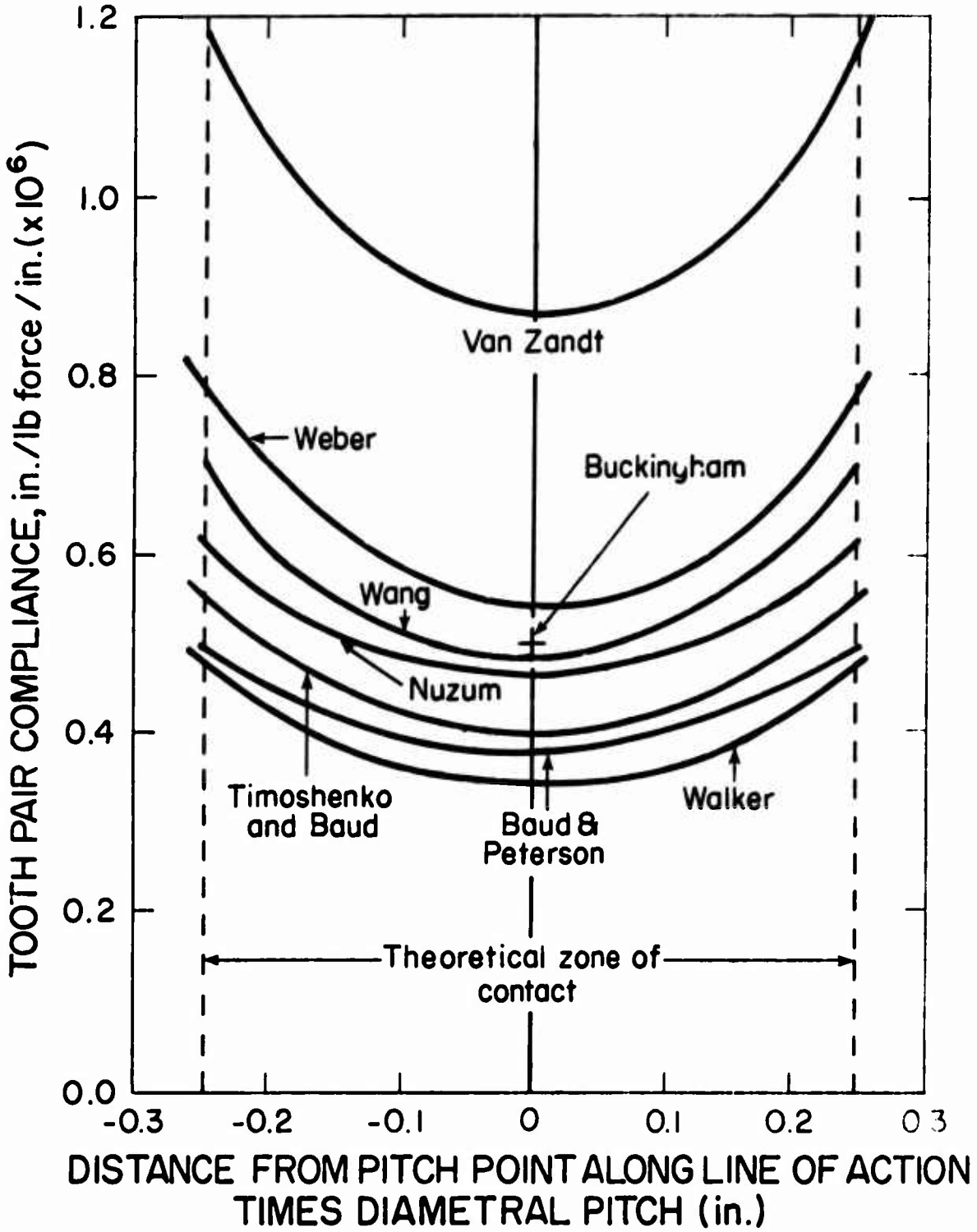

Figure 6. Typical Plots of Tooth Pair Compliance Versus Contact Position.

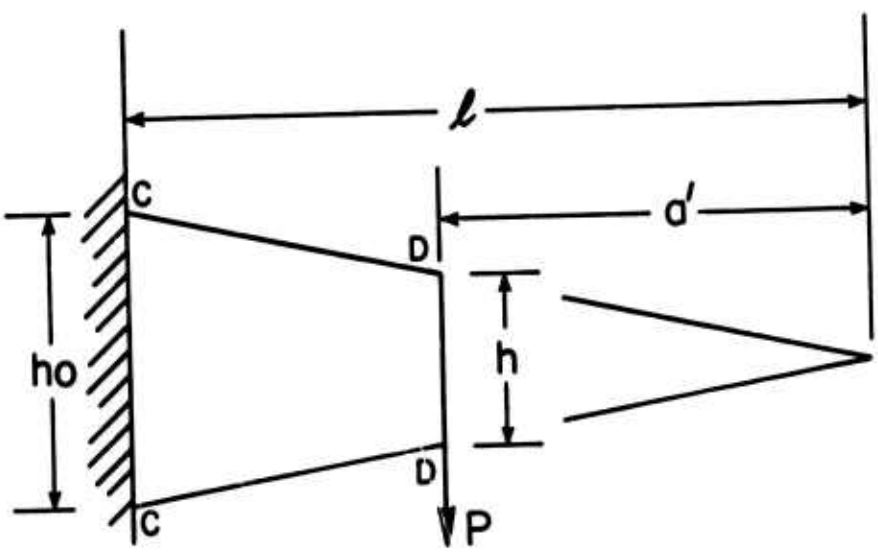

Figure 7. Tooth Model Analyzed for Deflection by Timoshenko and Baud.

$$b = 3.04\sqrt{\frac{P}{E}\frac{r_g r_p}{r_g + r_p}} \qquad (4)$$

Maximum deflections under load were shown to be negligible in comparison to manufacturing errors of the day.

In a subsequent paper published in 1929, Baud and Peterson used Timoshenko's equations to obtain the variation of tooth pair compliance as a function of position of the point of contact along the arc of action.[29] The model they used for tooth bending was similar to Timoshenko's. The load used in their equations was equal to the component of tooth force which is perpendicular to the center of the tooth, with the deflections being geometrically resolved to the pressure line. Figure 8 shows the total compliance and the individual compliance components as calculated for a single tooth pair. Figure 9 shows the mesh compliance when load-sharing was included in their calculations.

In 1938, H. Walker performed an experimental investigation of tooth pair compliance.[30,31] His testing apparatus consisted of a nonrotating gear to which a load could be applied by a lever arm arrangement. Load geometry could be changed by varying the position of the gear center with respect to the point of force application. Figure 10 shows results obtained when the load at a given contact position was varied. Figure 11 shows the results of varying contact position for given loads. Based on his experimental data, Walker was able to conclude that the mesh compliance was independent of diametral pitch. He also showed that mesh compliance was essentially a linear function of load. Other investigators have also found these two ideas to be true.

A more rigorous theoretical approach was taken by Weber.[32] His analysis was utilized in the modelling procedures used in the research program discussed in this report. His method is detailed in Chapter 4.

The above procedures determine gear tooth deflections on the basis of beam analysis. In the case of wide face-width spur gears or helical gears, an analysis on the basis of plate theory, as performed by Wellauer and Seireg,[33] is appropriate. However, the gears used in the program discussed in this report have narrow enough face widths to be considered as a beam.

LOAD DISTRIBUTION

An area of design interest somewhat similar to the determination of dynamic factors concerns the calculation of load distribution factors. Because of surface asperities, misalignment, etc., the tooth load may not be evenly spread across the tooth face. In gear design, load factors are used to account for load concentrations on the tooth which otherwise could possibly

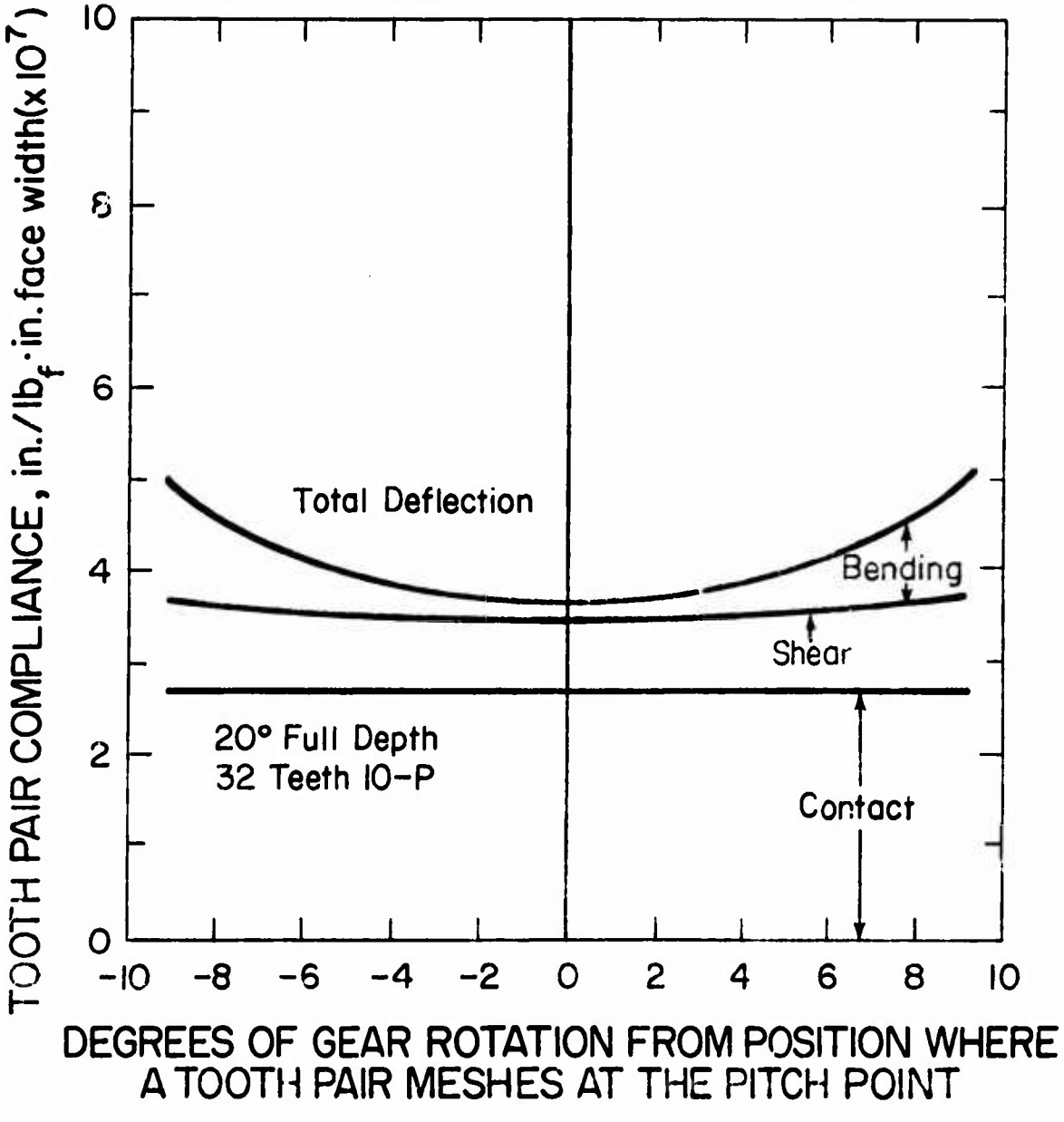

Figure 8. Tooth Pair Compliance Versus Contact Position as Calculated by Baud and Peterson.

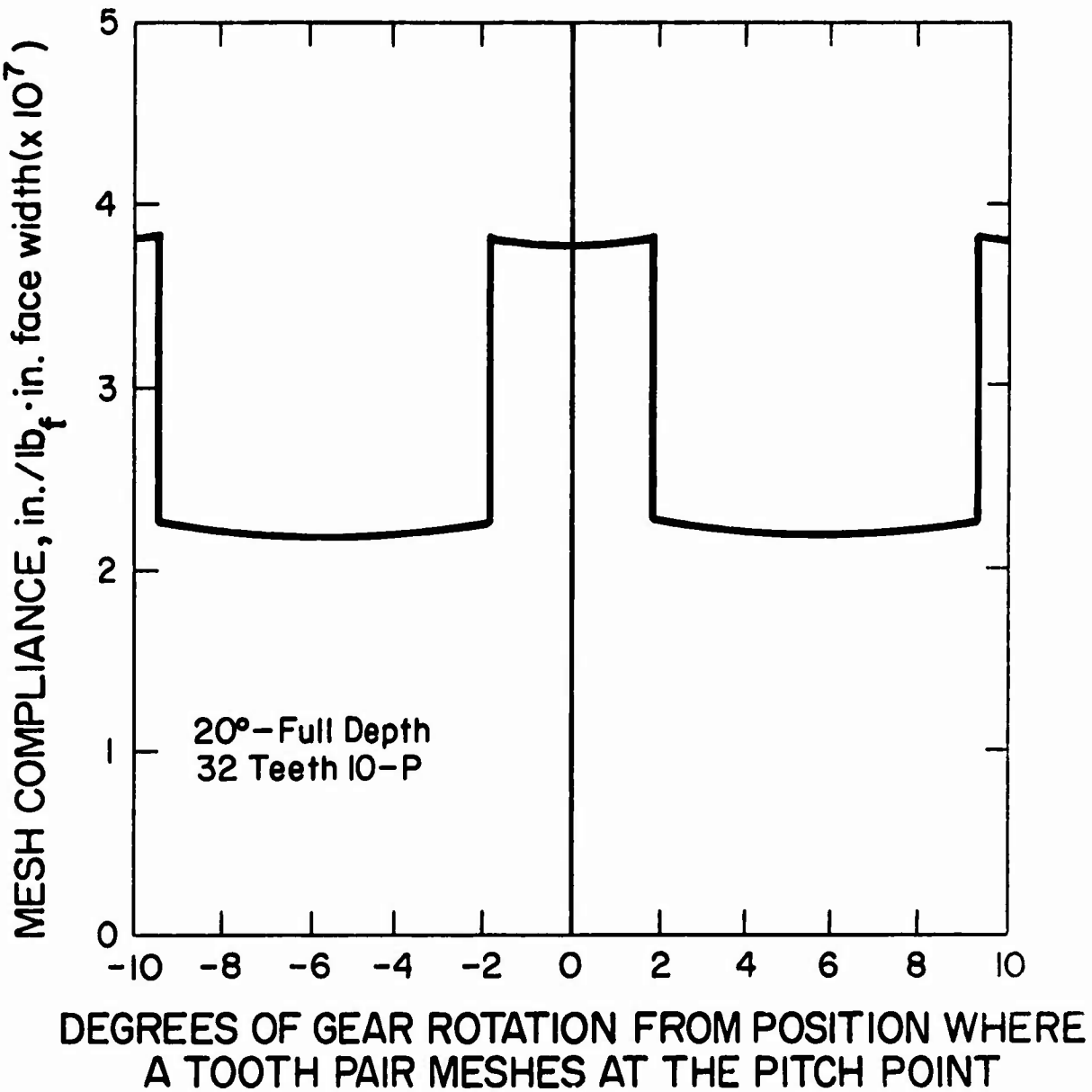

Figure 9. Mesh Compliance Versus Contact Position as Calculated by Baud and Peterson.

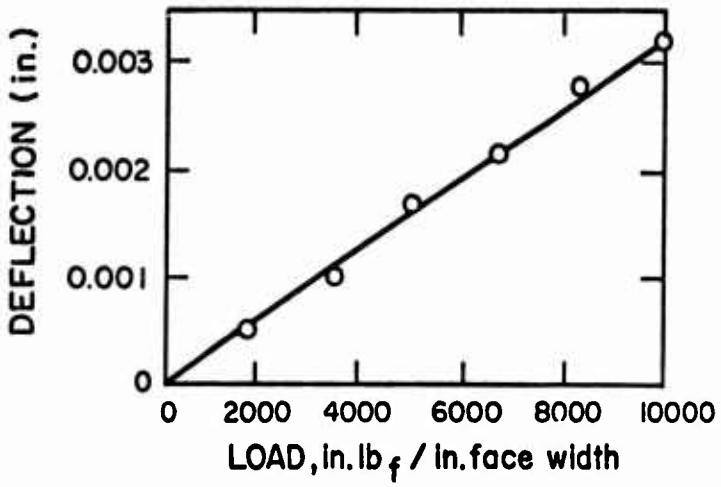

Figure 10. Tooth Deflection Versus Load as Experimentally Determined by Walker.

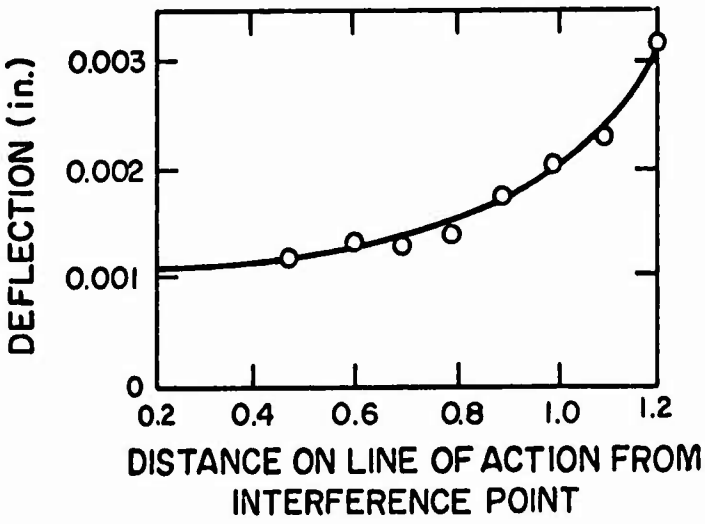

Figure 11. Tooth Deflection Versus Distance on Line of Action as Determined by Walker.

cause tooth breakage. Use of load distribution factors is appropriate when considering the dynamic response of geared systems. However, in the narrow face-width gears used in this study, load distribution factors were found to be negligible.

A number of investigators, e.g., Poritsky et al.,[34] Weber,[35] Trbojevic,[36,37] and Conry,[38] have studied load distribution factors.

GEAR NOISE

An area of strong interest in gear dynamic analysis is the effort to predict and control gear noise. Most of the work performed in this area has been on a semiempirical basis. Beuler of Volkswagen presented a study of geometrical manufacturing variables on gear noise.[39] Some work relating gear noise output to gear quality control was published by Bradley.[40]

An analytical development in the area of noise was presented by Welbourn.[41] In it, he performed a Fourier analysis of gear tooth errors and used this information to determine the relative effect of tooth errors on gear noise. Work of a similar nature has been performed by Mechanical Technology Incorporated.[42-45] They determined Fourier components due to tooth profile and tooth deflections and used this information in a Holzer-type torsion vibration analysis to predict vibration and noise.

OTHER WORK

There have been a number of other studies which cannot be categorized in the areas discussed previously. Several investigators have studied torsional dynamics of geared systems. Tordion used an impedance approach to determine natural frequencies, but did not determine instantaneous loads.[46] Wang developed a computation procedure to predict torsional dynamic response which accounted for all system components, including gears, shafting, and keyway deflections.[47] He used an average mesh stiffness value in his computations. Fukuma, Furukawa, and Aida presented similar work, which included shaft bending deflections.[48]

Another interesting study was presented by Wallace and Seireg,[49] who used a finite element approach to study the dynamic stress and deflection in a gear tooth due to a moving load along the gear tooth profile.

SUMMARY

There has been difficulty in the development of gear diagnostic procedures because of a lack of adequate analytical models. This deficiency has required gear diagnostic techniques to be developed almost entirely on the basis of extensive testing. An adequate modelling of geared system dynamic response, including the effect of tooth surface faults, is a necessary tool for use in diagnostic system development. While portions of the studies and work performed in the area of gear dynamics may be applied to models of

gears with tooth surface faults, the problem as a whole has not been adequately analyzed. Work already presented may be used to gain insight and direction in the development of models for analysis of gears with tooth faults.

TESTING APPARATUS

Experimental data were necessary in order to provide a method of verifying theoretical predictions. For this purpose, a test stand was designed and experiments performed. The gearbox used on the test stand is a Generator Offset Quill Drive from a UH-1 helicopter. This gearbox is instrumented to provide pertinent data from tests which included the operation of both "good" gears and gears containing faults manufactured on the tooth surfaces.

TEST STAND

Figure 12 shows a schematic of the test stand. The system is driven by a General Electric Model 26-G-440 Direct Current Electric Dynamometer which is operated as a motor. This motor provides up to 20 hp at 5000 rpm and has variable speed controls. The motor is coupled to a Lebow Model 1104 Torquemeter which is rated at 500 in.-lb and 9000 rpm. The torquemeter includes a built-in magnetic pickup to provide a speed signal. The output shaft of the torquemeter is then coupled to the input spiral bevel gear on the gearbox. Figure 13 shows the system from the motor to the gearbox (gearbox on the right).

The gearbox is loaded via a generator and resistor bank. The generator used is a Bendix 30B37-37-A DC Starter Generator which is rated at 30 V, 300 A with an operation range of 4500-8000 rpm and is the same one used with the gearbox in general helicopter operation. The load resistance for the generator is provided by twelve 1-ohm resistors wired in such a manner that by using the five knife switches shown on the control board, any parallel combination of from one to twelve resistors is realizable. Thus, load resistance is variable from 1 to 1/12 ohm. Figure 14 shows the configuration of the generator with respect to the gearbox, and Figure 15 shows the load resistance bank. A rheostat is also located on the resistor bank for controlling the generator field and, thus, the output voltage.

GEARS

The gearbox contains three gears as shown in Figure 16. The driving gear is on the left, while the generator driver gear is on the right. The three gears are straight spur gears having the design parameters shown in Table I. The overall gear ratio through the gearbox is one; i.e., the input speed to the gearbox is the same speed as that of the generator drive shaft. The ratio between each gear pair is 1.35 and 0.746, respectively. The design contact ratio is 1.75. Gears were tested both in "good" condition and with faults manufactured into them. The faults were designed to simulate pitch-line pitting and were produced by electrochemically etching a line at the pitch line of the gear. Figure 17 shows a sketch of the faults. Two sizes of faults were used: a 0.020-inch-wide fault as shown in Figure 18 and a 0.050-inch-wide fault as shown in Figure 19. A gear which had a 0.020-inch-wide fault on two teeth which were separated by two teeth without any faults was also tested. Profile checks for gears with and without faults are shown in Appendix I.

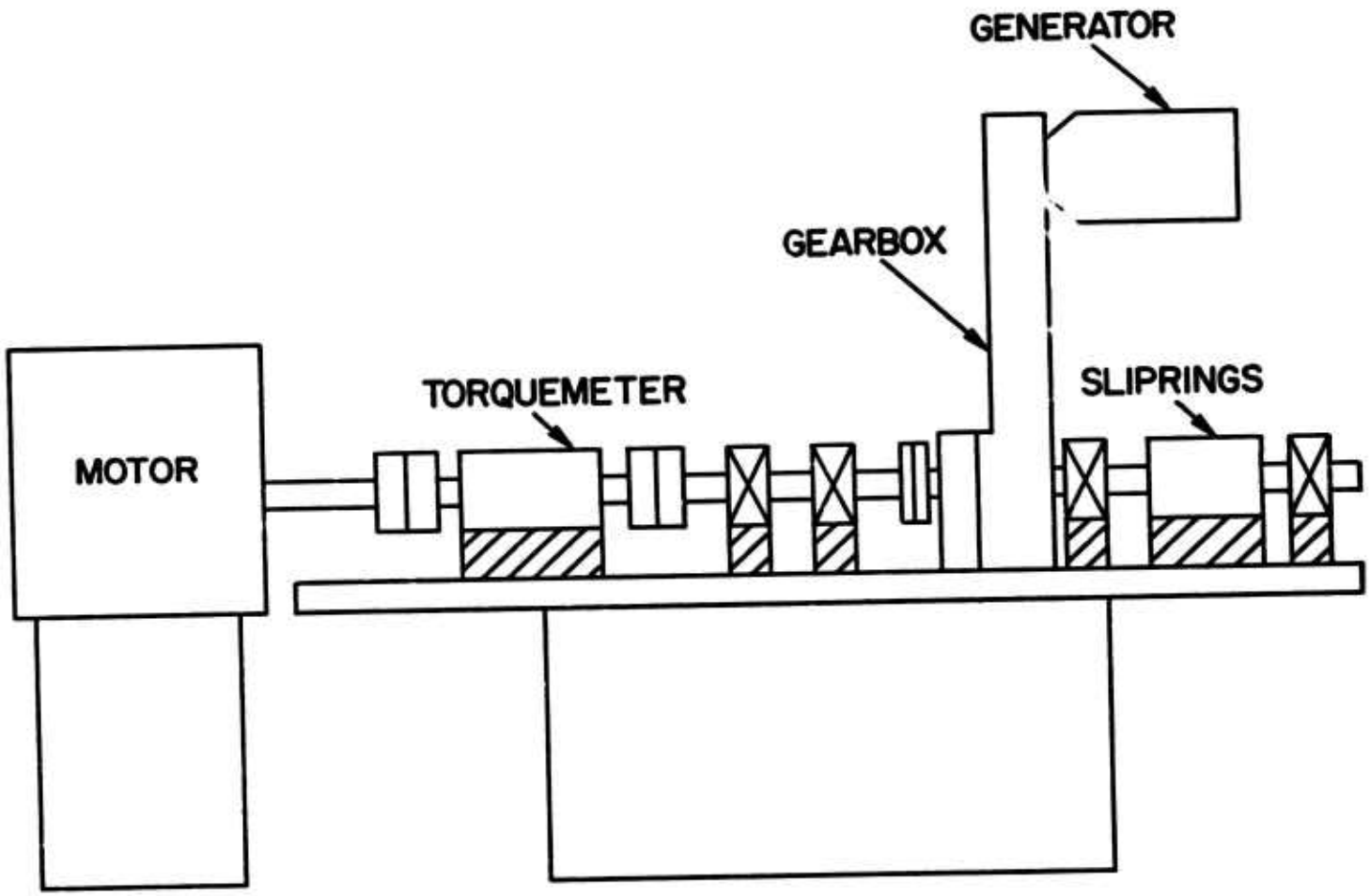

Figure 12. Schematic of Test Stand Apparatus.

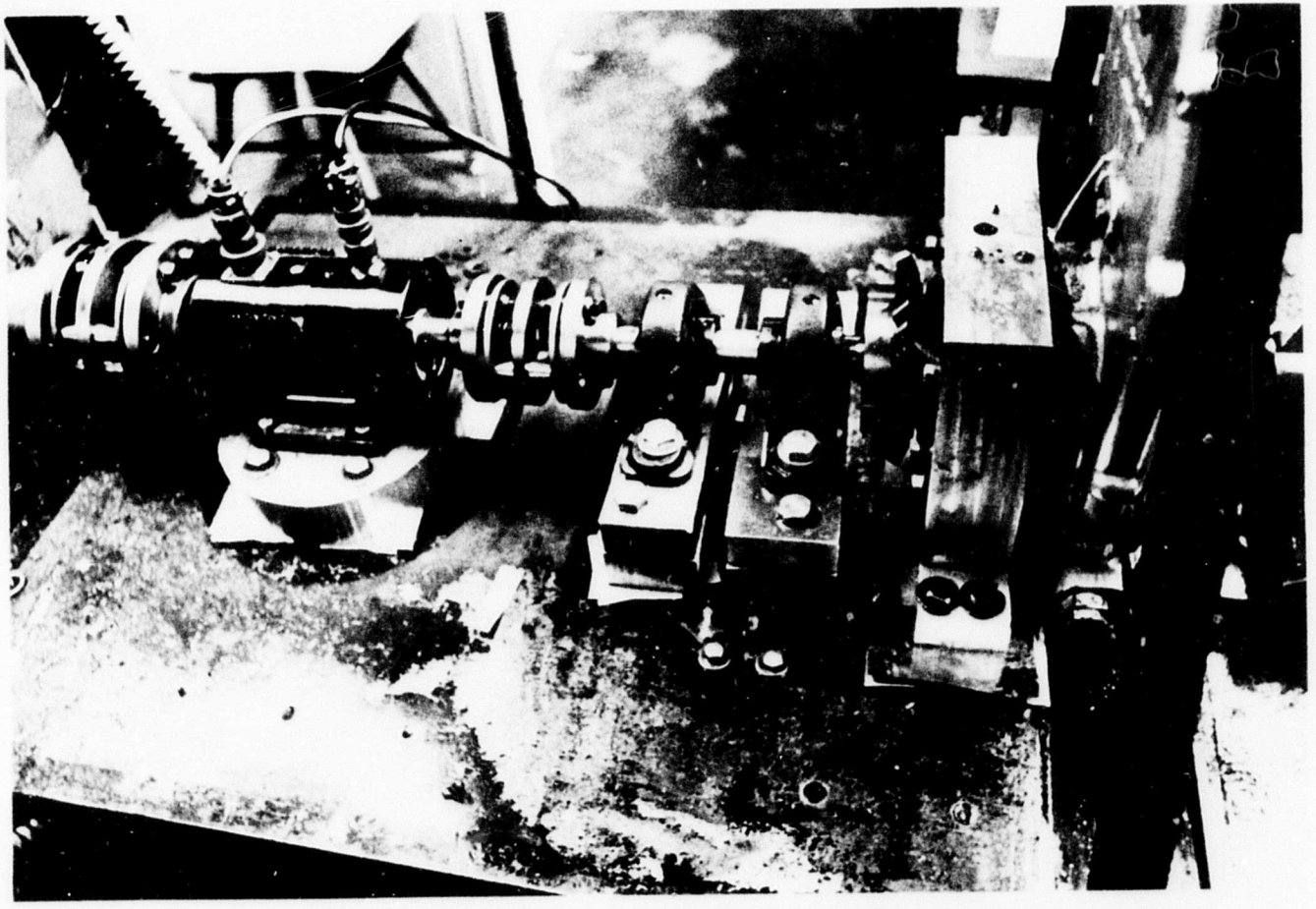

Figure 13. Test Stand Showing Torquemeter and Motor Coupling.

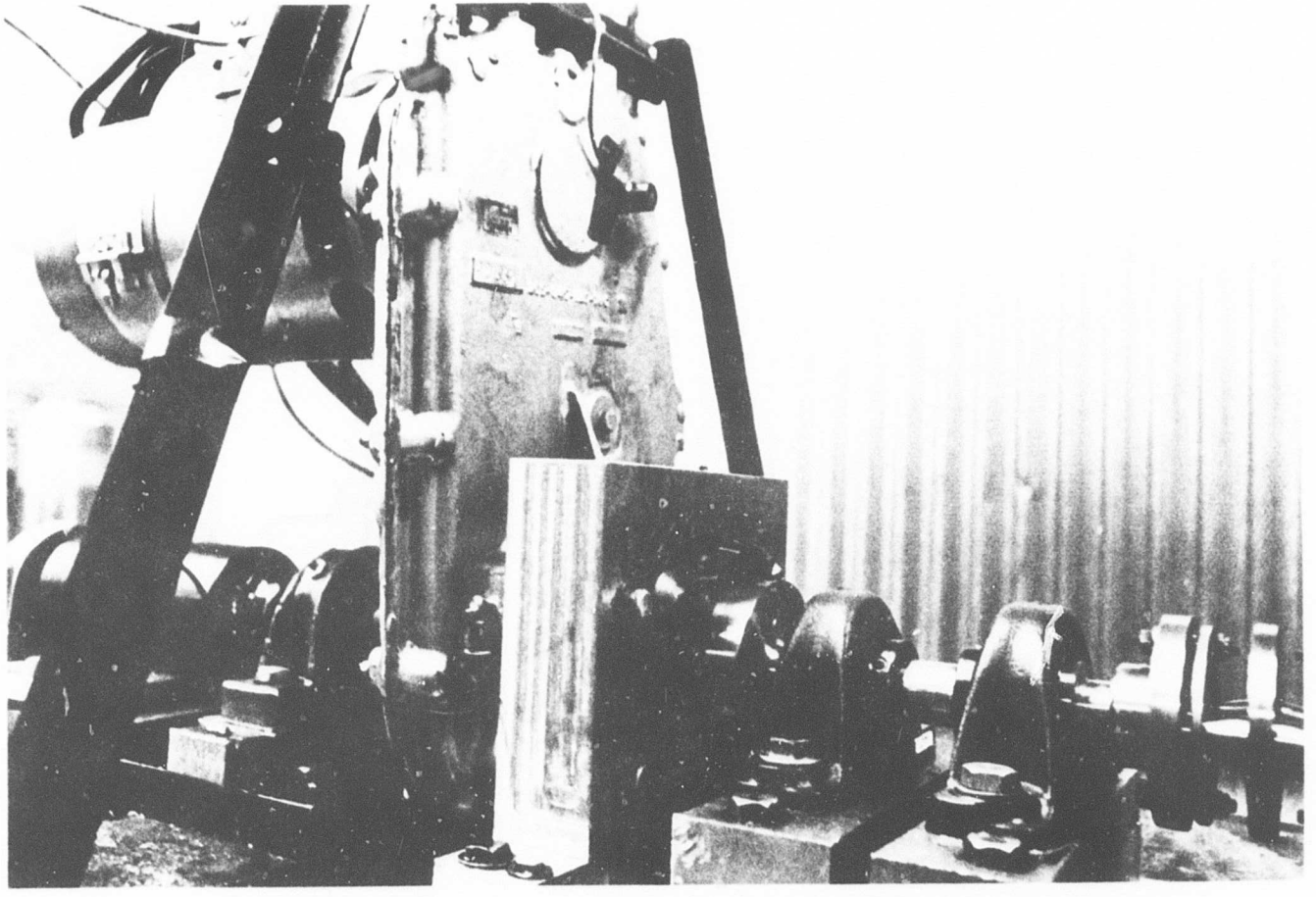

Figure 14. Test Stand Showing Gearbox, Generator, and Sliprings.

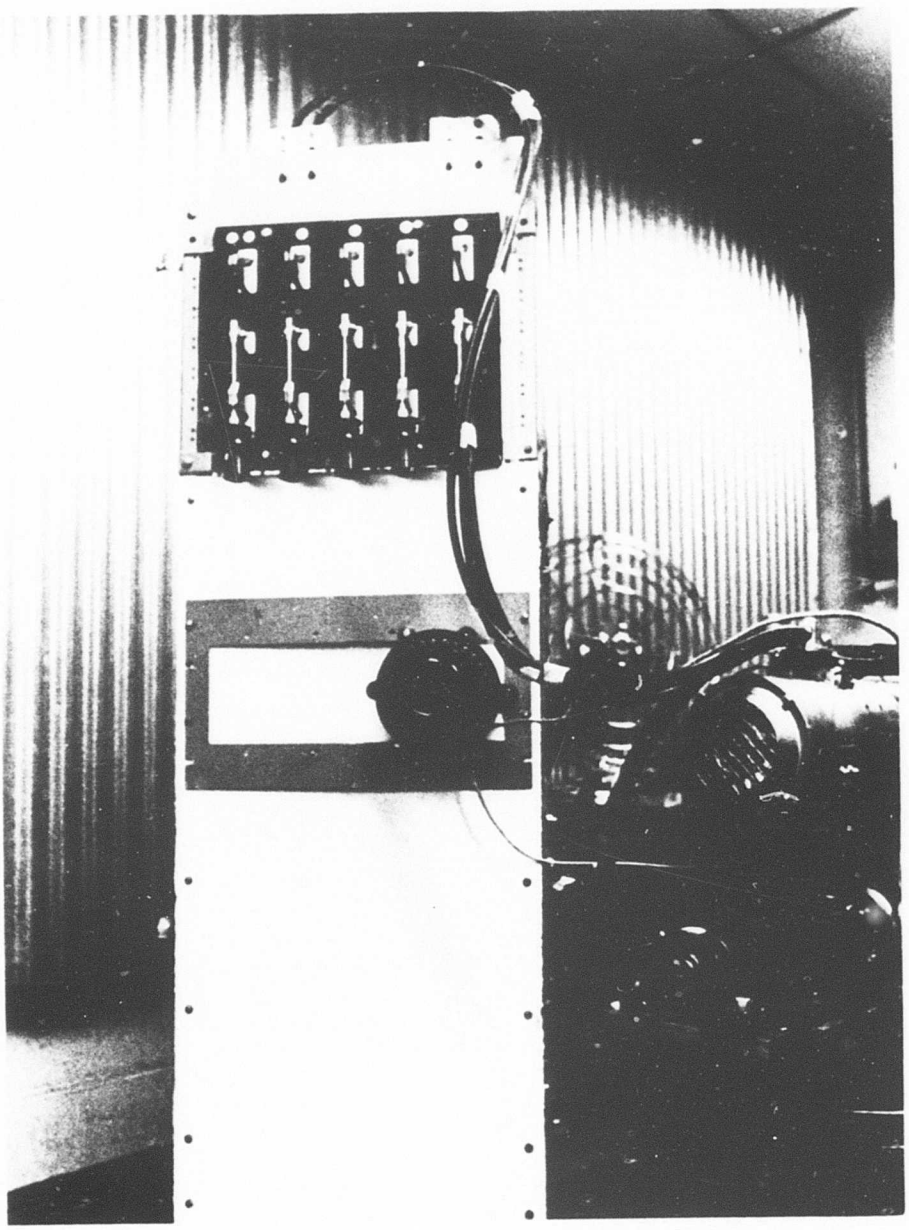

Figure 15. Generator Loading System.

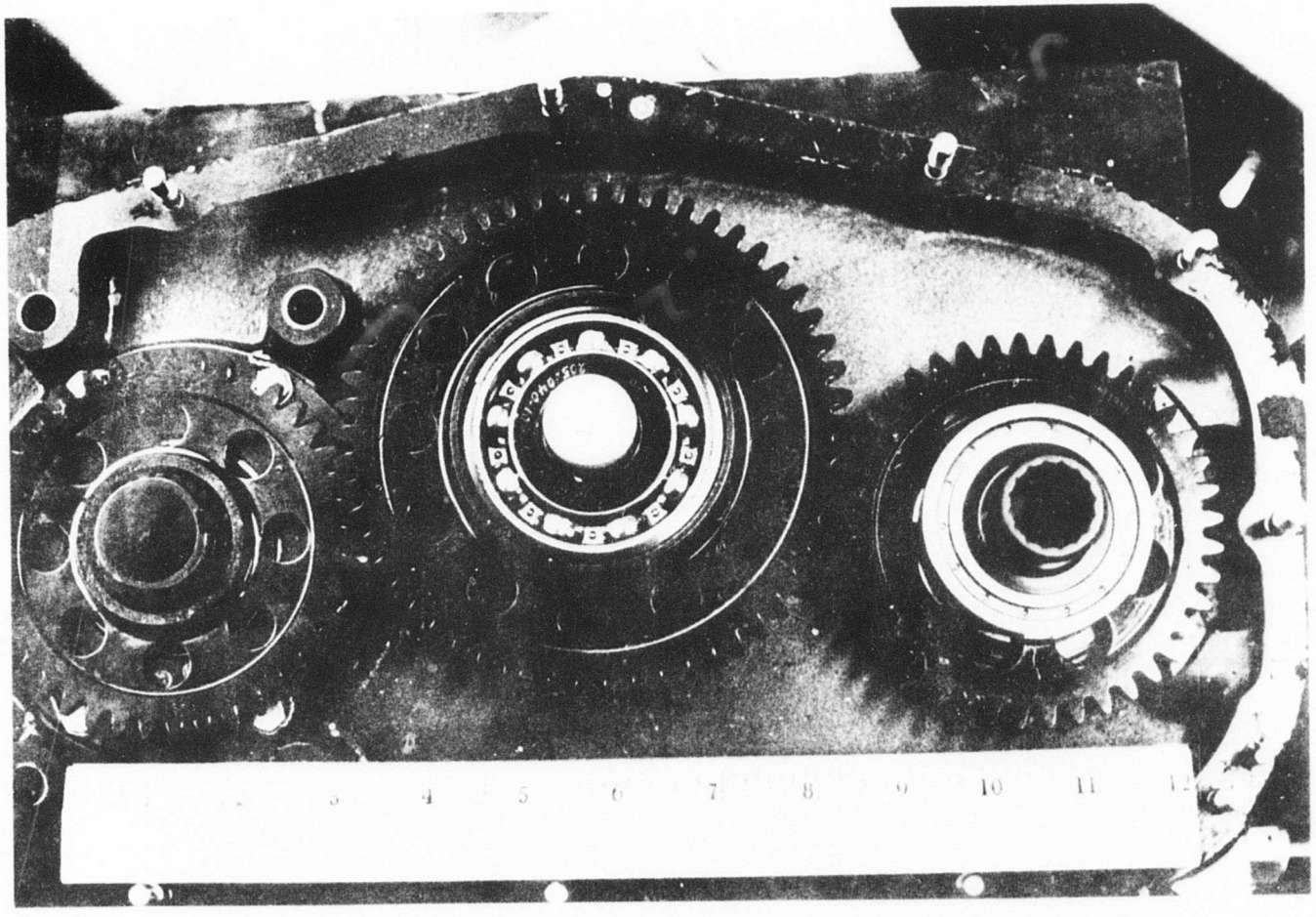

Figure 16. View of Opened Gearbox.

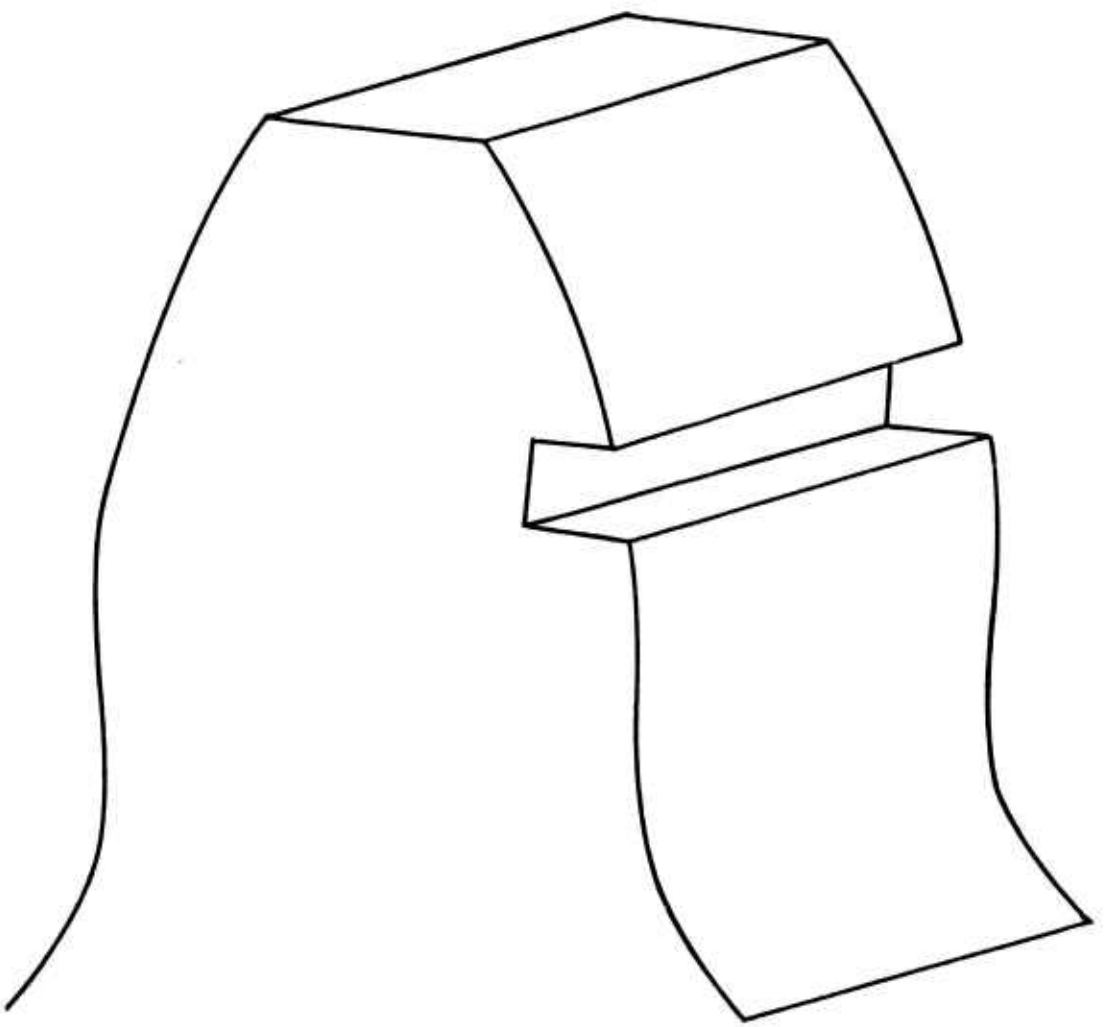

Figure 17. Sketch of Gear Tooth With Fault.

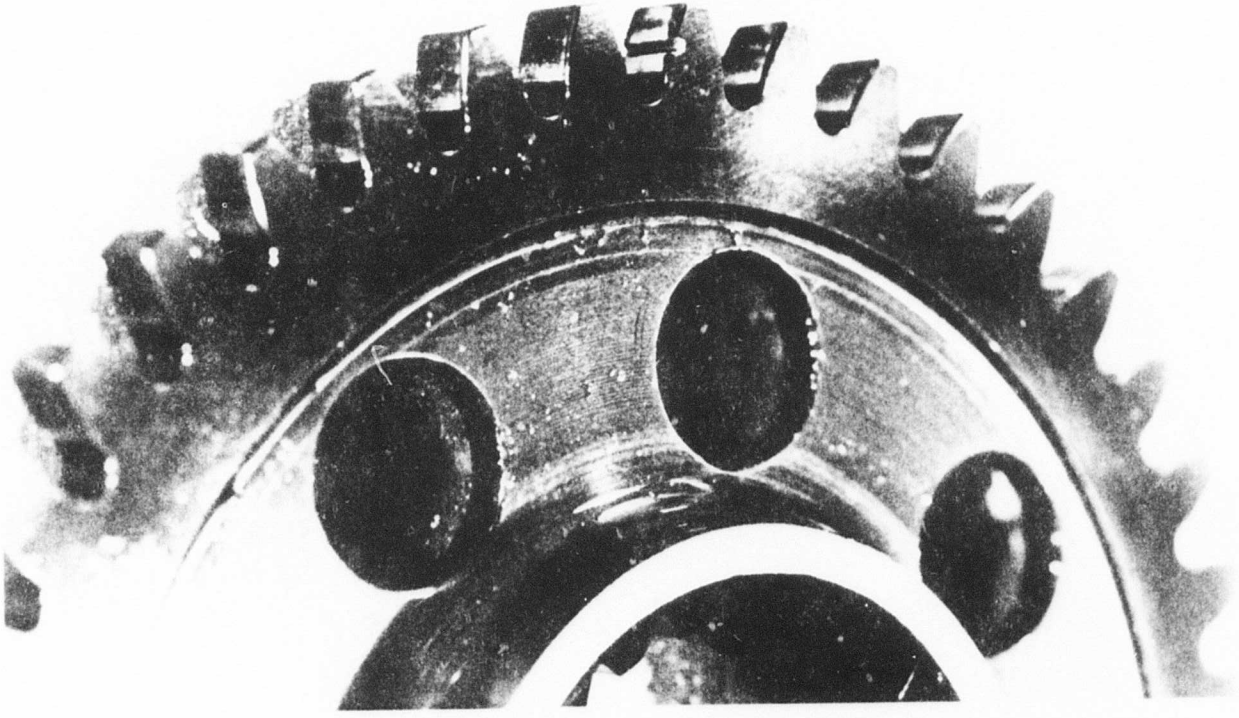

Figure 18. Gear With 0.020-Inch-Wide Tooth Fault.

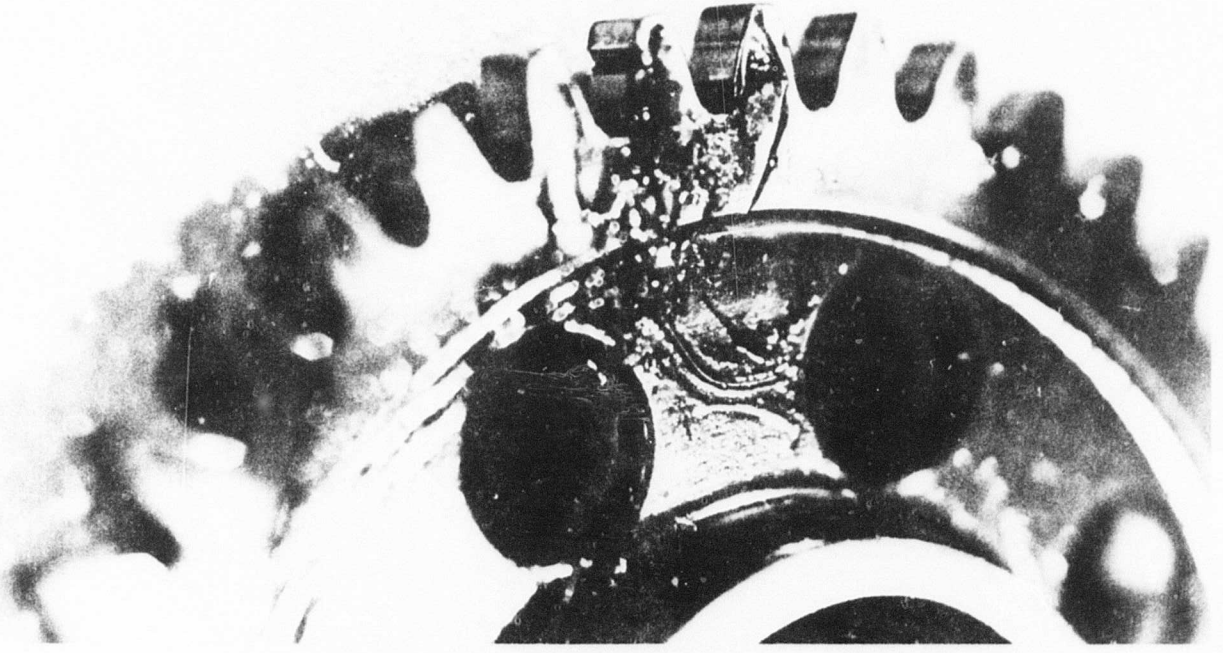

Figure 19. Gear With 0.050-Inch-Wide Tooth Fault.

TABLE I. GEAR PARAMETERS

	Pinion	Idler	Gear
Number of teeth	41	55	41
Diametral pitch (1/in.)	10	10	10
Pressure angle (deg)	20	20	20
Pitch diameter (in.)	4.10	5.5	4.10
Face width (in.)	0.20	0.40	0.20
Circular pitch (in.)	0.3142	0.3142	0.3142

TRANSDUCERS

A number of parameters were monitored during the test program. A wide variety of accelerometer positions are possible on the gearbox. However, three positions appeared to provide the greatest amount of information, and these were used more extensively than others. Figure 20 shows a Brüel and Kjäer 4344 accelerometer which was stud-mounted near the input bearing of the gearbox. Figure 21 shown an Endevco 2215 accelerometer which was epoxied to the face of the gearbox housing. Figure 22 shows a Brüel and Kjäer 4344 accelerometer which was stud-mounted near the output bearings of the gearbox.

Strain gages were mounted at the root fillets of specific gear teeth to provide information on the dynamic strain occurring during meshing. Figure 23 shows a typical mounting configuration of three strain gage bridges on a gear. Active gages were mounted on the dedendum of three consecutive gears. Dummy gages were mounted in the middle of teeth away from the active gages as well as on the opposite face of the gear (not shown in Figure 23). The strain gage signals are transmitted from the gear via a set of 18 channel Superior Carbon Sliprings. The position of the slipring assembly is shown in Figure 14.

Torque and speed were monitored with signals provided by the torquemeter. Output power was monitored with a voltmeter and the knowledge of load resistance.

SIGNAL CONDITIONING AND ANALYSIS EQUIPMENT

Figure 24 shows some of the signal conditioning and analysis equipment used in testing. Kistler, Kristal, and Unholtz Dickie charge amplifiers are used with the accelerometer inputs. Honeywell Accudata strain gage signal conditioners and an input amplifier are used with the strain and torque signals. An EPUT counter is used with the tachometer signal.

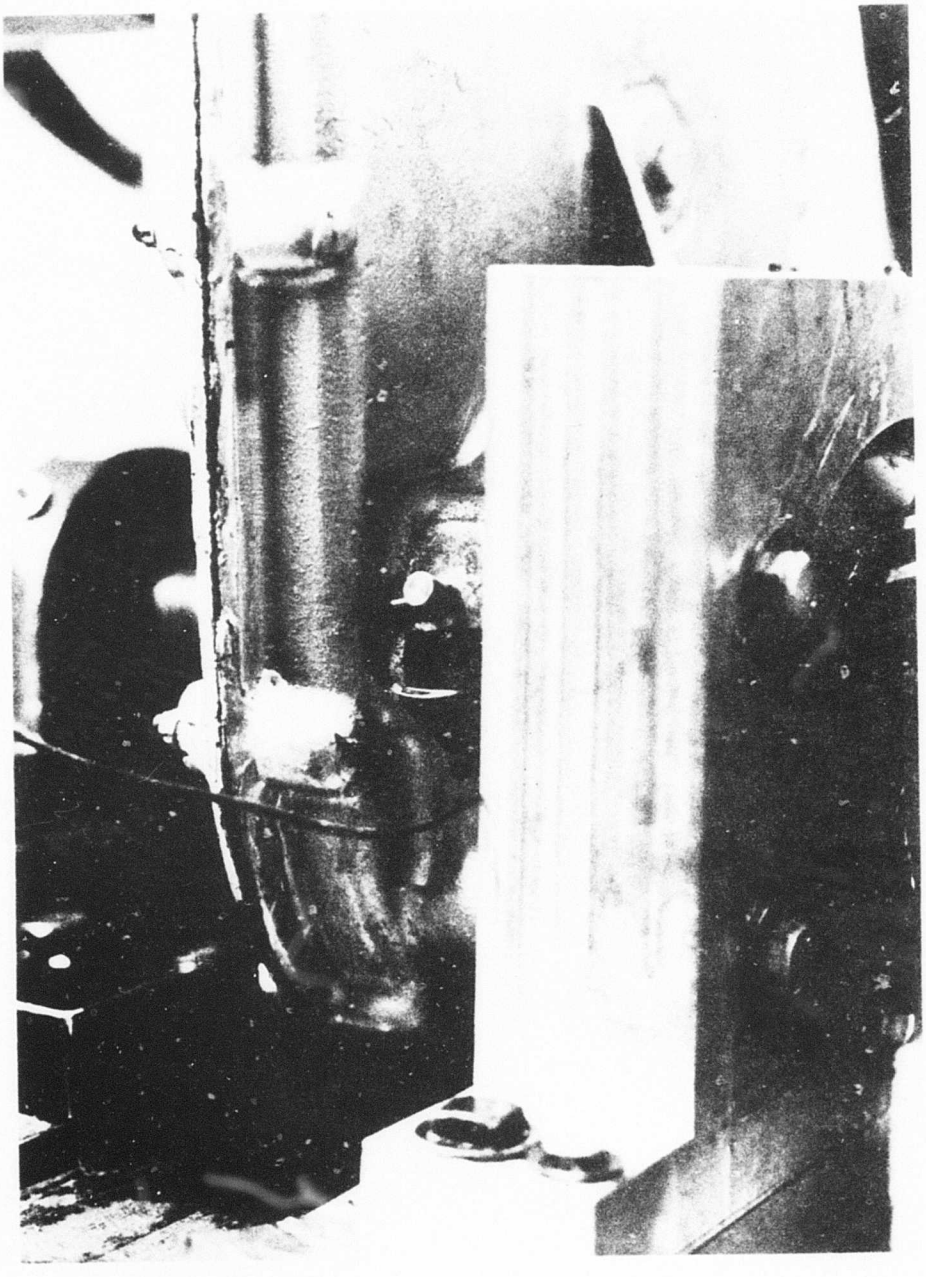

Figure 20. Mounting Position of Accelerometer Near Input Bearing.

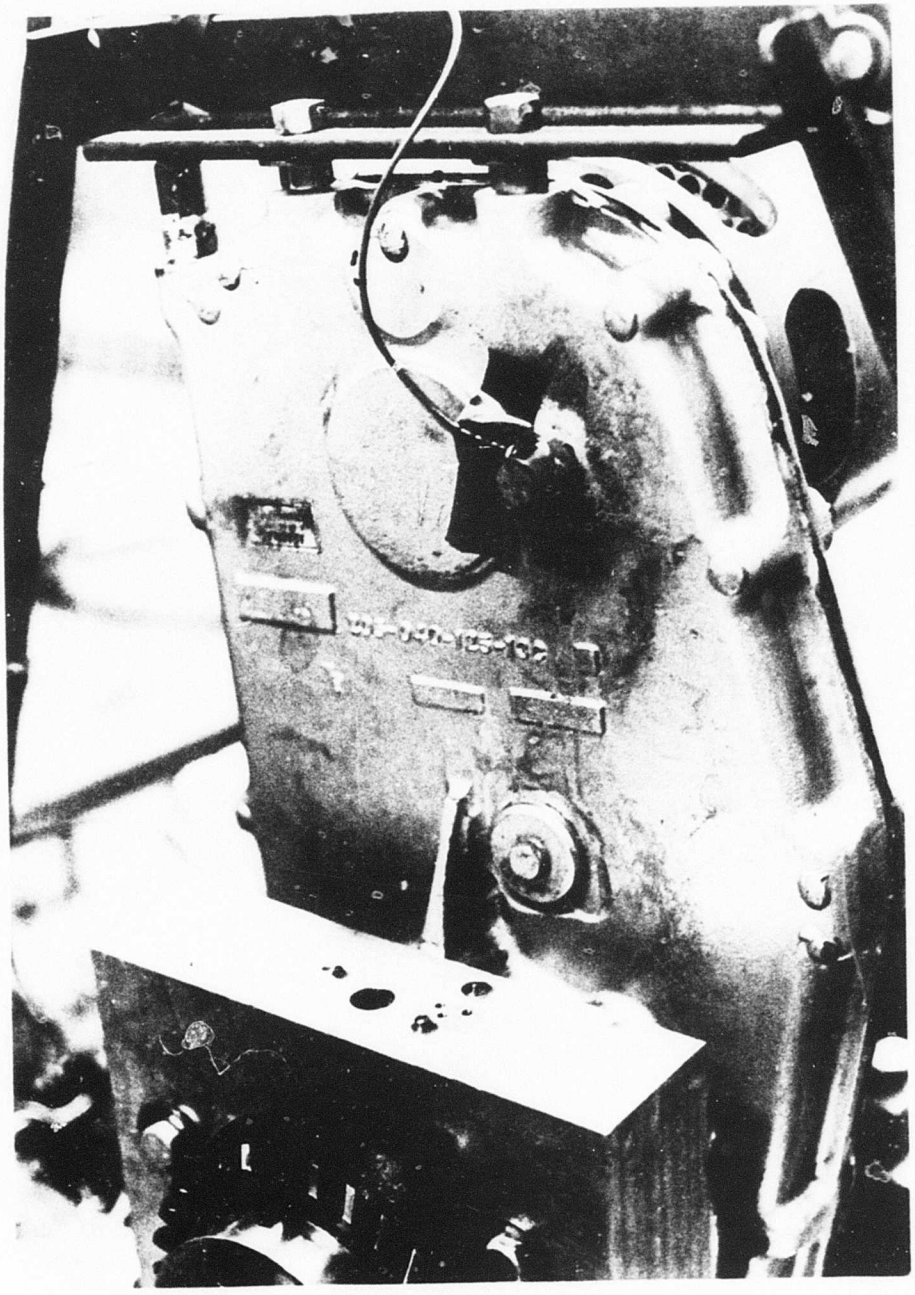

Figure 21. Mounting Position of Accelerometer on Gearbox Housing Face.

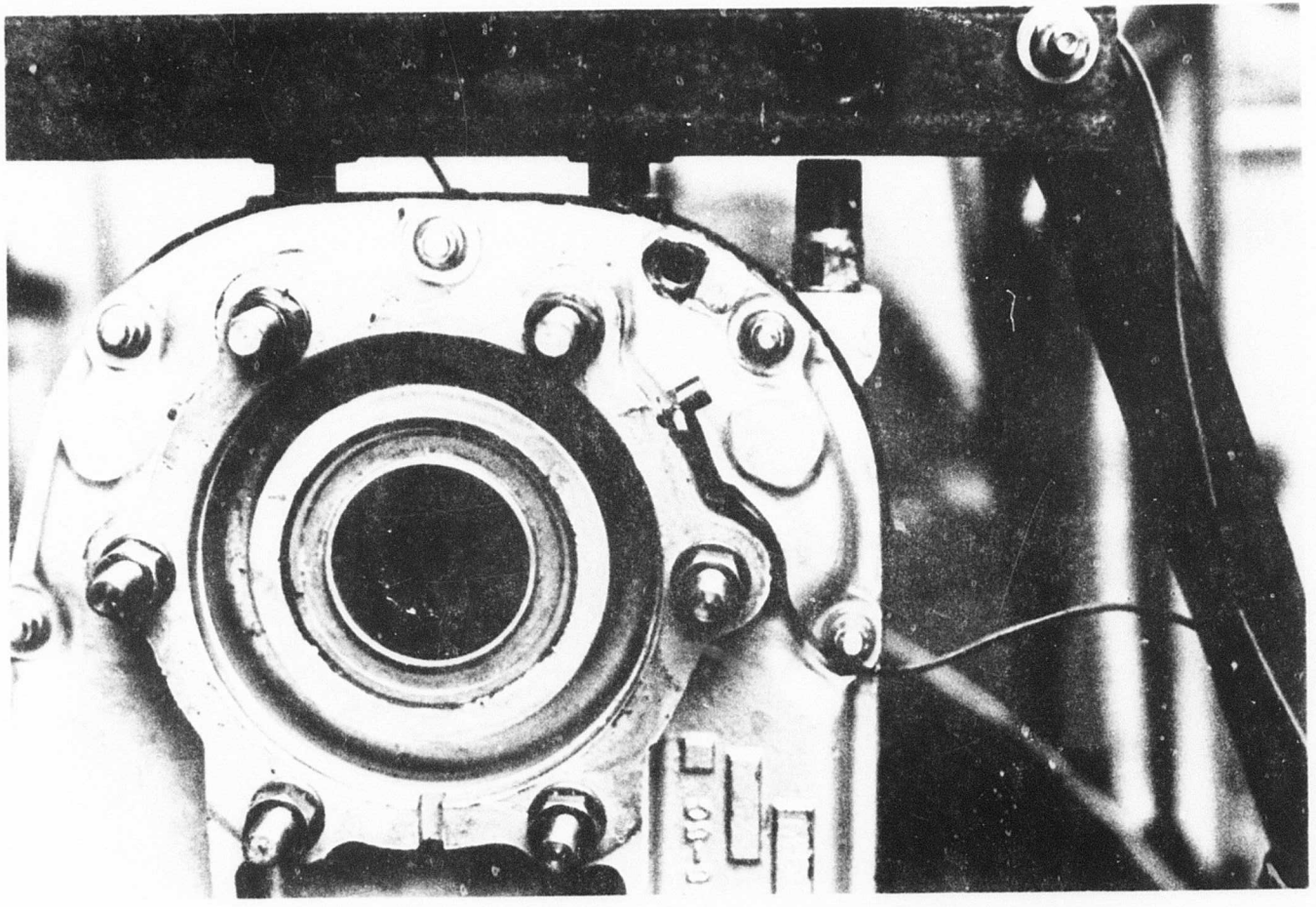

Figure 22. Mounting Position of Accelerometer Near Output Bearing.

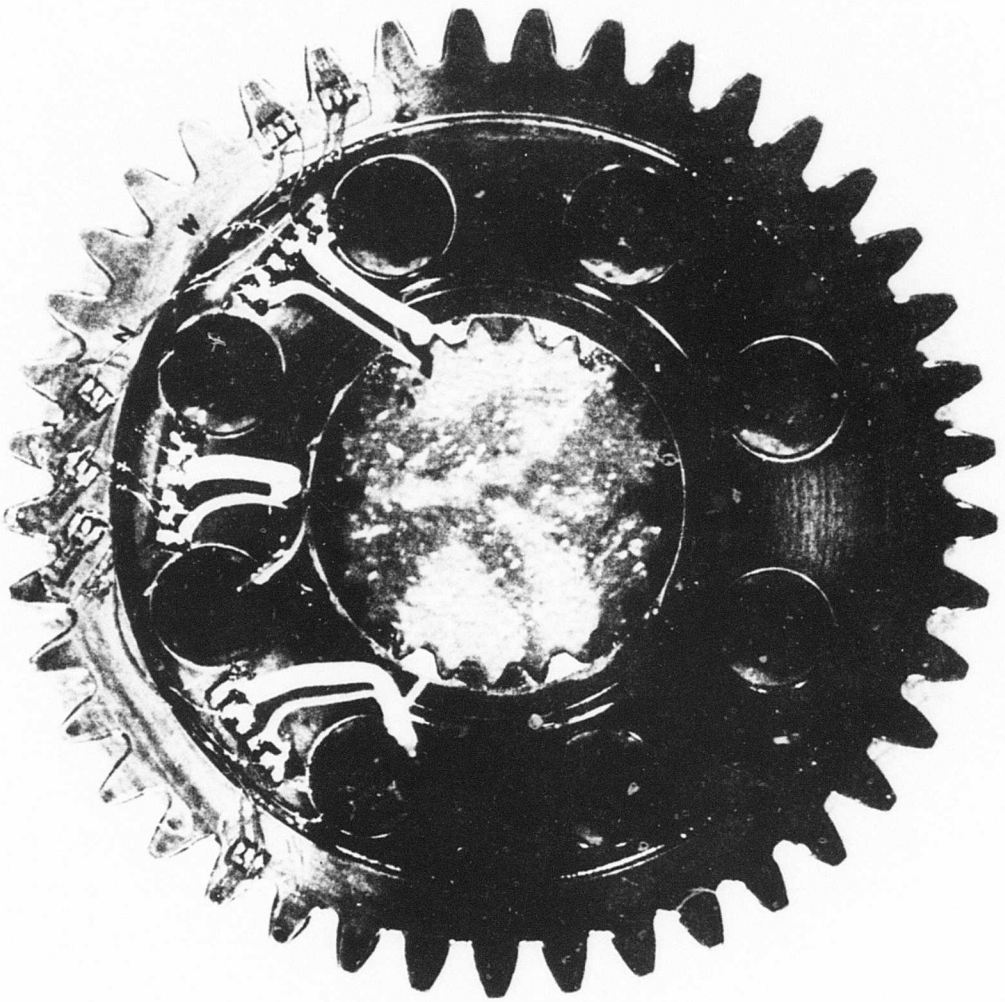

Figure 23. Strain Gaged Gear.

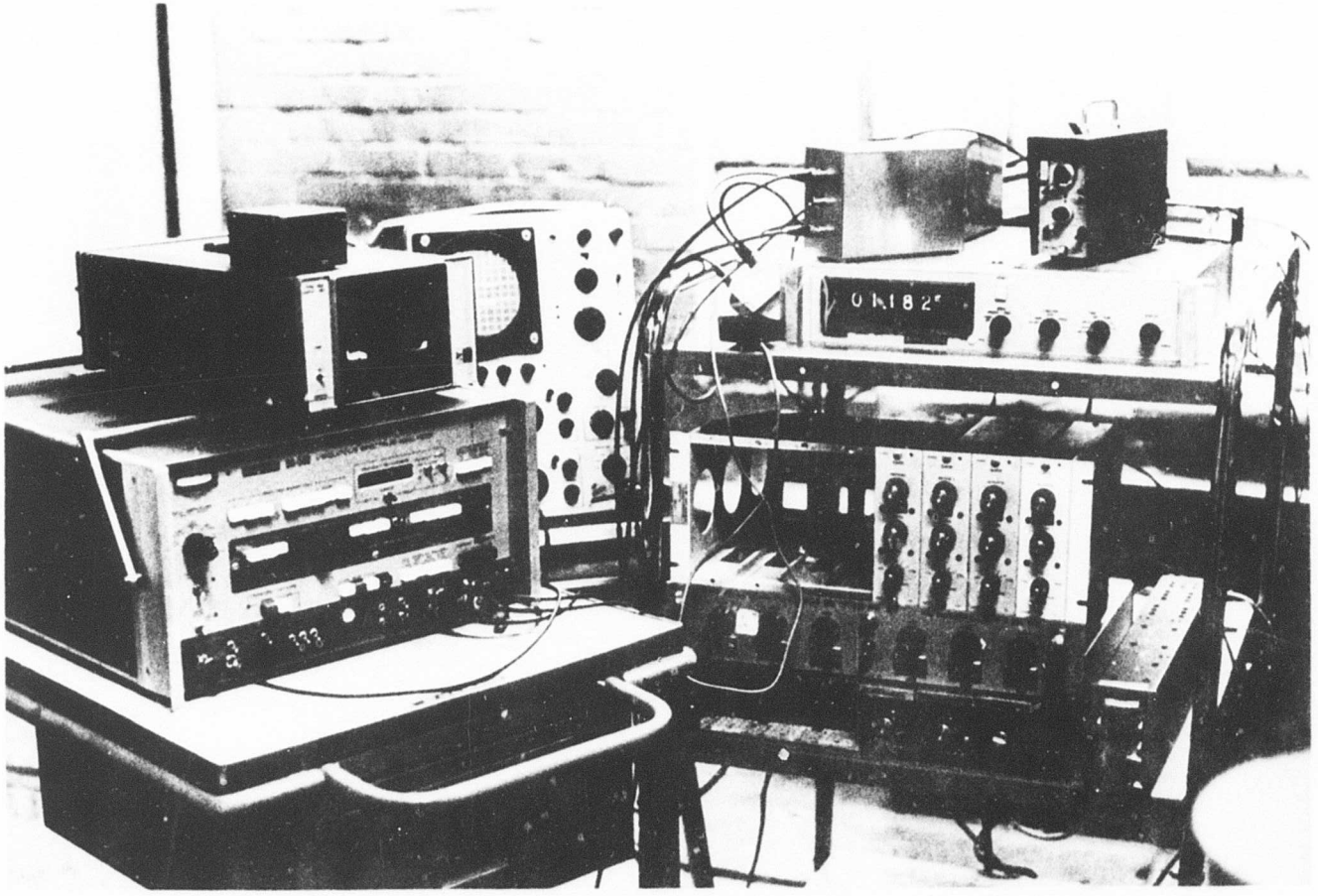

Figure 24. Experimental Data Signal Conditioning and Analysis Equipment.

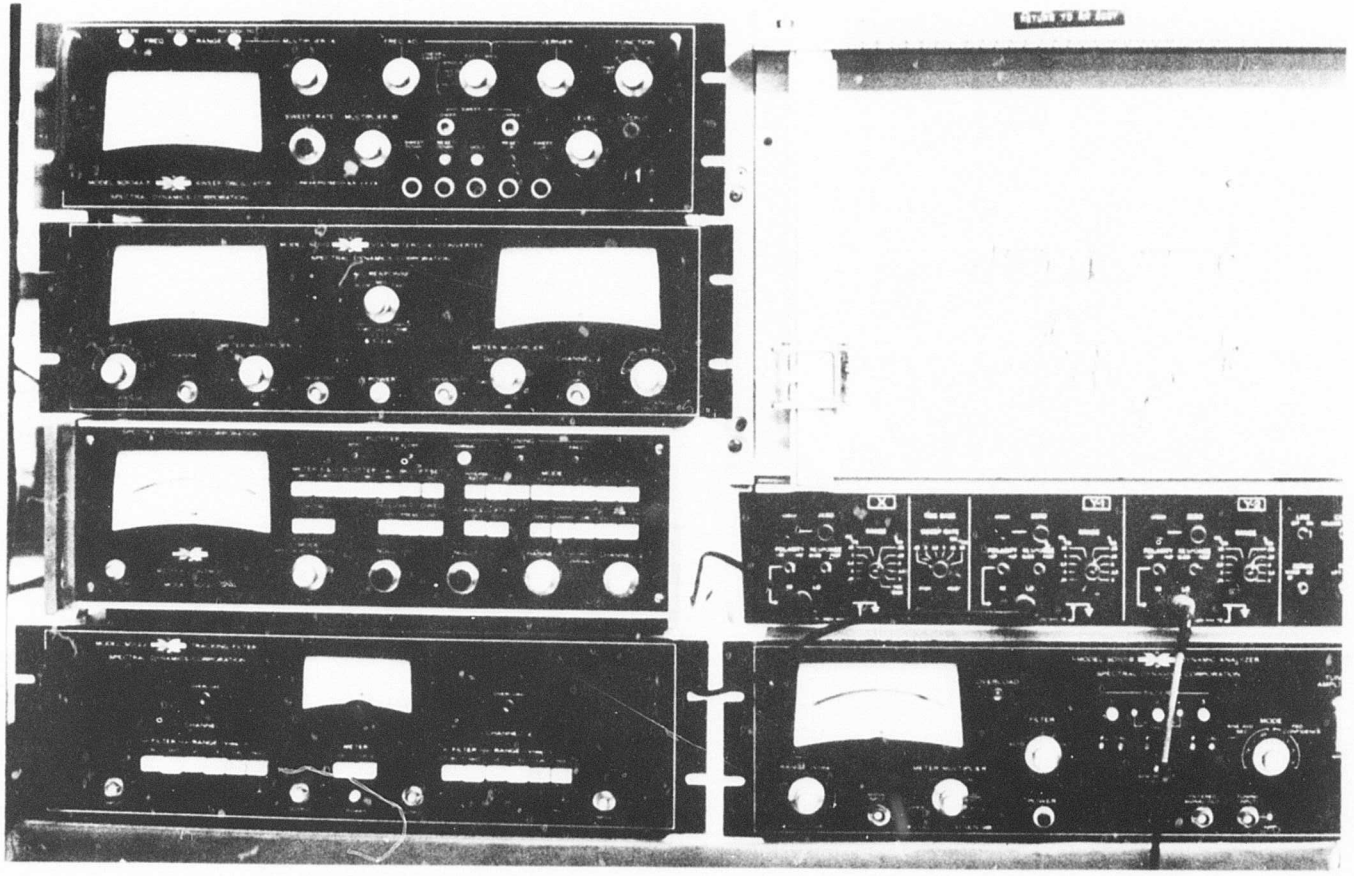

Figure 25. Transfer Function and Impedance Analyzer.

Data were either analyzed on-line or tape-recorded and analyzed later. A Precision Instruments 6100 FM tape recorder with three available channels was used for the tape recording.

Much of the data analysis was done with a Federal Scientific UA-500 Ubiquitous Spectrum Analyzer. This instrument provides the Fourier components of signals fed into it either directly from the instrumentation during test runs or from taped data.

Transfer function and impedance tests were performed on the test stand with the use of the Spectral Dynamics Model SD1002E Mechanical Impedance Systems, shown in Figure 25. Excitation was provided with an MB Electronics 50-pound shaker.

THEORETICAL ANALYSIS

A theoretical analysis of the geared system which was being used for the generation of test data was performed. This analysis resulted in a model which provides both frequency-domain and time-domain response information for the system when all the gears are in good condition and also when gears contain tooth surface faults. The model consists of a torsional dynamic analysis of the geared system and a separate determination of the gear mesh stiffness functions. In both analyses, modifications are incorporated to account for the effects of tooth surface faults.

TORSIONAL DYNAMIC ANALYSIS

The gears contained in the gearbox are modeled as shown in Figure 26, with the equivalent rotational inertias of the gears coupled by a linear spring connecting their base circles. The spring stiffness is a function of the meshing position of the gear teeth.

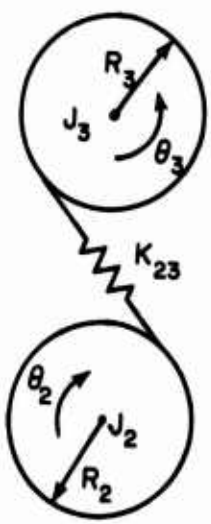

Figure 26. Torsional Model of a Gear Pair.

To determine the overall response of the geared system, a lumped parameter torsional analysis of the system shown in Figure 27 is performed. The following are the pertinent parameters shown in the figure and used in this analysis:

J_1	inertia of shafting and input gear, in.-lb·s^2
J_2	inertia of spur gear pinion, in.-lb·s^2
J_3	inertia of idler spur gear, in.-lb·s^2
J_4	inertia of spur gear, in.-lb·s^2
J_5	inertia of generator, in.-lb·s^2
K_{23}	linear spring coefficient of pinion-idler mesh, lb/in.
B_{23}	linear damping coefficient of pinion-idler mesh, lb/in.·s^{-1}
K_{34}	linear spring coefficient of idler-gear mesh, lb/in.
B_{34}	linear damping coefficient of idler-gear mesh, lb/in.·s^{-1}
K_{t12}	torsional spring coefficient of input shafting, in./lb·rad^{-1}
B_{t12}	torsional damping coefficient of input shafting, in.-lb/rad·s^{-1}
K_{t45}	torsional spring coefficient of spur gear shaft, in.-lb/rad
B_{t45}	torsional damping coefficient of spur gear shaft, in.-lb/rad·s^{-1}
θ_1, θ_2, θ_3, θ_4, θ_5	angular rotation of inertias, rad
e_g	generator output voltage, V
i_g	generator output current, A
R_g	generator output load, Ω
K_g	generator voltage constant, V/rad·s^{-1}
K_T	generator current constant, in.-lb/A
R_2	radius of pinion base circle, in.

R_3 radius of idler base circle, in.

R_4 radius of gear base circle, in.

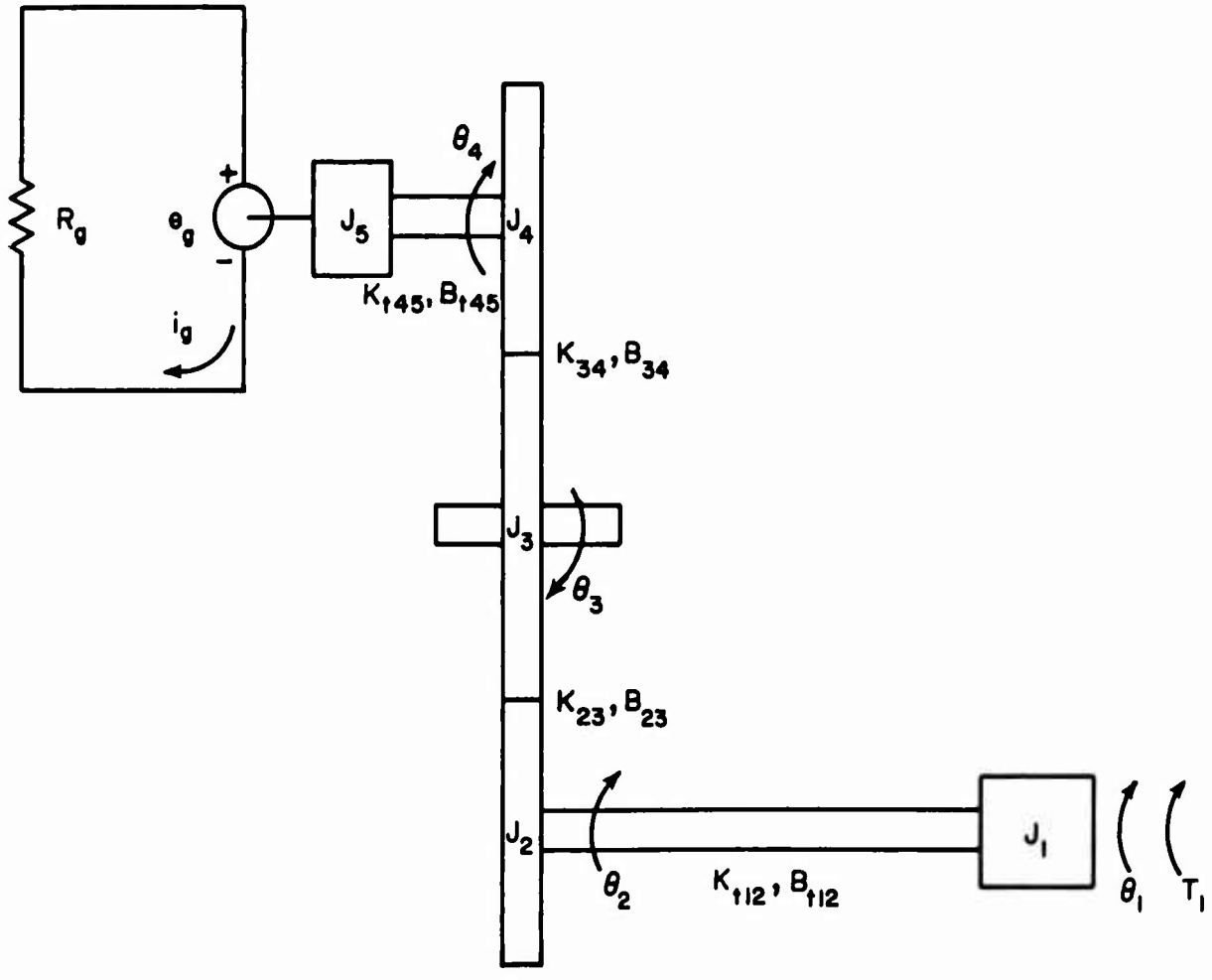

Figure 27. Torsional Model of the Geared System.

The analysis of the torsional mode of vibration of the system was performed since this was expected to be the primary mode of vibration encountered. To translate from the torsional response of the system to lateral accelerations monitored on the gearbox, experimentally generated transfer function information between the gear mesh and the housing is used. The system is excited by both the input driving torque and the variations of the mesh stiffness which occur as a function of gear rotational position.

The electric generator is considered to operate with a constant field voltage and negligible armature inductance. Load resistance is kept at a constant value.

Torque balances for each of the lumps are written as follows:

$$J_1\ddot{\theta}_1 = K_{t12}(\theta_2-\theta_1) + B_{t12}(\dot{\theta}_2-\dot{\theta}_1) + T_1 \tag{5}$$

$$J_2\ddot{\theta}_2 = -K_{t12}(\theta_2-\theta_1) - B_{t12}(\dot{\theta}_2-\dot{\theta}_1) + K_{23}R_2(R_3\theta_3-R_2\theta_2) + B_{23}R_2(R_3\dot{\theta}_3-R_2\dot{\theta}_2) \tag{6}$$

$$J_3\ddot{\theta}_3 = -K_{23}R_3(R_3\theta_3-R_2\theta_2) - B_{23}R_3(R_3\dot{\theta}_3-R_2\dot{\theta}_2) + K_{34}R_3(R_4\theta_4-R_3\theta_3) + B_{34}R_3(R_4\dot{\theta}_4-R_3\dot{\theta}_3) \tag{7}$$

$$J_4\ddot{\theta}_4 = -K_{34}R_4(R_4\theta_4-R_3\theta_3) + B_{34}R_3(R_4\dot{\theta}_4-R_3\dot{\theta}_3) + K_{t45}(\theta_5-\theta_4) + B_{t45}(\dot{\theta}_5-\dot{\theta}_4) \tag{8}$$

$$J_5\ddot{\theta}_5 = -K_{t45}(\theta_5-\theta_4) - B_{t45}(\dot{\theta}_5-\dot{\theta}_4) - K_T i_g \tag{9}$$

Use of Kirchoff's Law on the generator loop yields

$$K_g\dot{\theta}_5 - i_g R_g = 0 \tag{10}$$

It is convenient to first rearrange the equations in the following form:

$$\ddot{\theta}_1 = \frac{1}{J_1}\left[K_{t12}(\theta_2-\theta_1) + B_{t12}(\dot{\theta}_2-\dot{\theta}_1) + T_1\right] \tag{11}$$

$$\ddot{\theta}_2 = \frac{1}{J_2}\left[K_{23}R_2^2\left(\frac{R_3}{R_2}\theta_3-\theta_2\right) + B_{23}R_2^2\left(\frac{R_3}{R_2}\dot{\theta}_3-\dot{\theta}_2\right) - K_{t12}(\theta_2-\theta_1) - B_{t12}(\dot{\theta}_2-\dot{\theta}_1)\right] \tag{12}$$

$$\ddot{\theta}_3 = \frac{1}{J_3}\left[K_{34}R_3R_4\left(\theta_4-\frac{R_3}{R_4}\theta_3\right) + B_{34}R_3R_4\left(\dot{\theta}_4-\frac{R_3}{R_4}\dot{\theta}_3\right) - K_{23}R_3R_2\left(\frac{R_3}{R_2}\theta_3-\theta_2\right) - B_{23}R_3R_2\left(\frac{R_3}{R_2}\dot{\theta}_3-\dot{\theta}_2\right)\right] \tag{13}$$

$$\ddot{\theta}_4 = \frac{1}{J_4}\left[K_{t45}(\theta_5-\theta_4) + B_{t45}(\dot{\theta}_5-\dot{\theta}_4) - K_{34}R_4^2\left(\theta_4 - \frac{R_3}{R_4}\theta_3\right)\right.$$
$$\left. -B_{34}R_4^2\left(\dot{\theta}_4 - \frac{R_3}{R_4}\dot{\theta}_3\right)\right] \tag{14}$$

$$\ddot{\theta}_5 = \frac{1}{J_5}\left[-K_{t45}(\theta_5-\theta_4) - B_{t45}(\dot{\theta}_5-\dot{\theta}_4) - K_T i_g\right] \tag{15}$$

$$i_g = \frac{1}{R_g}K_g\dot{\theta}_5 \tag{16}$$

Parameters representing a relative rotation between the system inertias are now defined as

$$\psi_1 = \theta_2 - \theta_1 \tag{17}$$

$$\psi_2 = \frac{R_3}{R_2}\theta_3 - \theta_2 \tag{18}$$

$$\psi_3 = \theta_4 - \frac{R_3}{R_4}\theta_3 \tag{19}$$

$$\psi_4 = \theta_5 - \theta_4 \tag{20}$$

The utility of these parameters is seen if we consider the response of the system rotational angles. Figure 28 shows a typical response curve of one of the angles, θ_1. The response is a perturbation about a steadily increasing ramp function. This ramp increases at a rate corresponding to the input speed. The perturbations are the dynamic effects of the system's stiffnesses, inertias, and damping. Unless the driving shafts reverse direction, the rotational angles will continue to grow. As time progresses, the percentage variation due to the dynamic perturbations will become smaller and smaller. Computationally, the perturbations become more difficult to resolve. And, since vibrations caused by this relative motion between the inertias are the desired results, it is these parameters which are of primary interest.

The new parameters may be differentiated once with the result

$$\dot{\psi}_1 = \dot{\theta}_2 - \dot{\theta}_1 \tag{21}$$

$$\dot{\psi}_1 = \frac{R_3}{R_2}\dot{\theta}_3 - \dot{\theta}_2 \tag{22}$$

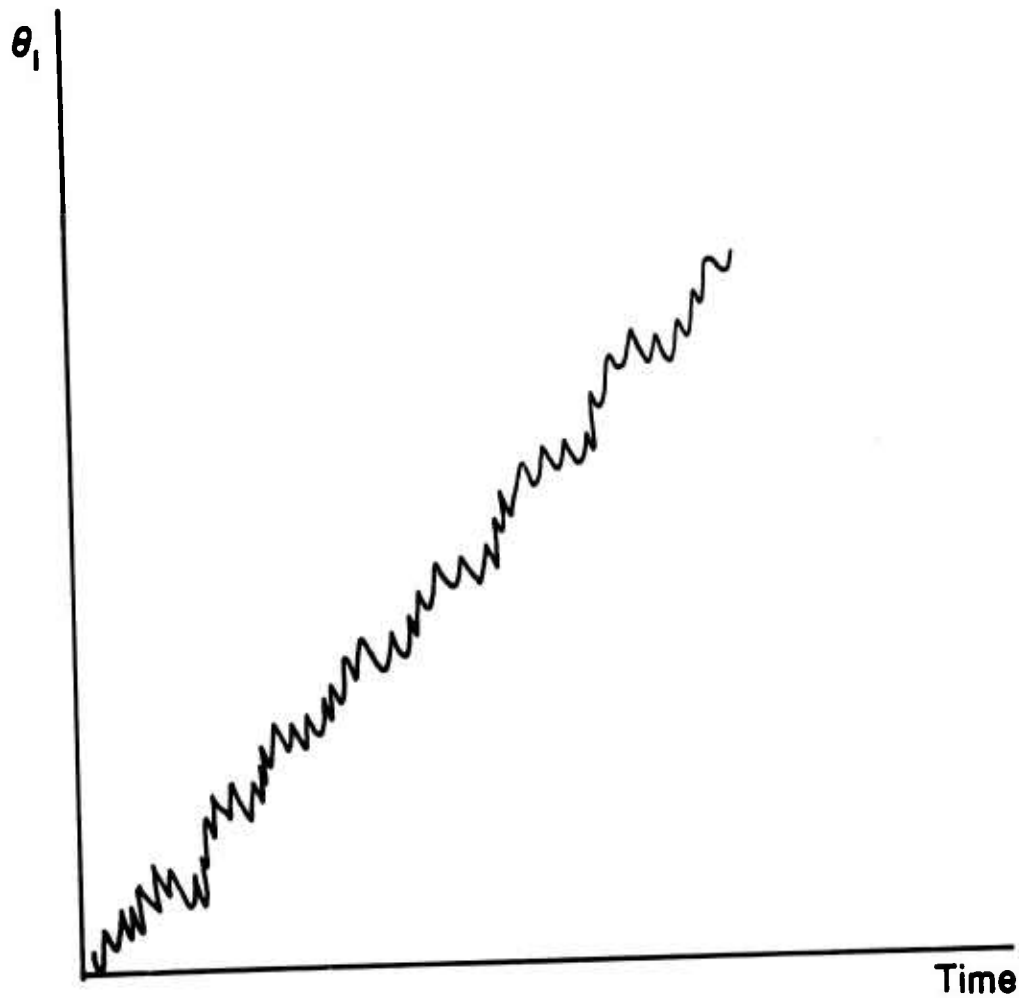

Figure 28. Typical Rotational Response of a Gear.

$$\dot{\psi}_3 = \dot{\theta}_4 - \frac{R_3}{R_4}\dot{\theta}_3 \tag{23}$$

$$\dot{\psi}_4 = \dot{\theta}_5 - \dot{\theta}_4 \tag{24}$$

Combining Equations (11-24) yields

$$\ddot{\theta}_1 = \frac{1}{J_1}\left(K_{t12}\psi_1 + B_{t12}\dot{\psi}_1 + T_1\right) \tag{25}$$

$$\ddot{\theta}_2 = \frac{1}{J_2}\left(K_{23}R_2^2\psi_2 + B_{23}R_2^2\dot{\psi}_2 - K_{t12}\psi_1 - B_{t12}\dot{\psi}_1\right) \tag{26}$$

$$\frac{R_3}{R_2}\ddot{\theta}_3 = \frac{R_3}{R_2}\frac{1}{J_3}\left(K_{34}R_3R_4\psi_3 + B_{34}R_3R_4\dot{\psi}_3 - K_{23}R_3R_2\psi_2 - B_{23}R_3R_2\dot{\psi}_2\right) \tag{27}$$

$$\ddot{\theta}_4 = \frac{1}{J_4}\left(K_{t45}\psi_4 + B_{t45}\dot{\psi}_4 - K_{34}R_4^2\psi_3 - B_{34}R_4^2\dot{\psi}_3\right) \tag{28}$$

$$\ddot{\theta}_5 = \frac{1}{J_5}\left(-K_{t45}\psi_4 - B_{t45}\dot{\psi}_4 - K_T i_g\right)$$

$$i_g = \frac{1}{R_g}K_g\dot{\theta}_5 \tag{16}$$

In the system analyzed,

$$R_2 = R_4 \tag{30}$$

Thus,

$$\frac{R_3}{R_2} = \frac{R_3}{R_4} \tag{31}$$

Using Equation (31) and differentiating Equations (20-23) we find:

$$\ddot{\psi}_1 = \ddot{\theta}_2 - \ddot{\theta}_1 \tag{32}$$

$$\ddot{\psi}_2 = \frac{R_3}{R_2}\ddot{\theta}_3 - \ddot{\theta}_2 \tag{33}$$

$$\ddot{\psi}_3 = \ddot{\theta}_4 - \frac{R_3}{R_2}\ddot{\theta}_3 \tag{34}$$

$$\ddot{\psi}_4 = \ddot{\theta}_5 - \ddot{\theta}_4 \tag{35}$$

Equations (24-29) may now be combined with Equations (32-35). It should be noted that these equations contain position-varying coefficients due to the gear stiffness function. This fact eliminates the possibility of an easily

determined closed-form solution for system response. Therefore, the solution is obtained by using a numerical intergration scheme via CSMP (Continuous System Modelling Program) on the IBM 370/165, as explained in Appendix II.

GEAR STIFFNESS CALCULATIONS

As previously discussed, the mesh stiffness of a gear varies as a function of gear rotational position. This variation is a result of both the complex gear tooth shape and the load-sharing which is exhibited between gear tooth pairs. The approach which was taken to determine the tooth stiffness function was a combination of an elastic strain energy approach and a classical Hertzian contact procedure developed by Weber[32] and used by Richardson,[19] Wang,[47] and others. The analysis considers all tooth stiffness to be concentrated in the tooth mesh; i.e., the gear web stiffness is considered negligible.

The generalized approach is to separately determine the tooth-bending and Hertzian compliances. These are then summed to provide total tooth pair compliance. Load-sharing considerations are then used to determine the total mesh stiffness function.

In calculating the stiffness functions, a static analysis is performed with respect to tooth geometry. The teeth are assumed to mesh solely along the line of action. Any dynamic actions or tooth errors which will cause motion off the line of action are not included in this analysis. Such meshing action would cause changes in load-sharing and would require an iterative solution procedure in order to locate the actual points of tooth contact.

Bending Compliance

Figure 29 shows the tooth model as analyzed. The force F_L is imposed on the tooth at a given contact position. Based on the contact position, an angle θ (the angle between the direction of force application and a perpendicular to the tooth centerline) and the height Y_L above the tooth root circle are determined. Using these two parameters, the load force is resolved into a moment M, a shear force Q, and a normal force N, all referenced to the tooth centerline. These are expressed as follows:

$$Q = F_L \cos\theta \tag{36}$$

$$N = F_L \sin\theta \tag{37}$$

$$M = Q(Y_L - Y) \tag{38}$$

Coordinates used are Y (the distance from the tooth root circle at any given position on the tooth) and X(Y) (the half-thickness of the tooth at any point).

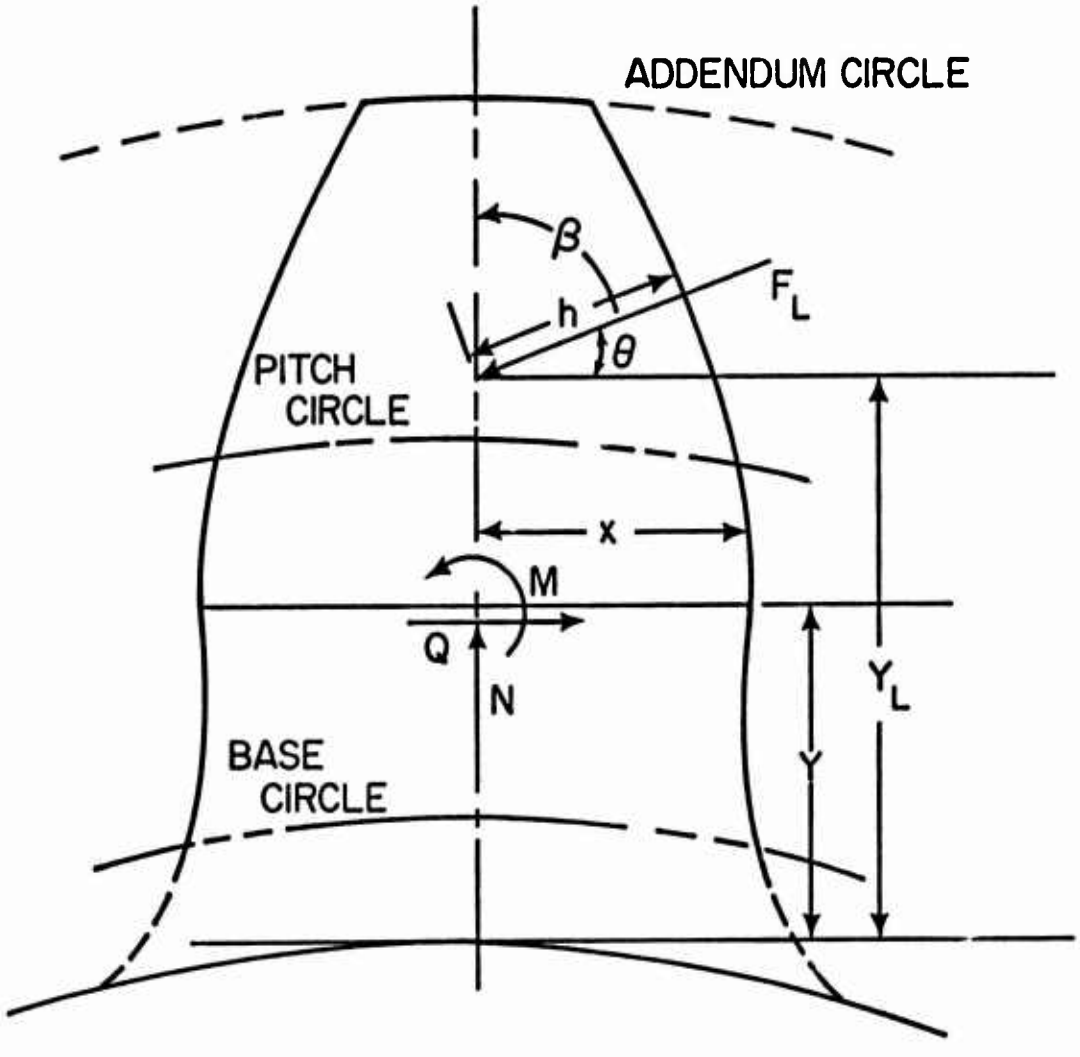

Figure 29. Tooth Model Used in Stiffness Calculations.

The deflection work is equated to the strain energy to give

$$\frac{1}{2} F_L \delta_B = \frac{1}{2} \int_0^{Y_L} \frac{M^2}{EI} dY + \frac{1}{2} \int_0^{Y_L} \frac{kQ^2}{GA} dY + \frac{1}{2} \int_0^{Y_L} \frac{N^2}{EA} dY \tag{39}$$

where δ_B = tooth deflection due to bending, in.
F_L = force imposed upon the tooth, lb
M = moment on tooth resolved to tooth centerline, in.-lb
E = Young's modulus, lb/in.^{2}
I = tooth moment of inertia, in.^{4}
k = correction factor used to account for nonuniform shear distribution
Q = shear on tooth resolved to tooth centerline, lb
A = tooth cross-sectional area, in.^{2}
N = normal force on tooth referenced to tooth centerline, lb

$$I = \frac{W(2X)^3}{12} \tag{40}$$

$$A = W(2X) \tag{41}$$

where 2X = thickness of tooth, in.

Combining Equations (38-41) and dividing by 1/2 F_L gives

$$\delta_B = \frac{1}{F_L} \int_0^{Y_L} \frac{12Q^2(Y_L-Y)^2}{EW(2X)^3} dY + \frac{1}{F_L} \int_0^{Y_L} \frac{kQ^2}{GW(2X)} dY + \frac{1}{F_L} \int_0^{Y_L} \frac{N^2}{EW(2X)} dY \tag{42}$$

A new parameter F_o is defined to represent the normalized tooth force

$$F_o = \frac{F_L}{W} \tag{43}$$

where W = facewidth, in.

Combining Equations (36-42) gives

$$\delta_B = \frac{12F_o \cos^2(\theta)}{E} \int_0^{Y_L} \frac{(Y_L-Y)^2}{(2X)^3} dy + \frac{kF_o \cos^2(\theta)}{G} \int_0^{Y_L} \frac{dy}{(2X)} + \frac{F_o \sin^2(\theta)}{E} \int_0^{Y_L} \frac{dy}{(2X)} \tag{44}$$

A shear correction factor of 1.2 (that used for rectangular beams)[50] is also used with the resulting bending compliance expression

$$C_{mB} = \frac{\delta_B}{F_o} = \frac{12\cos^2(\theta)}{E}\int_0^{Y_L}\frac{(Y_L-Y)^2}{(2X)^3}\,dY + \left[\frac{1.2\cos^2(\theta)}{G} + \frac{\sin^2(\theta)}{E}\right]\int_0^{Y_L}\frac{dY}{(2X)} \tag{45}$$

It should be noted that this compliance is defined with respect to a given tooth meshing position through the parameters Y, X, Y_L, and θ.

Hertzian Compliance

The equations used to describe the Hertzian or contact deflection and, thus, Hertzian compliance are a modification of those used to describe contact between two cylinders.[51,52] First, the width of the contact strip (b) between the two contacting teeth is found:

$$b = \sqrt{\frac{4F_o}{\pi}\left(\frac{r_G r_P}{r_G+r_P}\right)\frac{2}{E}(1-\nu)^2} \tag{46}$$

where
- b = width of contact strip, in.
- r_G = distance from contact point to tangent line of base circles on gear, in.
- r_P = distance from contact point to tangent line of base circles on pinion, in.
- ν = Poisson's ratio

The Hertzian deflection is now expressed as

$$\delta = \frac{2F_o(1-\nu^2)}{\pi E}\left[\ell n\frac{2h_G}{b} + \ell n\frac{2h_P}{b} - \frac{\nu}{1-\nu}\right] \tag{47}$$

where
- h_G = distance from contact point to the tooth centerline of gear along the angle of tooth loading, in.
- h_P = distance from contact point to the tooth centerline of pinion along the angle of tooth loading, in.

Expressing this in terms of compliance,

$$C_H = \frac{\delta_H}{F_o} = \frac{2(1-\nu)^2}{\pi E}\left[\ell n\frac{2h_G}{b} + \ell n\frac{2h_P}{b} - \frac{\nu}{1-\nu}\right] \tag{48}$$

It should be noted in the expressions for Hertzian compliance that a non-linearity with respect to load force is involved; i.e., the width of the contact strip is a function of load force. In calculation of this compliance, the mean value of tooth force is used to find the contact width.

Mesh Stiffness

Equations (45-47) are solved to provide compliance values as a function of meshing position. Details of geometric relationships and computations are given in Appendixes III and IV. To find overall mesh stiffness, an expression is first used for gear pair total compliance; i.e.,

$$C_{Total} = C_{B\ gear} + C_{B\ pinion} + C_H \tag{49}$$

The gear pair stiffness is the inverse of this compliance; i.e.,

$$K_{pair} = \frac{1}{C_{Total}} \tag{50}$$

To determine the complete mesh stiffness function, tooth pair load sharing must be introduced. Load sharing occurs at the distance of the normal pitch from either end of the line of action as shown in Figure 30. This allows determination of the positions at which more than one tooth pair are in contact and, thus, where load-sharing must be included in the analysis.

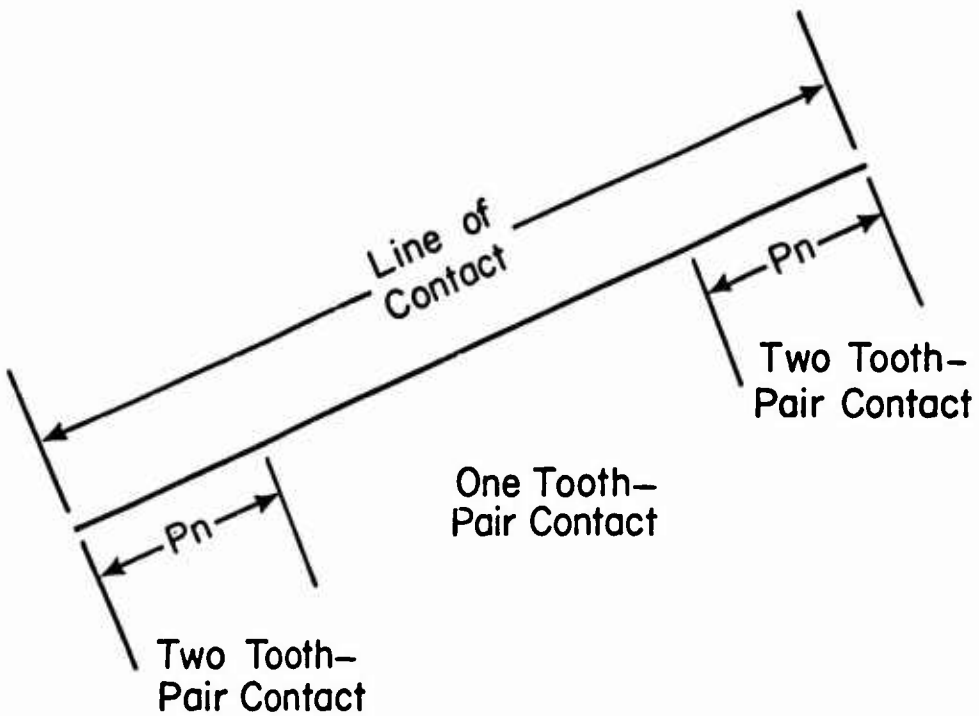

Figure 30. Tooth Load Sharing Positions.

When more than one tooth pair are in contact, the constraint that the rigid body motion of each pair must be equal is used.

$$\delta_1 = \frac{F_1}{K_1} \tag{51}$$

$$\delta_2 = \frac{F_2}{K_2} \tag{52}$$

$$\delta = \delta_1 = \delta_2 \tag{53}$$

$$F_{Total} = F_1 + F_2 \tag{54}$$

F_1 = force on first tooth pair, lb
K_1 = stiffness of first tooth pair, lb/in.
δ_1 = deflection of first tooth pair, in.
F_2 = force on second tooth pair, lb
K_2 = stiffness of second tooth pair, lb/in.
δ_2 = deflection of second tooth pair, in.
F_{Total} = total force on mesh, lb

Combining Equations (51-54), we get

$$\frac{F_{Total}}{\delta} = K_1 + K_2 \tag{55}$$

Thus, to compute the effective mesh stiffness, the individual stiffnesses are added in the manner of springs in parallel. Figure 31 is a graphical representation of this procedure. This stiffness, which is used in the torsional dynamic analysis, it represented as a periodic function of gear rotation.

EFFECT OF FAULTS

The previous analysis referred to gear in "good" condition, i.e., exhibiting no tooth surface faults. To predict the response of gears having faults, two modifications were made in the analysis. A recalculation of stiffness to include the fault effect on the stiffness functions was m de. As an approximation to the tooth impact which occurs at the mesh, a torque impact was also introduced into the torsional dynamic equations.

Stiffness for Tooth With Fault

The first manifestation of the tooth surface fault is introduced in terms of the tooth thickness (2X). The thickness function is modified by the amount of material which is missing due to the fault (see Figure 32). This change in thickness causes a change in the gear tooth bending compliance.

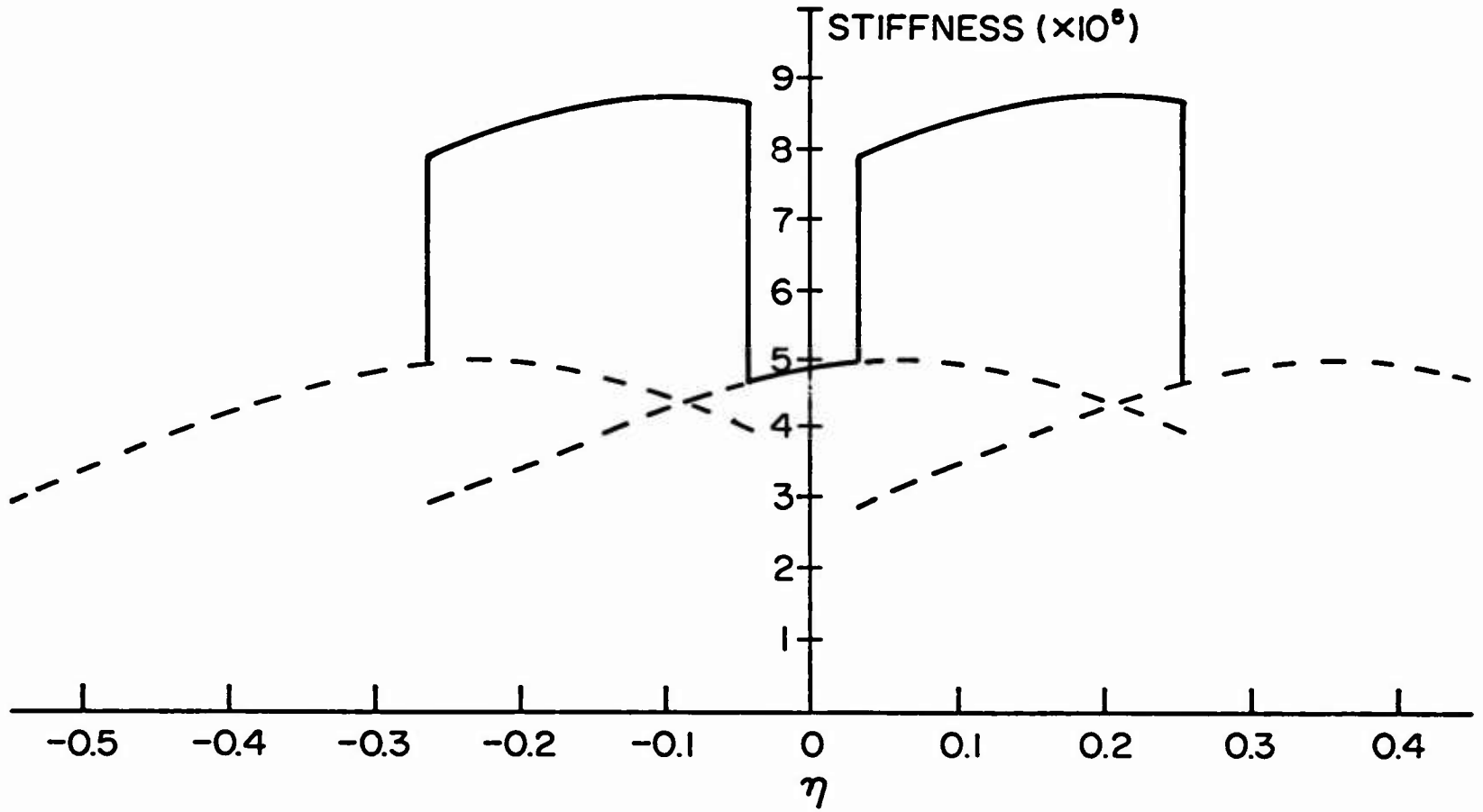

Figure 31. Calculation of Gear Stiffness.

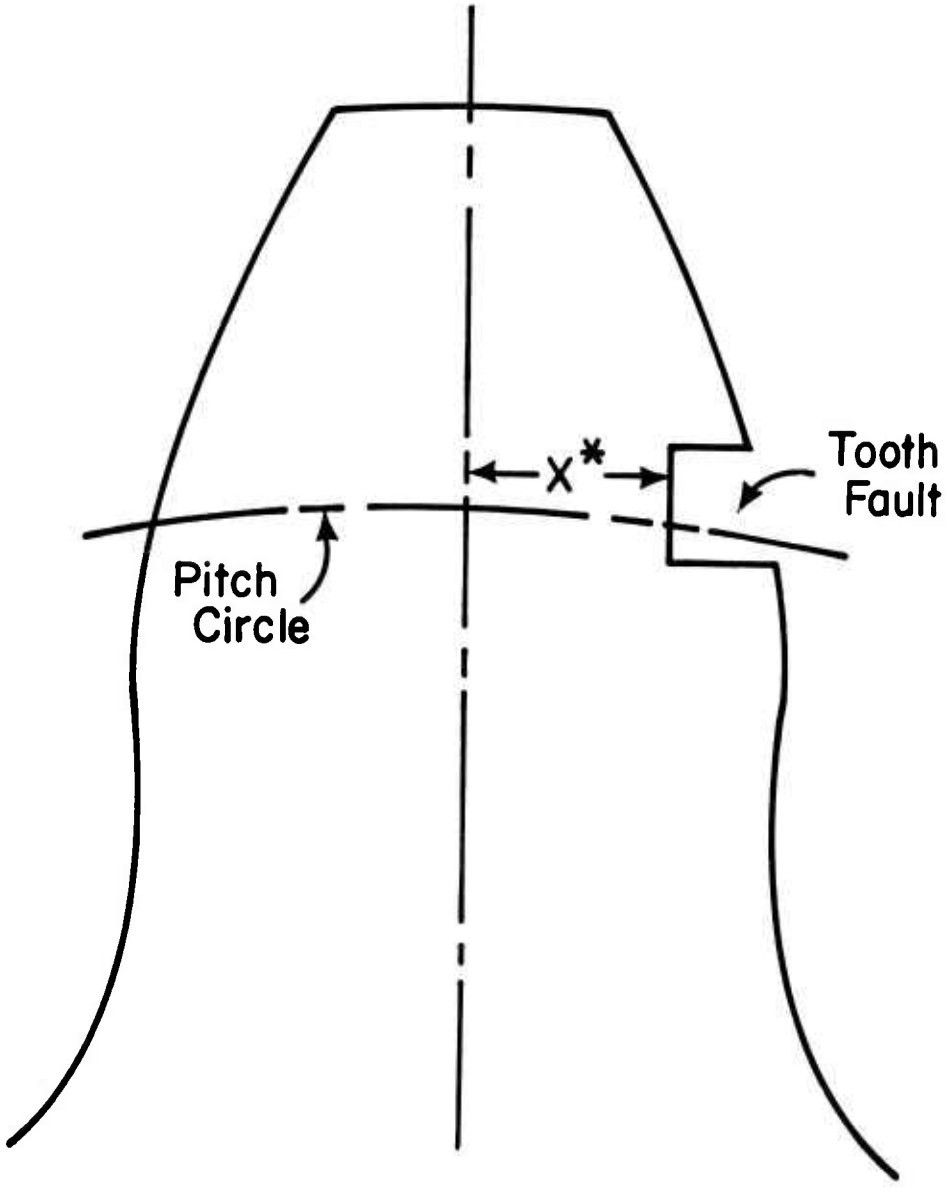

Figure 32. Model of Tooth Fault.

The Hertzian compliance analysis is also affected by the modified tooth profile. Whenever the fault is in mesh, the width of the contact strip is modified by the amount of overlap between the fault and the original contact strip. If the overlap of the fault is greater than the width of the contact strip, it is also assumed that contact is momentarily lost. When this effect occurs, the stiffness function is set equal to zero. The three considerations discussed as effects of a fault are incorporated into the calculation of a second stiffness function for a tooth with a fault (see Appendix IV). Whenever contact is lost in the mesh, it is assumed that damping effects are also lost. Thus, when mesh stiffness goes to zero, mesh damping also goes to zero in the torsional analysis.

Torque Impact

Whenever contact is lost because of a fault, the gears can freewheel; i.e., the pinion tends to accelerate since it has no resisting torque, while the idler gear tends to decelerate because of the loss of its driving torque. When contact is reestablished, an instantaneous velocity difference between the two teeth is present which causes an impact at the mesh.

This impact is approximated as a torque upon the gear mesh. The change in angular momentum between the gears determines the impact amplitude.

$$T_{IMP} = \frac{J_2\Delta\dot{\theta}_2(t^*) - J_3\Delta\dot{\theta}_3(t^*)}{\tau_{IMP}} \qquad (56)$$

where T_{IMP} = amplitude of torque impact, in.-lb

$\Delta\theta_2(t^*)$ = change in velocity of pinion at time of contact, rad/s

$\Delta\theta_3(t^*)$ = change in velocity of gear at time of contact, rad/s

τ_{IMP} = length of time of impact, s

The impact is entered in the analysis as torques caused by equal and opposite forces acting on the spring connecting the two inertias of the gear mesh (J_2,J_3). These torques are included in Equations (6) and (7) whenever tooth contact reaches the end of the fault width.

The impact is expected to assume a triangular shape with respect to time (see Figure 33). However, because of the fixed-interval integration routine used, the rectangular model of the impact, as shown by the dashed lines, is used. The energy content of the impact is unchanged with this model and more repeatability of results is obtainable. This is the result of the fixed-interval integration procedure used in the simulation which does not necessarily perform the computation at the same point on the impact each time the fault enters the mesh.

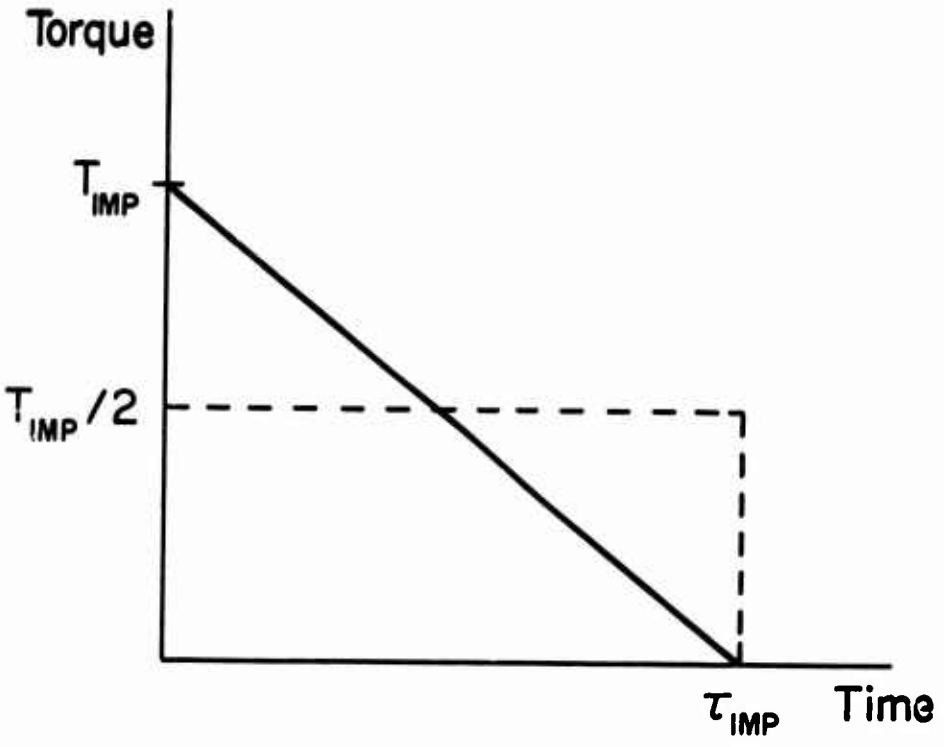

Figure 33. Model of Torque Impact Shape.

SUMMARY

A set of torsional dynamic equations was written to describe relative motion between the inertias of the model. The stiffness function of the gear mesh was also described via a strain energy analysis. Modifications to the stiffness function and the inclusion of a torque impact were described to account for gear tooth faults in mesh.

EXPERIMENTAL RESULTS

Experiments were performed using the equipment described in the section on test apparatus. Acceleration, torque, speed, and strain data were monitored for a variety of test conditions and a number of different gears. The standard test procedure used an input speed of 4500 ± 10 rpm, with an output power level of 8 ± 0.5 kW. These conditions fall within the operating range of the gearbox while in normal helicopter usage. Tests were also performed at other speed and load conditions to determine these effects on overall response data.

GEARS

A total of seven gears (spur pinion, generator drive, transmission) were used in the test program. These gears are manufactured to be symmetric and reversible, thus giving the possibility of 14 distinct sets of tooth surfaces. Table II lists the gears by serial number and testing condition. The notations R and L refer to the right and left sides of the gear tooth, respectively (viewed with the serial number facing up). The table describes whether a given gear side was run, what the surface conditions of the teeth were (i.e., if the gear contained a fault or not), and if the gear had strain gages mounted on it.

TABLE II. GEARS TESTED

Gear No.		Condition
B12 - 1659	R	Run, Good
	L	Run, Small Fault
W12 - 3231	R	Not Run
	L	Run, Large Fault, Gaged
B12 - 1475	R	Not Run
	L	Run, Good, Gaged
W12 - 3204	R	Run, Good
	L	Run, Double Fault
W12 - 3191	R	Run, Good, Gaged
	L	Not Run
W12 - 3183	R	Not Run
	L	Run, Good
W12 - 3115	R	Run, Small Fault, Gaged
	L	Run, Good

TIME-DOMAIN ACCELERATION AND TORQUE RESPONSE

Gearbox acceleration signals are among the parameters of most interest, both with respect to experimental information and comparison to theoretical results. Acceleration data presented was monitored at one of three positions as shown in Figures 20, 21, and 22 (near the gearbox input bearing, on the face of the gearbox, and near the output bearing). The position which provided the greatest response to faults was at the input bearing since this was the closest monitoring position to the gear mesh which had faulty gears implanted in it.

Figure 34 shows typical torque and acceleration signals for the system when all the gears were in good condition. The top trace in the figure is the torque signal. The straight line is the zero torque level. The input torque has a mean level with a superimposed oscillation at the input shaft frequency. This oscillation was deduced to be the result of mounting procedures and fixtures used in the test stand. Accordingly, this information was used as an input in the system simulation. The bottom trace in the figure is for the input bearing accelerometer, the top trace in figure (b) is the gearbox housing accelerometer signal, and the bottom trace in figure (b) is the output bearing accelerometer signal. The primary oscillatory component of these signals occurs at the gear meshing frequency. Some "beating" or modulation effects at the shaft rotational frequency may also be noted.

Figure 35 contains data similar to that of Figure 34 for a gearbox containing a gear with a small (0.020-inch-wide) tooth surface fault. The top trace in each of the scope photos is the tachometer signal. Some small spikes occurring at a repetition rate which corresponds to the shaft rotational frequency may be seen in the acceleration signal. The repetition rate corresponds to the frequency at which the fault enters mesh. The presence of the spike is evident but not very large. Figure 35 presents data for the gearbox when a gear with a large (~0.05-inch-wide) fault had been implanted. The presence of this spike is more evident.

Differences between good gears and those with faults are seen in the acceleration data. However, because of the magnitudes of the spikes, it is questionable as to whether the presence of these spikes could be used solely as a gear condition indicator or whether they would be dismissed as anomalies in the test procedure if the gear condition was unknown. The use of time summation as an analysis procedure has been suggested for use in such cases.[8] However, based on the predominance of energy in the signal at the gear meshing frequency and its harmonics, it is quite doubtful whether a summation at the shaft period would produce useful information.

ACCELERATION FREQUENCY SPECTRA

The major portion of the analysis of data was performed using frequency spectra of the input bearing acceleration. These frequency analyses were obtained with the use of a real-time analyzer for data taken both directly from the test stand and from taped data which were analyzed off-line.

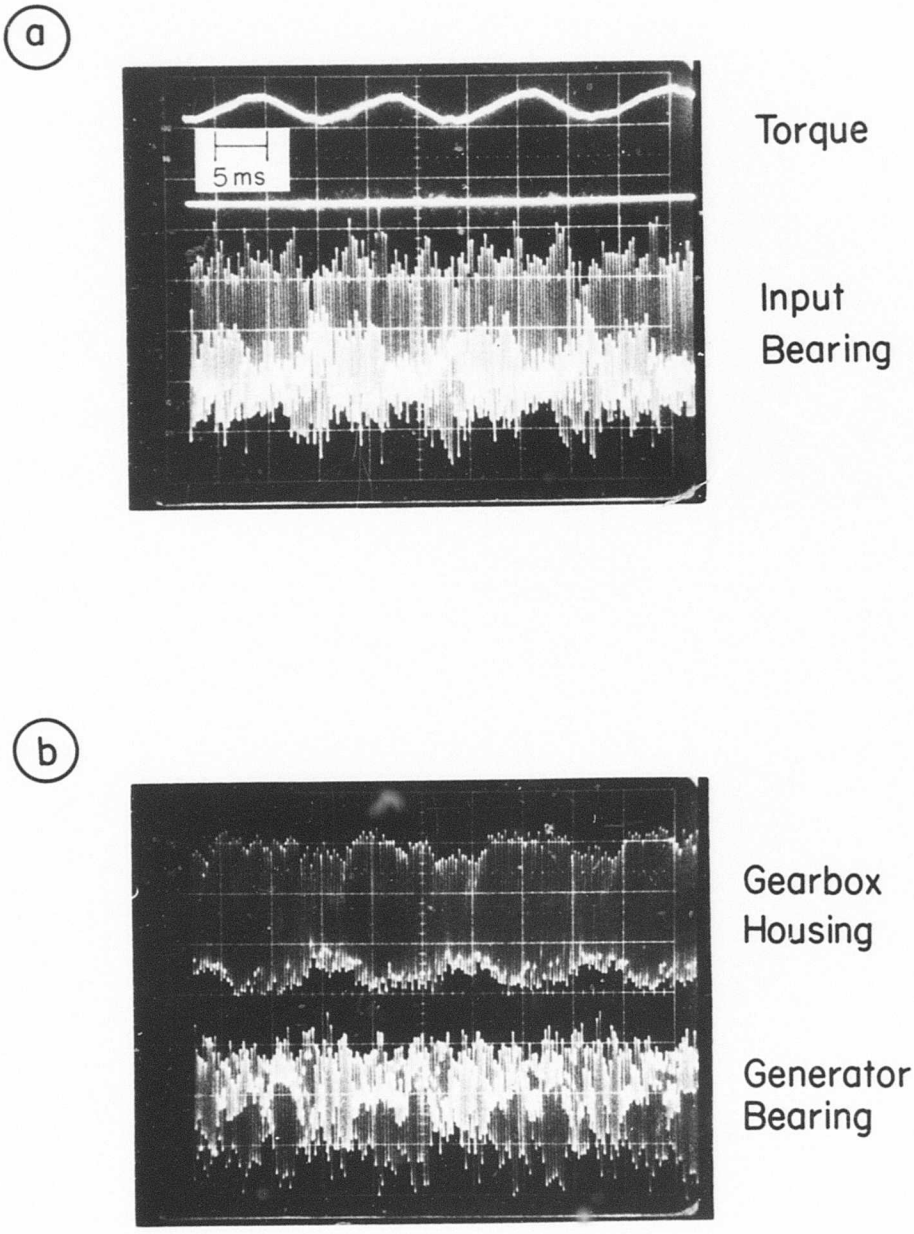

Figure 34. Time Response of Acceleration and Torque (Good Gears).

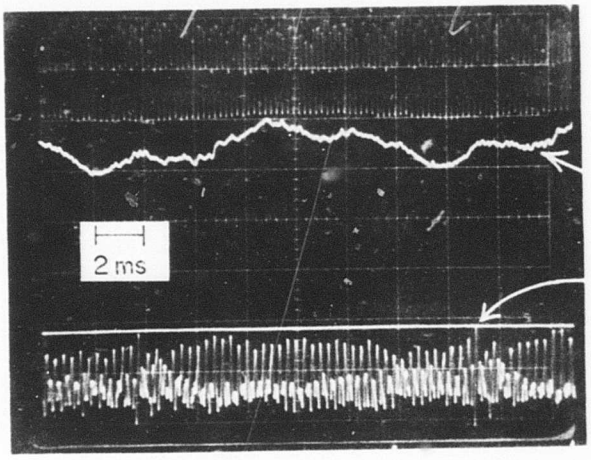

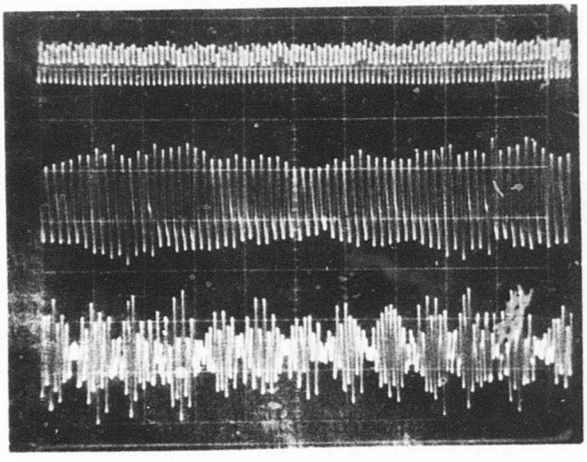

Figure 35. Time Response of Acceleration and Torque (Small Fault).

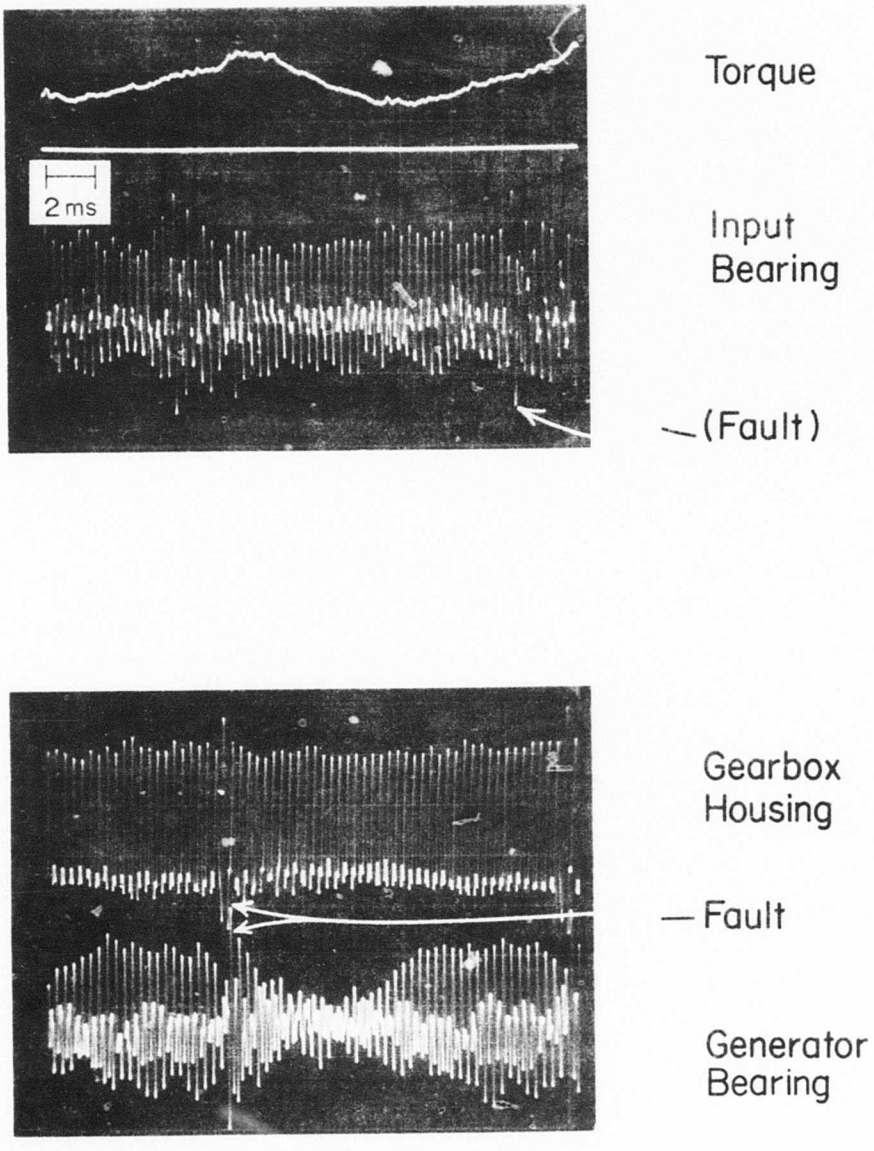

Figure 36. Time Response of Acceleration and Torque (Large Fault).

Figure 37 shows typical spectra for the input bearing accelerometer when the gearbox contained all good gears. The input shaft frequency is 75 Hz and the fundamental gear meshing frequency is 3075 Hz. In Figure 37a (0-10 kHz), the fundamental component and the first two harmonics may be seen. Also evident are sidebands (primarily about the first and second mesh harmonics). It is quite evident that the primary composition of the signal is due to the gear meshing frequency and harmonics. Figure 37b (0-50 kHz) shows more of the harmonic train. It is interesting to note that the first harmonic has a larger amplitude than the fundamental gear meshing frequency, something which is contrary to the expected result.

Figure 38 shows spectra when the gearbox contained a gear having a small (0.020-inch-wide) fault. With a fault present the amplitude at the meshing frequency is increased. This amplitude is now also greater than that of the first harmonic. There is the appearance of a larger amount of energy at multiples of the shaft frequency (the sawtooth effect which may be observed). Figure 39 shows spectra when a gear containing a large fault (0.050 inch wide) was tested. The same effects as noted for the small fault may be observed, with the sawtooth effect having still higher amplitudes. Figure 40 presents spectra obtained when the gear tested contained two faulty teeth. Again, the increases in amplitude and sawtooth effect are evident. Gears with faults on more teeth, as might be indicative of normal gear tooth failures, were not tested because of the magnitude of machining required.

Another effect which is especially evident in Figure 39 is a periodicity in the sawtooth effect. An enveloping periodic amplitude change occurs with a spacing which corresponds to the lowest torsional resonance of the system. This is particularly noticeable at frequencies between the gear meshing frequency and its first harmonic in Figure 39.

Figures 41-44 display the variation in test to test amplitudes at various selected frequencies. Amplitudes at the meshing frequency and its harmonics are displayed in terms of decibels referenced to 0.05 g (0.05 g = 0 dB). The vertical lines on the plots of the amplitude of meshing frequency and its first two harmonics are mean values for good and faulty gears, respectively. The mean value of the meshing frequency is approximately 9 dB higher for faulty gears than for good gears. Table III displays the amplitudes of the mean values and also the mean amplitude plus and minus one

TABLE III. VARIATIONS IN SPECTRAL AMPLITUDES (dB) OF GEARS TESTED

Frequency	Good Gears			Faulty Gears		
	$\bar{X}$	$\bar{X} - \sigma$	$\bar{X} + \sigma$	$\bar{X}$	$\bar{X} - \sigma$	$\bar{X} + \sigma$
Gear Meshing	35.3	31.9	37.7	44.5	42.2	46.2
First Harmonic	42.5	32.1	47.1	39.4	34.8	42.4
Second Harmonic	26.8	20.2	30.5	27.6	21.4	31.2

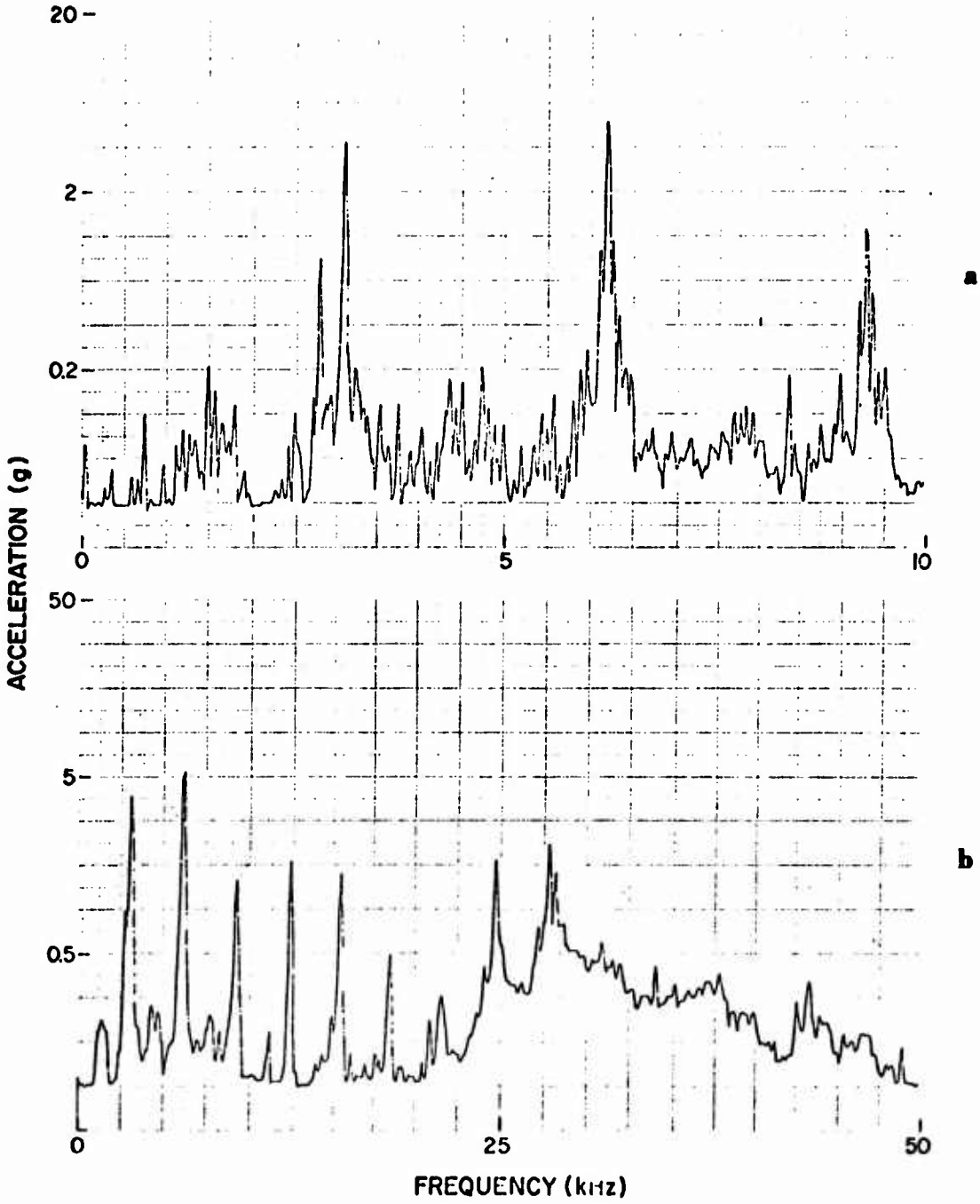

Figure 37. Acceleration Spectra at Input Bearing (Good Gears).

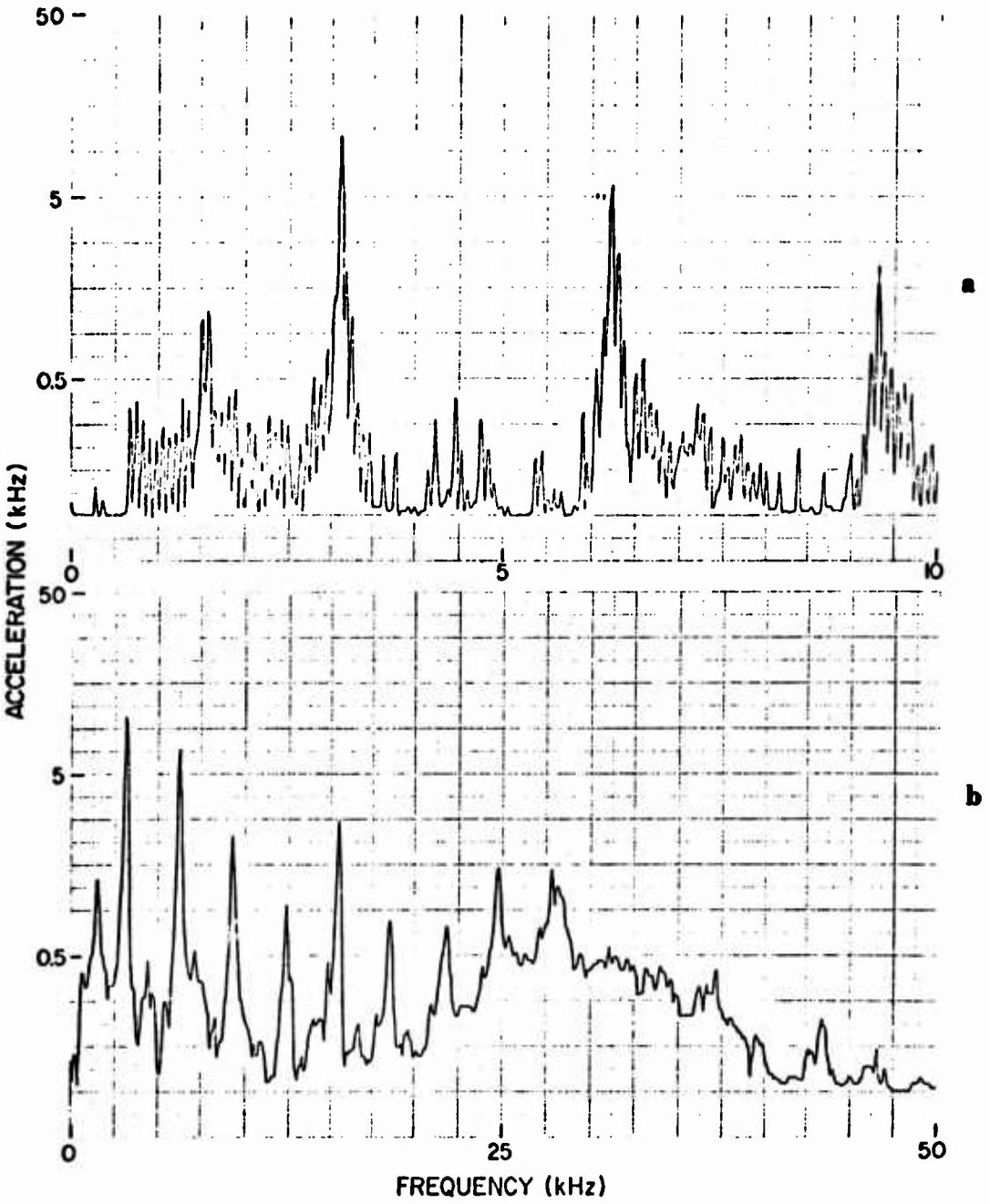

Figure 38. Acceleration Spectra at Input Bearing (Small Fault).

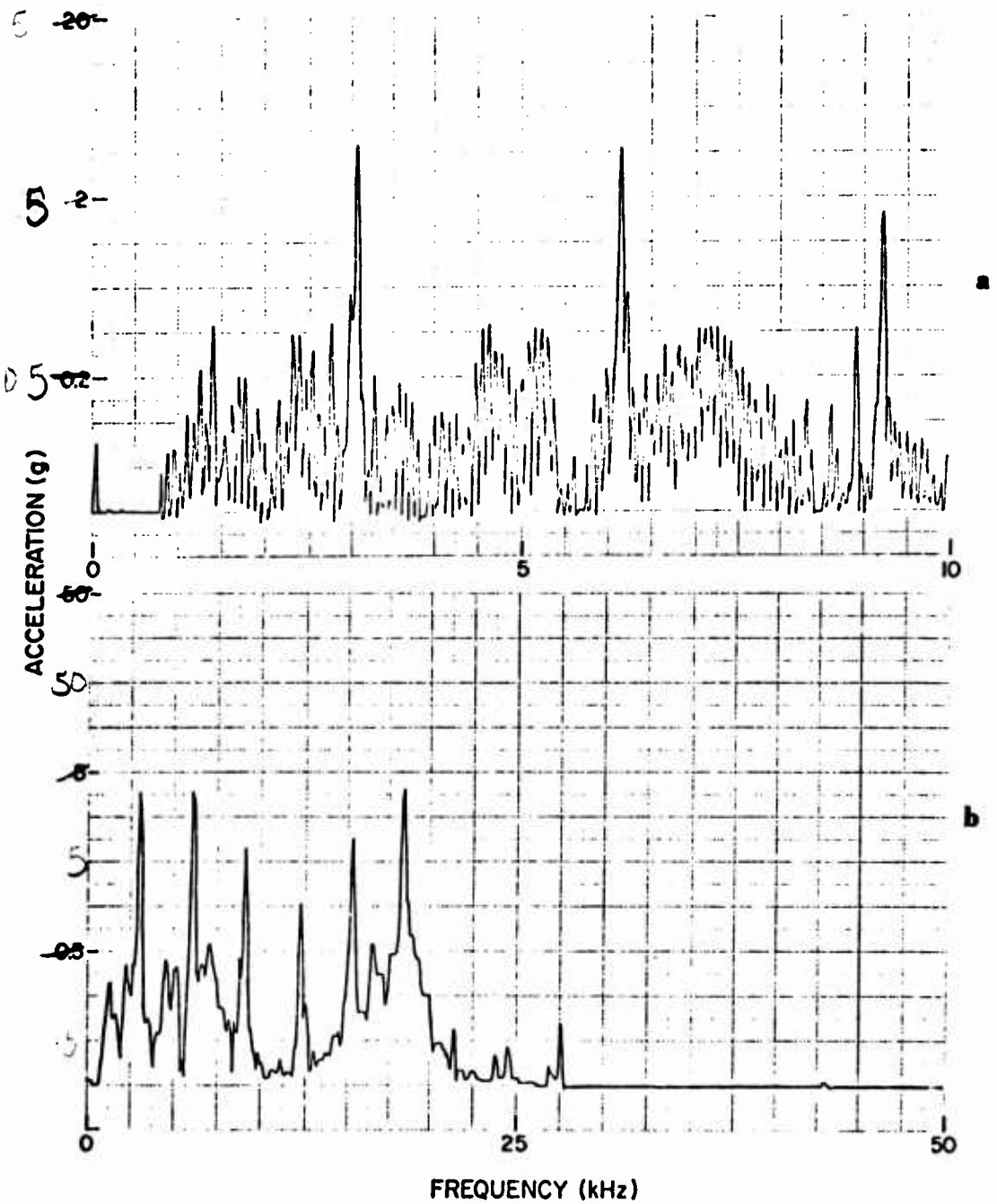

Figure 39. Acceleration Spectra at Input Bearing (Large Fault).

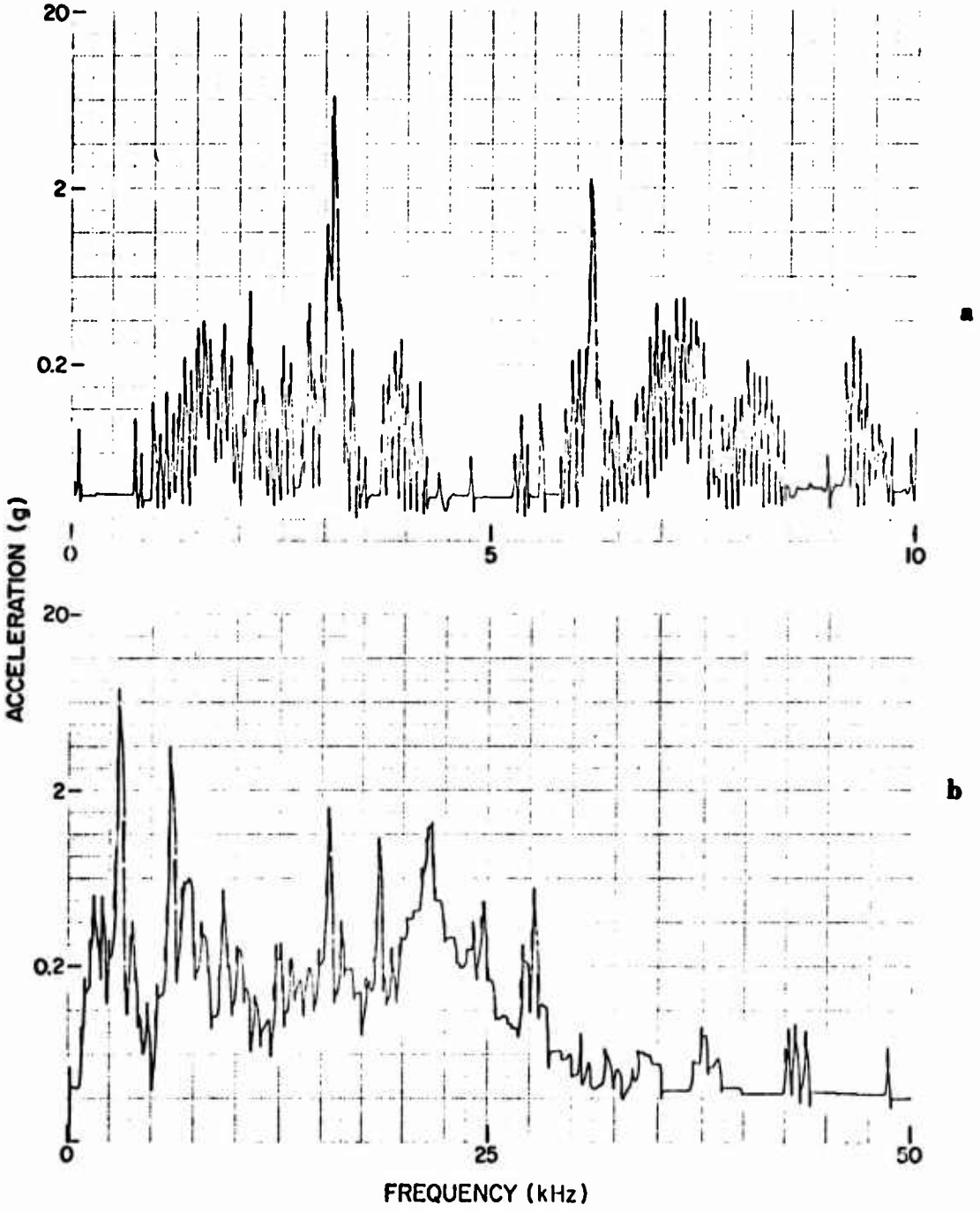

Figure 40. Acceleration Spectra at Input Bearing (Double Fault).

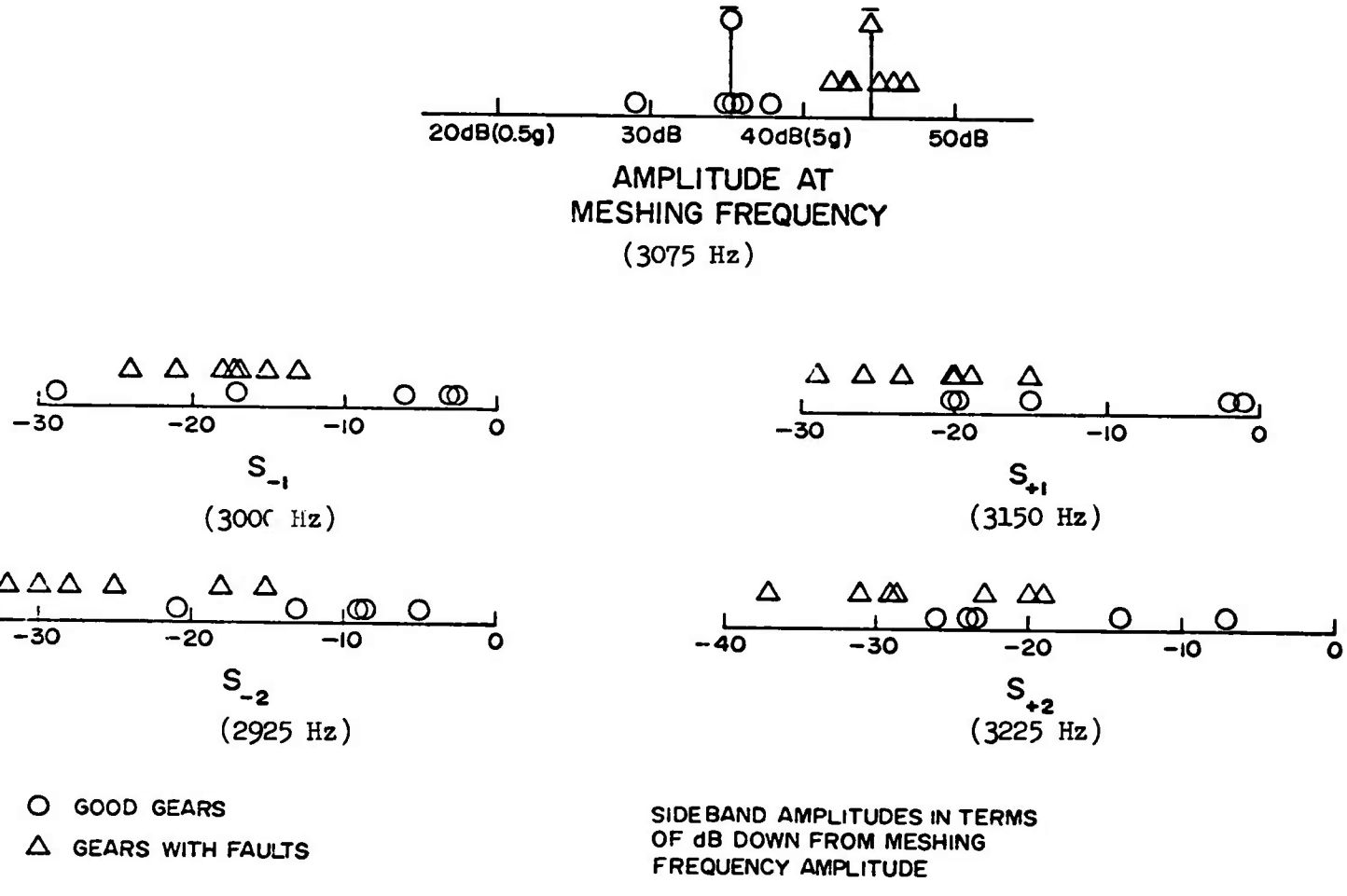

Figure 41. Distribution of Spectral Amplitude at Meshing Frequency and Sidebands at Input Bearing Sensor Location.

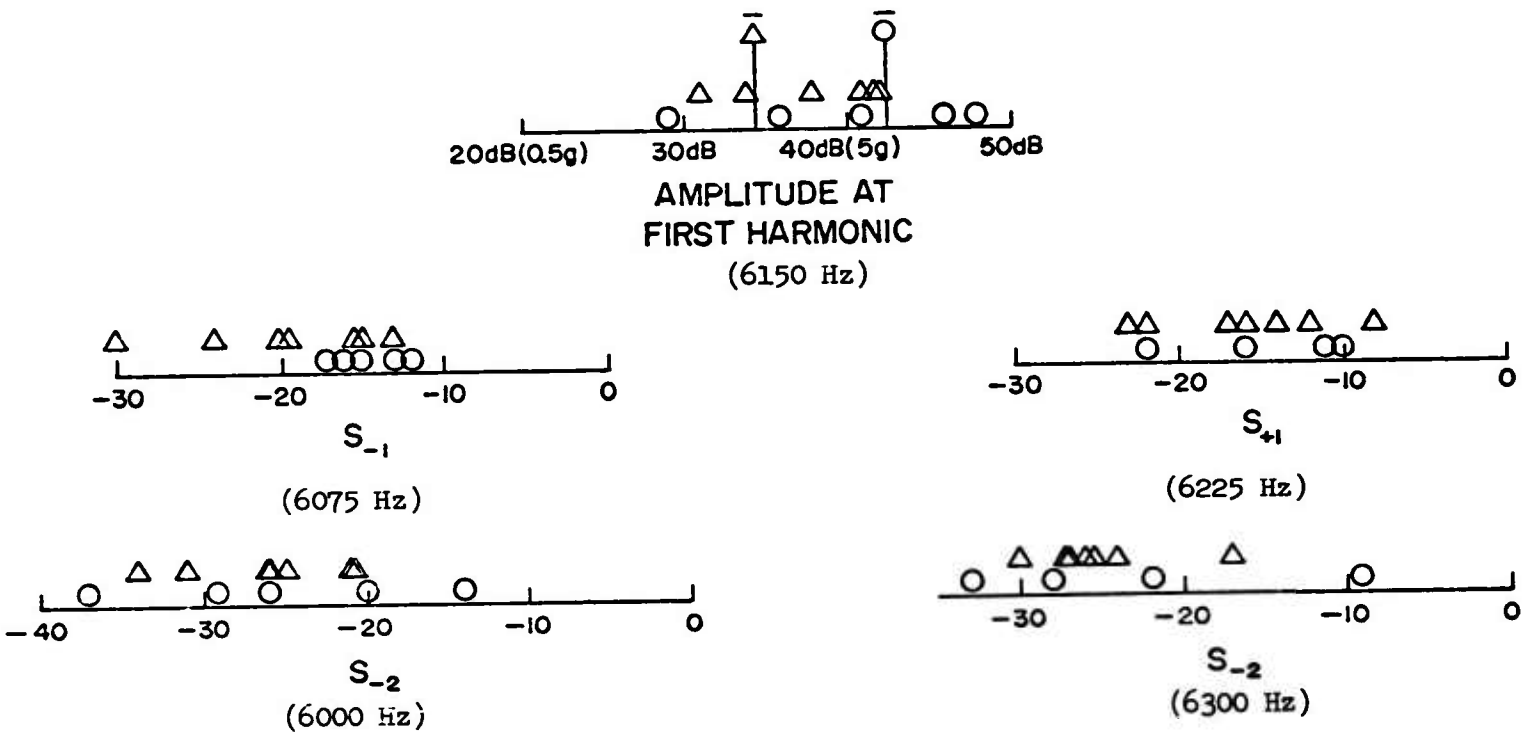

Figure 42. Distribution of Spectral Amplitudes at First Harmonic and Sidebands at Input Bearing Sensor Location.

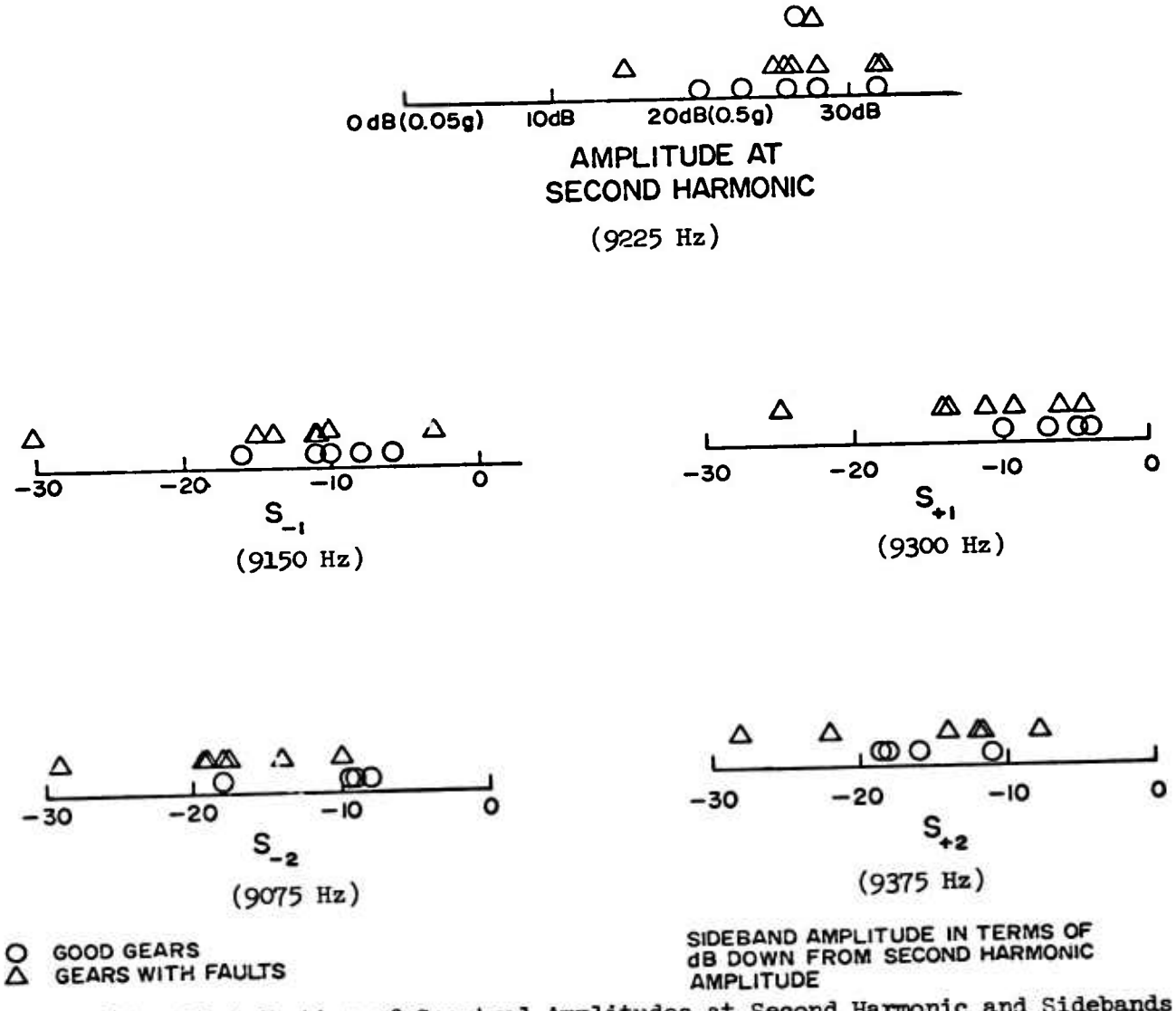

Figure 43. Distribution of Spectral Amplitudes at Second Harmonic and Sidebands at Input Bearing Sensor Location.

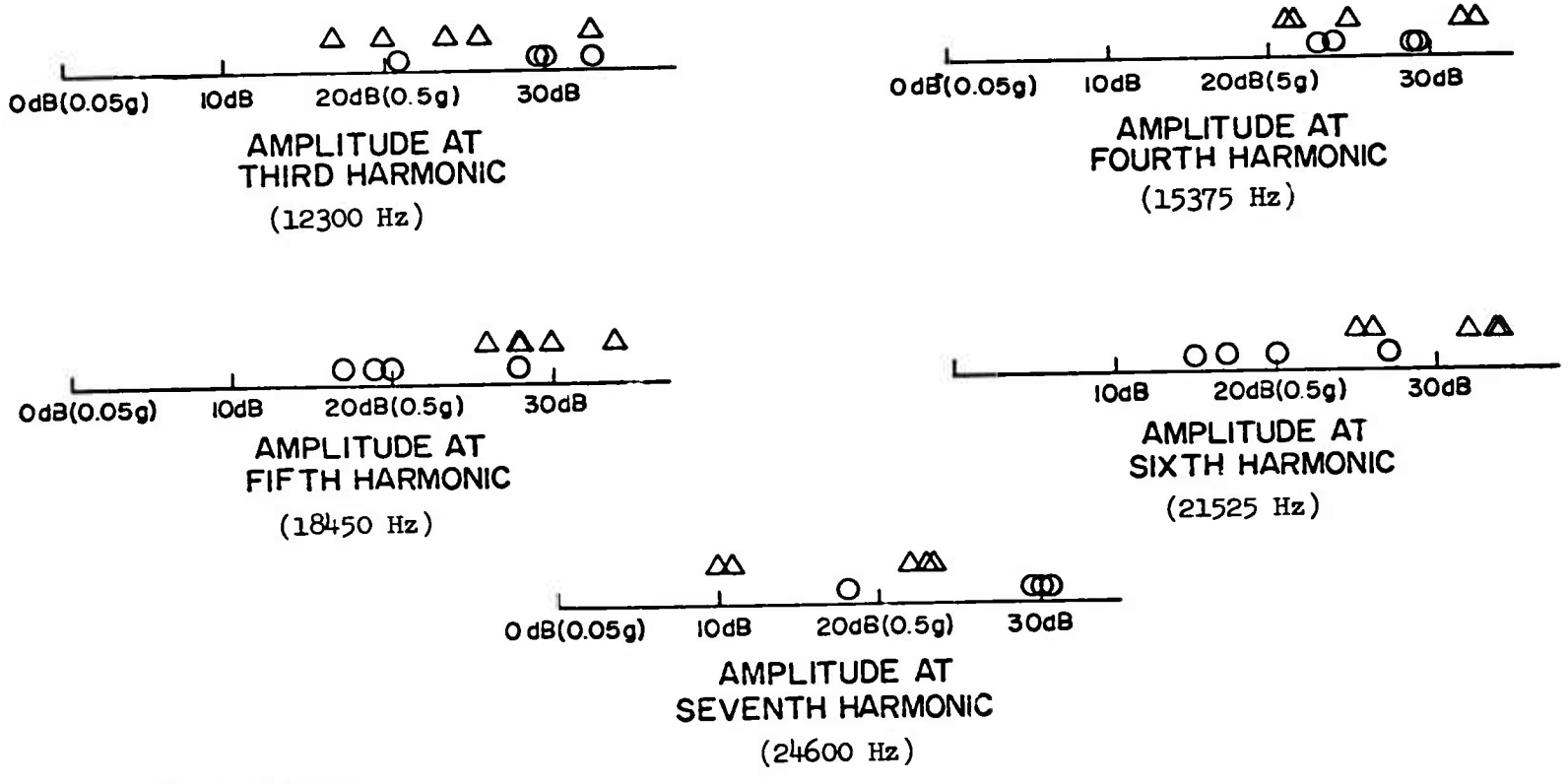

Figure 44. Distribution of Spectral Amplitudes at Third Through Seventh Harmonic at Input Bearing Sensor Location.

standard deviation. The changes caused by gear faults are not very distinct in the harmonics of the meshing frequency or sidebands as data points tend to overlap. While the presence of a tooth surface fault undoubtedly affects spectral amplitudes of these frequencies, other operating parameters of the gearbox must also strongly affect them. This suggests that the primary information with respect to fault indication lies in the amplitude of the gear-meshing frequency and the presence of energy at multiples of the rotational frequency, the sawtooth effect.

Figure 45 shows typical spectra for good gears when load was set to 70% of the standard operating load. No great amount of deviation from the effects noted under full load were observed. Figures 46, 47, and 48 show the variations at various spectral frequencies for good and bad gears at the reduced load condition. Again amplitudes at the meshing frequency and first harmonics appear higher for faulty gears, but no clear-cut pattern is evident in the sideband information. Other data were taken at 40% of the standard operating load. The spectra contained an increase of harmonic content, and gears were much noisier at this operating condition.

Figures 49 and 50, respectively, display spectra of acceleration monitored at the generator output bearing when the gearbox contained all good gears and when a faulty gear was implanted. Differences may be noted in the amplitudes at the meshing frequency and harmonics when a faulty gear was present. The faulty gear also shows some evidence of the sawtooth effect. Figures 51, 52, and 53 show the distribution of spectral amplitudes from test to test. No clear patterns in this data are evident, suggesting that because of the distance of the accelerometer from the meshing position of the faulty gear, the fault's effect on the vibration at this position is attenuated. It might be noted that there is a strong spectral component in the data at approximately 2600 Hz and at harmonics of this frequency. This frequency appears to be the frequency of passing of generator commutator bars.

Figures 54 and 55 show spectra of acceleration monitored on the gearbox housing for the case of good and bad gears. The distribution of spectral amplitudes shown in Figure 56 again indicates no strong correlation of the spectral components with fault presence. This might again be expected because of the number of interfaces interposed between the mesh of the faulty gear and this accelerometer position.

Mention should be made of the fact that in all but one of the tests performed, the tooth fault was present on only one tooth. In actual gear operation, it is quite likely that the type of fault introduced (pitch-line) pitting) will occur on a number of teeth and in most cases on all teeth. This would greatly increase the forces being generated in the gear mesh which would likely cause stronger manifestations of fault presence in acceleration signals monitored at positions such as the generator output bearing or gearbox housing. In this study, the effects of faults were strong enough at the input bearing position to provide the necessary information.

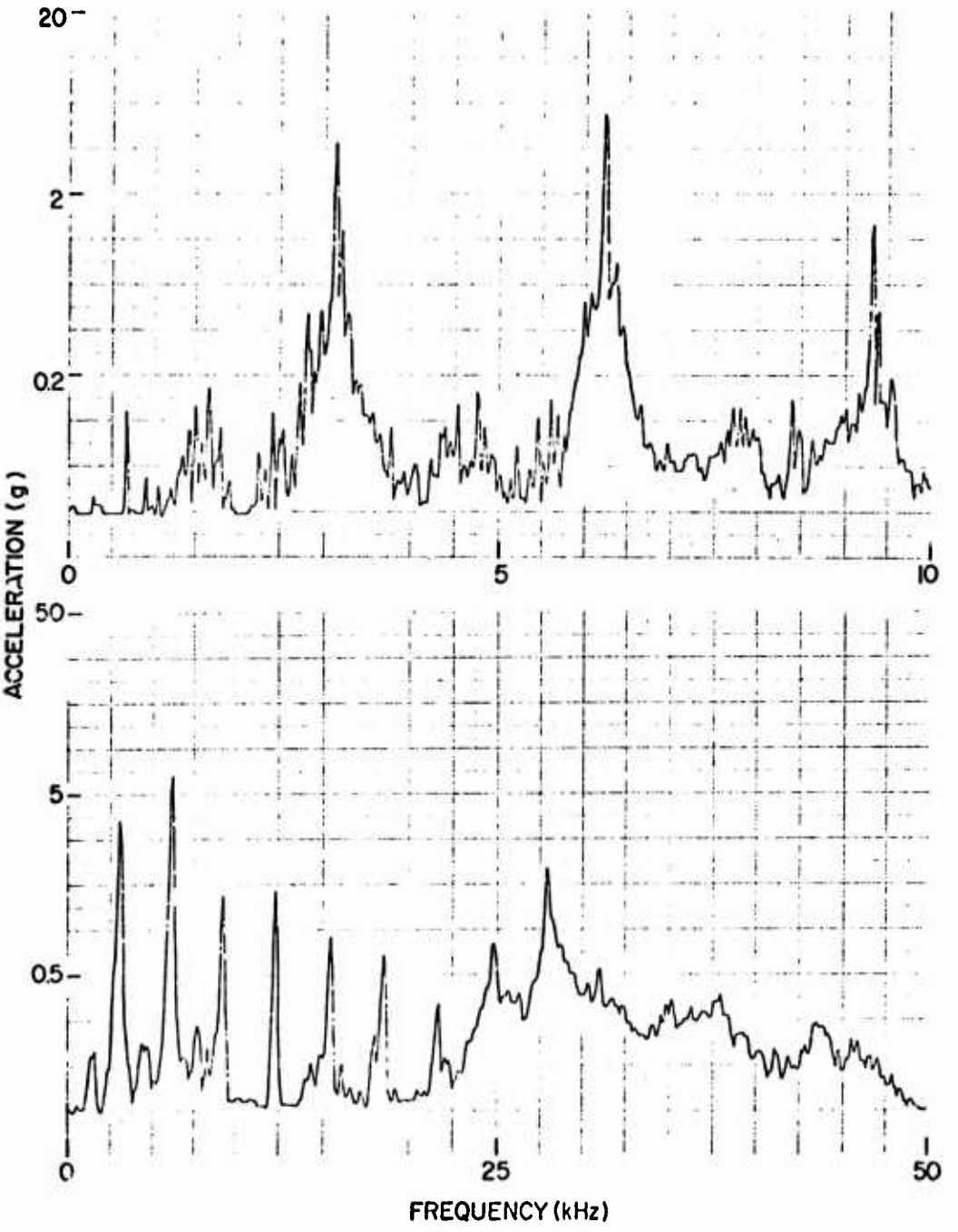

Figure 45. Acceleration Spectra at Input Bearing for 70% Load.

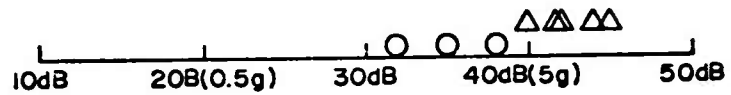

AMPLITUDE AT
MESHING FREQUENCY
(3075 Hz)

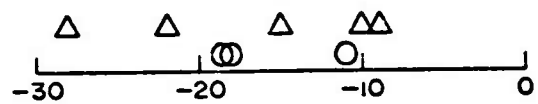

S_{-1}

(3000 Hz)

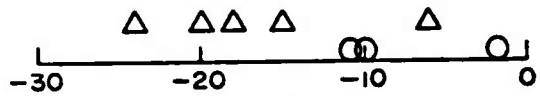

S_{+1}

(3150 Hz)

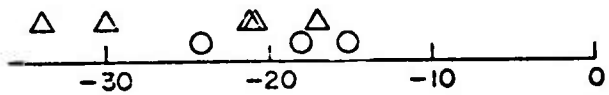

S_{-2}
(2925 Hz)

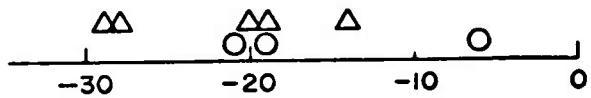

S_{+2}
(3225 Hz)

○ GOOD GEARS
△ GEARS WITH FAULTS

SIDEBAND AMPLITUDES IN TERMS OF
dB DOWN FROM MESHING FREQUENCY
AMPLITUDE

Figure 46. Distribution of Spectral Amplitudes at Pinion Meshing Frequency and Sidebands a . Input Bearing Sensor Location Under 70% Load.

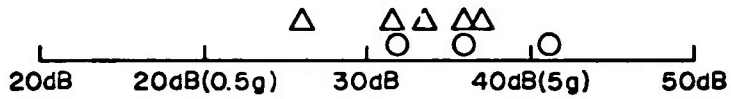

AMPLITUDE AT
FIRST HARMONIC

(6150 Hz)

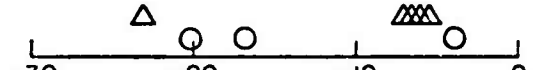

S_{-1}

(6075 Hz)

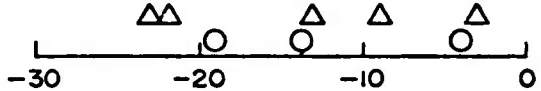

S_{+1}

(6225 Hz)

S_{-2}

(6000 Hz)

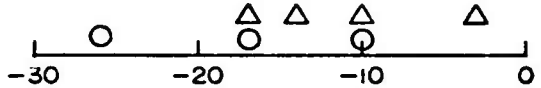

S_{+2}

(6300 Hz)

○ GOOD GEARS

△ GEARS WITH FAULTS

SIDE BAND AMPLITUDES IN TERMS OF
dB DOWN FROM FIRST HARMONIC
AMPLITUDE

Figure 47. Distribution of Spectral Amplitudes at Pinion First Harmoic and Sidebands at Input Bearing Sensor Location Under 70% Load.

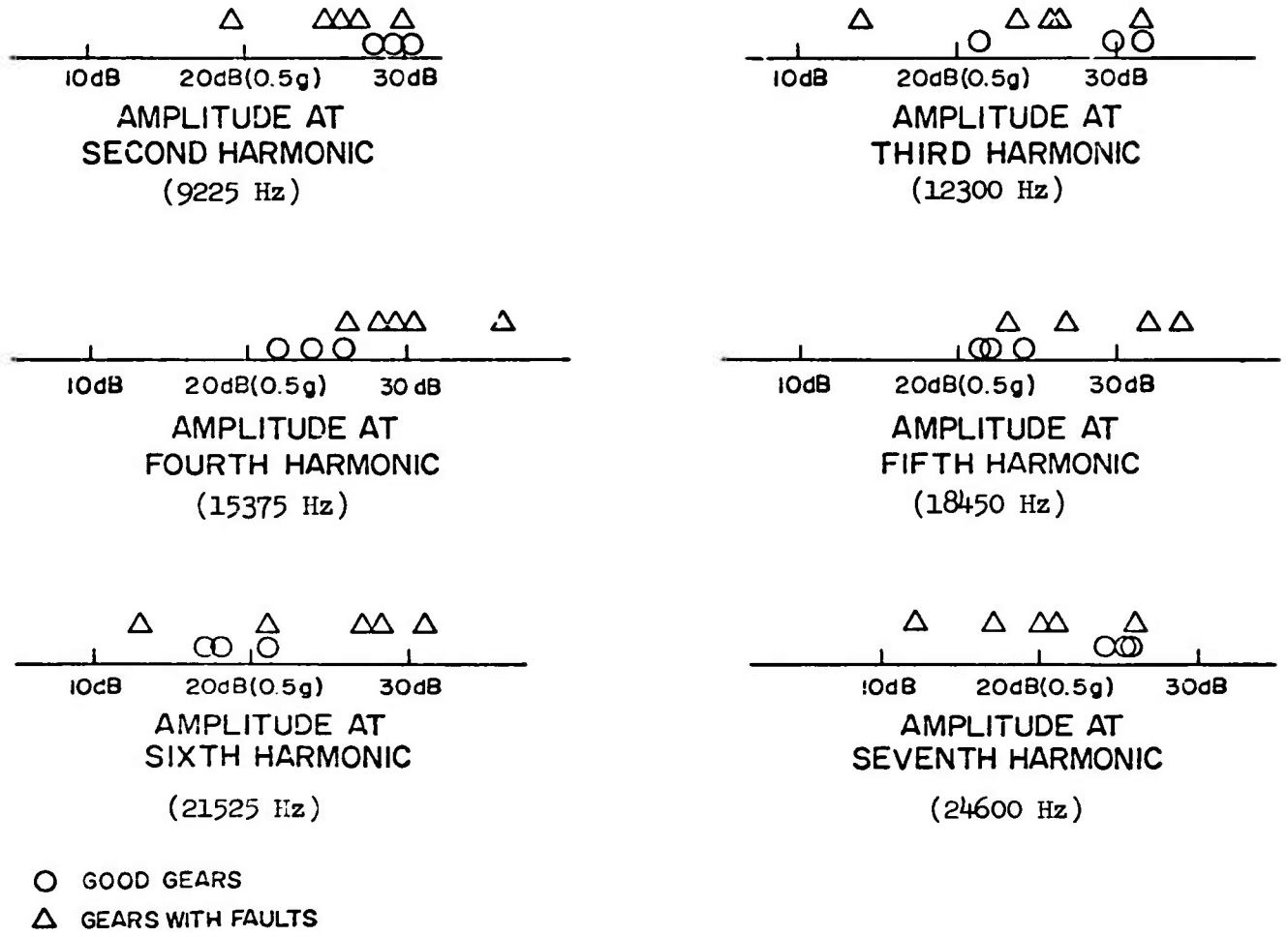

Figure 48. Distribution of Spectral Amplitudes at Pinion Second Through Seventh Harmonic at Input Bearing Sensor Location Under 70% Load.

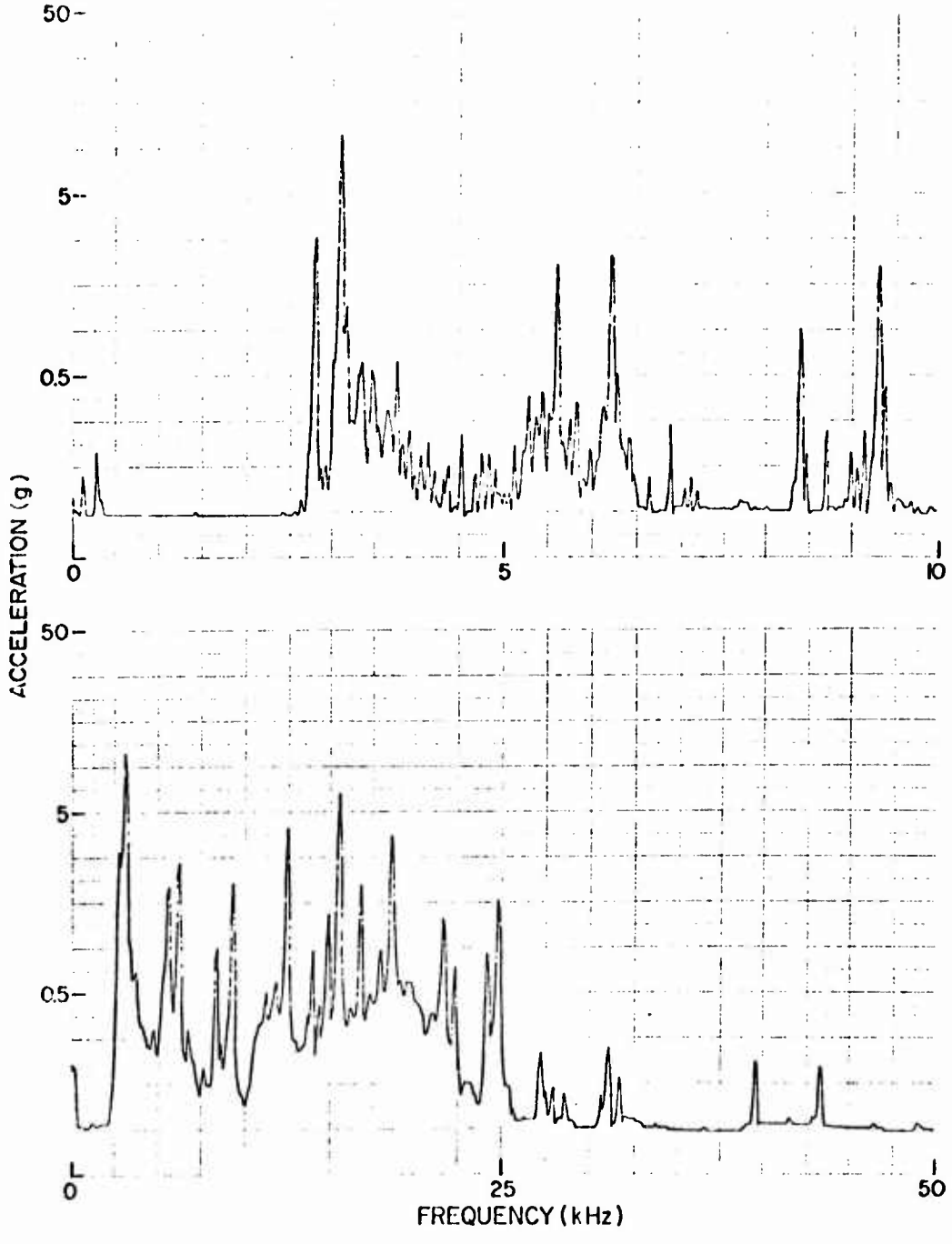

Figure 49. Acceleration Spectra at Generator Output Bearing (Good Gear).

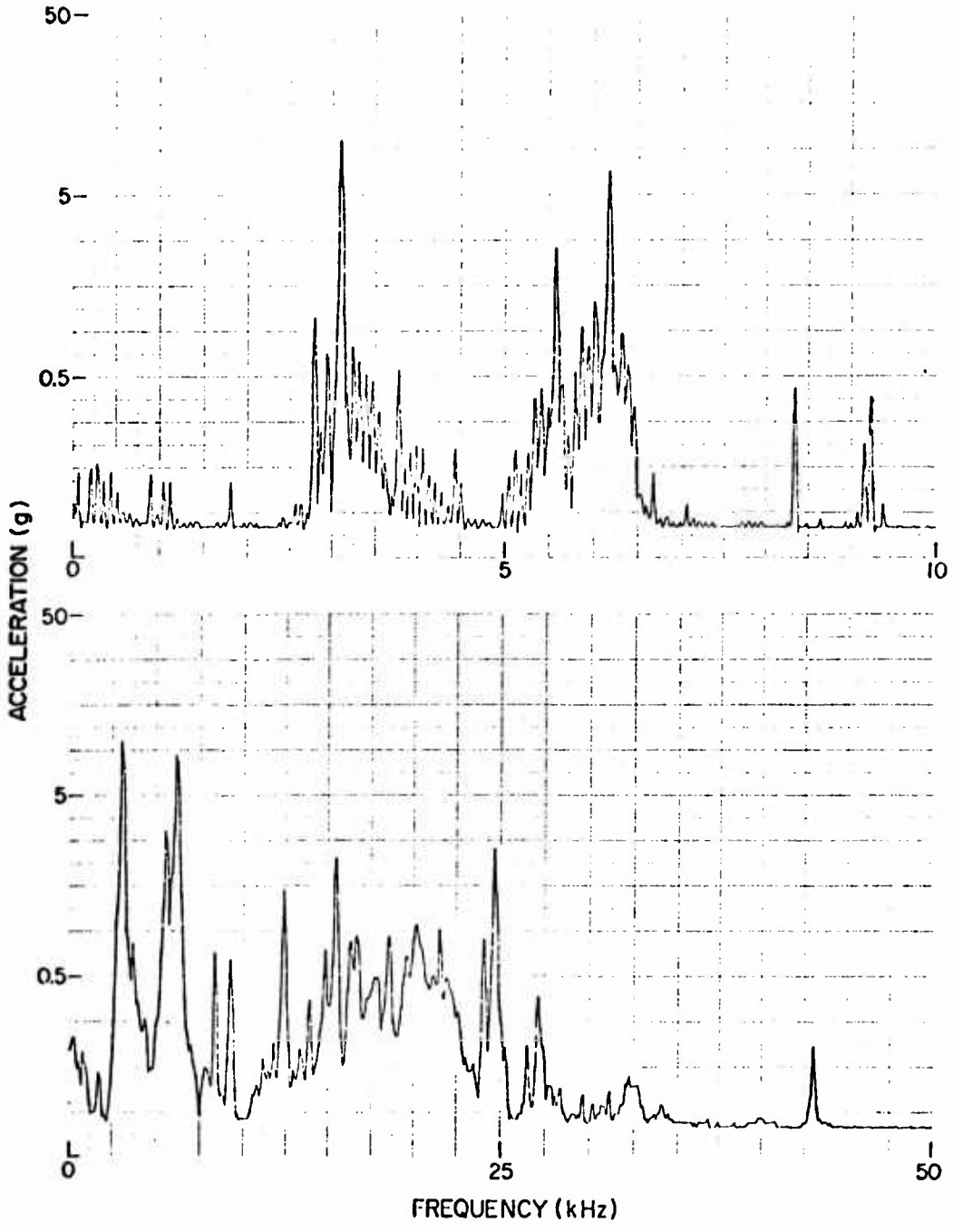

Figure 50. Acceleration Spectra at Generator Output Bearing (Gear Fault).

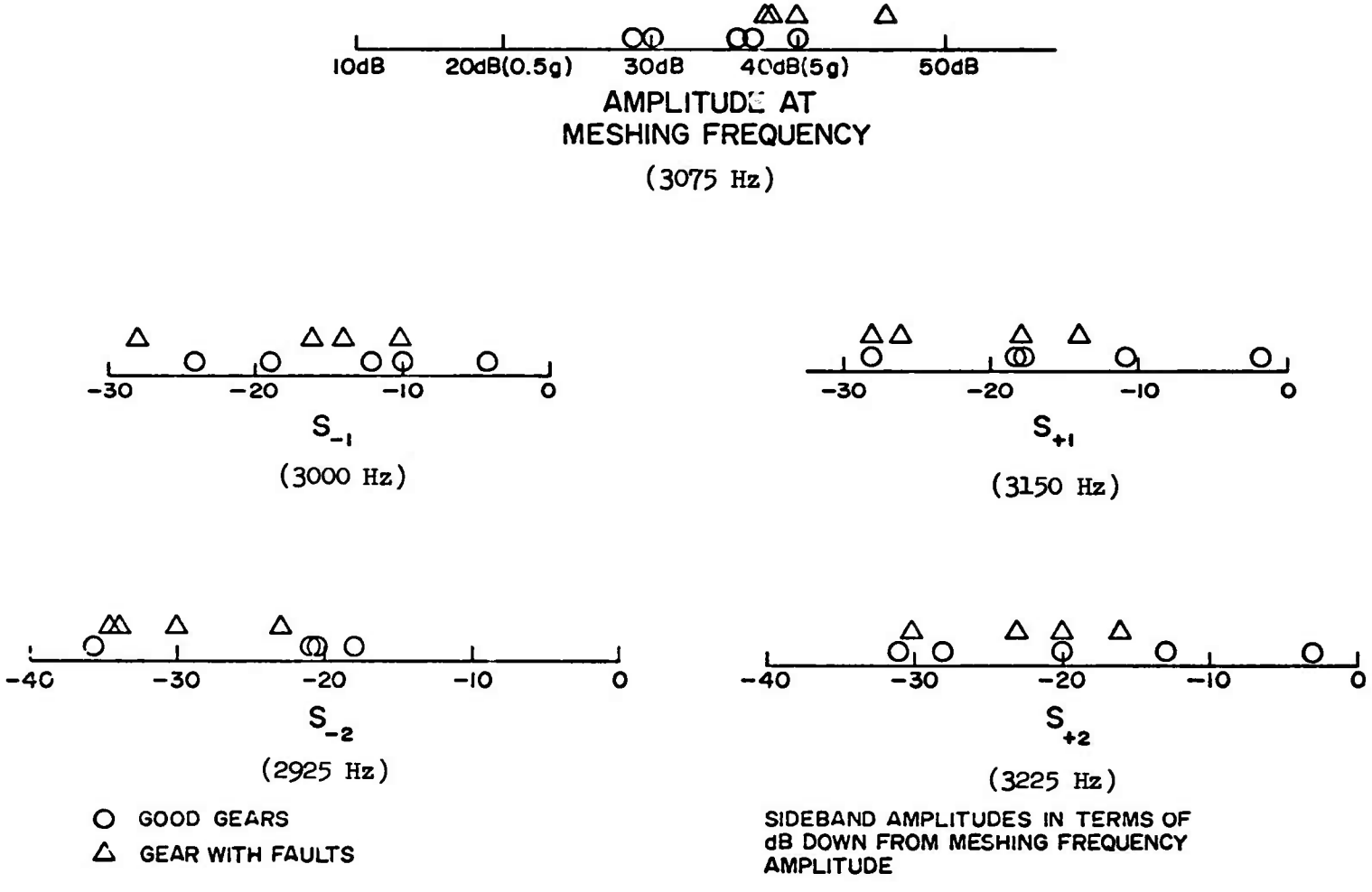

Figure 51. Distribution of Spectral Amplitudes at Pinion Meshing Frequency and Sidebands at Generator Output Bearing Sensor Location.

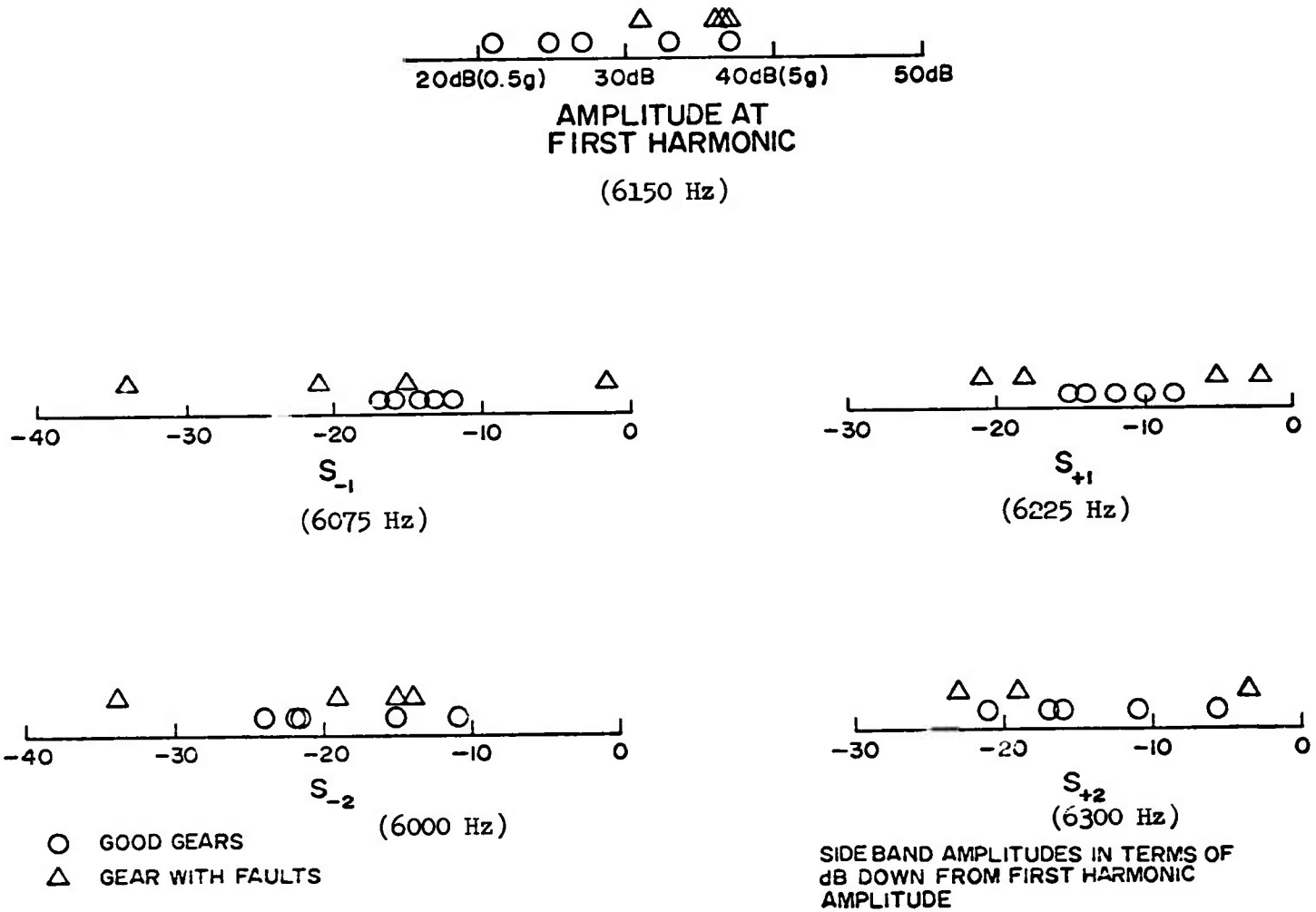

Figure 52. Distribution of Spectral Amplitudes at Pinion First Harmonic and Sidebands at Generator Output Bearing Sensor Location.

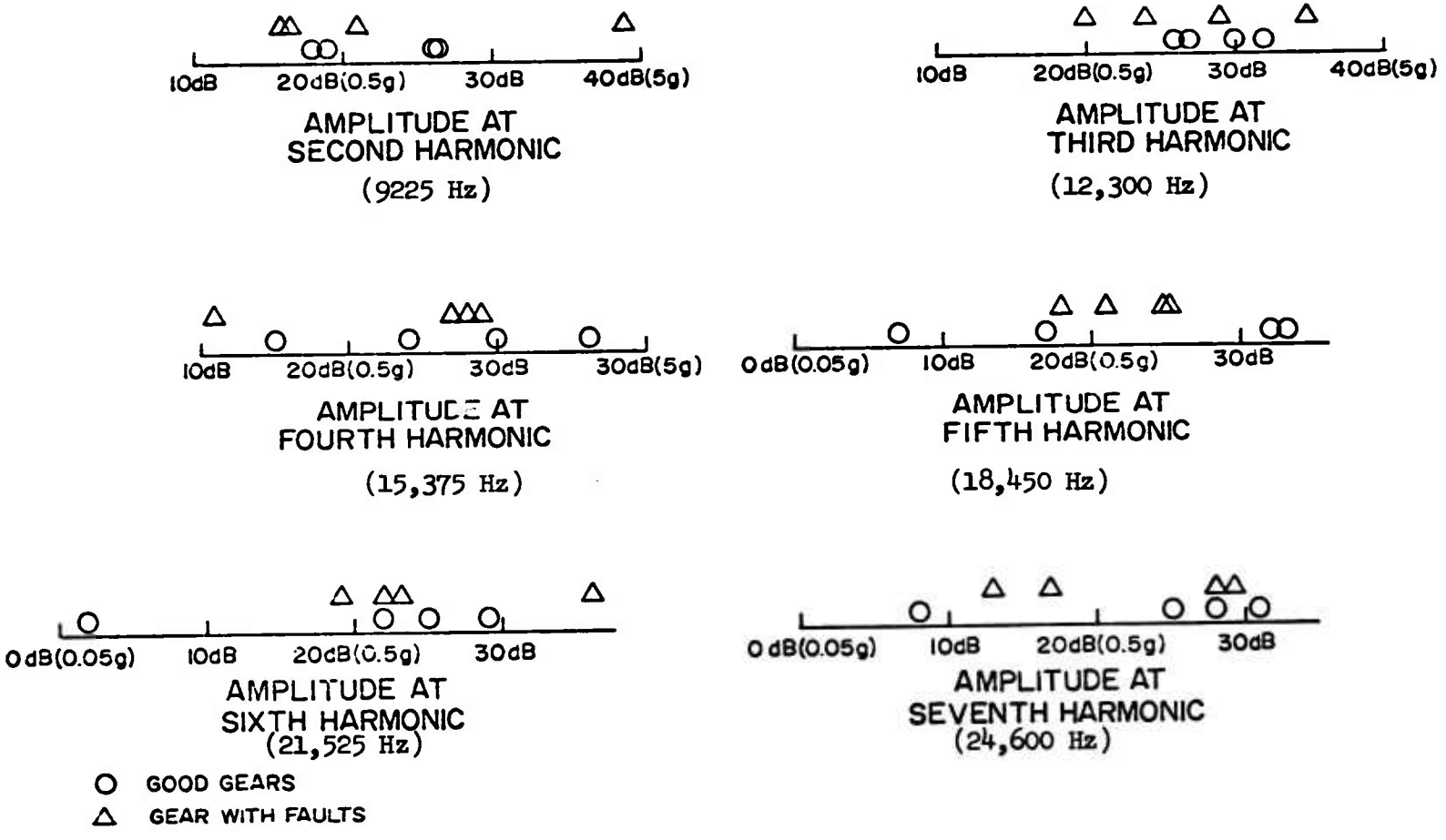

Figure 53. Distribution of Spectral Amplitudes at Pinion Second Through Seventh Harmonic at Generator Output Bearing Sensor Location.

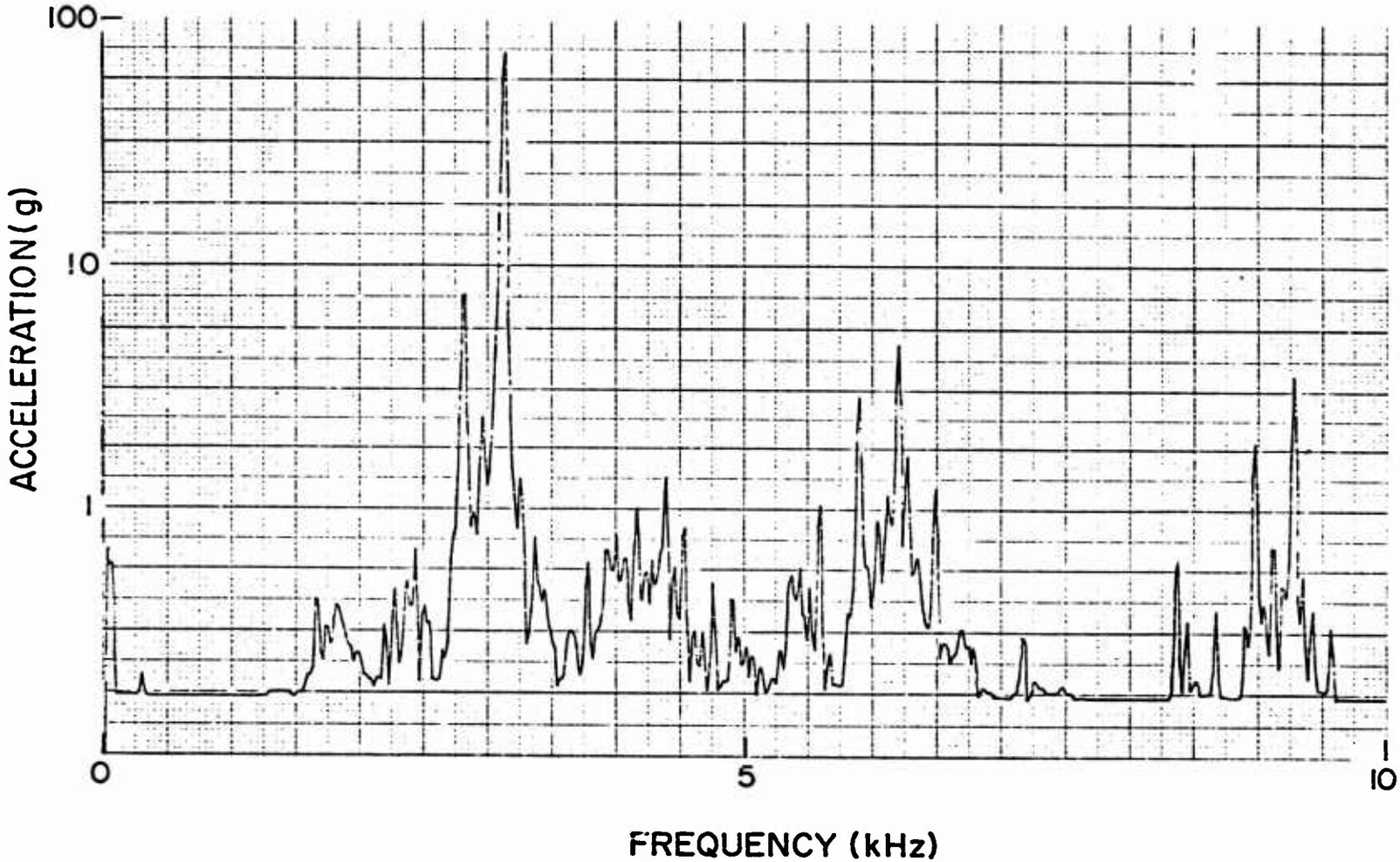

Figure 54. Acceleration Spectra at Gearbox Housing (Good Gears).

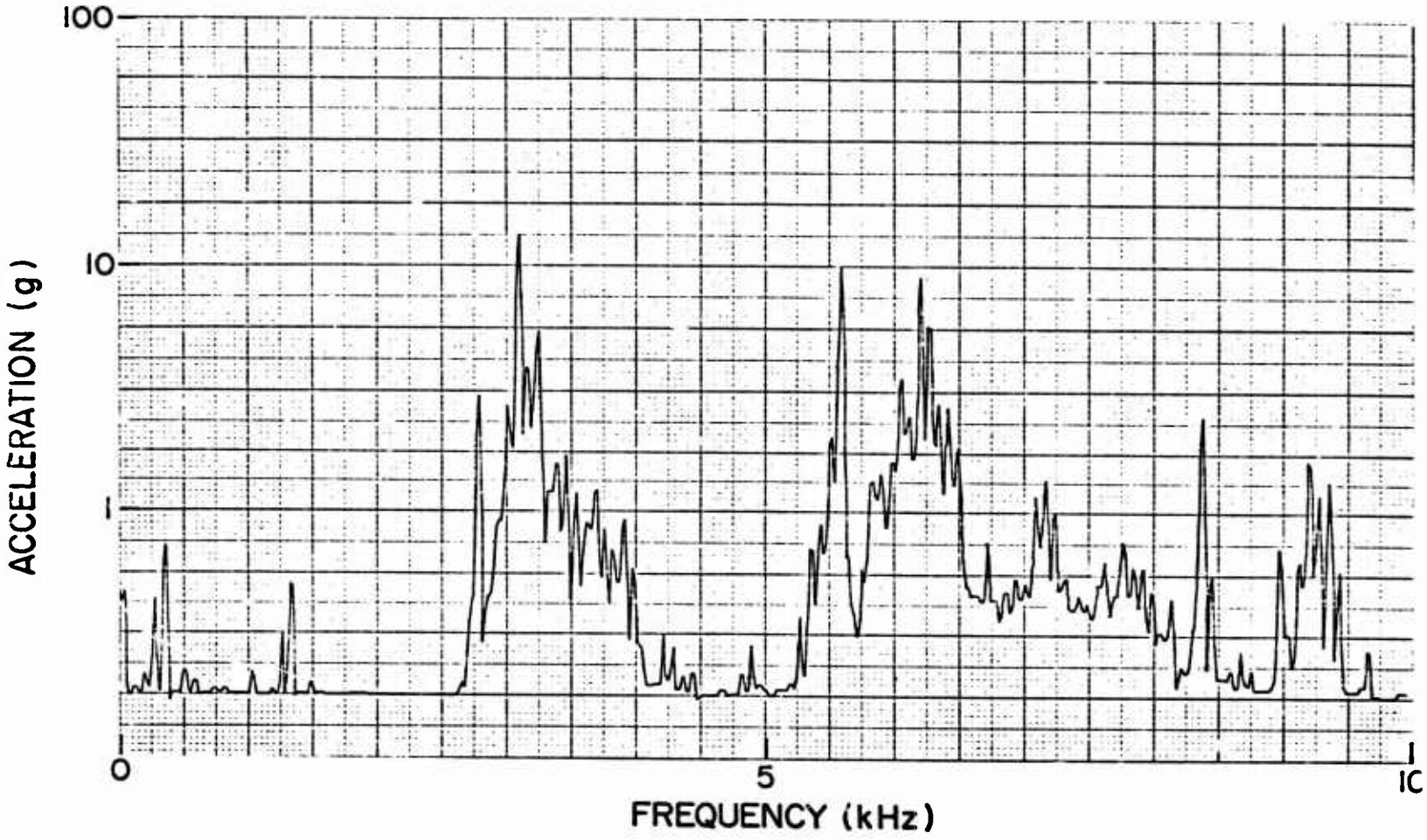

Figure 55. Acceleration Spectra at Gearbox Housing (Faulty Gears).

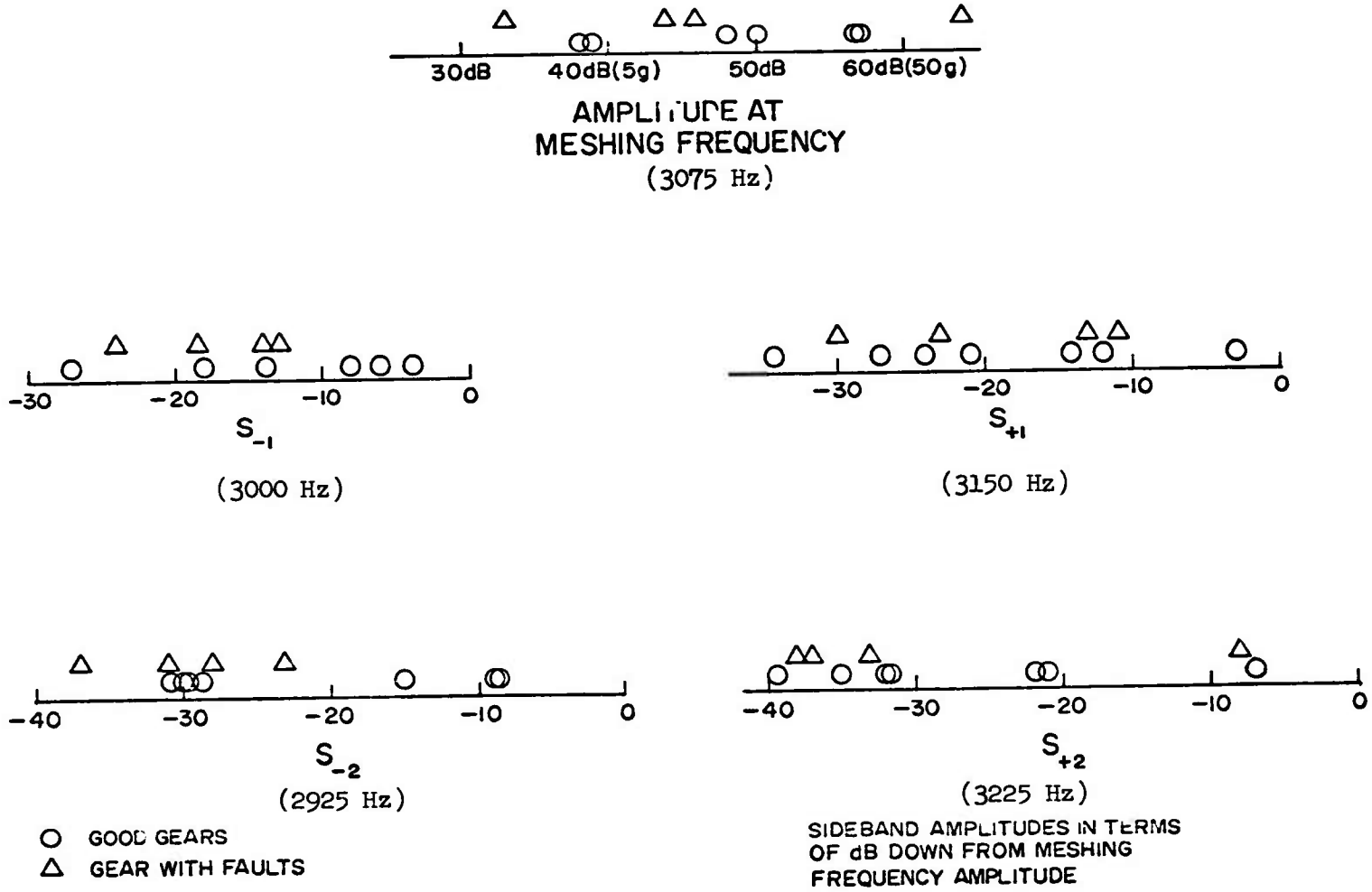

Figure 56. Distribution of Spectral Amplitudes at Pinion Meshing Frequency and Sidebands at Gearbox Housing Sensor Location.

Tests were also performed to determine the effects of speed variations between 3700 and 4800 rpm. While there was some variation in amplitudes of the meshing frequency and its harmonics as speed was varied, no large changes in the amplitudes as the result of torsional resonances were observed.

STRAIN GAGE DATA

Strain gages were mounted on the pinion to allow monitoring of dynamic strain while the gear was in operation. Figure 57 shows typical signals taken from a gear in good condition. The traces represent three consecutive teeth on the gear. In Figure 57a, a complete meshing cycle may be observed. The time between the appearance of the large spikes corresponds to the rotational period of the gear. The smaller spikes occur at the gear meshing frequency and represent dynamic hoop stresses of the gear wheel. The higher frequency component evident in the signal is caused by a deficiency of the tape recorder which allowed some of the carrier frequency to "leak" into the data. Figure 57b presents the individual tooth contact in more detail. Evident in this picture by the amplitude of strain is the shift between one tooth-pair and two tooth-pair load sharing. As may also be seen from the figure, shifts in load sharing are not as abrupt as static analysis predicts. Based on the figure, a contact ratio of between 1.9 and 2.0 could be found, as opposed to the value of 1.75 calculated analytically. This is probably the result of dynamic deflections encountered in the mesh.

Figure 58 shows torque and strain data from a gear which contained a small fault. Figure 59 shows similar data for the gear containing a large fault. Again larger strain amplitudes are evident at the gear rotational period while smaller oscillations appear at the gear-meshing frequency. There are also some smaller spikes caused by interactions of the dummy gages. The data show the tooth strains to be significantly different for faulty gears. Oscillations in the faulty gears occur as the result of the tooth-bending response to the impulsive loading caused by the fault. There is also some evidence of loss of contact as the fault passes through the meshing position.

SUMMARY

It was seen that the effects of the fault introduced into the geared system may be observed in the gearbox vibration time-domain signals. The presence of the spikes in the acceleration signals lends credence to the introduction of an impact force into the geared system as a result of the fault. It might be noted here that impacts in the mesh might also be caused by gear tooth pitch errors, assembly difficulties, and misalignment.

Plots of the input torque show oscillations about the mean value. This information is used in the simulation as an input to the geared system. Strain gage data show both low mesh damping and indications of loss of contact as the fault passes through the mesh. Both results are useful as inputs to the simulation study.

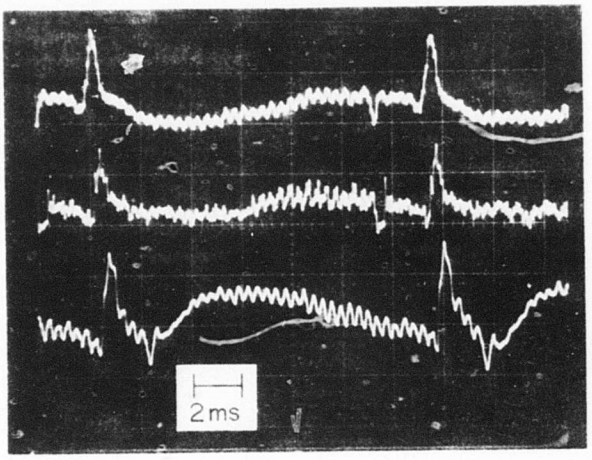

(a)

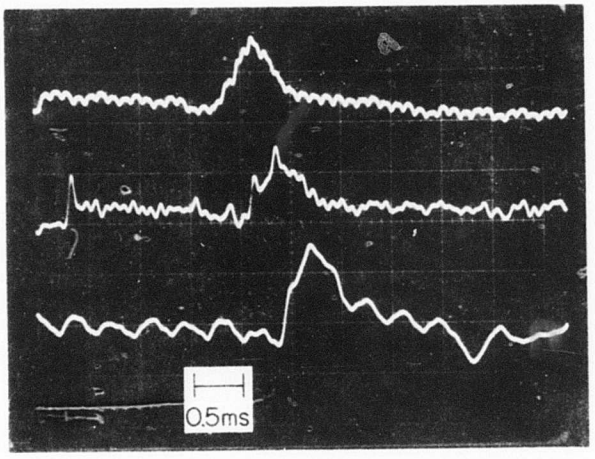

(b)

Figure 57. Strain Response for Good Gears.

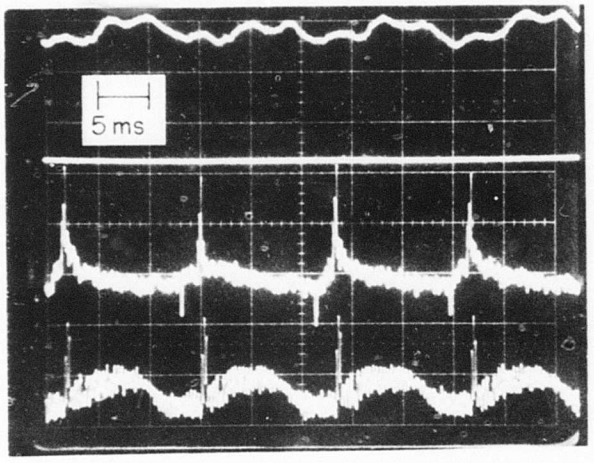

(a)

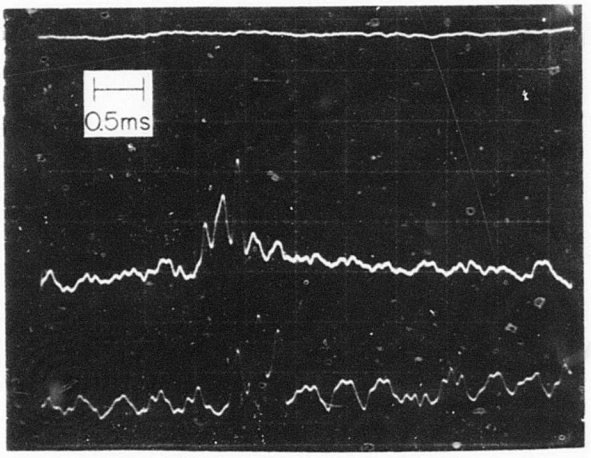

(b)

Figure 58. Strain Signals for Gear With a Small Fault.

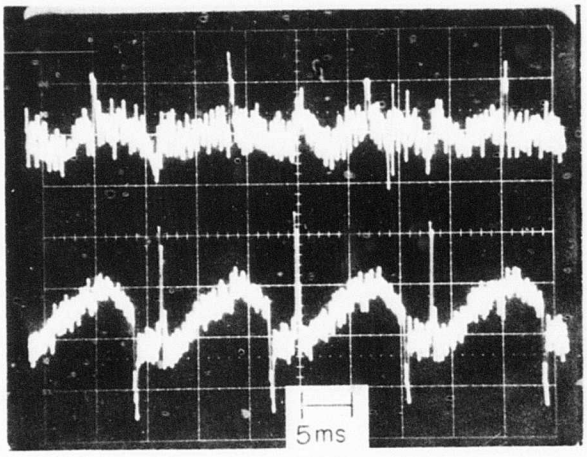

(a)

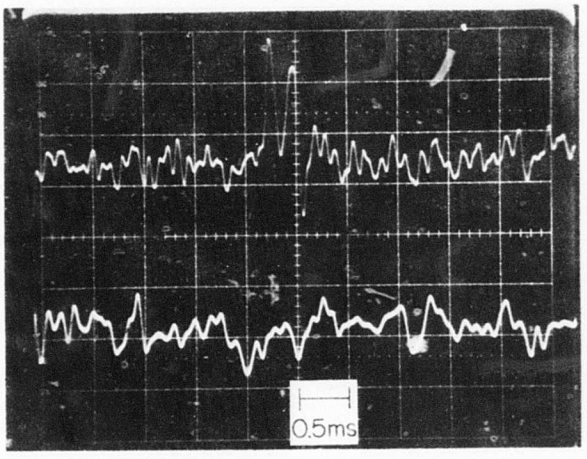

(b)

Figure 59. Strain Signals for Gear With a Large Fault.

The primary information with respect to discrimination of data on the basis of fault presence occurs in the spectra of the input bearing acceleration. Amplitudes at the meshing frequency are significantly higher for gears with faults, and a sawtooth consisting of multiples of shaft rotational frequency is also seen for faulty gearing. The effects of faults on sidebands and harmonics are not readily evident since distinctions between good and bad gears were not observed. Response information is also shown to be a strong function of position of the transducer with respect to fault position, since forces generated by the fault tend to be attenuated and distorted by signal transmission paths.

SIMULATION RESULTS

The equations presented in the Theoretical Analysis section were simulated and solved on the Ohio State IBM System 370/165 computer. Figure 60 presents a flow diagram of the solution process. Stiffness functions for both good gears and those with faults are calculated, and impact amplitudes due to faults are computed. These data are then used in the torsional dynamic simulation where the geared system's time response is calculated. The output of this analysis is then digitally sampled and stored. If time-domain response data are desired, they may be read out at this time. The data may also be fed through a Fast Fourier Transform subroutine which calculates the frequency spectrum of the system's dynamic response. At this point, the frequency spectrum may be either read out directly or modified by any desired transfer function and then read out. In this study, output data were plotted with the use of a Calcomp Plotter; however, the data are also available for any other output procedure that is desired.

MESH STIFFNESS FUNCTIONS

As a first step in the analysis, mesh stiffness functions are calculated. Figures 61 and 62 present the calculation procedure for good gears. In Figure 61, gear compliance is plotted versus η (distance along the line of action from the pitch point). The bending compliance for the gear and pinion and the Hertzian compliance for the pair of teeth are shown along with the total tooth pair compliance function. The use of load-sharing considerations allows calculation of the mesh stiffness function apportioned to each tooth on the gear in the manner shown in Figure 62. The parameter KAP is a computational dummy variable which is proportional to the gear rotational position.

Figures 63 and 64 represent compliance and stiffness functions for the gear mesh when a small fault (0.020 in. wide) is present on a tooth. As explained previously, when the contact strip of the tooth pair is contained within the fault width, contact is assumed to be lost, causing Hertzian compliance and, thus, total compliance to become infinite. This makes stiffness values zero in that range, as shown in Figure 64. In the torsional simulation, mesh damping is set to zero when the stiffness value is zero. Figures 65 and 66 show similar compliance and stiffness curves for the case of a fault width of 0.050 inch.

One other stiffness function was calculated to determine the effect of change in load sharing a system response. The plot of Figure 67 shows the stiffness function when the gear mesh contact ratio is 1.92.

IMPACT AMPLITUDE

In order to calculate the amplitude of the torque impulse caused by a tooth fault, velocity differences as a function of fault width were determined. Torsional dynamic simulation was used for this purpose. At the point of

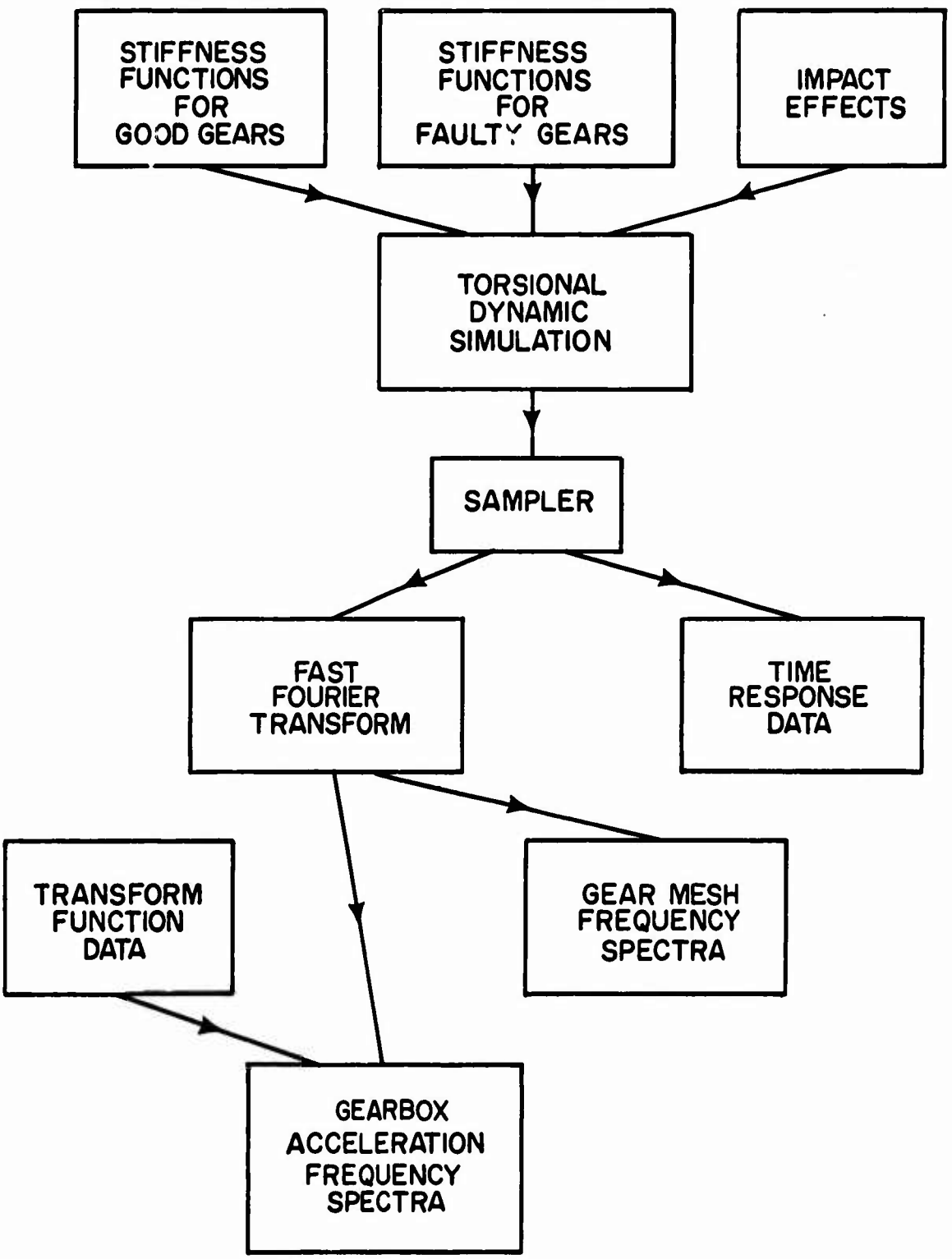

Figure 60. Flow Diagram of System Simulation.

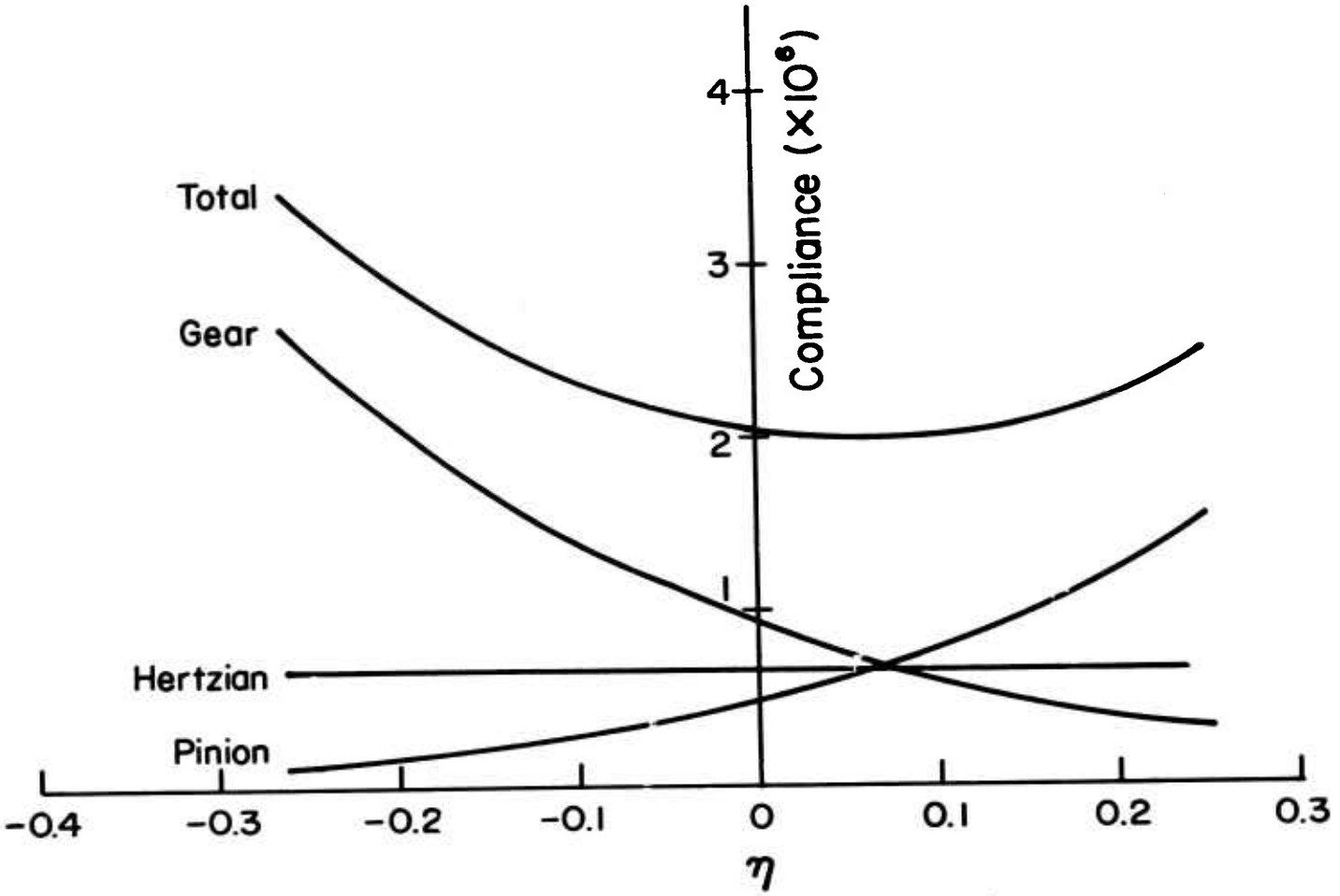

Figure 61. Tooth Pair Compliance (Good Gears).

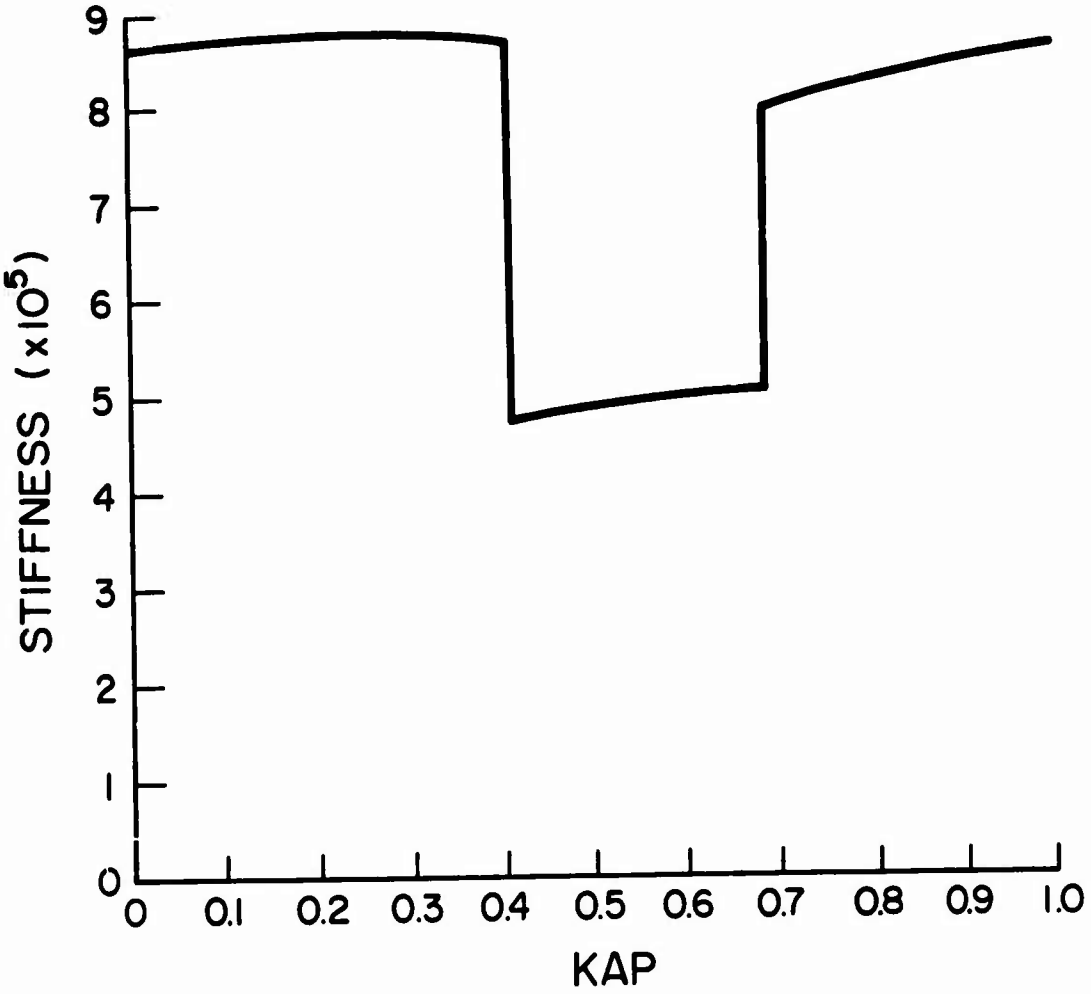

Figure 62. Gear Mesh Stiffness Versus KAP (Good Gear).

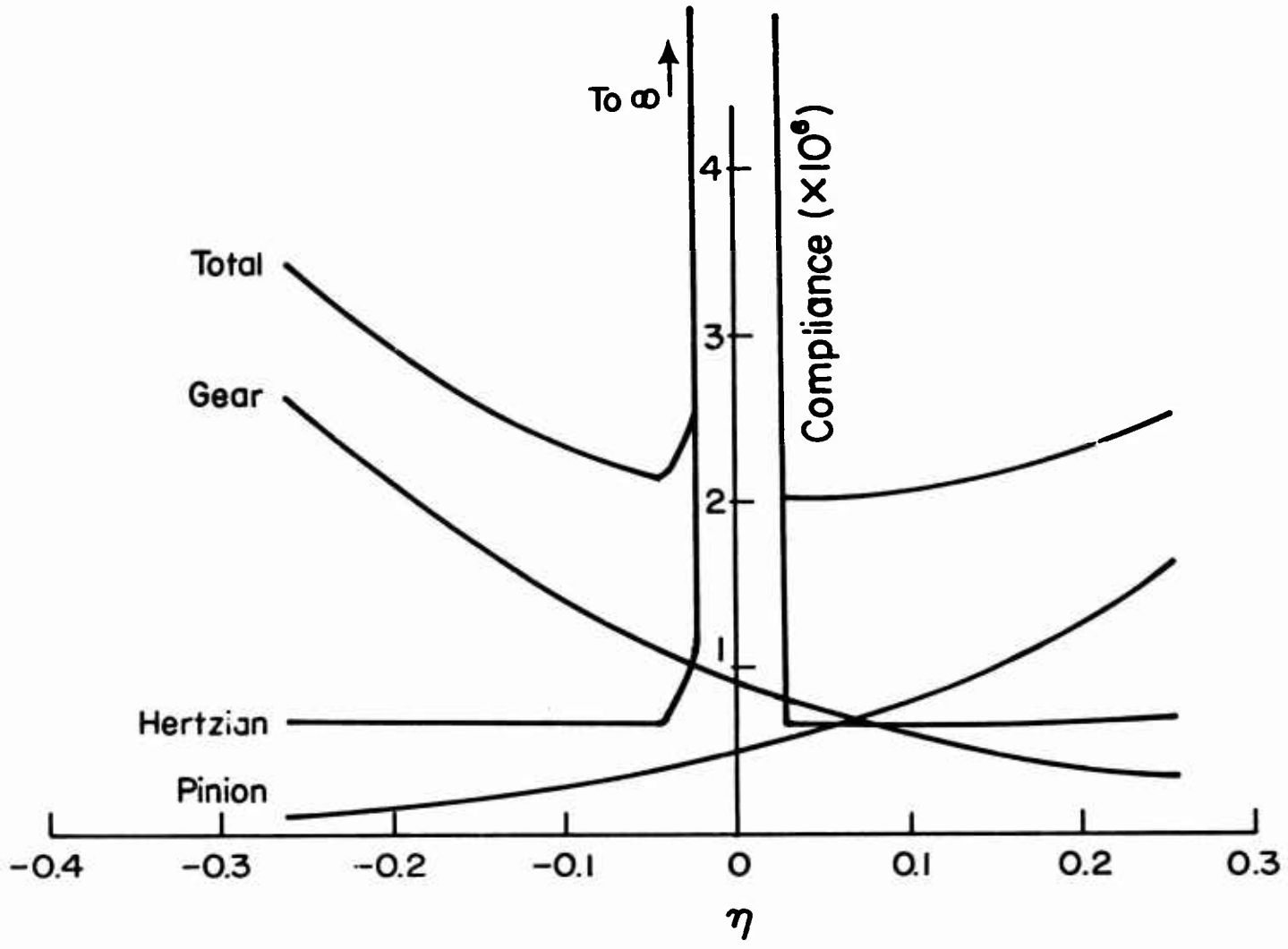

Figure 63. Tooth Pair Compliance (Small Fault, 0.020 Inch Wide).

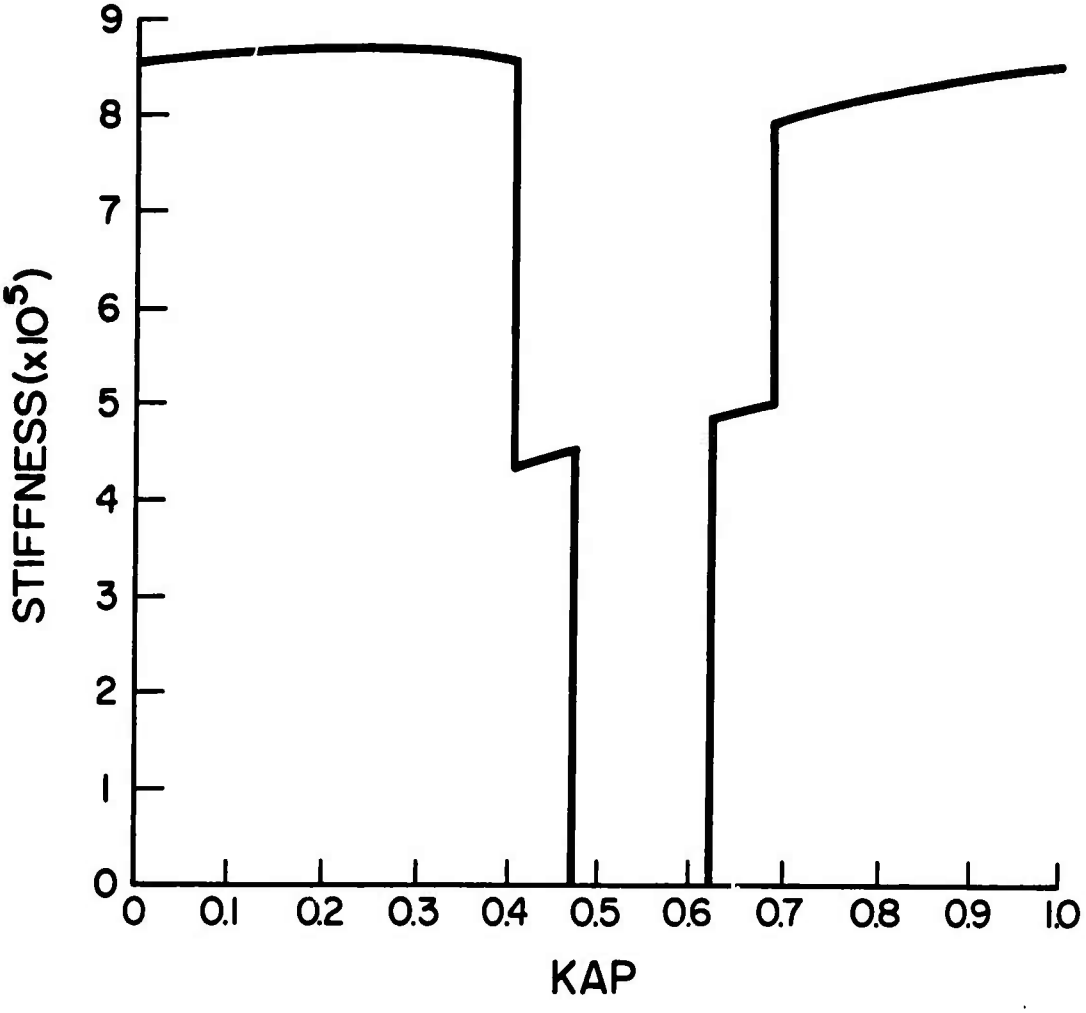

Figure 64. Gear Mesh Stiffness Versus KAP (Small Fault, 0.020 Inch Wide)

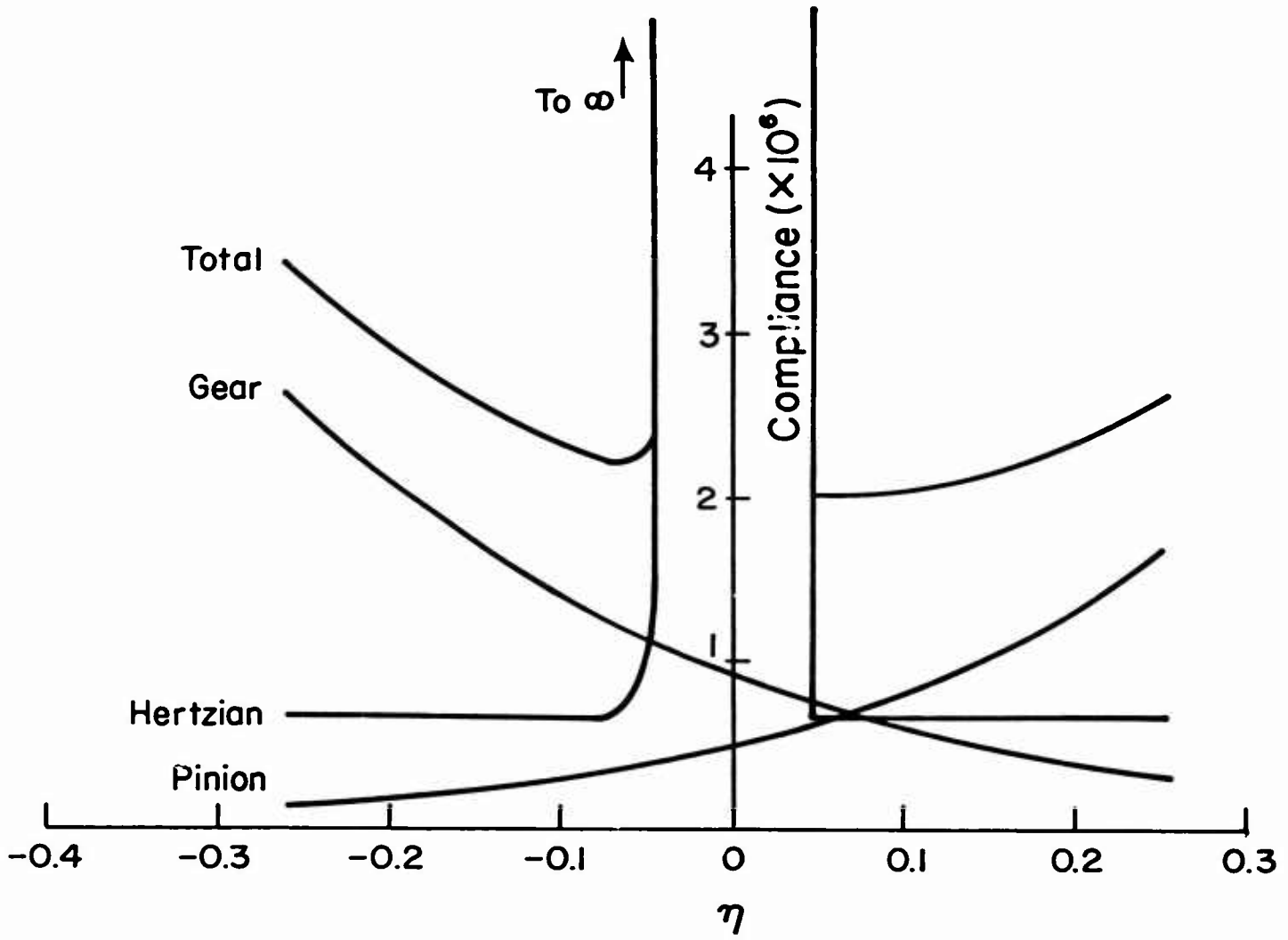

Figure 65. Tooth Pair Compliance (Large Fault, 0.050 Inch Wide).

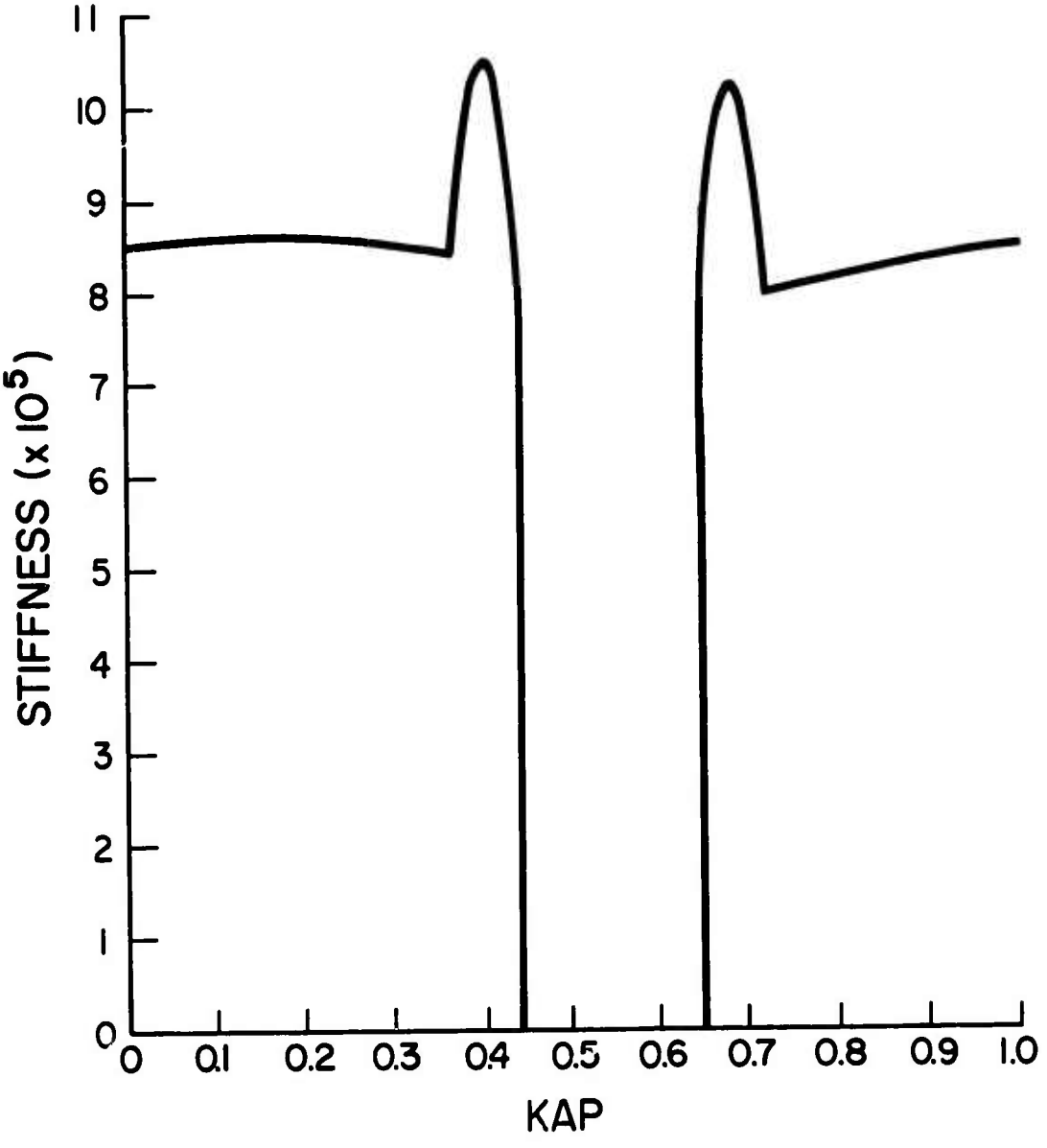

Figure 66. Gear Mesh Stiffness Versus KAP (Large Fault, 0.050 Inch Wide).

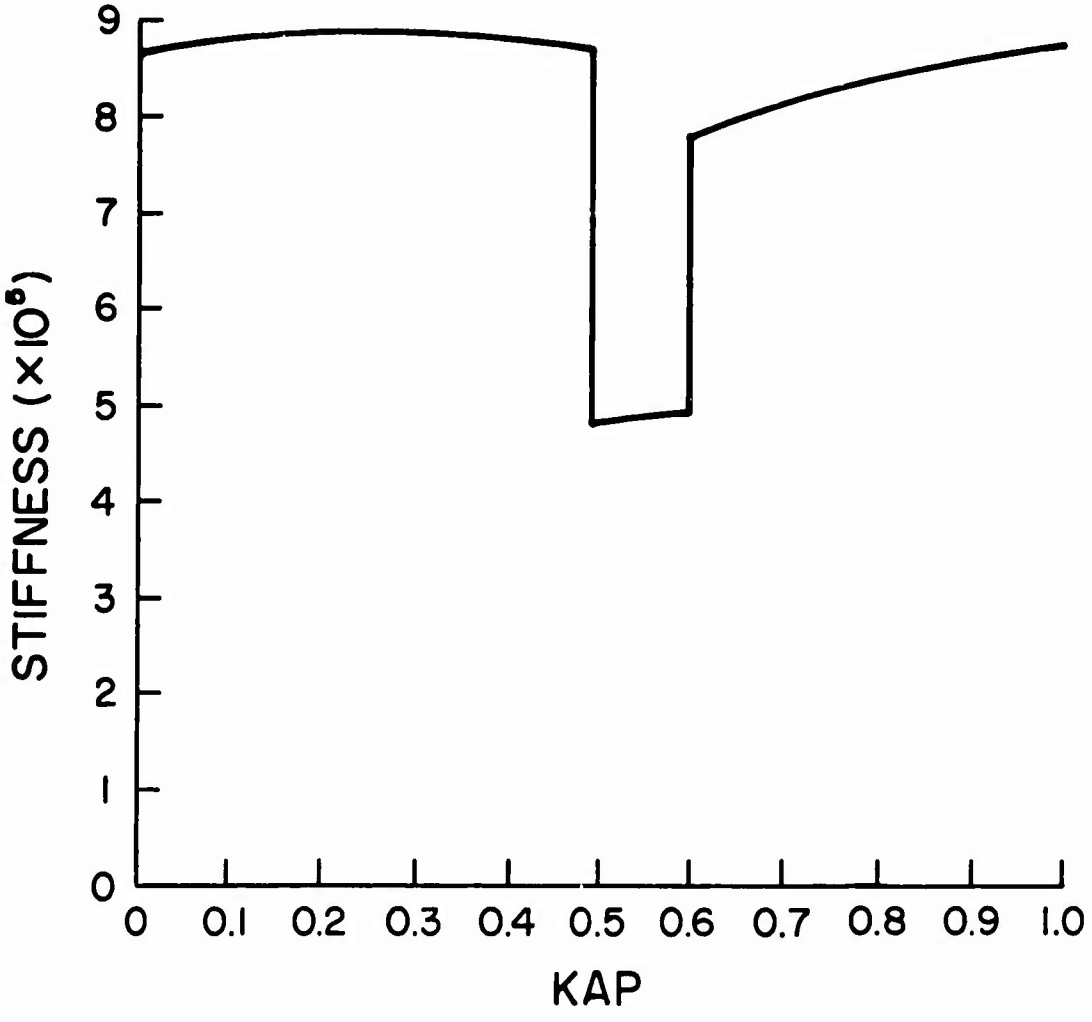

Figure 67. Gear Mesh Stiffness Versus KAP (Contact Ratio = 1.92).

initiation of contact, the fault, mesh stiffness, and damping were set to zero, allowing the geared system to "freewheel", i.e., operate with a loss of contact between two of the gears. From the response data under this condition, Figure 68 shows approximate values of velocity differences of the gear and pinion and time spent in the fault as a function of fault width on the tooth. Fault widths are scaled in terms of the parameter KAP. Based on the desired fault width, values may be read from the plot and inserted into the torsional dynamic simulation.

TIME-DOMAIN RESPONSE

Time-domain response data was one of the outputs available from the simulation. Figures 69-73 show response plots of ψ_1, ψ_2, ψ_3, ψ_4, and $\ddot{\psi}_2$ for the good gears. Amplitudes are presented in terms of radians for angular displacement and rad/s^2 for angular acceleration. Evident in all of the plots are oscillations at the gear-meshing frequency (the result of the mesh stiffness variations) and also at the input shaft rotational frequency (the result of the input torque variation). Figures 69 and 72 (ψ_1 and ψ_4, respectively) show less of the effect of the gear-meshing frequency. This is to be expected since these parameters represent relative rotation along shafting of the system rather than between gears. The displacement plots show an oscillation about a nonzero mean level. This level corresponds to a wrap-up angle of the torsional system as the result of transmitted load torques. The acceleration plot of Figure 73 shows a "beating" at the shaft frequency which should be indicative of sidebanding in the frequency analysis.

Figures 74 and 75 represent the response of ψ_2 and $\ddot{\psi}_2$ when the large fault (0.050 in.) is introduced into the analysis. The fault produces the large spike in the response with a repetition rate of once per shaft revolution which corresponds to the rate at which the fault passes through the meshing position. The relative amplitude of the spike with respect to the steady-state oscillation is larger than was seen in experimental data. This is reasonable since there is likely to be a good deal of attenuation of the spike as it passes from the gear mesh to accelerometer monitoring positions on the gearbox.

FREQUENCY SPECTRA

The primary comparison of experimental and theoretical data was performed in the frequency domain. The frequency transform used on the simulation data is a 1024 input point FFT analysis performed on data sampled at 20 kHz. This provides output information from 0-10 kHz having a bandwidth of 19.5 Hz, which is comparable to that obtained with the real-time analyzer on the experimental data. Six averages of the spectral amplitudes are performed to lower noise levels. A second-order anti-aliasing filter is used with a break frequency of 9 kHz. Data are presented from 0-7 kHz to minimize any other aliasing effects which may be present.

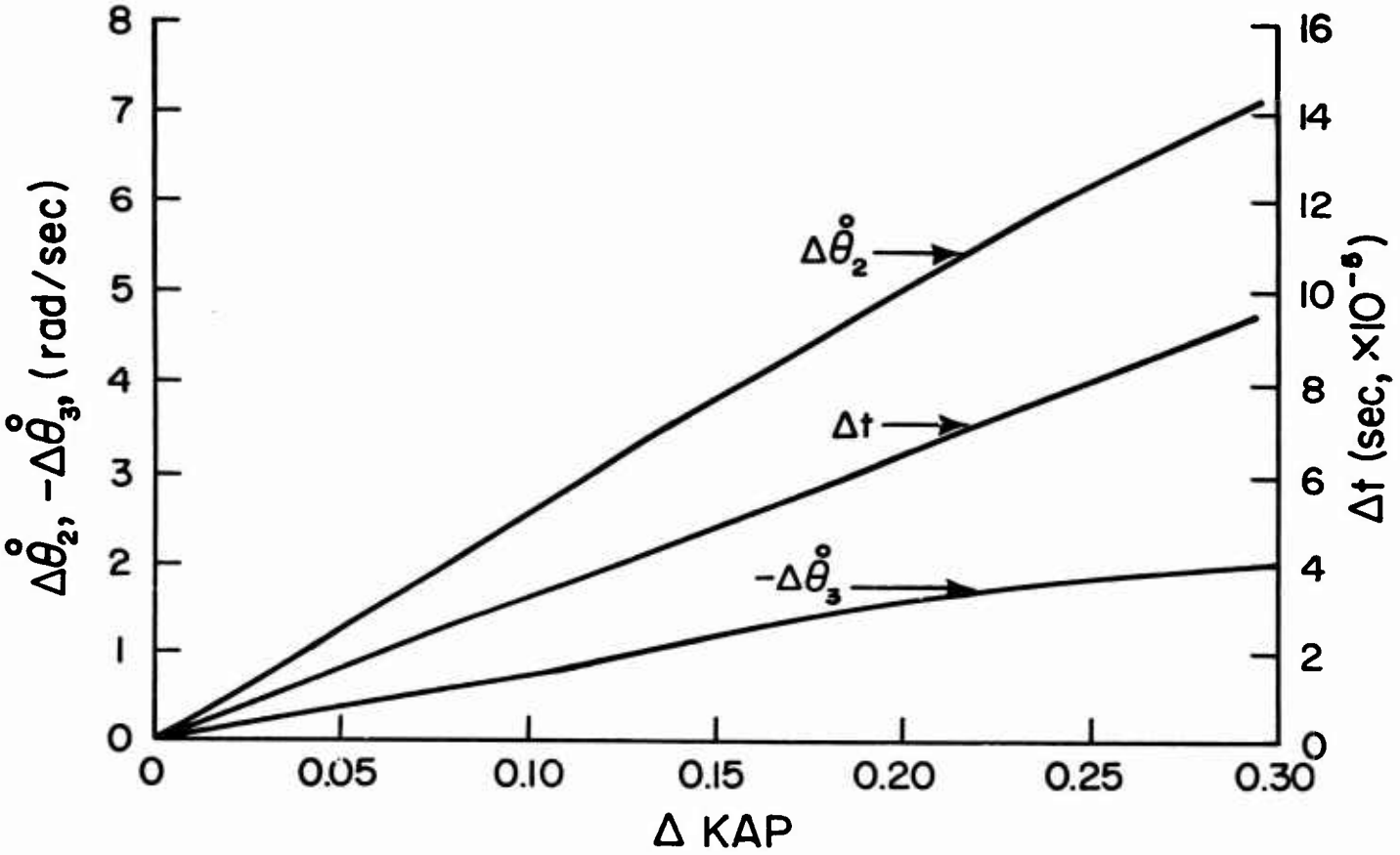

Figure 68. Velocity Differences and Fault Time for Freewheeling Gear.

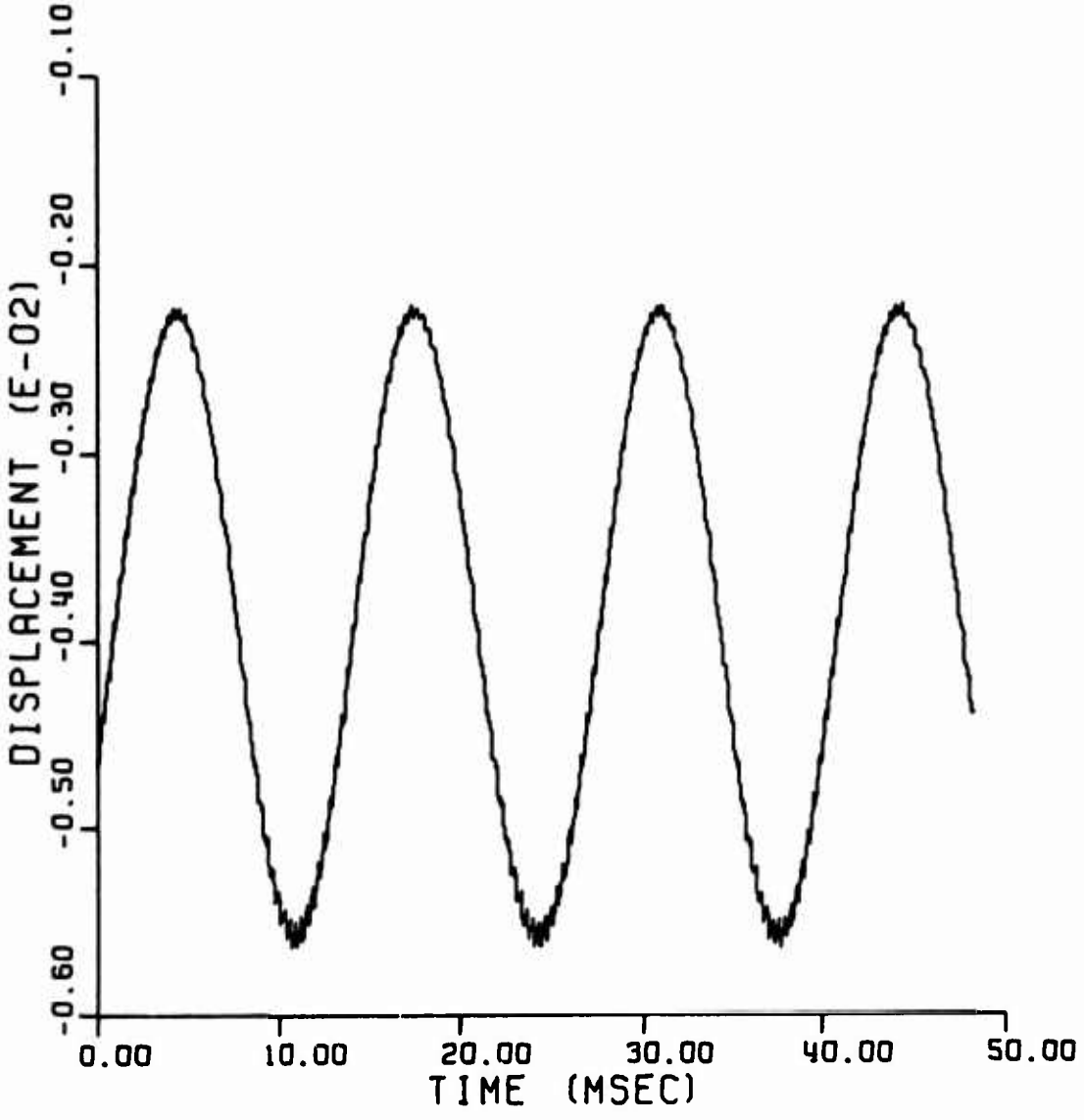

Figure 69. Response of Ψ_1 (Good Gear).

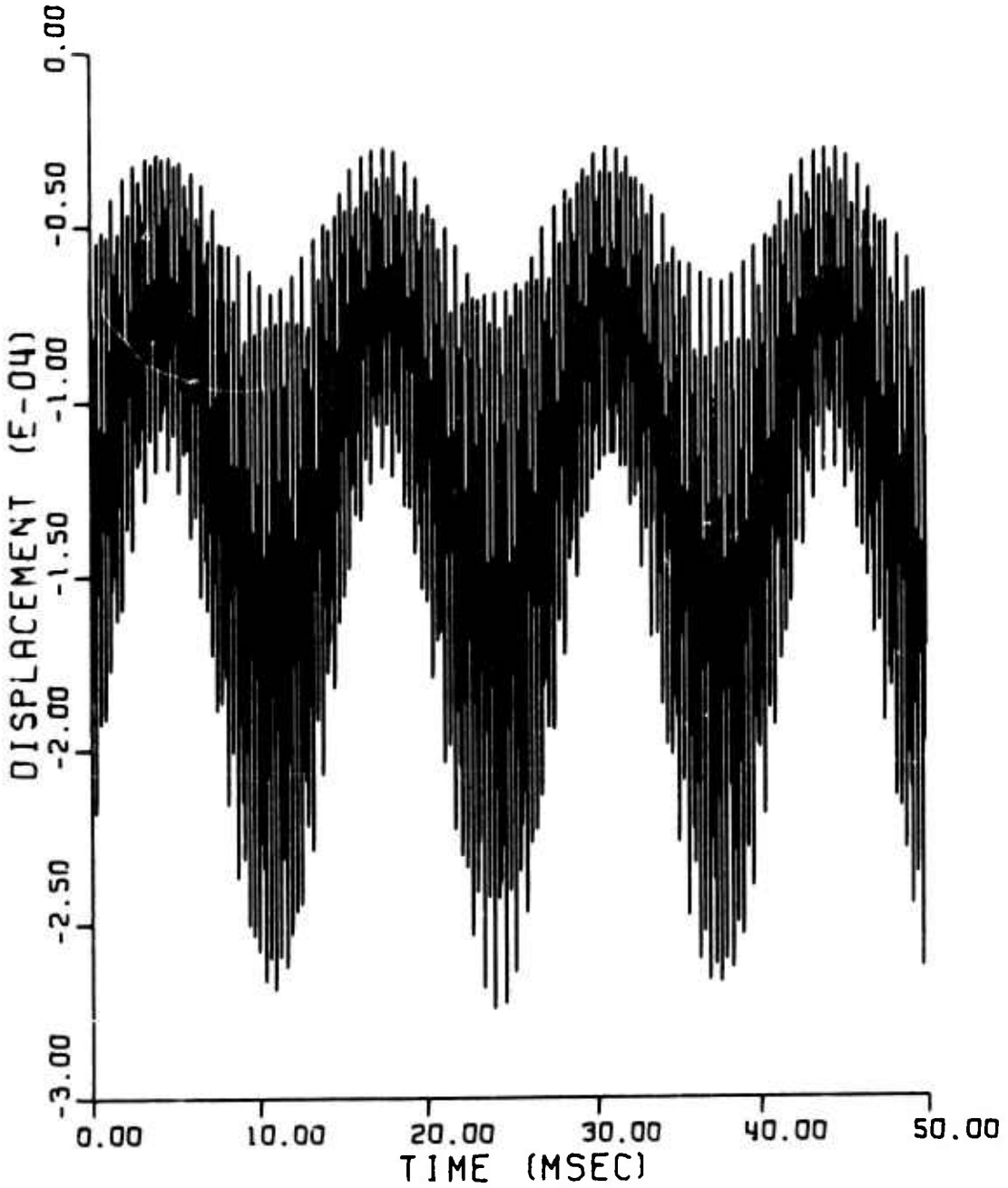

Figure 70. Response of J_2 (Good Gear).

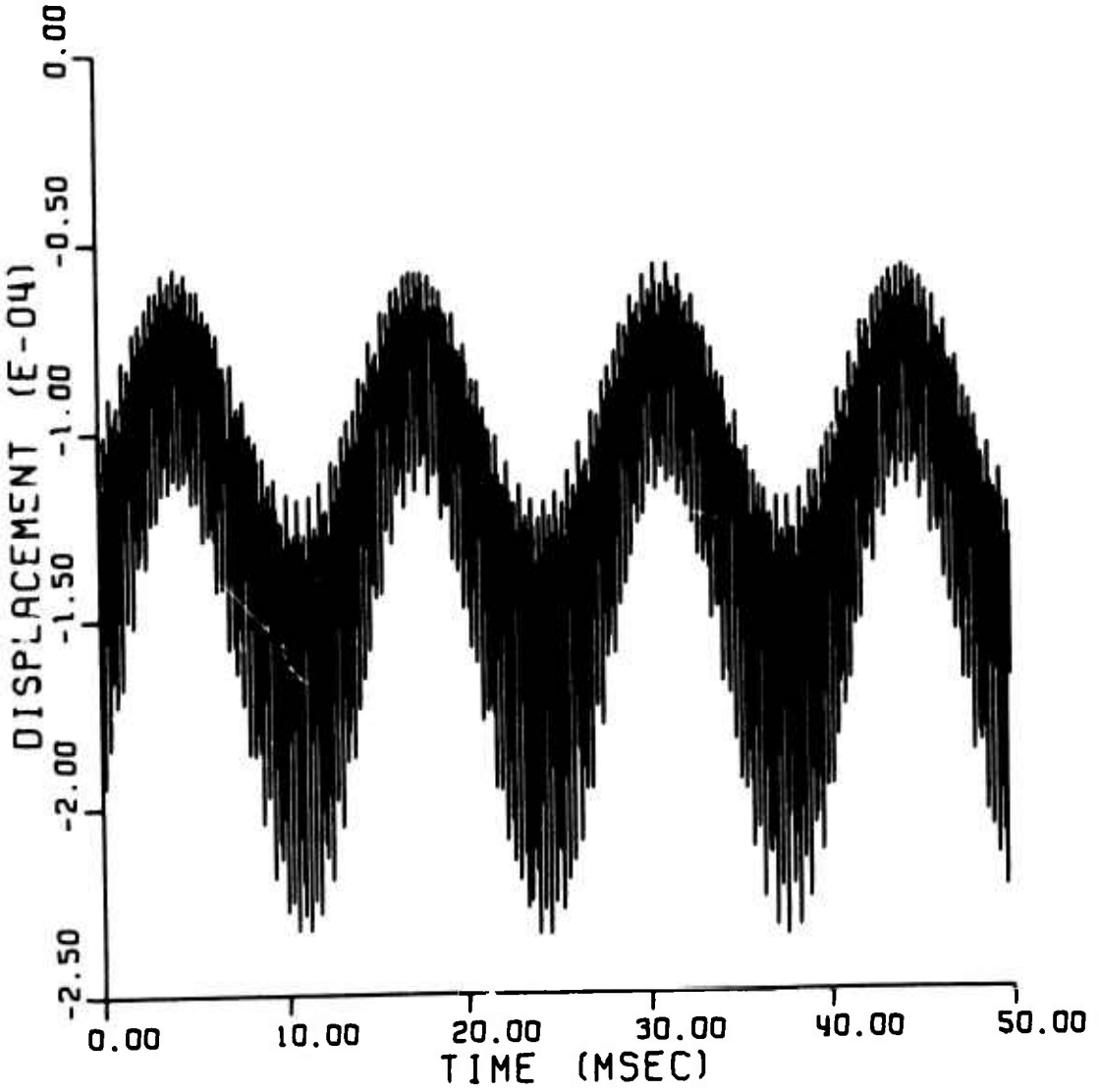

Figure 71. Response of ψ_4 (Good Gear).

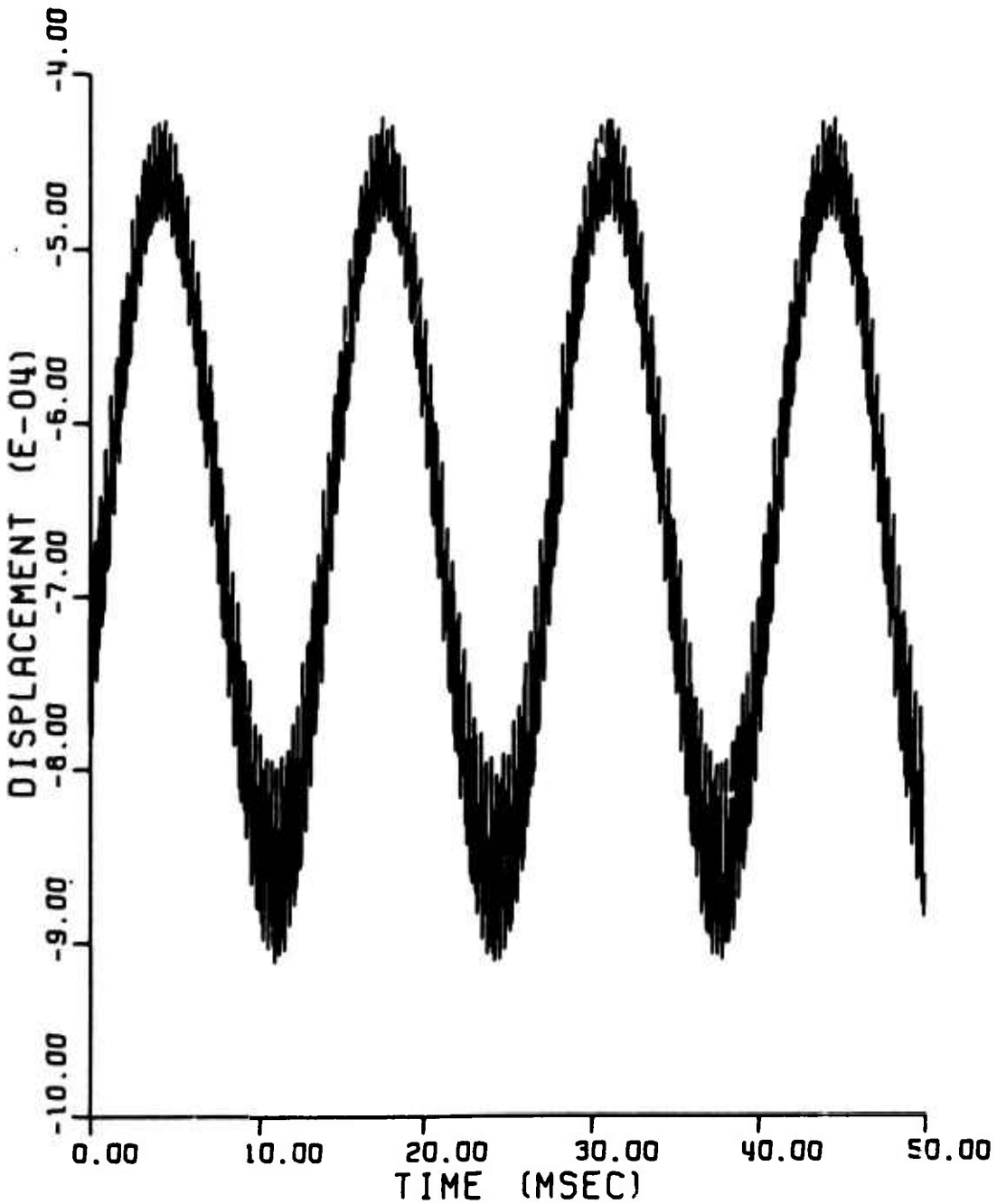

Figure 72. Response of ψ_4 (Good Gear).

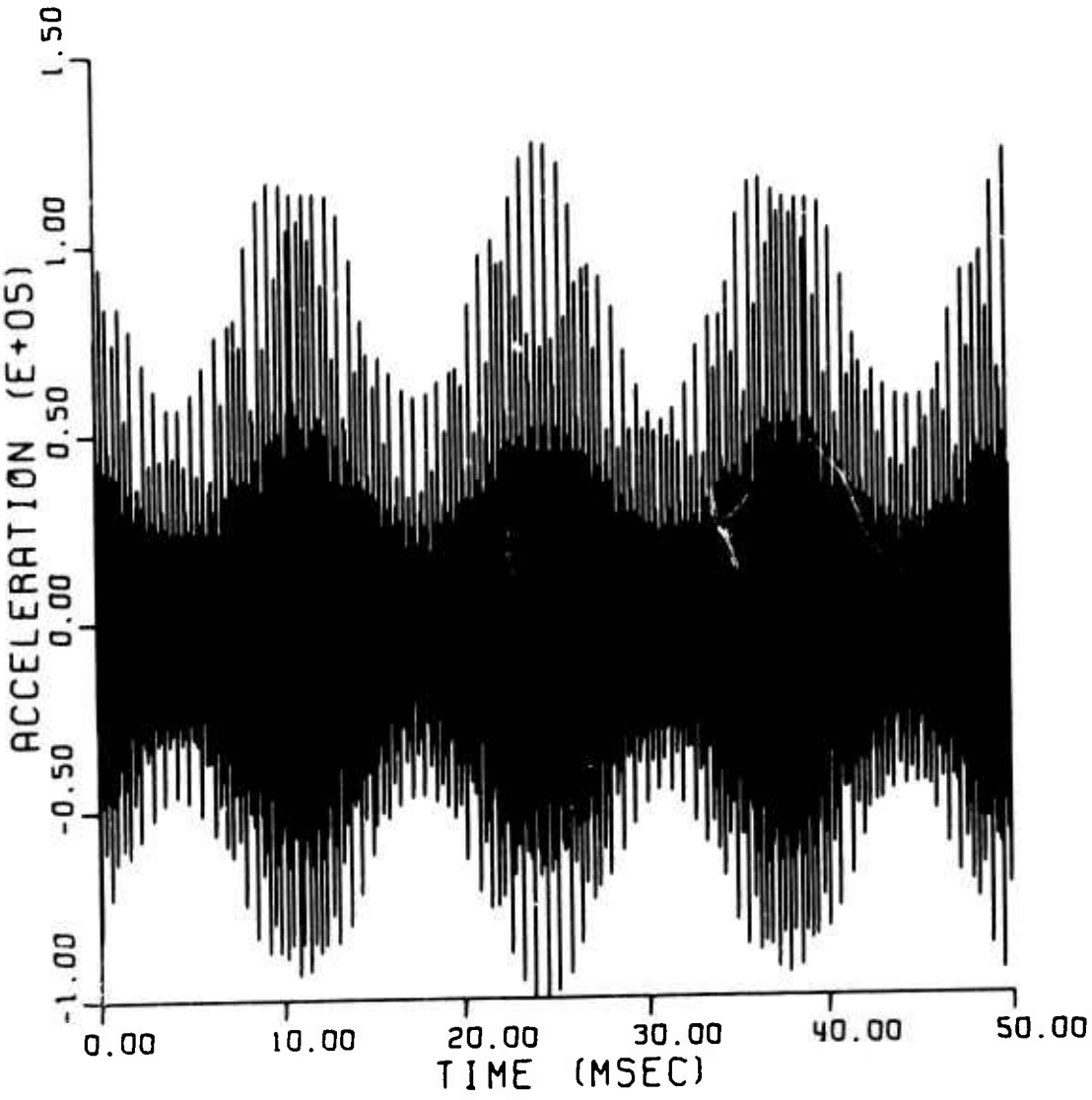

Figure 73. Response of ψ_1 (Good Gear).

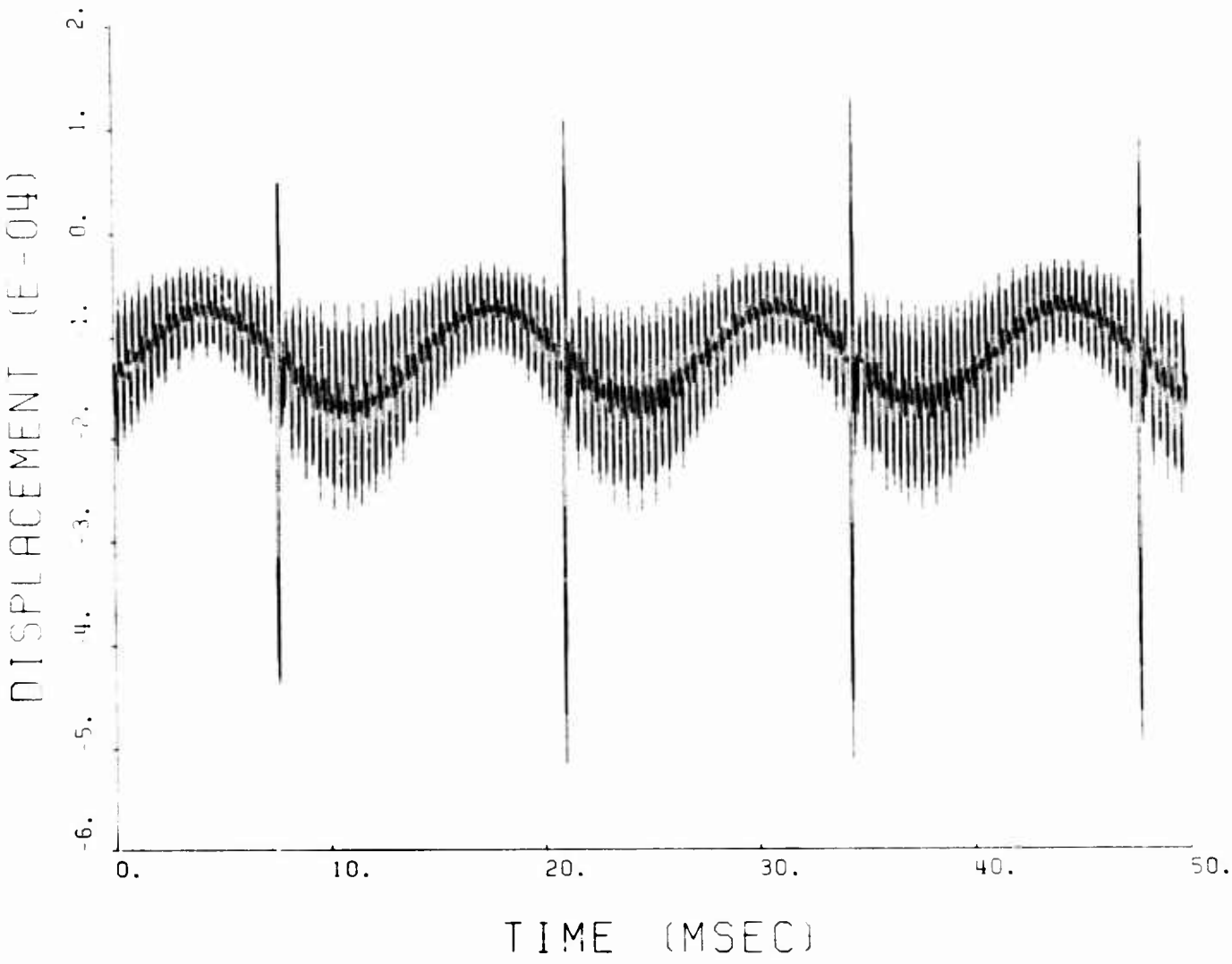

Figure 74. Response of ψ_2 (0.050-Inch-Wide Fault).

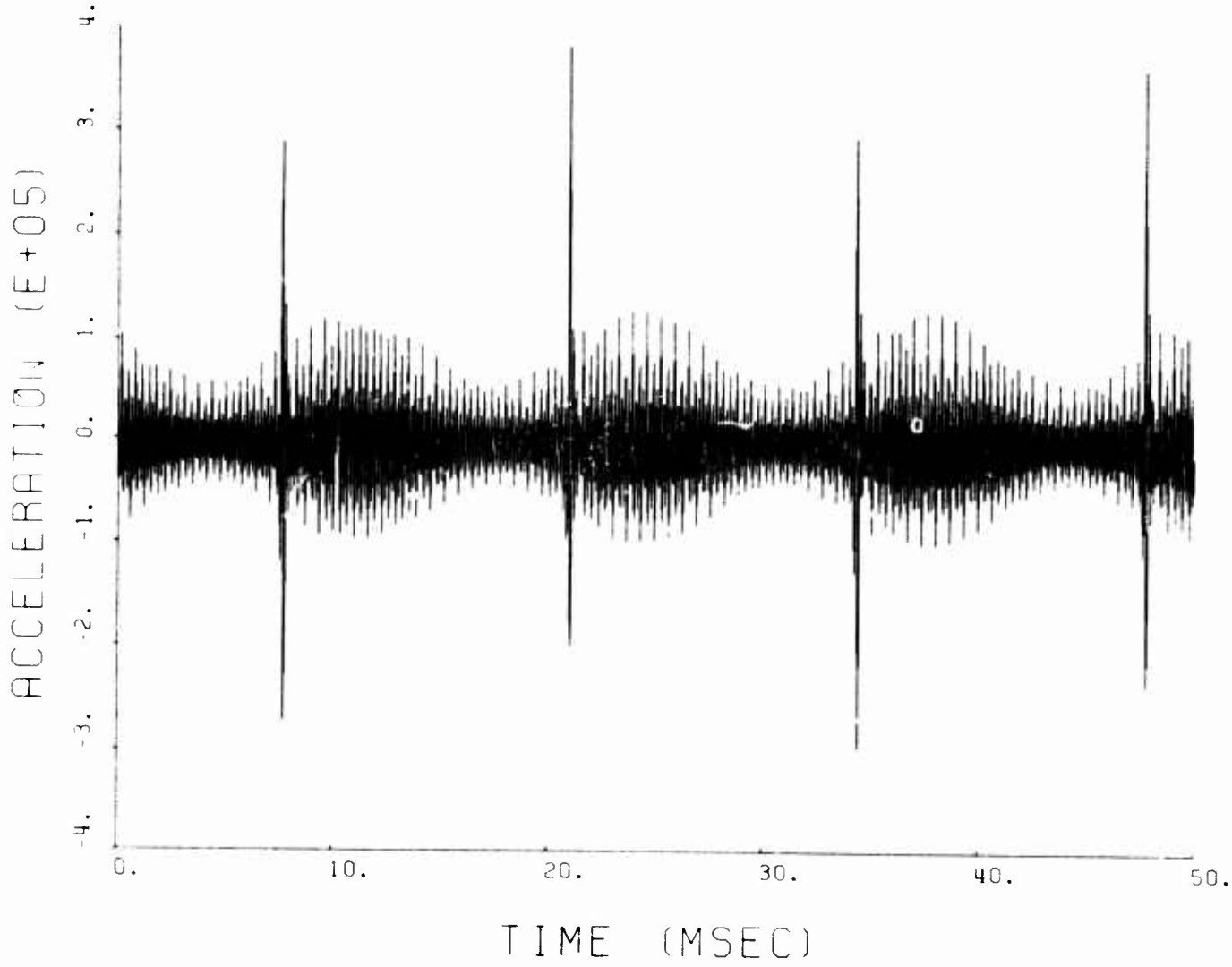

Figure 75. Response of $\ddot{y}_2$ (0.050-Inch-Wide Fault).

Figures 76-80 show frequency spectra for ψ_1, ψ_2, ψ_3, ψ_4, and $\ddot{\psi}_2$ when no gear faults are present. Obvious peaks in the spectra may be seen at 3075 and 6150 Hz, which are the gear meshing frequency and its first harmonic, respectively. Also present are sideband frequencies at ± 75 Hz, ± 150 Hz, etc., about these two peaks. A large peak is also seen at 75 Hz, the input shaft rotational frequency. There are also frequency components in the regions near 1500 and 4500 Hz. The exact origin of these components has not been ascertained, but they appear in the experimental results and may be the result of nonlinear effects of the system. These peaks are more predominant in the acceleration data of Figure 80. Torsional resonant frequencies for the simulation were calculated using a Holzer analysis, the results of which are shown in Table IV. Since the mesh stiffness is variable,

TABLE IV. SIMULATION TORSIONAL RESONANCES VIA HOLZER ANALYSIS

One Tooth-Pair Stiffness (Hz)	Two Tooth-Pair Stiffness (Hz)
458	464
918	943
4247	5644
5264	6974

mean values of single tooth-pair stiffness and double tooth-pair stiffness were used in calculating two sets of natural frequencies. Actual resonant values will lie somewhere within this range; however, no strong components in the spectra were observed at these frequencies.

One fact which may be noted from the spectra is that the relationship of

$$\ddot{\psi}_2 = \omega^2(\psi_2) \tag{57}$$

is not followed at all frequencies. It is felt that this is a result of the smoothing and computational errors induced by the double integration used to calculate angular displacement from acceleration. However, the amplitudes of the frequencies at which differences occur are such that little effect on the meshing frequency is expected.

Figures 81-84 show the frequency spectra of ψ_2 and $\ddot{\psi}_2$ when fault effects have been introduced into the analysis; ψ_2 and $\ddot{\psi}_2$ have been analyzed since they represent the relative displacement and acceleration of the gear mesh in which the fault is encountered and, thus, should show the strongest effects of the faults. In Figures 81 and 82, the 0.020-inch-wide fault has been introduced, while in Figures 83 and 84 the 0.050-inch-wide fault was introduced. In the case where faults are introduced, amplitudes at the

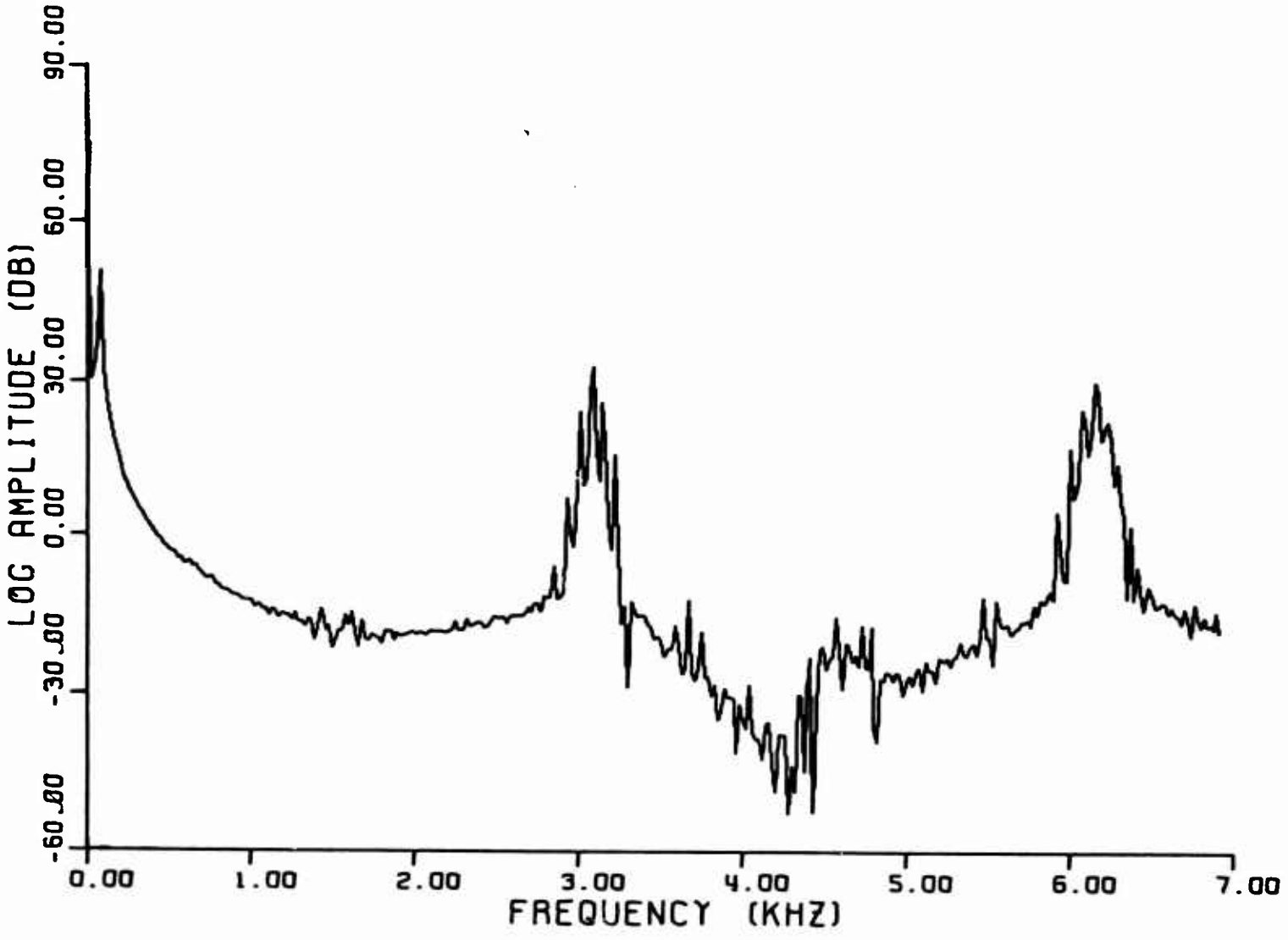

Figure 76. Spectrum of ψ_1 (Good Gear, 0 dB = 10^{-5} rad).

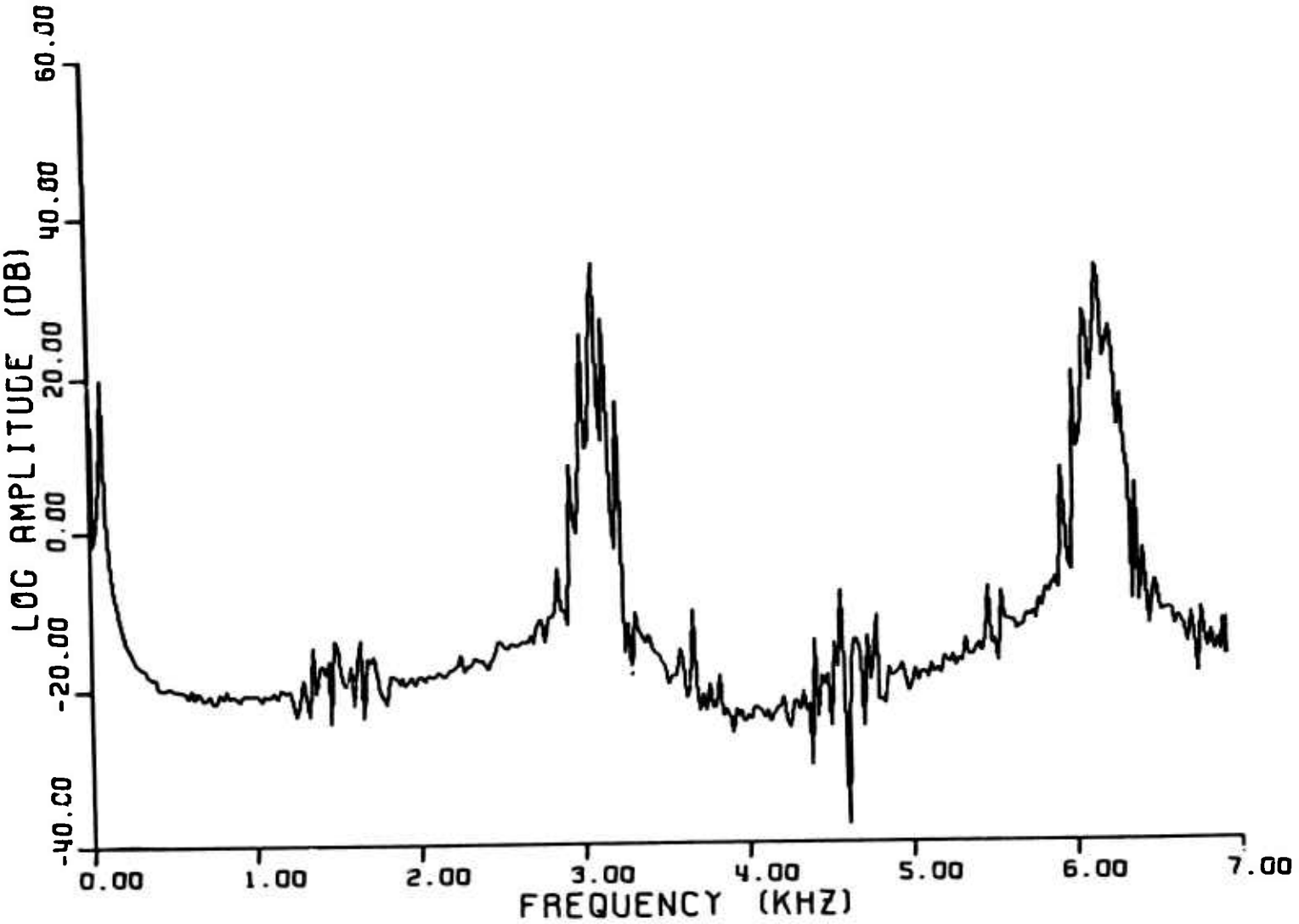

Figure 77. Spectrum of ψ_2 (Good Gear, 0 dB = 10^{-5} rad).

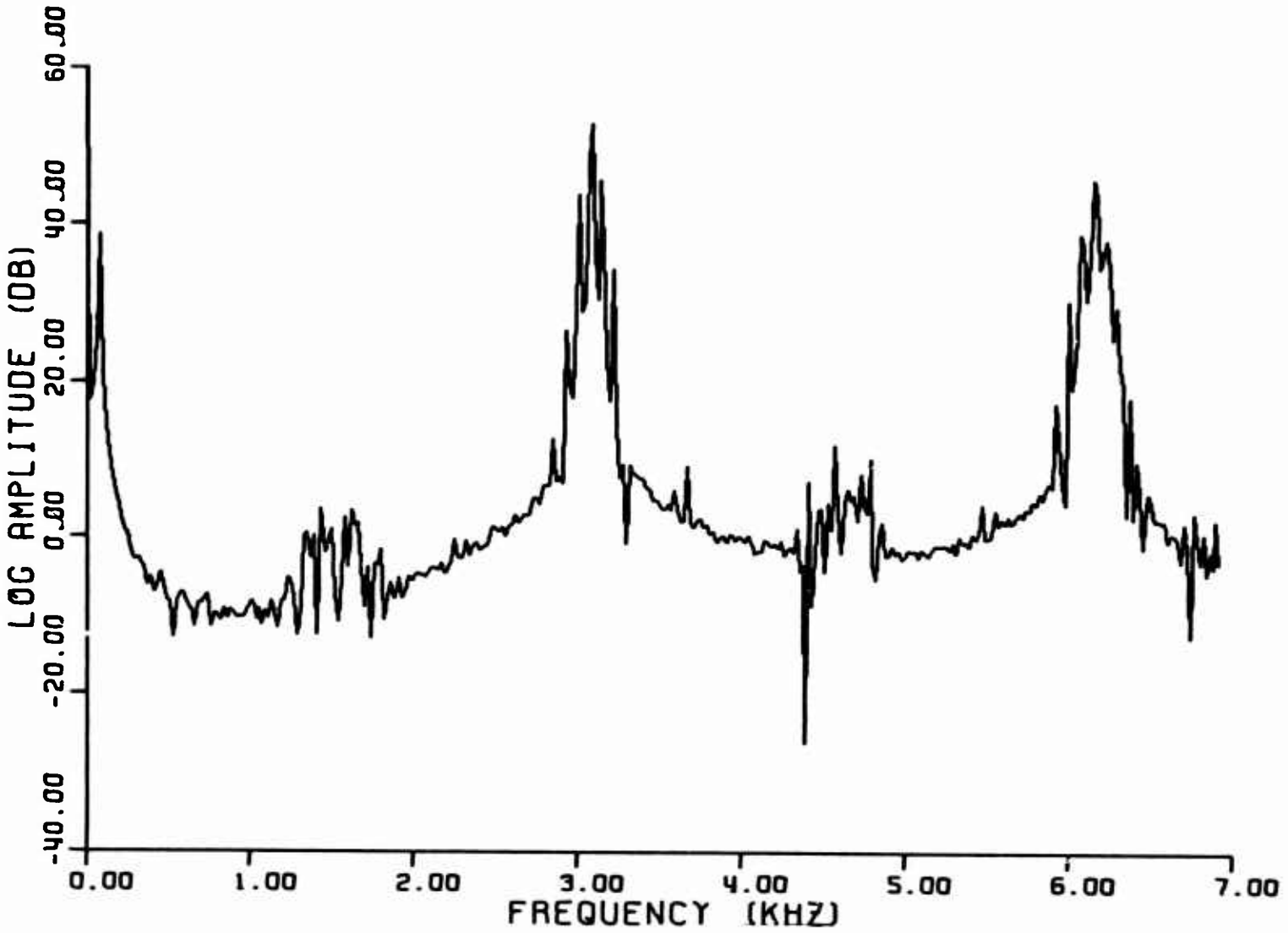

Figure 78. Spectrum of ψ_3 (Good Gear, 0 dB = 10^{-6} rad).

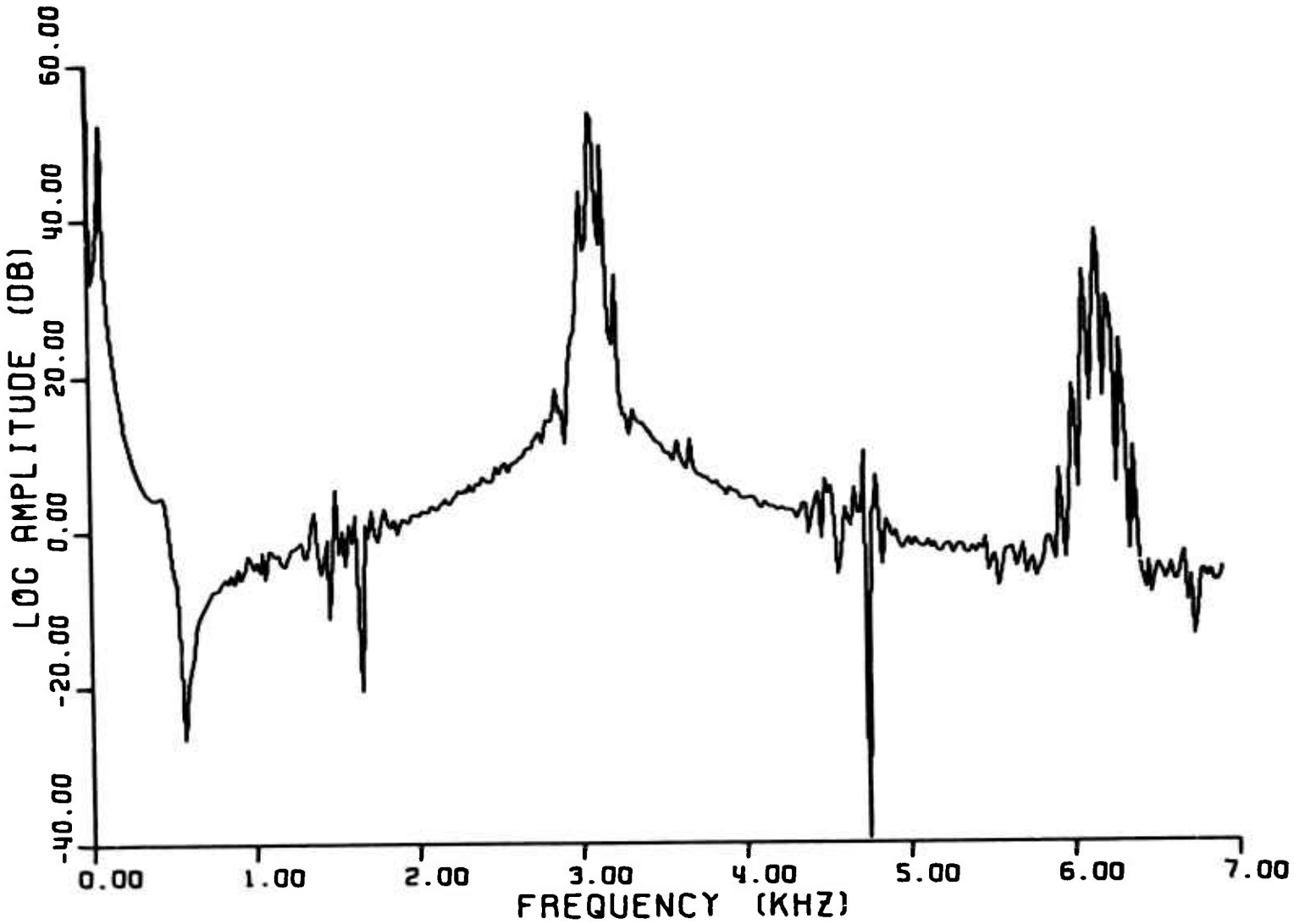

Figure 79. Spectrum of ψ_4 (Good Gear, 0 dB = 10^{-6} rad).

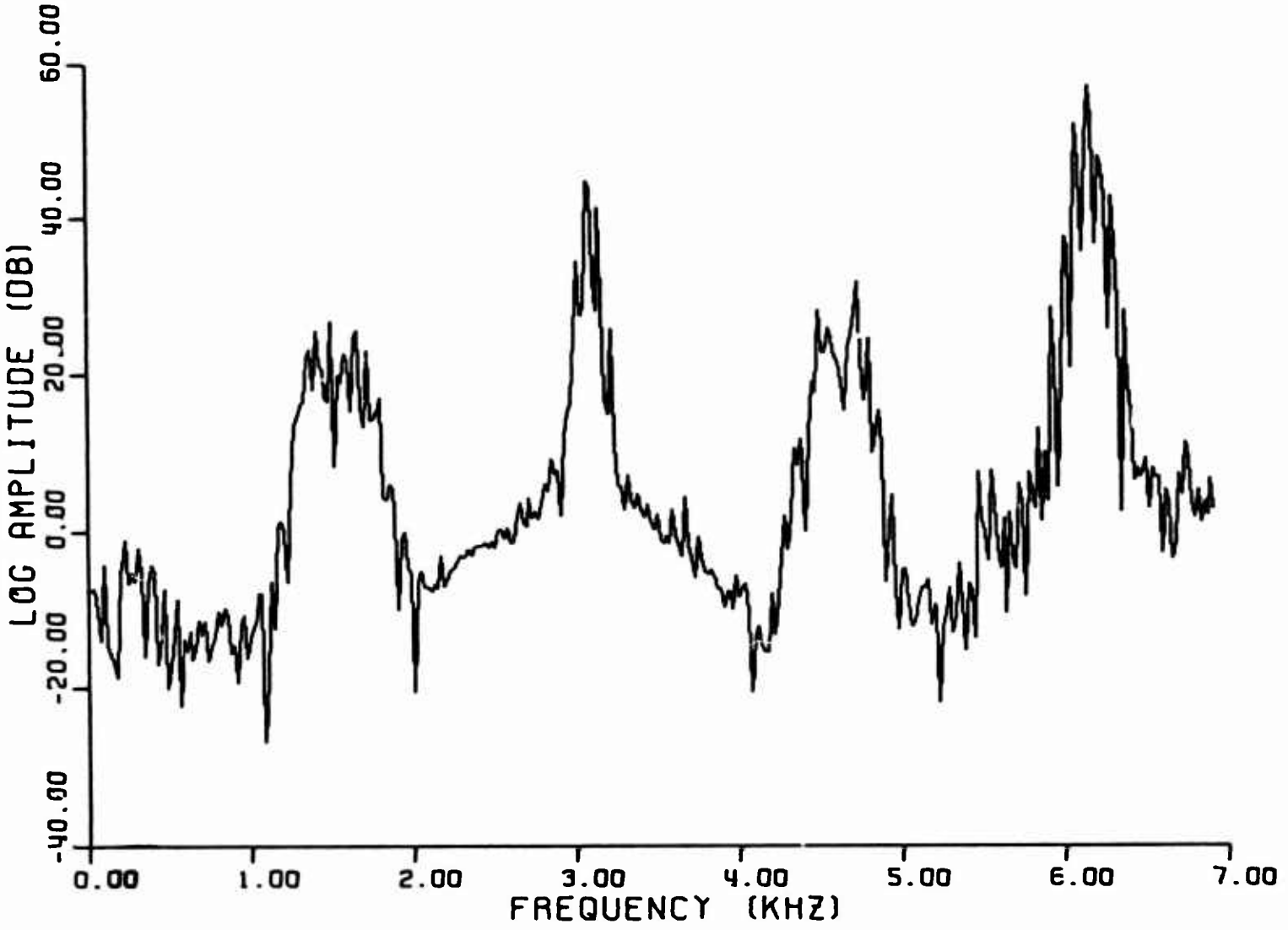

Figure 80. Spectrum of $\ddot{\psi}_2$ (Good Gear, 0 dB = 10^3 rad/s^2).

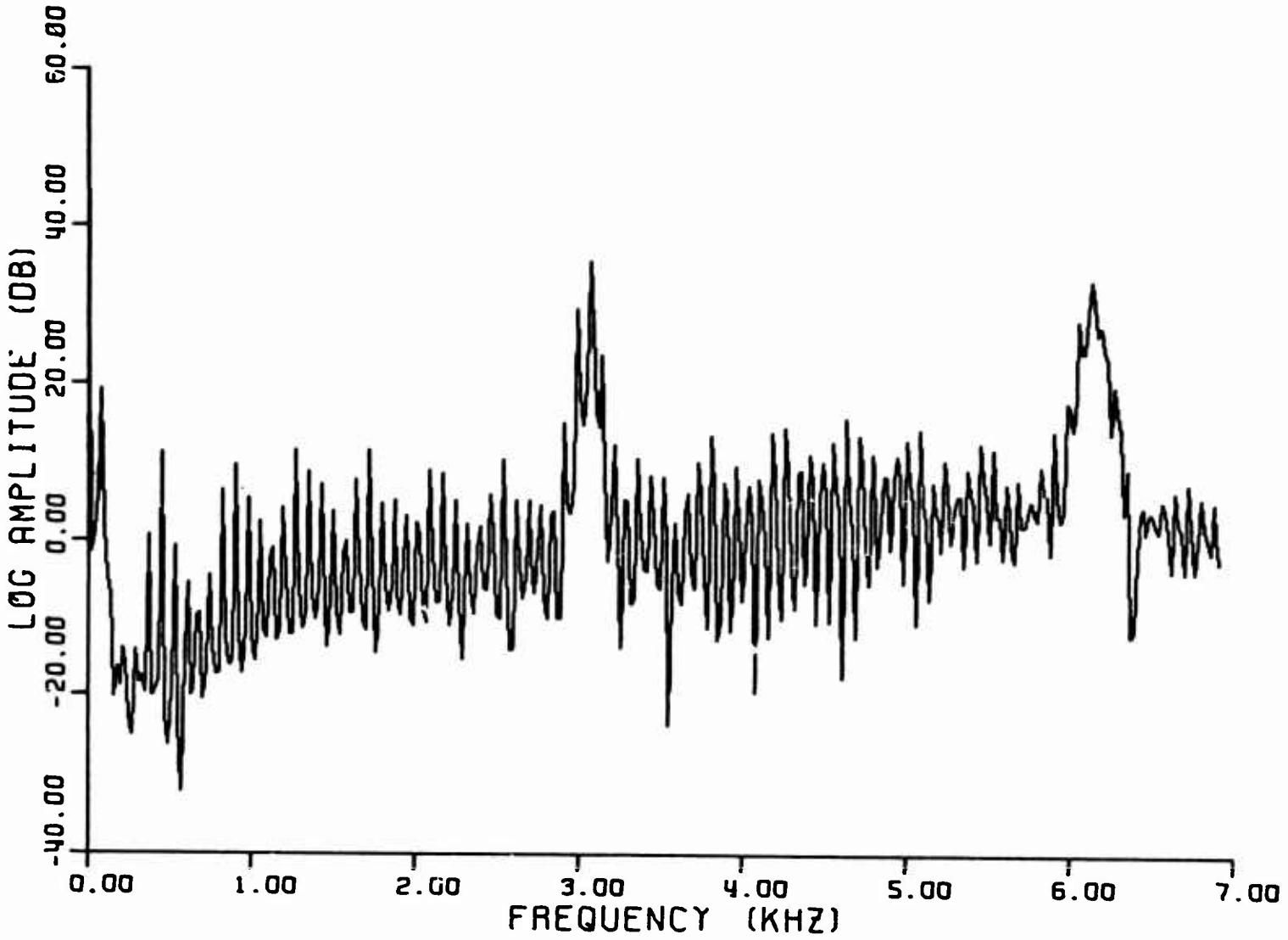

Figure 81. Spectrum of ψ_2 (0.020-Inch-Wide Fault, 0 dB = 10^{-5} rad).

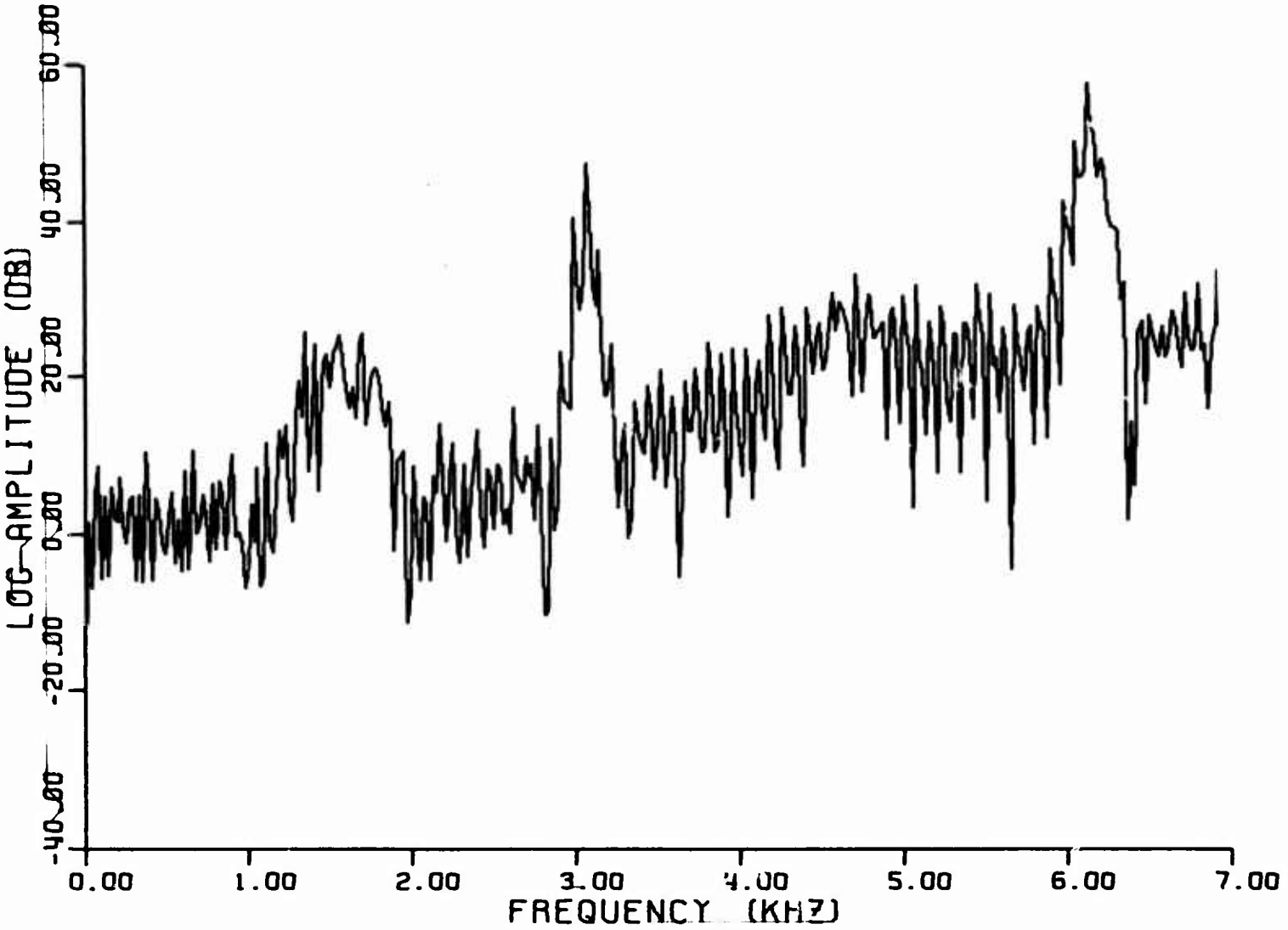

Figure 82. Spectrum of $\ddot{\psi}_2$ (0.020-Inch-Wide Fault, 0 dB = 10^3 rad/s^2).

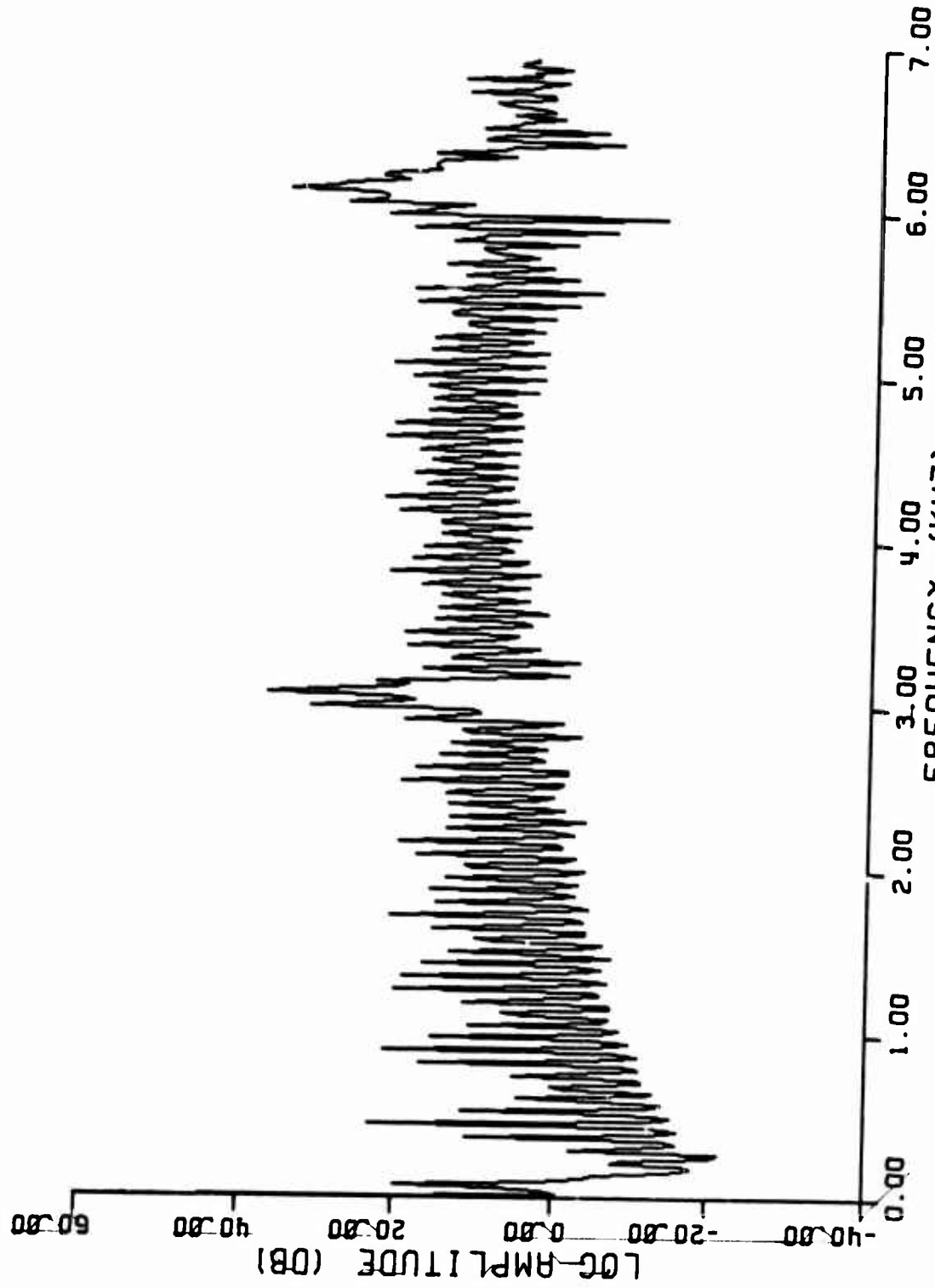

Figure 83. Spectrum of ψ_2 (0.050-Inch-Wide Fault, 0 dB = 10^{-5} rad).

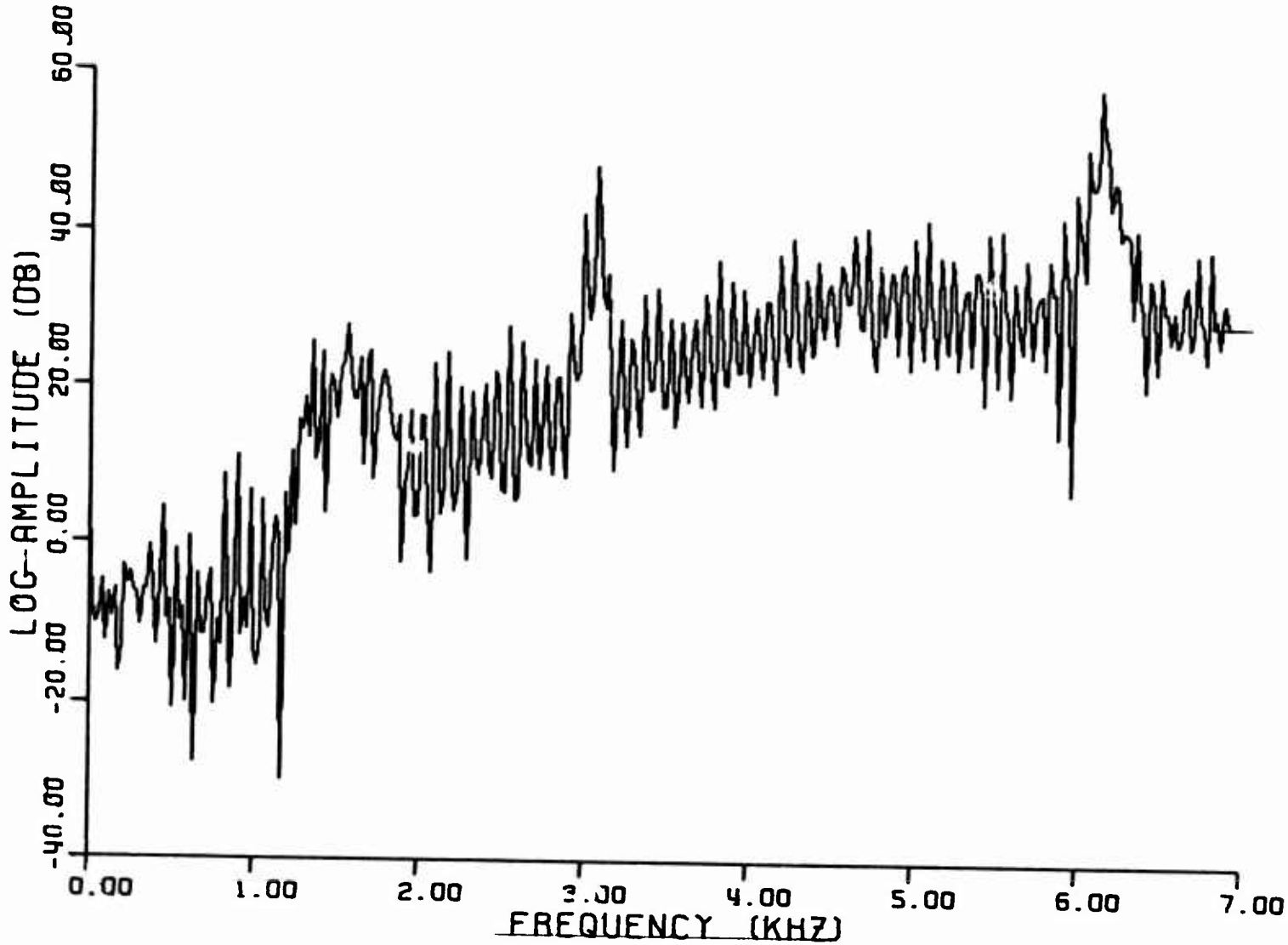

Figure 84. Spectrum of $\ddot{\psi}_2$ (0.050-Inch-Wide Fault, 0 dB = 10^3 rad/s^2).

meshing frequency and its first harmonic increase as shown in Table V. The

TABLE V. SPECTRAL AMPLITUDES OF SIMULATION RESULTS (dB)

	ψ_2			$\ddot{\psi}_2$		
Frequencies	Good Gear	Small Fault	Large Fault	Good Gear	Small Fault	Large Fault
Gear Meshing	31.3	35.5	37.1	42.5	46.7	48.4
1st Lower S.B.	25.3	29.5	31.4	34.4	40.7	42.4
2nd Lower S.B.	8.4	15.3	19.4	7.8	23.0	30.0
1st Upper S.B.	27.0	23.8	23.0	41.3	36.4	35.0
2nd Upper S.B.	16.6	12.7	17.2	25.8	24.1	29.2
1st Harmonic	28.7	33.3	35.2	57.2	57.9	58.6
1st Lower S.B.	27.7	28.2	27.8	52.3	50.3	51.1
2nd Lower S.B.	20.1	18.0	22.7	37.5	42.9	45.7
1st Upper S.B.	25.6	27.4	23.3	48.1	48.1	47.0
2nd Upper S.B.	17.1	20.1	16.7	43.1	39.2	40.5

increases are greater at the meshing frequency, and a further increase is seen with an increase in fault size. The changes in sideband amplitudes do not follow a distinct pattern. The changes in amplitude at the meshing frequency are not as great as those seen in the test data, but the simulation response data is quite repeatable, at least with respect to peak amplitudes, so the statistical variations encountered in the experimental data are not present. Comparison of the figures also shows the introduction of the sawtooth effect of peaks at multiples of the shaft rotational frequency. Amplitudes of this phenomenon are further increased when fault size is increased. An interesting pattern may be observed in these peaks. At intervals of approximately 450 Hz, a frequency beating occurs in which the envelope of amplitudes alternately increases and decreases. This spacing corresponds to the lowest torsional resonance of the system. It is interesting to note that a similar effect was seen in the experimental data illustrated in Figure 39.

An experimental transfer function between acceleration at the gear mesh and gearbox input bearing acceleration was obtained as described in Appendix V. This information was then used along with simulation response data to produce the frequency spectra of Figures 85, 86, and 87, which represent acceleration of a good gear, a gear with a 0.020-inch-wide fault, and a gear with a 0.050-inch-wide fault, respectively. While amplitude increases at the meshing frequency and the sawtooth effect is somewhat apparent, overall correlation with experimental results is not extremely good. Peak spectral amplitudes of the acceleration at gear meshing frequency and its first harmonic fall in the range of 5-10g, which is the same range noted in experimental data. However, differences are observed in the overall shapes of the spectra. One reason for the differences is the lack of inclusion of bending response in the simulation, since it is purely torsional in nature. The manner of producing the transfer function is also suspect. Much more work

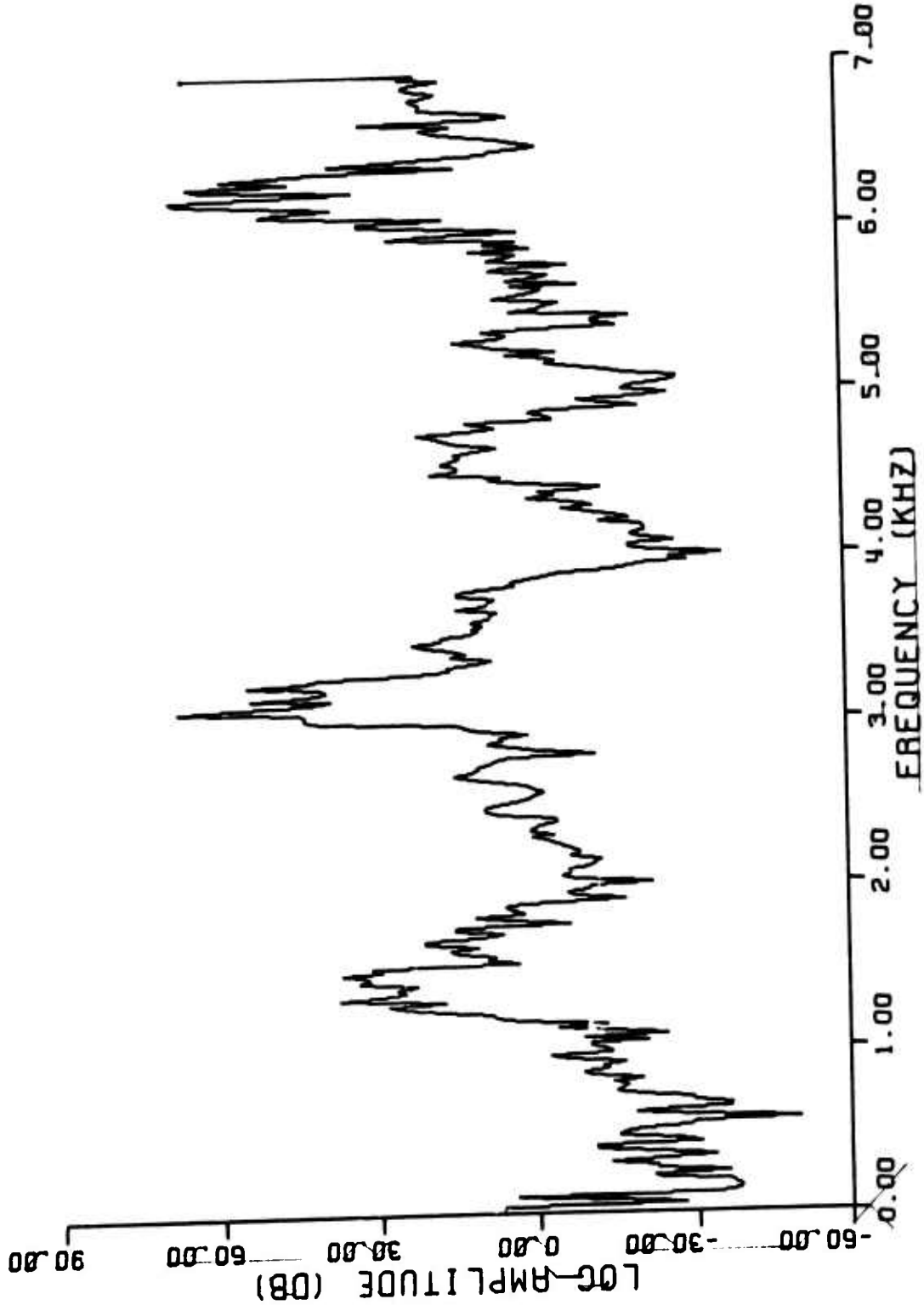

Figure 85. Spectrum of Transformed Acceleration (Good Gear, 0 dB = 5.9g).

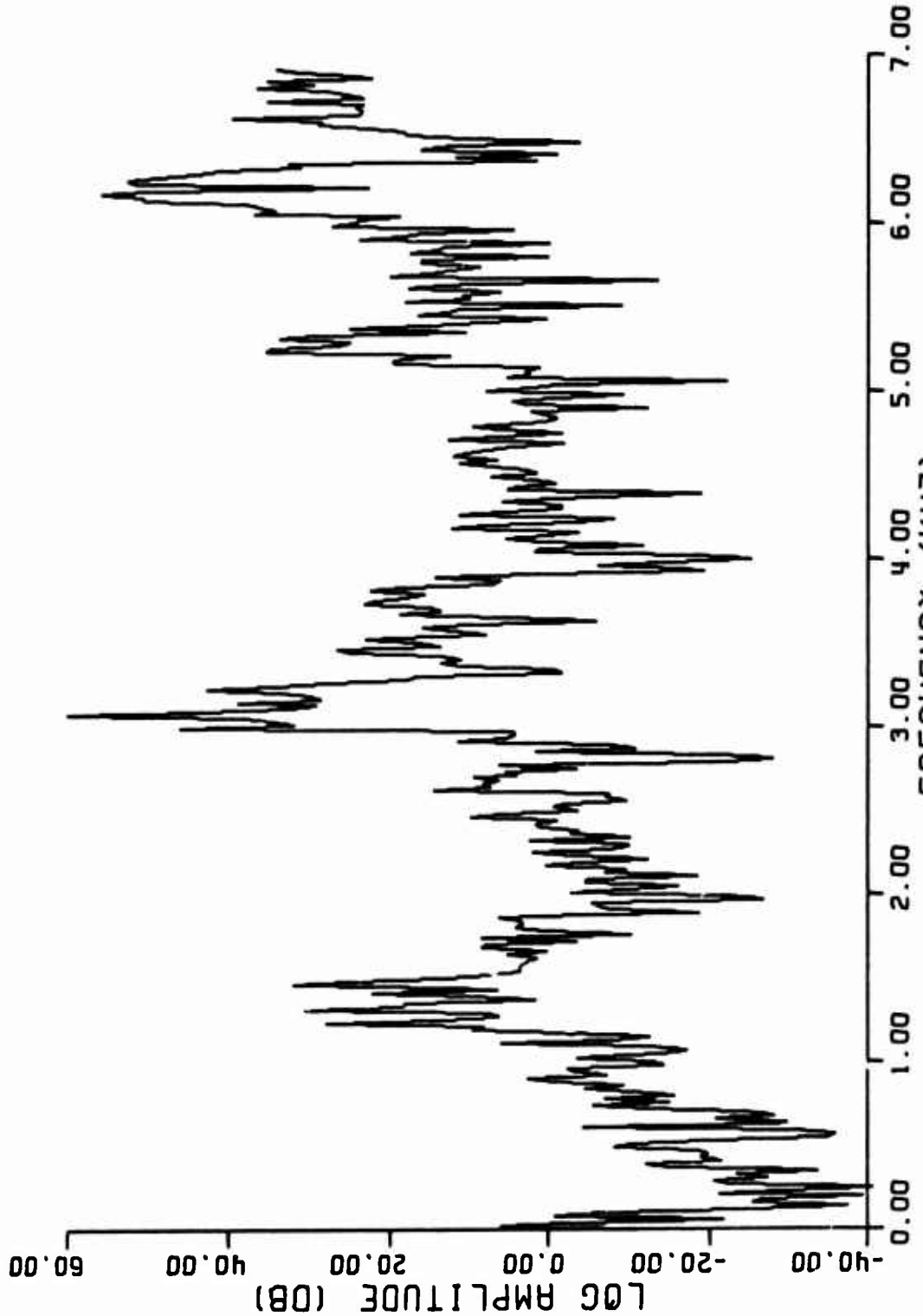

Figure 86. Spectrum of Transformed Acceleration (0.020-Inch-Wide Fault, 0 dB = 5.9g).

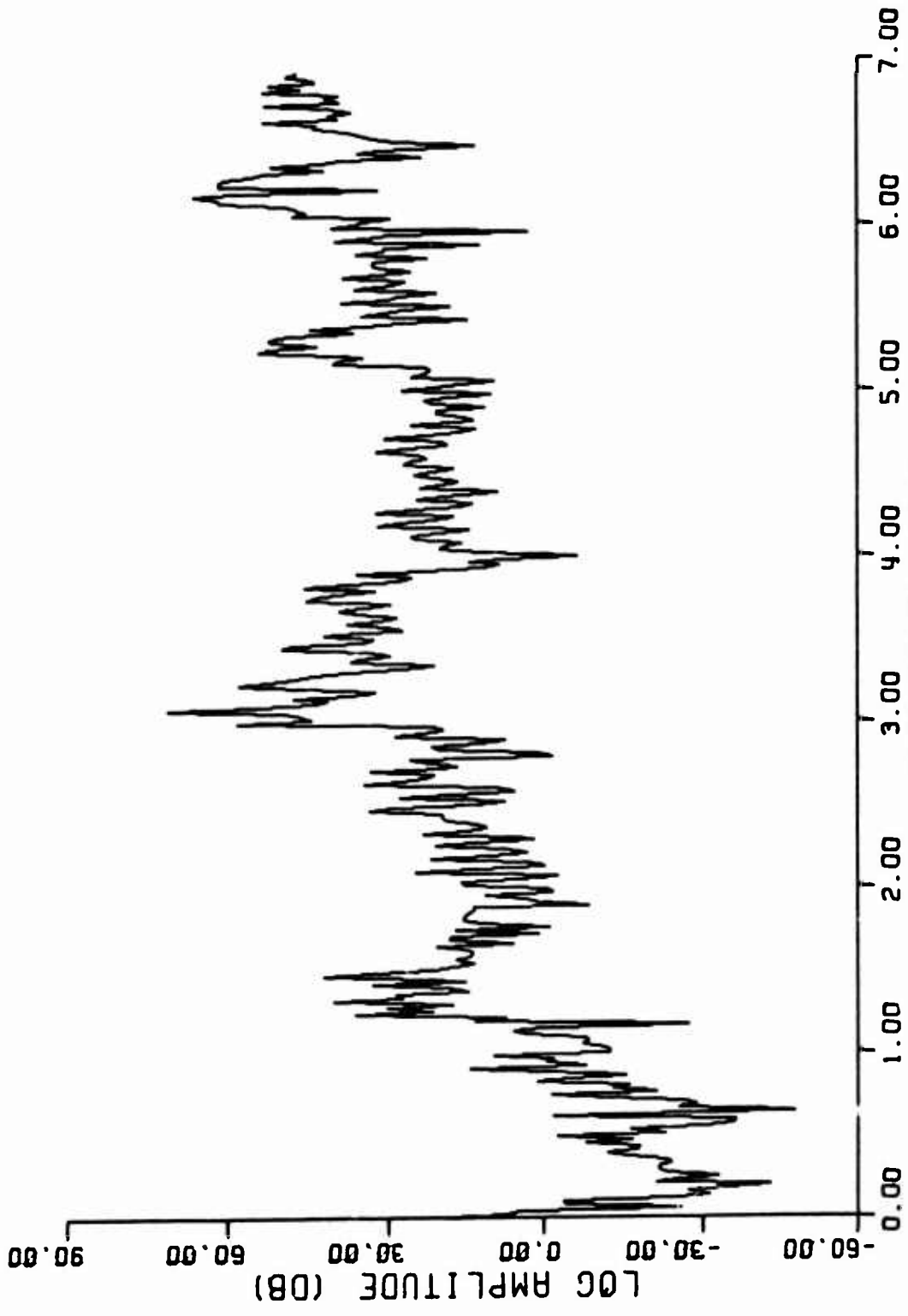

Figure 87. Spectrum of Tranformed Acceleration (0.050-Inch-Wide Fault, 0 dB = 0.5lg).

is necessary in order to develop techniques to obtain more reliable transfer function information of gear mesh systems of the type included in this study.

Information was desired on the effect of changing certain system input parameters on the frequency spectra. Figures 88 and 89 show the effect of changing the amount of torque oscillation while keeping the mean values constant. In Figure 88 there is no oscillation, and in Figure 89 the oscillation is approximately 23% of the mean value. This contrasts to the oscillation of approximately 46% which was used in the previous results and is shown in Figure 77. As seen from these figures there is a change of one or two decibels in the amplitudes at the meshing frequency and its first harmonic. A dramatic change is evident, though in the sideband frequencies. The amplitude and number of sidebands decrease as a function of the torque oscillation. This is in opposition to the lack of any dramatic changes in sidebanding as a result of fault introduction in either experimental or simulation spectra. This would lead to the conclusion that fault presence is not the major mechanism involved in changes in sidebanding.

The two mechanisms introduced into the simulation as a result of fault presence were a special stiffness function for a faulty tooth and a torque impact due to the fault. The relative effects of these two mechanisms are shown in Figure 90 and 91. In Figure 90, an impact is introduced without the special stiffness function; the reverse is true in Figure 91. Both spectra show similar characteristics of relatively the same order of magnitude and, thus, are responsible in combination for producing the overall response to a faulty gear as seen in Figure 75.

Figure 92 shows a spectrum for the system for good gears when the contact ratio of 1.92 was used. Amplitudes are slightly lower, as might be expected, since the overall effect is to make the system somewhat stiffer and because the length of time spent in single tooth-pair contact is shorter.

As mentioned in the section on experimental results, it is unlikely that a tooth fault of the type used in this study would occur on only one tooth. For this reason, the spectrum of Figure 93 was run showing the effect of the fault stiffness variation when a fault was introduced on every tooth. As may be seen, amplitudes at all frequencies are greatly increased. There is no evidence of the sawtooth effect since the excitations due to the fault occur at the gear-meshing frequency. The effect of the torque impact is not shown since an impact occurring at a repetition rate corresponding to the gear-meshing frequency would produce significant energy at frequencies beyond the present capabilities of the model. Modifications could produce this capability but at extreme penalties in computational costs.

SUMMARY

Some evidence of the fault in the form of spikes was noted in the time-domain response. Changes at the gear-mesh frequency and harmonics are also

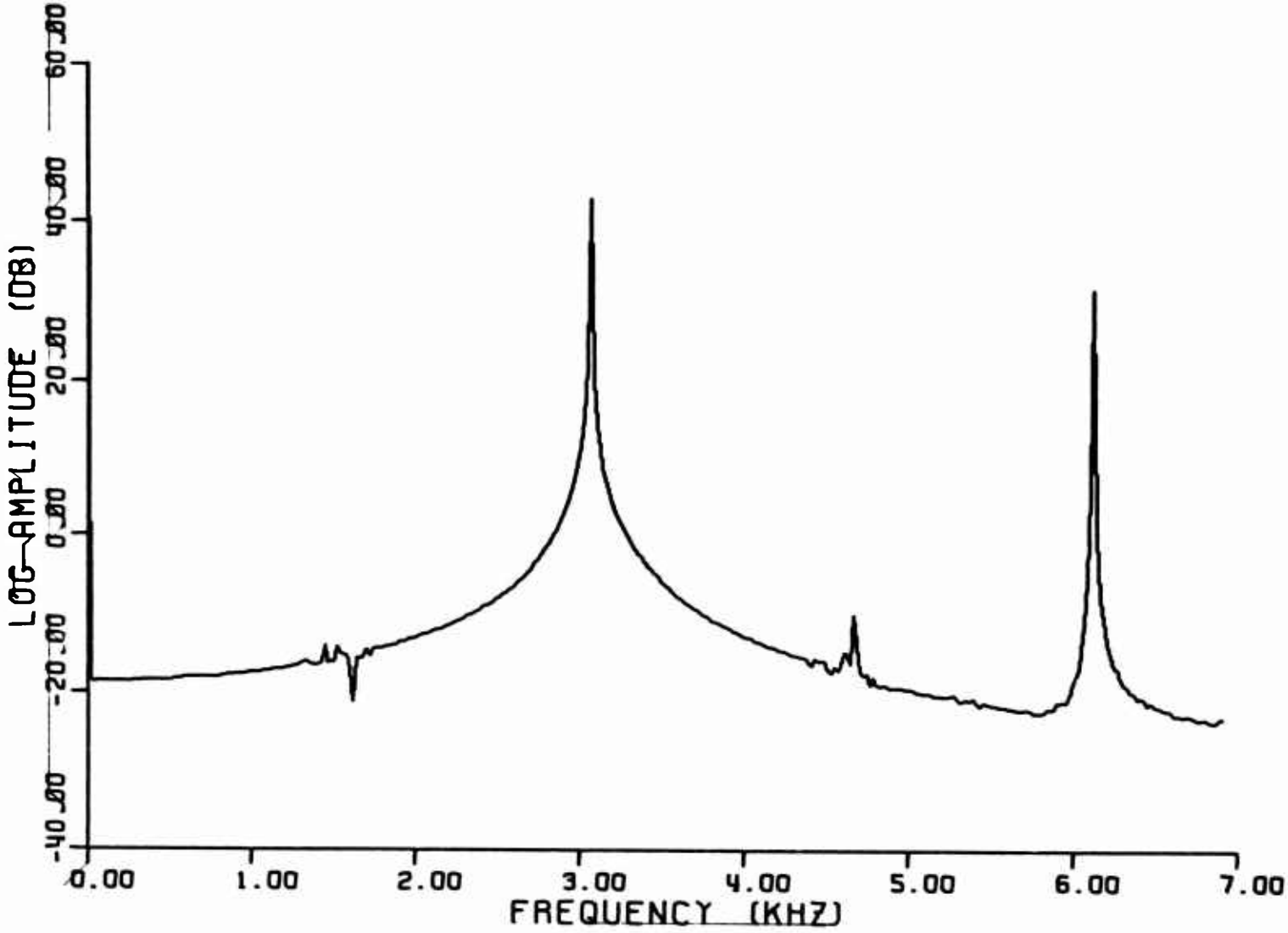

Figure 88. Spectrum of ψ_2 With No Torque Oscillation (0 dB = 10^3 rad/s^2).

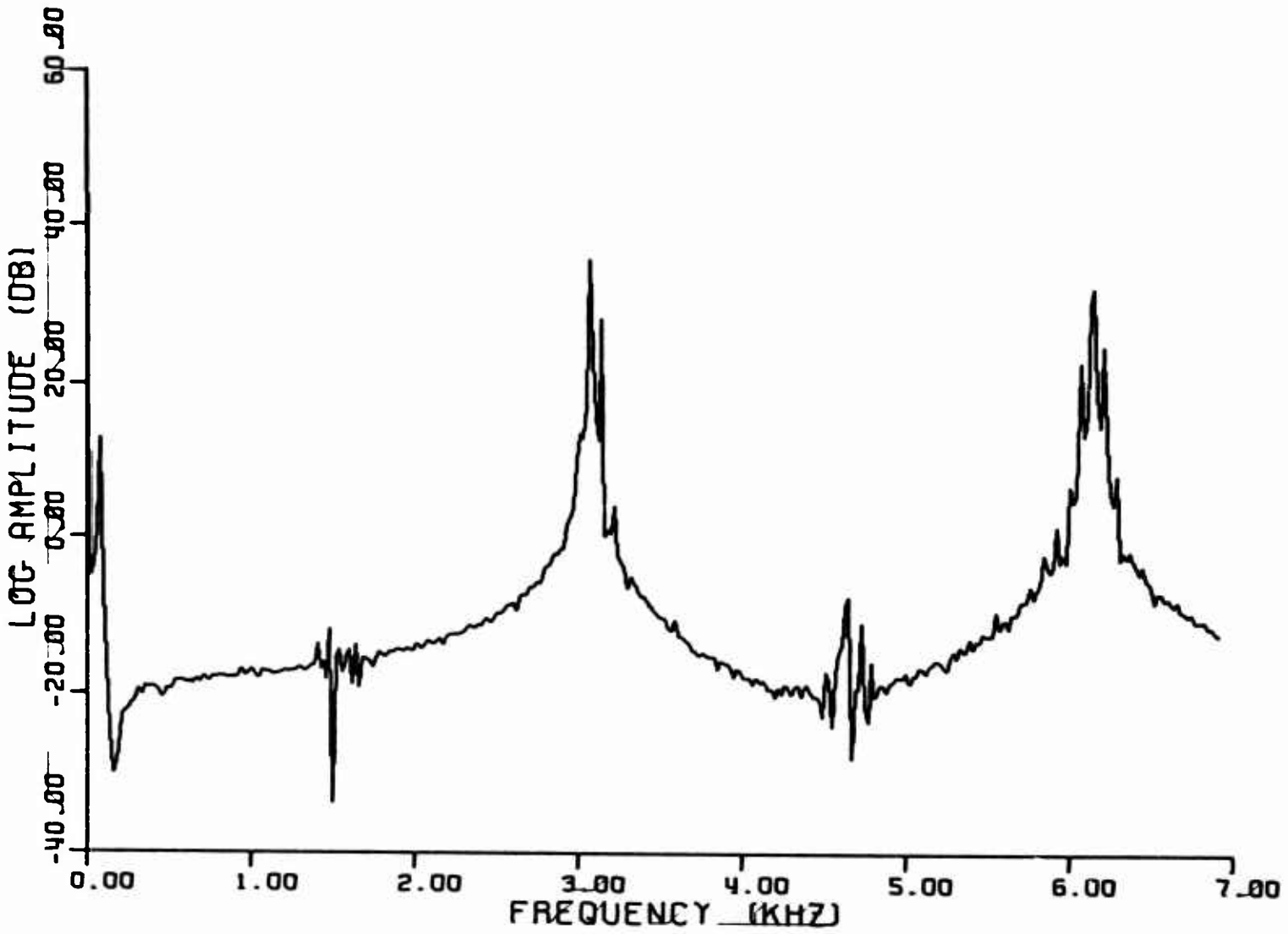

Figure 89. Spectrum of ψ_2 With 23% Torque Oscillation (0 dB = 10^3 rad/s^2).

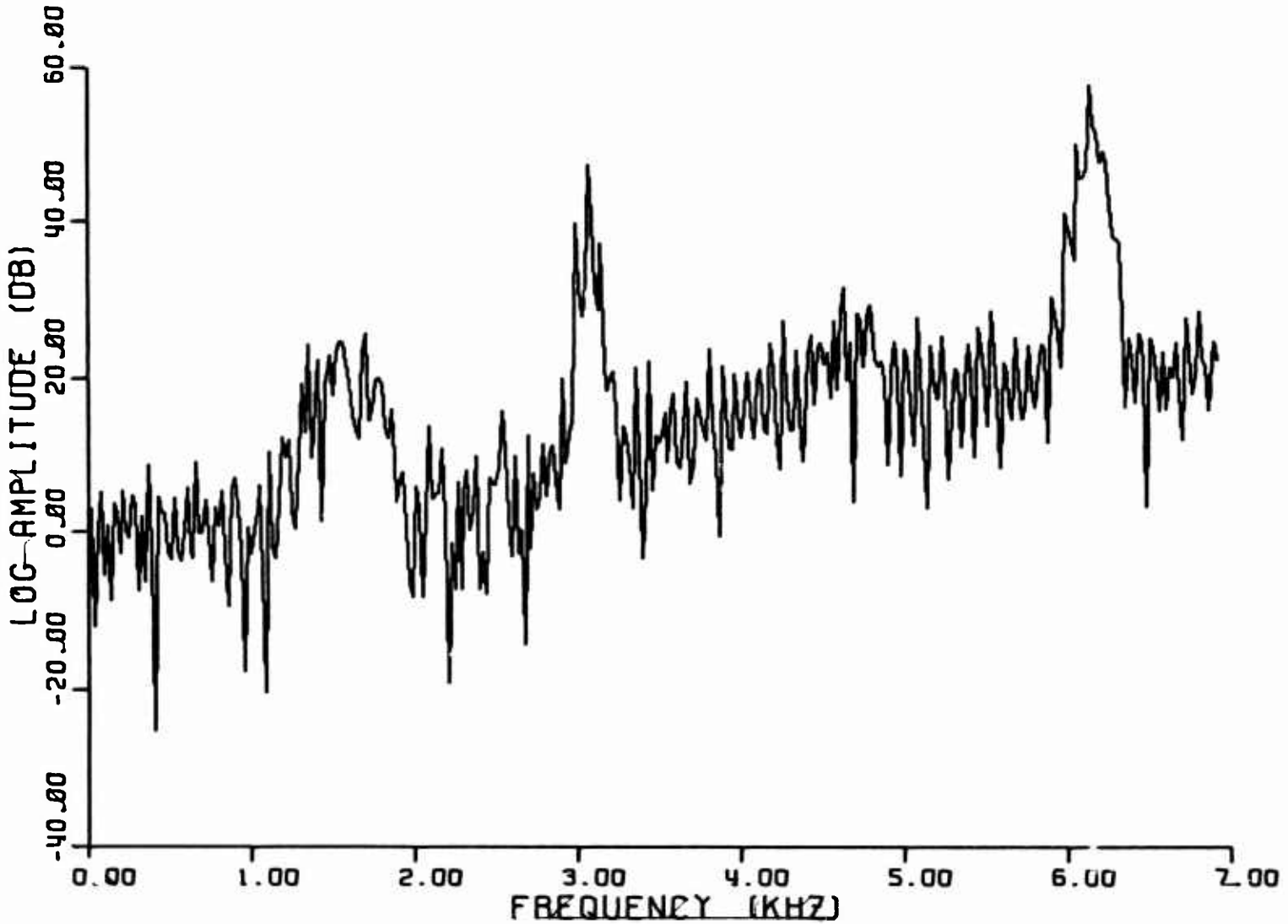

Figure 90. Spectrum of $\ddot{\psi}_2$ With 0.020-Inch-Wide Fault and No Fault Stiffness Variation (0 dB = 10^3 rad/s^2).

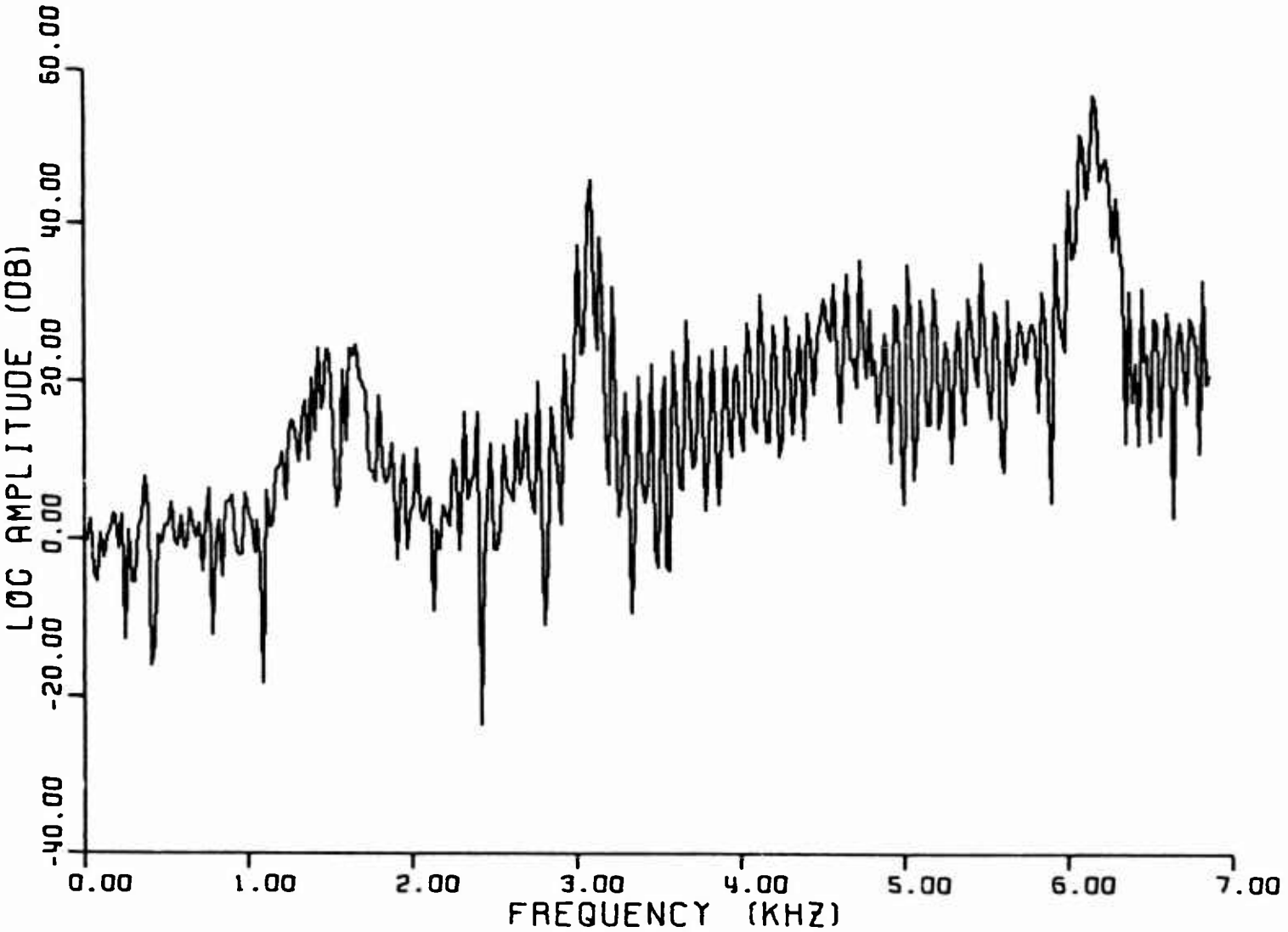

Figure 91. Spectrum of $\ddot{\psi}_2$ With 0.020-Inch-Wide Fault and No Torque Impulse (0 dB = 10^3 rad/s^2).

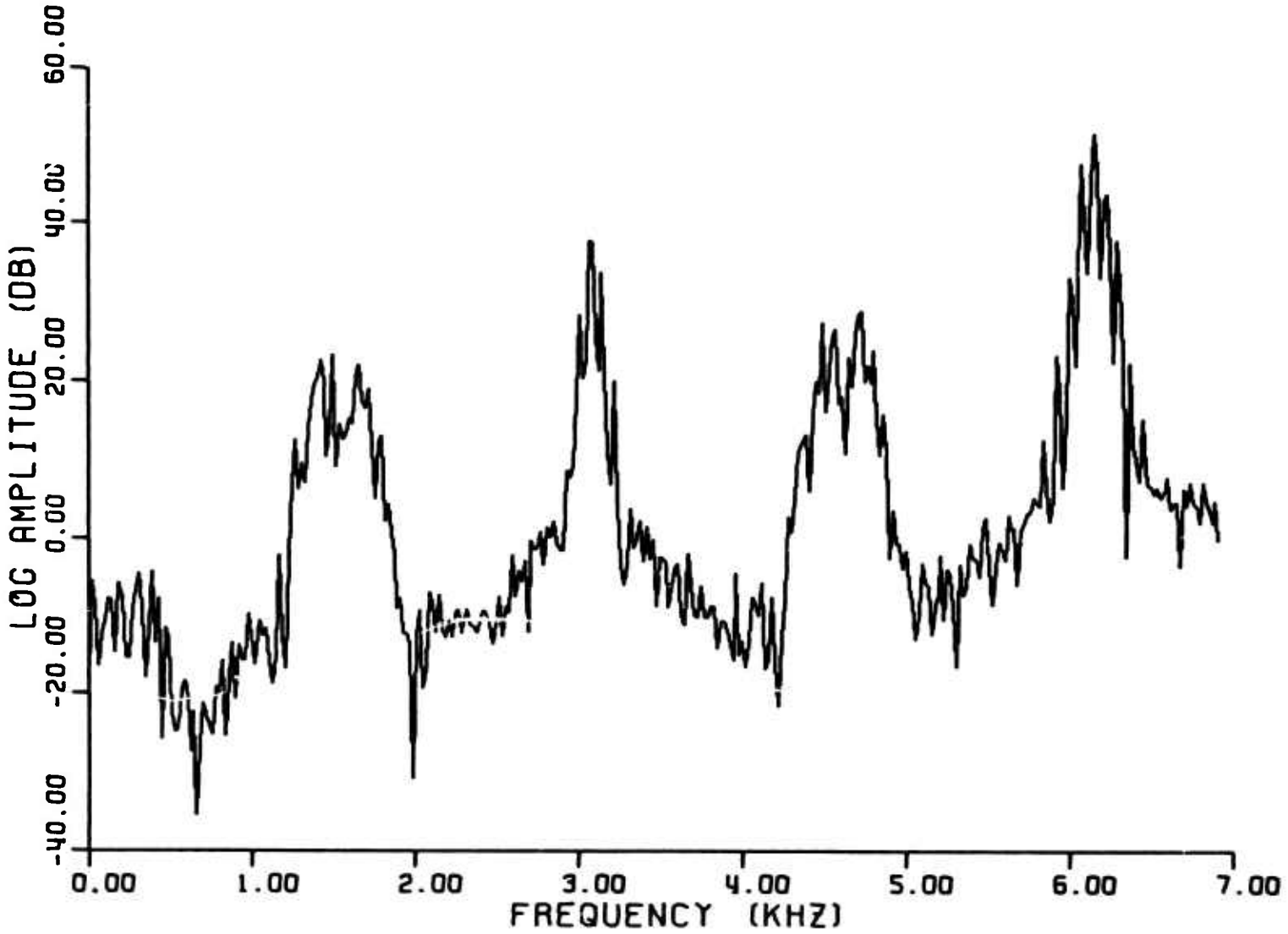

Figure 92. Spectrum of $\ddot{\psi}_2$ With Contact Ratio of 1.92 (0 dB = 10^3 rad/s^2).

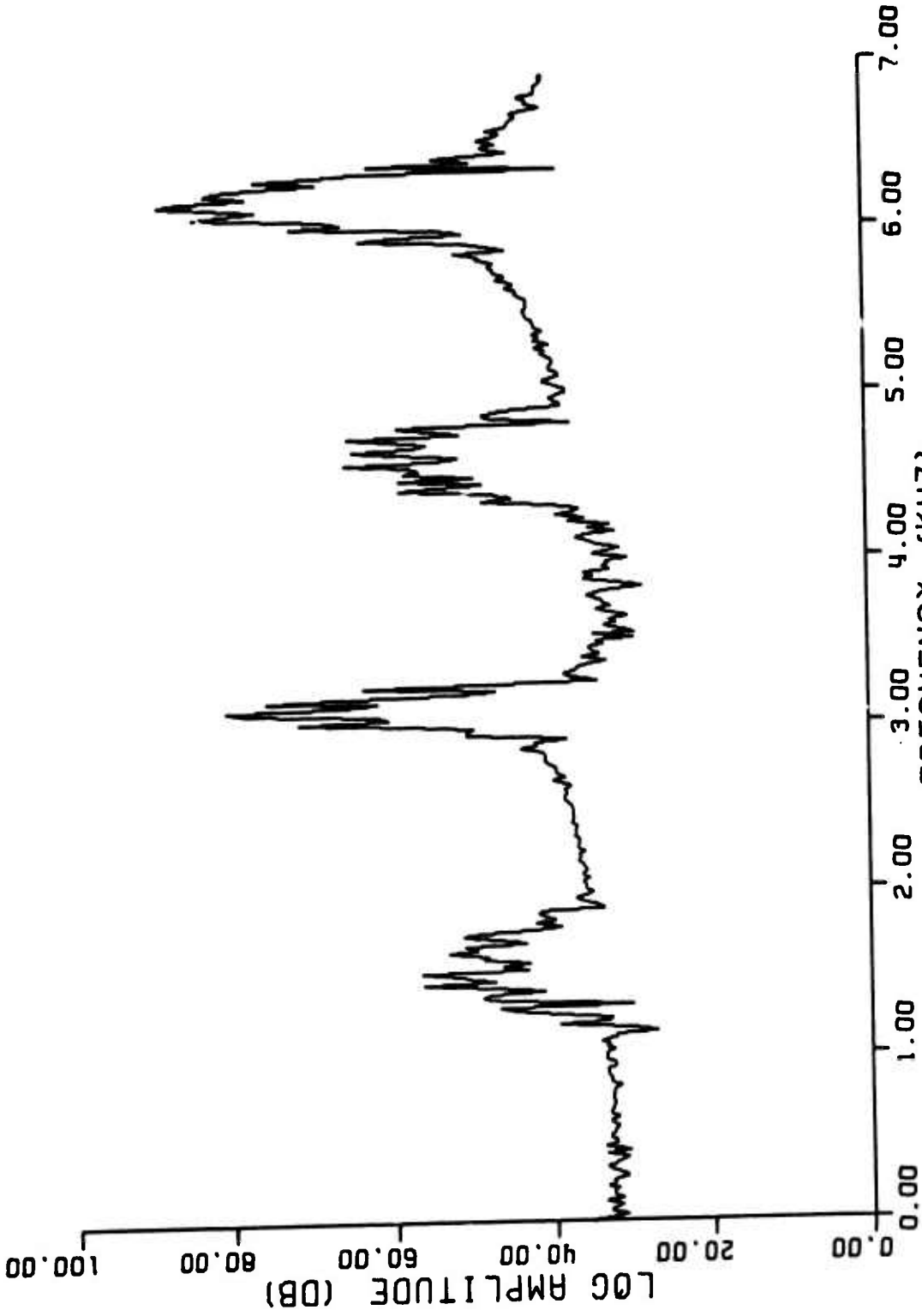

Figure 93. Spectrum of $\ddot{\psi}_2$ With Fault on Every Tooth.

evident in the frequency spectra. When a fault is introduced, the amplitude of the gear-meshing frequency increases, a sawtooth effect at multiples of the input shaft frequency occurs, and a periodicity in the sawtooth corresponding to approximately the first torsional resonance of the dynamic model is seen. All three effects correspond to changes noted in experimental data.

It was found that changes in sidebanding occurred as a result of an input torque oscillation rather than as a direct result of fault introduction. It was also determined that changes in frequency spectra of gears with faults were a composite effect of stiffness variations and torque impacts caused by the faults. This would lead to the assumption that similar spectral changes would be noted when types of faults which do not cause loss of contact and subsequent stiffness variations are analyzed. Such faults (e.g., wearing or scoring) could induce impacts alone into the geared system. Finally, when faults are present on each tooth of the gear, the amplitudes of both time-domain and spectral information were significantly increased.

CONCLUSIONS

As a general conclusion of the research program, it may be stated that the analysis and modelling procedures employed provide an effective method for determining the changes encountered in a geared system's response as a result of tooth surface faults. In analyzing the comparison of response data for good and bad gears from both the simulation and experiments, the following more specific conclusions are offered:

1. Fault presence in a single tooth of a gear causes three major differences in system frequency spectra; i.e.,
    a. increases in amplitude at the gear-meshing frequency,
    b. a sawtooth effect consisting of energy at multiples of the input shaft frequency, and
    c. a periodicity in the sawtooth effect corresponding to the system's lowest torsional resonance.
2. The effects of fault presence on harmonics of the gear-meshing frequency and sidebands of both the gear-meshing frequency and its harmonics do not follow any distinct pattern.
3. Fault presence may be noted in time-domain data by the presence of spikes in the data.

Simulation response data provided the following further conclusions:

1. The major factor affecting sideband generation, in this study, was an input torque oscillation which was felt to be the result of mounting fixtures and system alignment.
2. Fault effects were the results of both stiffness variations (the result of loss of contact at the fault) and torque impacts (the result of velocity differences when contact is reestablished).
3. The relative effects due to the stiffness variations and torque impacts are of the same magnitude.

A deficiency in the model was evidenced by difficulties encountered in predicting the exact amplitudes (in either the frequency or time-domains) of vibrations as measured on the outside of the gearbox. Reasons for this were as follows:

1. The model analyzed purely torsional motion without accounting for bending effects.
2. Accurate transfer function information between the gear mesh and accelerometer positions was not obtained.

While the study did not develop a specific vibration diagnostic technique, it is felt that the results obtained will be useful in the following ways:

1. An understanding and explanation (which were not previously available) of the mechanisms involved in the gear mesh as a result of fault presence have been developed.

2. A simulation of a geared system's response to one type of tooth surface fault has been developed, spectral changes as a result of fault presence have been noted, and the results have correlated with experimental results.
3. The model, as developed, shows distinct possibilities for extension to other fault types to allow its use as a general-purpose gear response predictor.

RECOMMENDATIONS

Based on the results of this study, there are two areas in which further development work should be considered. One involves extension of the capabilities of the model as developed, and the other involves more sophisticated analytical work which may be performed in the area of gear dynamic analysis.

Further development of the model would consist of:

1. Testing to provide a larger data base for analysis of the model, including

    a. more gears,
    b. more types of faults,
    c. variation in fault position, and
    d. variations in the severity of the faults.

2. Testing to provide better transfer function information between the gear mesh and external gearbox transducer positions.

3. Combination of bending effects with simulation results.

4. Redesign of test stand fixtures to eliminate the torque oscillations (if possible).

5. Addition of more lumps to the torsional model; i.e., providing more detailed analysis of the driving section of the test stand and of the generator.

The acquisition of more data could provide better statistical information on data variations. The amount of data taken in the study was not large enought for a very valid statistical analysis. The use of better transfer function information and the inclusion of bending effects should permit better correlation of specific amplitudes between the simulation results and measured experimental data. The torque variation was the major factor in changing sideband amplitudes. If this variation is diminished or eliminated, more subtle changes as the result of fault presence may be distinguishable. The addition of more lumps to the torsional model is a natural extension which brings the model closer to its natural continuous state. Limitations are reached, however, at the point where increased computational burdens are not offset by improvements in the simulation response.

There are two areas in which further theoretical development could proceed; i.e.,

1. The inclusion of provisions to allow tooth contact off the line-of-action.

2. Two-dimensional modelling of the gear tooth.

If analysis were extended to motion off the line-of-action, noninvolute contact could be considered. This would provide results for faults which cause major tooth profile modifications such as wear or manufacturing errors. It could also allow the inclusion in the analysis of noninvolute gears. The inclusion of another dimension in the analysis would allow results to apply to spur gears with larger facewidths, as well as bevel and helical gears. There would also be provisions for analyzing faults which are more two-dimensional in nature than pitch-line pitting; e.g., scoring, spalling, etc.

As a general recommendation for both extension of the present model and the development of more sophisticated models, hybrid computation should be considered. The complexity of the model, switching facilities, logic, and function storage required make pure analog simulation unfeasible, but purely digital analysis also presents problems. The large frequency range which the system exhibits requires very small computing intervals for any numerical integration scheme, making computing quite expensive. Thus, a hybrid simulation which would allow analog solution of the differential equations with the digital capabilities of logic, switching, and iterative computations appears to be the optimum computation technique.

LITERATURE CITED

1. Houser, D. R., and Drosjack, M. J., VIBRATION SIGNAL ANALYSIS TECHNIQUES, The Ohio State University, USAAMRDL Technical Report 73-101, Eustis Directorate, U. S. Army Air Mobility Research and Development Laboratory, Fort Eustis, Virginia, December 1973, AD 776 397.

2. SHOCK PULSE METER, SKF MEPA-10A, Shock Pulse Instrumentation Discussion by SKF Industries.

3. Broderick, J. J., Burchill, R. F., and Clark, H. L., DESIGN AND FABRICATION OF PROTOTYPE SYSTEM FOR EARLY WARNING OF IMPENDING BEARING FAILURES, Mechanical Technology Incorporated, Control Number MFS-21877, George Marshall Space Flight Center, NASA, Huntsville, Alabama, January 1972.

4. Weichbrodt, Bjorn, and Bowden, Frank J., INSTRUMENTATION FOR PREDICTING BEARING DAMAGE, General Electric Company, Technical Report RADC-TR-69-437, Rome Air Development Center, Griffiss Air Force Base, New York, March 1970, AD-869 633.

5. Kirschmann, A. E., TF-34 ENGINE VIBRATION ANALYZER, FINAL REPORT, General Electric Company, Contract 62269-70-C-0315, Work Item 7, NASC., Washington, D. C., 10 June 1971.

6. Frarey, J. L., DEVELOPMENT OF GEAR FAILURE DETECTION METHODS, Mechanical Technology Incorporated, Report No. MTI70TR76, Office of Naval Research, Washington, D. C., December 31, 1970, AD 720 735.

7. Haskin, L. B., and Schlereth, F. H., MECHANICAL FAILURE DETECTION, General Electric Company, Office of Naval Research, Washington D. C.

8. Thompson, R. A., and Weichbrodt, Bjorn, GEAR DIAGNOSTICS AND WEAR DETECTION, ASME Paper No. 69-VIBR-10, Presented at Vibration Conference, Philadelphia, Pa., March 30-April 2, 1969.

9. Buckingham, E., ANALYTICAL MECHANICS OF GEARS, FIRST ED., McGraw-Hill Book Company, Inc., New York, Toronto, and London, 1949.

10. Fisher, A., THE USE OF SPEED FACTORS IN CALCULATING THE LOAD CARRYING CAPACITY OF HELICAL GEARS, Machinery, Vol. 98, March 8, 1961, p. 545.

11. Buckingham, E., DYNAMIC LOADS ON GEAR TEETH, American Society of Mechanical Engineers Research Report, 1931.

12. Tuplin, W. A., DYNAMIC LOADS ON GEAR TEETH, Machinery Design, October 1953, p. 203.

13. Attia, A. Y., DYNAMIC LOADING OF SPUR GEAR TEETH, Journal of Engineering for Industry, Vol. 81, Series B, p. 1, February 1959.

14. Reswick, J. B., DYNAMIC LOADS ON SPUR AND HELICAL GEAR TEETH, Transactions of the American Society of Mechanical Engineers, Vol. 77, p. 635, July 1954.

15. Niemann, G., and Rettig, H., ERRORS INDUCED BY DYNAMIC GEAR TOOTH LOADS, Presented at International Gearing Conference, London, England, 23-25 September 1958.

16. Harris, S. L., DYNAMIC LOADS ON THE TEETH OF SPUR GEARS, Proceedings of the Institution of Mechanical Engineers, London, Vol. 172, p. 187, 1958.

17. Gregory, R. W., Harris, S. L., and Munro, R. G., DYNAMIC BEHAVIOR OF SPUR GEARS, Proceedings of the Institution of Mechanical Engineers, Vol. 178, Part 3J, p. 166, 1963-64.

18. Munro, R. G., THE DYNAMIC BEHAVIOUR OF SPUR GEARS, Unpublished Ph. D. Dissertation, University of Cambridge, England, 1962.

19. Richardson, H. H., STATIC AND DYNAMIC LOAD, STRESS, AND DEFLECTION CYCLES IN SPUR-GEAR SYSTEMS, Unpublished Sc. D. Thesis, Massachusetts Institute of Technology, 1958.

20. Kasuba, R., AN ANALYTICAL AND EXPERIMENTAL STUDY OF DYNAMIC LOADS ON SPUR GEAR TEETH, Unpublished Ph. D. Dissertation, University of Illinois, 1962.

21. Hahn, W. F., STUDY OF INSTANTANEOUS LOAD TO WHICH GEAR TEETH ARE SUBJECTED, Unpublished Ph. D. Dissertation, University of Illinois, 1969.

22. Seireg, A., and Houser, D. R., EVALUATION OF DYNAMIC FACTORS FOR SPUR AND HELICAL GEARS, A.S.M.E. Journal of Engineering for Industry, Vol. 92, Series B, No. 2, May 1970.

23. Houser, D. R., and Seireg, A., AN EXPERIMENTAL INVESTIGATION OF DYNAMIC FACTORS IN SPUR AND HELICAL GEARS, A.S.M.E. Journal of Engineering for Industry, Vol. 92, Series B, No. 2, May 1970.

24. Ichimaru, K., and Hirano, F., DYNAMIC BEHAVIOR OF HEAVILY-LOADED SPUR GEARS, A.S.M.E. Paper 72-PTG-14, 1972.

25. Utagawa, M., MEASUREMENTS OF DYNAMIC LOADS ON GEAR TEETH, Proceedings of the 6th Japan National Congress for Applied Mechanics, pp. 489-492, 1956.

26. Tobe, T., DYNAMIC LOADS ON SPUR GEAR TEETH, Bulletin of J.S.M.E., Vol. 4, No. 14, p. 417, 1961.

27. Tobe, T., and Nobuo, T., DYNAMIC LOADS ON SPUR GEAR TEETH CAUSED BY TEETH IMPACT, Bulletin of J.S.M.E., Vol. 16, No. 96, pp. 1031-1037, June 1073.

28. Timoshenko, S., and Baud, R. V., THE STRENGTH OF GEAR TEETH, Mechanical Engineering, Vol. 48, p. 1108, 1926.

29. Baud, R. V., and Peterson, R. E., LOAD AND STRESS CYCLES IN GEAR TEETH, Mechanical Engineering, Vol. 51, p. 653, 1929.

30. Walker, H., GEAR TOOTH DEFLECTION AND PROFILE MODIFICATION, The Engineer, Vol. 166, No. I, pp. 409-412, Oct. 14, 1938.

31. Walker, H., GEAR TOOTH DEFLECTION AND PROFILE MODIFICATION, The Engineer, Vol. 166, No. II, pp. 434-436, Oct. 21, 1938.

32. Weber, C., THE DEFORMATION OF LOADED GEARS AND THE EFFECT ON THEIR LOAD-CARRYING CAPACITY, Sponsored Research (Germany), British Department of Scientific and Industrial Research, Report No. 3 (1949).

33. Wellauer, E. J., and Seireg, A., BENDING STRENGTH OF GEAR TEETH BY CANTILEVER PLATE THEORY, A.S.M.E. Paper No. 59-A50, 1959.

34. Poritsky, H., Sutton, A. D., and Pernick, A., DISTRIBUTION OF TOOTH LOAD ALONG A PINION, Transactions of A.S.M.E., Journal of Applied Mechanics, pp. A-T8-A-86, June 1945.

35. Weber, C., THE DEFORMATION OF LOADED GEARS AND THE EFFECT ON THEIR LOAD-CARRYING CAPACITY, Part 1, DSIR, London, Sponsored Research (Germany), Report No. 5, 1950.

36. Trbojevic, M. D., LOAD DISTRIBUTION ON HELICAL GEAR TEETH, PART 1, The Engineer, pp. 187-190, August 9, 1957.

37. Trbojevic, M. D., LOAD DISTRIBUTION ON HELICAL GEAR TEETH, PART 2, The Engineer, pp. 222-224, August 16, 1957.

38. Conry, T. F., and Seireg, A., A MATHEMATICAL PROGRAMMING METHOD FOR DESIGN OF ELASTIC BODIES IN CONTACT, A.S.M.E. Transactions, Journal of Applied Mechanics, 1970.

39. Beuler, E., INFLUENCES ON THE NOISE OF TRANSMISSIONS, S.A.E. Paper #680051, Presented Jan. 8-12, 1968, Detroit.

40. Bradley, W. A., SOUND GEAR QUALITY, Mechanical Engineering, October 1972.

41. Welbourn, D. B., GEAR ERRORS AND THEIR RESULTANT NOISE SPECTRA, Institution of Mechanical Engineers, June 1970.

42. Laskin, I., Orcutt, F. K., and Shipley, E. E., ANALYSIS OF NOISE GENERATED BY UH-1 HELICOPTER TRANSMISSION, Mechanical Technology Incorporated, USAAVLABS Technical Report 68-41, U. S. Army Aviation Materiel Laboratories, Fort Eustis, Virginia, June 1968, AD 675 457.

43. Badgley, R. H., and Laskin, I., PROGRAM FOR HELICOPTER GEARBOX NOISE PREDICTION AND REDUCTION, Mechanical Technology Incorporated, USAAVLABS Technical Report 70-12, U. S. Army Aviation Materiel Laboratories, Fort Eustis, Virginia, March 1970, AD 869 822.

44. Badgley, R. H., and Chiang, T., INVESTIGATION OF GEARBOX DESIGN MODIFICATIONS FOR REDUCING HELICPOTER GEARBOX NOISE, Mechanical Technology Incorporated, USAAMRDL Technical Report 72-6, Eustis Directorate, U. S. Army Air Mobility Research and Development Laboratory, Fort Eustis, Virginia, March 1972, AD 742 735.

45. Badgley, R. H., RECOMMENDED DESIGN MODIFICATIONS TO THE CH-47 FORWARD ROTOR-DRIVE GEARBOX FOR REDUCTION OF HIGH-FREQUENCY VIBRATION AND NOISE, Mechanical Technology Incorporated, USAAMRDL Technical Report 73-33, Eustis Directorate, U. S. Army Air Mobility Research and Development Laboratory, Fort Eustis, Virginia, June 1973, AD 769 062.

46. Tordion, G. V., THE MECHANICAL IMPEDANCE APPROACH TO THE DYNAMICS OF GEARED SYSTEMS, Paper presented to 47th Annual Meeting of AGMA, Hot Springs, Va., June 2-5, 1963.

47. Wang, C. M., and Morse, T. E., Jr., TORSIONAL RESPONSE OF A GEAR TRAIN SYSTEM, A.S.M.E. Journal of Engineering for Industry, 1971.

48. Fukuma, M., Furukawa, T., and Aida, T., FUNDAMENTAL RESEARCH ON GEAR NOISE AND VIBRATION, Bulletin of J.S.M.E., Vol. 16, No. 97, pp. 1094-1107, July 1973.

49. Wallace, D. B., and Seireg, A., COMPUTER SIMULATION OF DYNAMIC STRESS, DEFORMATION, AND FRACTURE OF GEAR TEETH, A.S.M.E. Paper #72-PTG-4, 1972.

50. Van Den Broek, J. A., ELASTIC ENERGY THEORY, Second Edition, John Wiley and Sons, Inc., New York, 1942, p. 172.

51. Hertz, H., ON THE CONTACT OF ELASTIC BODIES, Journal Für Die Reine und Angewandte Mathematik, 92, pp. 156-171, 1881.

52. Hertz, H., ON THE CONTACT OF RIGID ELASTIC SOLIDS AND ON HARDNESS, Verhandlungen des Vereins zur Beforderung des Gewerbefleisses, Nov. 1882.

APPENDIX I
GEAR MEASUREMENTS

Typical measurements for the gears used in the test program were obtained from the manufacturer and are shown in Figures 94, 95, and 96. Included in the charts are profile and spacing checks as well as a lead check on the pinion. From Figures 94 and 96, it may be seen that the spur pinion and generator drive gear are very close to a perfect involute with variations of less than 0.0001 inch. The chart of the idler gear (Figure 95) shows the presence of profile modifications of up to 0.0002 inch. These modifications are of a type used to compensate for gear tooth deflections under load. The spacing charts for the gears show a maximum tooth-to-tooth variation of 0.0001 inch and total spacing error of 0.0005 inch. No significant lead error on the pinion is indicated by the lead check.

Figures 97, 98, and 99 show profile checks measured after testing was completed for several of the gears. There is little indication of any large-scale wear on the gears, which would be the expected result because of the limited number of hours of service of the gears. The charts in Figures 98 and 99 show the gears which had faults manufactured into them. The depths of the faults are not accurately portrayed because of limitations of the measuring device. There is no indication from the measurements that there were any significant profile variations from tooth to tooth on the same gear or from gear to gear. There is some wear (up to 0.0001 in.) shown near the tooth roots on some of the gears, but this is not too significant and falls within manufacturing specifications.

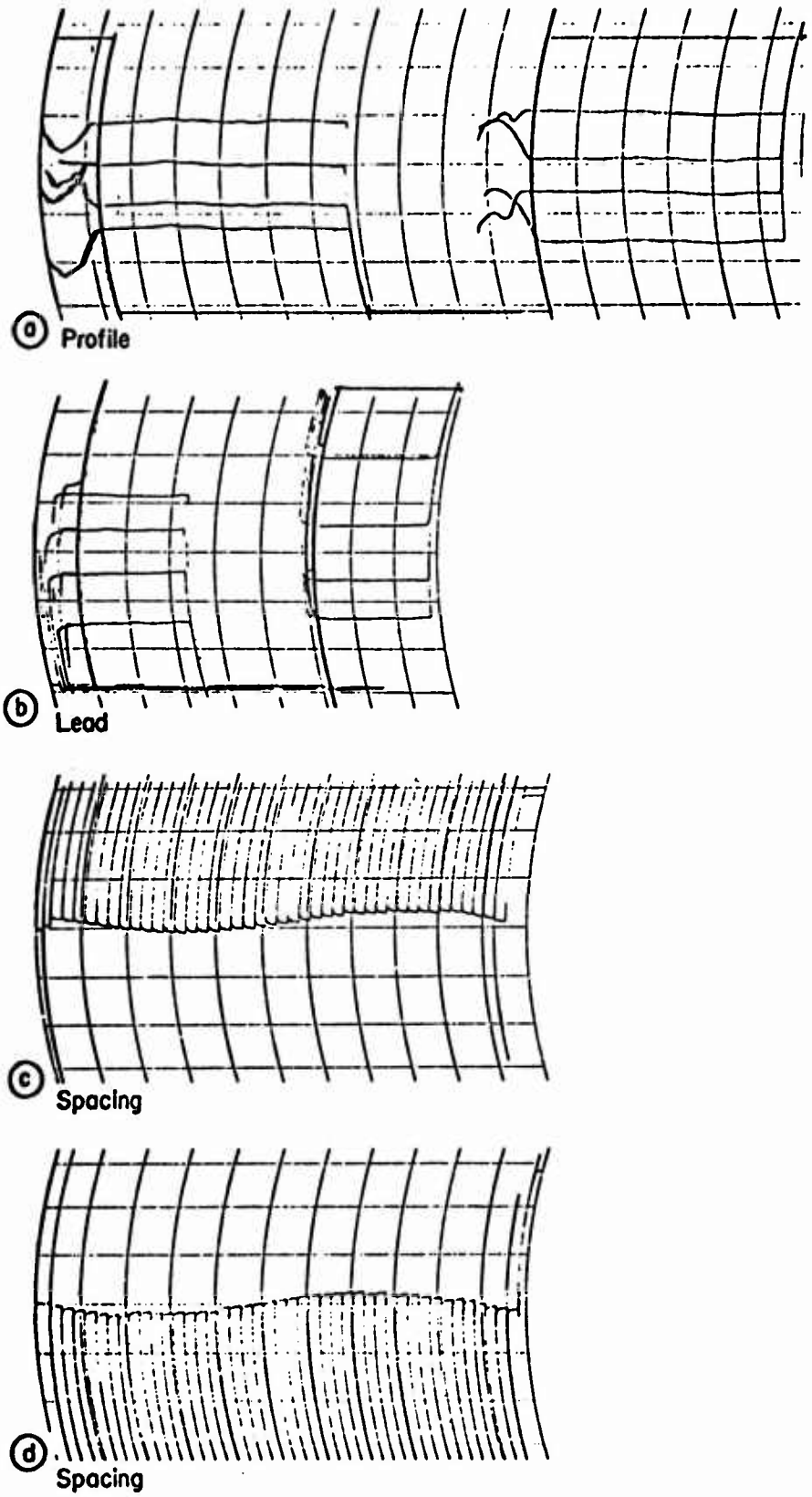

Figure 94. Gear Measurements for Typical New Pinion.

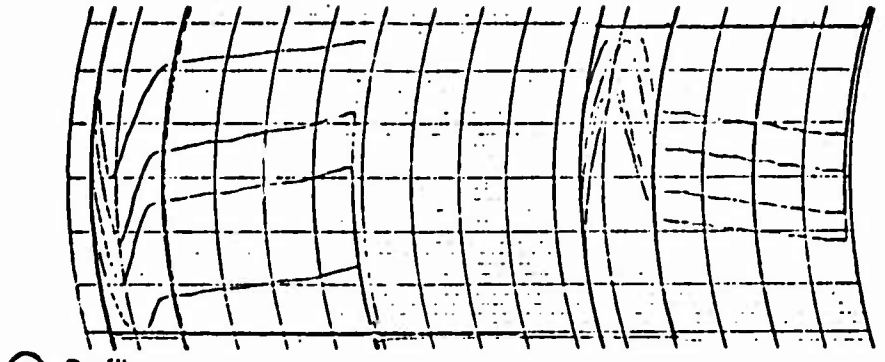

ⓐ Profile

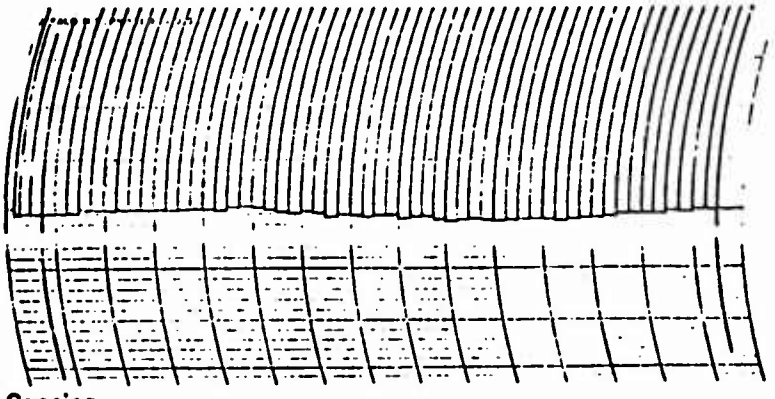

ⓑ Spacing

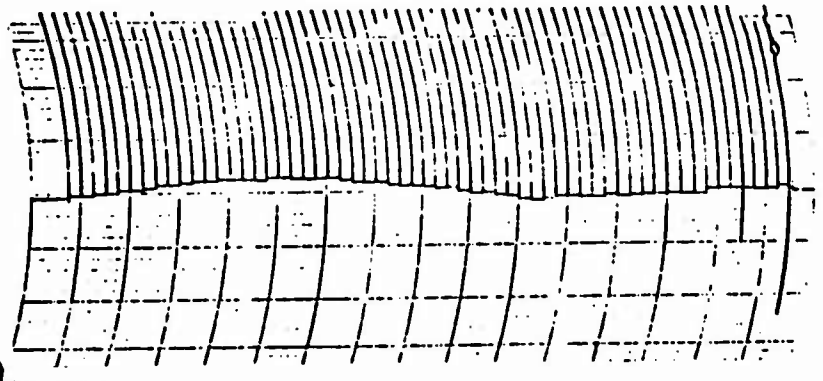

ⓒ Spacing

Figure 95. Gear Measurements for Typical New Idler.

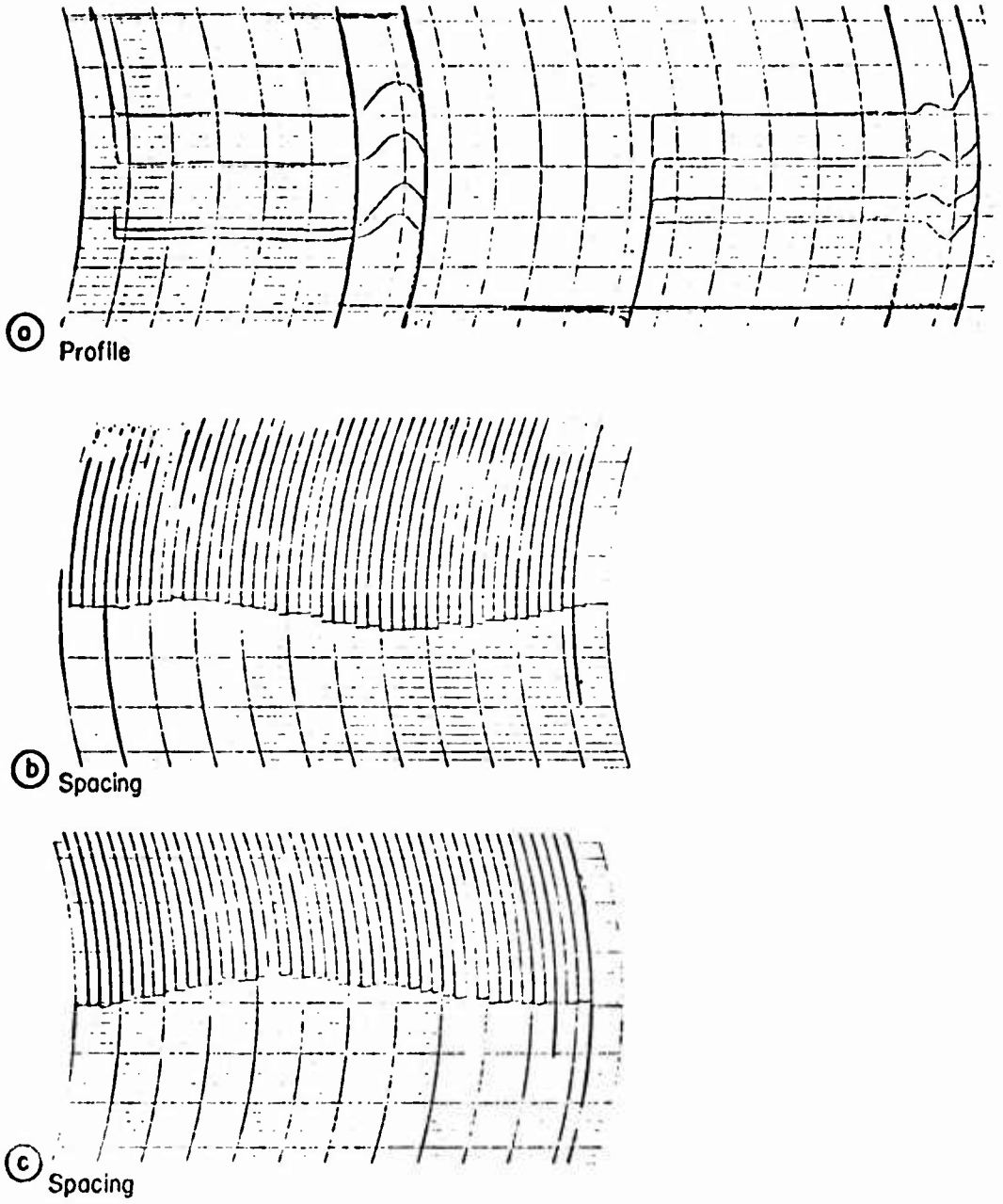

Figure 96. Gear Measurements for Typical New Generator Drive Gear.

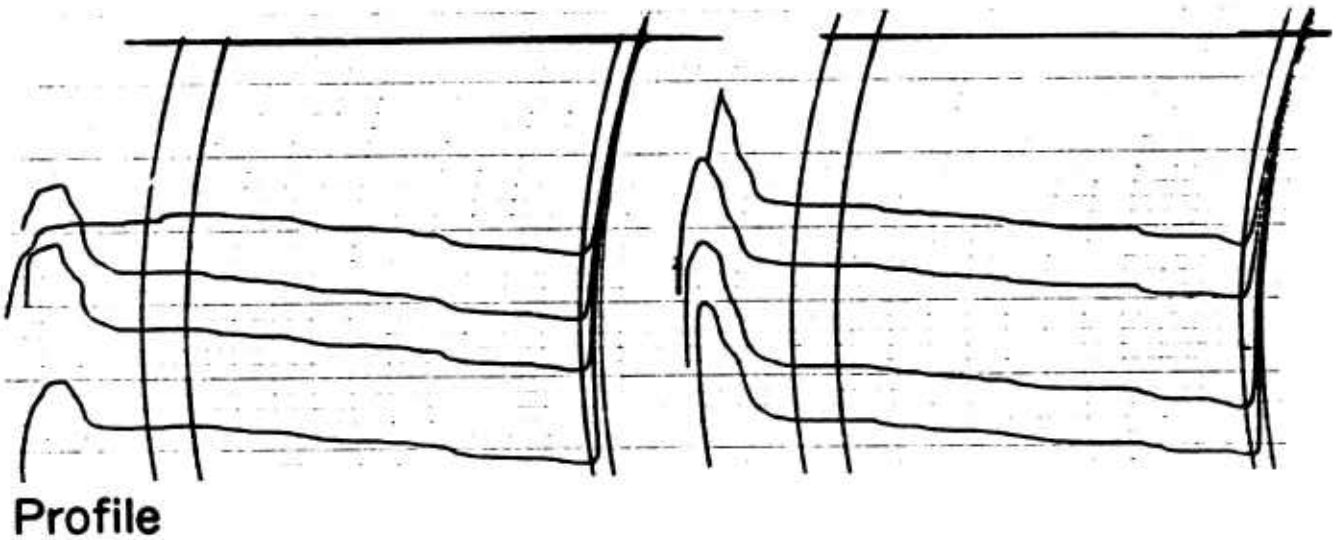

Figure 97. Profile Measurements for Idler Gear After Testing.

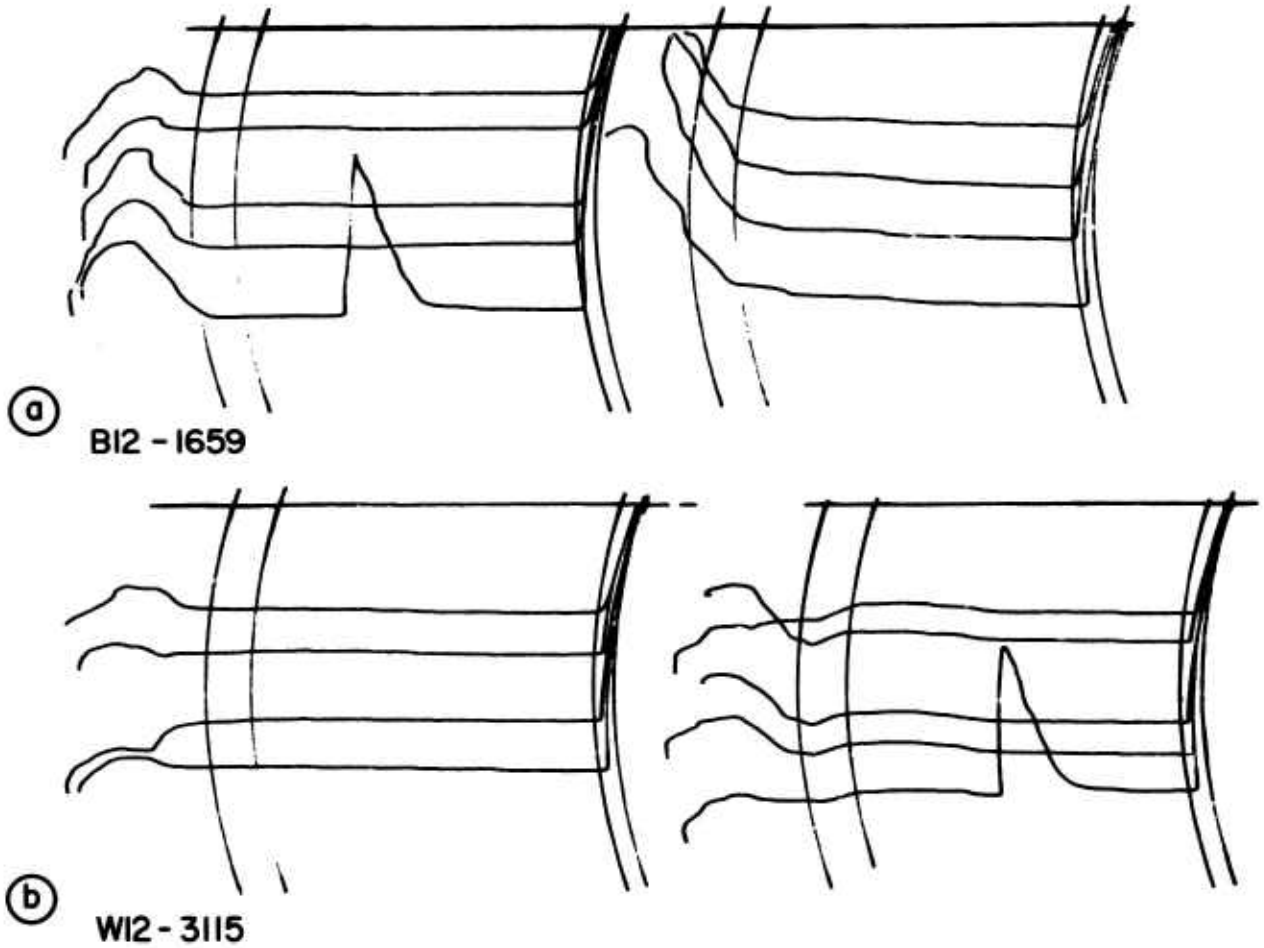

Figure 98. Profile Measurements for Pinion After Testing.

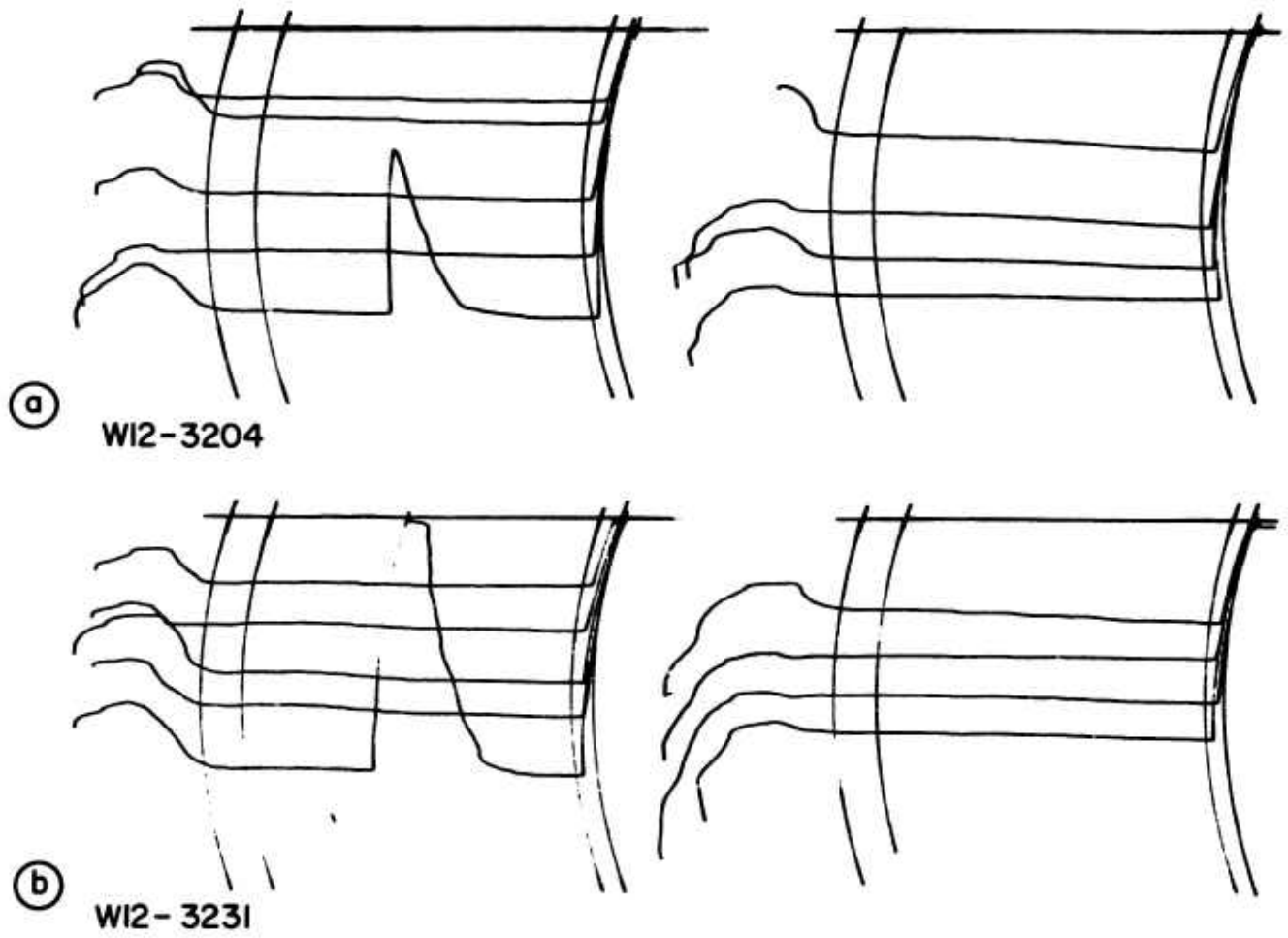

Figure 99. Profile Measurements for Pinion After Testing.

APPENDIX II
COMPUTER PROGRAM: TORSIONAL DYNAMIC SIMULATION

The torsional dynamic equations are solved via the IBM Continuous Systems Modelling Program (CSMP). The response data are sampled and stored, and then a frequency analysis is performed with the use of the FOUR2 (Fast Fourier Transform) Subroutine of the IBM Scientific Subroutine Package.

The following input data are required on PARAM cards for the dynamic analysis:

GOOD = indicator of whether geared system has any faults. If GOOD $\geq$ 2, system is in "good" condition.
WDTH = fault width, rad
PI = 3.14159
NP = number of teeth on the pinion
J1 = inertia of shafting and input gear, in.-lb·s^2
J2 = inertia of spur gear pinion, in.-lb·s^2
J3 = inertia of idler spur gear, in.-lb·s^2
J4 = inertia of spur gear, in.-lb·s^2
J5 = inertia of generator, in.-lb·s^2
B12 = torsional damping coefficient of input shafting, in.-lb/rad·s^{-1}
B23 = linear damping coefficient of pinion-idler mesh, lb/in.·s^{-1}
B34 = linear damping coefficient of idler-gear mesh, lb/in.·s^{-1}
B45 = torsional damping coefficient of spur gear shaft, in.-lb/rad·s^{-1}
K12 = torsional stiffness of input shafting, in.-lb/rad
K45 = torsional stiffness of spur gear shaft, in.-lb/rad
R2 = spinion base radius, in.
R3 = idler base radius, in.
R4 = gear base radius, in.
SSHAFT = input shaft speed, rpm
KG = generator voltage constant, V/rad·s^{-1}
KT = generator current constant, in.-lb/A
RG = load resistance, Ω

To increase computing efficiency, a set of parameters is input which starts computed variables at a point in time at which the system is in steady-state oscillation. These parameters eliminate the computational transients encountered when starting an analysis from zero.

PS1D = initial value of ψ_1, rad
PS2D = initial value of ψ_2, rad
PS3D = initial value of ψ_3, rad
PS4D = initial value of ψ_4, rad
PS1V = initial value of $\dot{\psi}_1$, rad/s
PS2V = initial value of $\dot{\psi}_2$, rad/s
PS3V = initial value of $\dot{\psi}_3$, rad/s
PS4V = initial value of $\dot{\psi}_4$, rad/s
TH2D = initial value of θ_2, rad
E1 = initial value of derivative of filter output
E2 = initial value of filter output

There are ten parameters which are required by sampling and storage routine and the FFT analysis:

NPTS	= number of points in FFT analysis [must be power of 2 and equal to TABLE NR (1)]
INCR	= Sampling increment, s (less than or equal to the inverse of twice the highest frequency of interest. It must also be an integer multiple of TIMER parameter DELT).
IDATA	= number of Fourier components to be printed out.
AVG	= number of averages of Fourier components to be performed.
STIME	= starting time of sampling, procedure, s
WAA	= break frequency of anti-aliasing filter, rad/s
STIMEI	= STIME
ISIGN	= -1
IFORM	= 1
NDIM	= 1

Storage declarations are required based on the number of points in the transform (NPTS) and the number of averages to be performed (AVG.). The parameters are dimensioned in the following manner with actual numbers replacing the symbols:

W(NPTS), AMP (NPTS), and DBAMP (NPTS).
DATA (NPTS), RSPN (NPTS), and FRC (NPTS, AVG).

The format of the parameter cards is:

Column 1-5: PARAM
Colum 6: Blank
Column 7-72: Parameter name = (any format), etc.
Example: PARAM K12 = 8.43E + 04, K45 = 5.0E + 05

There are several initial condition parameters required also:

TABLE NR (1) = NPTS
INCON N = 0, NI = 1, I = 1, FLT = 0
INCON K23 = initial value of pinion-idler mesh stiffness
INCON K34 = initial value of idler-gear mesh stiffness.

The arbitrary function generator option (AFGEN) is used to input the gear mesh stiffness functions. The stiffness calculation programs provide punched card output formatted as required for the torsional dynamic program.

The input to the dynamic (DYNAM) portion of the program is the driving torque (TQIN) of the geared system. Any constant value or constant value plus oscillation may be used depending upon measured results from the test stand.

The parameters of the program correspond to the parameters of the theoretical analysis as follows:

A1 = $\ddot{\theta}_1$ TH1DOT = $\dot{\theta}_1$

A2 = $\ddot{\theta}_2$ TH2DOT = $\dot{\theta}$ TH2 = θ_2

A3 = $\frac{R_3}{R_2}\ \ddot{\theta}_3$ TH3DOT = $\dot{\theta}_3$

A4 = $\ddot{\theta}_4$ TH4DOT = $\dot{\theta}_4$

A5 = $\ddot{\theta}_5$ TH5DOT = $\dot{\theta}_5$

PS1 = ψ_1 PS1DOT = $\dot{\psi}_1$ PS1DDT = $\ddot{\psi}_1$

PS2 = ψ_2 PS2DOT = $\dot{\psi}_2$ PS2DDT = $\ddot{\psi}_2$

PS3 = ψ_3 PS3DOT = $\dot{\psi}_3$ PS3DDT = $\ddot{\psi}_3$

PS4 = ψ_4 PS4DOT = $\dot{\psi}_4$ PS4DDT = $\ddot{\psi}_4$

The statement :

```
E2DT = (WAA**2) *PS2-2.*.6*WAA*EDT-(WAA**2)*E
```

represents a second-order anti-aliasing filter with break frequency of WAA.

The NOSORT section of the program picks the value of gear mesh stiffness needed, determines if the system is to be analyzed with a fault, and picks the special stiffness and torque impact as may be required. The gear stiffness is clocked on a parameter going from 0 to 1 for start to end of the tooth. The program next routes the computer through the fault modification portion of the program depending upon the value of GOOD.

The first portion of the fault analysis determines if a faulty tooth is in mesh and, if so, uses the modified stiffness function. The program next sets mesh damping to zero whenever the stiffness is zero. The torque impact is also introduced at the appropriate contact point. Three parameters are associated with the fault insertion:

VPDEL = velocity difference of pinion caused by fault
VGDEL = velocity difference of gear caused by fault
FLTAU = time of impact duration

The following section of the program forms the sampler. The desired data point is sampled at the sampling interval (INCR) and stored in an array of dimension NPTS X AVG.

When the dynamic analysis is complete, the program enters the TERMINAL segment to perform the Fourier Transform and output the data. The routine performs successive transforms on the data and then uses an arithmetic averaging of the coefficients. The amplitudes of the transformed

coefficients are converted to decibels referenced to whatever value is convenient. The frequency response data are then available on a set of cards containing the frequency and decibel amplitudes. Cards are also punched with time and time-domain amplitude. The data are available for whatever further processing or plotting is desired. A listing of the program follows, with a sample set of parameters used in one of the runs.

```
TITLE TORSIONAL DYNAMIC SIMULATION OF OFFSET GEARBOX
*
STORAGE NR(1)
FIXED N,NDIM,ISIGN,IFORM,NR,I,NP,NPTS,IDATA,M,MI,Y,Q1,NI,AVG,J
/     DIMENSION W(1024),AMP(1024),DBAMP(1024)
/     COMPLEX DATA(1024),RSPN(1024),CABS,REAL,FRC(1024,6)
TABLE NR(1)=1024
INCON N=0,NI=1
INCON R23=7.52
INCON K23=8.614E+05,K34=8.599E+05
INCON I=1
INCON FLT=0.
PARAM GOOD=1
INIT
      WAA=2.*PI*FAA
      W1=2.*PI*SSHAFT/60.
      TH1V=W1
      ATTH=2.*PI/41.
      FLTCAL=(J2*VPDEL+J3*VGDEL)/((2.*FLTAU*(R2+R3))
NOSORT
      DO 5 I=1,NPTS
      DATA(I)=0.0
5     CONTINUE
SORT
*     THE AFGEN DETERMINES THE GEAR STIFFNESS AS A FUNCTION
*     OF GEAR ROTATION.  STFNS IS FOR A GOOD GEAR.  STFNS2 IS
*     FOR A GEAR WITH A FAULT.
AFGEN STFNS=0.0    ,0.8614,0.0373,0.8652,0.0745,0.8684,...
       0.1115,0.8709,0.1485,0.8728,0.1853,0.8741,0.2221,0.8748,...
       0.2587,0.8749,0.2952,0.8743,0.3316,0.8732,0.3679,0.8714,...
       0.4040,0.8690,0.4401,0.4726,0.4760,0.4732,0.5118,0.4834,...
       0.5475,0.4879,0.5831,0.4918,0.6185,0.4951,0.6538,0.4978,...
       0.6890,0.7949,0.7241,0.8046,0.7590,0.8137,0.7938,0.8222,...
       0.8285,0.8301,0.8631,0.8373,0.8975,0.8439,0.9318,0.8499,...
       0.9660,0.8552,1.0000,0.8599
AFGEN STFNS2=0.0    ,0.8568,0.0373,0.8603,0.0745,0.8631,...
       0.1115,0.8655,0.1485,0.8671,0.1853,0.8682,0.2221,0.8688,...
       0.2587,0.8685,0.2952,0.8678,0.3316,0.8663,0.3679,0.8643,...
       0.4040,0.8617,0.4401,0.4426,0.4760,0.0000,0.5118,0.0000,...
       0.5475,0.0000,0.5831,0.0000,0.6185,0.0000,0.6538,0.4953,...
       0.6890,0.7923,0.7241,0.8018,0.7590,0.8108,0.7938,0.8191,...
       0.8285,0.8268,0.8631,0.8338,0.8975,0.8401,0.9318,0.8460,...
       0.9660,0.8511,1.0000,0.8554
*
DYNAM
*
*     TORSIONAL DYNAMICS OF SYSTEM
      TQIN=330.+150.*SIN(W1*TIME)
      A1=(K12*PS1+B12*PS1DOT+TQIN)/J1
      A2=(K23*(R2**2)*PS2+B23*(R2**2)*PS2DOT-K12*PS1-B12*PS1DOT...
          -FLT*R2)/J2
      A3=(K34*R3*R4*PS3+B34*R3*R4*PS3DOT-K23*R3*R2*PS2...
          -B23*R3*R2*PS2DOT+FLT*R2)*R3/(J3*R2)
      A4=(K45*PS4+B45*PS4DOT-K34*(R4**2)*PS3-B34*(R4**2)*PS3DOT)/J4
      A5=-(K45*PS4+B45*PS4DOT+KT*TG)/J5
      TG=KG*TH5DOT/PG
      PS1DOT=A2-A1
      PS2DOT=A3-A2
      PS3DOT=A4-A3
      PS4DOT=A5-A4
      PS1DOT=INTGRL(PS1V,PS1DOT)
      PS2DOT=INTGRL(PS2V,PS2DOT)
```

```
      PS3DOT=INTGRL(PS3V,PS3DDT)
      PS4DOT=INTGRL(PS4V,PS4DDT)
      PS1=INTGRL(PS10,PS1DOT)
      PS2=INTGRL(PS20,PS2DOT)
      PS3=INTGRL(PS30,PS3DOT)
      PS4=INTGRL(PS40,PS4DOT)
      TH1DOT=INTGRL(W1,A1)
      TH2DOT=PS1DOT+TH1DOT
      TH3DOT=(PS2DOT+TH2DOT)*R2/R3
      TH4DOT=PS3DOT+R3*TH3DOT/R4
      TH5DOT=PS4DOT+TH4DOT
      TH2=INTGRL(TH20,TH2DOT)
*     ANTI-ALIASING FILTER
      F2DOT=-2.*.6*WAA*FDOT-(WAA**2)*F+(WAA**2)*PS2
      FDOT=INTGRL(F1,F2DOT)
      F=INTGRL(F2,FDOT)
NOSORT
*     GEAR STIFFNESS VALUES DETERMINED
      RTTH=TH2/ATTH
      M=RTTH
      KAP=(RTTH-M)
      KAP1=1.-KAP
      K34=AFGEN(STENS,KAP1)
      K34=1.0E+06*K34
      IF(GOOD-2)98,98,99
   99 K23=AFGEN(STENS,KAP)
      K23=K23*1.0E+06
      FLT=0.0
      GO TO 112
   98 RM=M
      RNP=NP
      KAP1=RM/RNP
      KAP4=M/NP+1./41.
      IF(KAP1-KAP4)105,106,106
  105 K23=AFGEN(STENS2,KAP)
      K23=K23*1.0E+06
      IF(K23-1.)77,77,78
   77 B23=0.
      GO TO 79
   78 B23=7.52
   79 CONTINUE
      GO TO 107
  106 K23=AFGEN(STENS,KAP)
      K23=K23*1.0E+06
      GO TO 111
  107 CONTINUE
  108 CONTINUE
*     INTRODUCTION OF IMPACT TORQUE INTO TORSIONAL DYNAMICS
      KAPFLT=0.620+FLTM*W1/(2.*ATTH)
      IF(KAP-.620)111,109,109
  109 IF(KAP-KAPFLT)110,111,111
  110 FLT=FLTCAL
      GO TO 112
  111 FLT=0.
  112 CONTINUE
*     SAMPLER
    7 IF(NI-AVG)8,8,11
    8 CONTINUE
      Y1=IMPULS(STIME1,INCR)
      Y2=(TIME-STIME)/INCR
      Y3=ZHOLD(Y1,Y2)
      Y4=Y3+0.1
```

```
      N=Y4
      FRC(N,NI)=ZHOLD(Y1,F)
 12   CONTINUE
      IF(N-NPTS)11,10,10
 10   NI=NI+1
      STIME=STIME+INCR*NPTS
11 CONTINUE
SORT
TERMINAL
*     FFT ANALYSIS AND) AVERAGER
      DO 20 I=1,AVG
      DO 21 J=1,NPTS
      RSPN(J)=FRC(J,I)
 21   CONTINUE
      NR(1)=1024
      NDIM=1
      ISIGN=-1
      IFORM=1
      CALL FOUR2(RSPN,NR,NDIM,ISIGN,IFORM)
      DO 22 J=1,NPTS
      DATA(J)=DATA(J)+RSPN(J)/AVG
 22   CONTINUE
 20   CONTINUE
      DO 23 I=1,IDATA
      AMP(I)=CABS(DATA(I))
      DBAMP(I)=20.*ALOG10(AMP(I)/1.0E-04)
      W(I)=(I-1.)/(INCR*NPTS)
*
*     AMP(N) IS THE ABSOLUTE AMPLITUDE OF THE FOURIER
*     COEFFICIENT.
*
23    WRITE(2,103)W(I),DBAMP(I)
103   FORMAT(F8.1,F9.2)
       DO 24 I=1,NPTS
500   TRA=REAL(FRC(I,3))
      TM=(I-1)*INCR
      WRITE(2,1000)TM,TRA
1000  FORMAT(2F14.5)
  24   CONTINUE
*
*     INCR IS THE SAMPLING INTERVAL.
*     INCR=1./(2.*FINT) WHERE FINT IS THE HIGHEST FREQUENCY
*     OF INTEREST IN HERTZ.
*     STIME IS THE TIME AT WHICH THE ANALYSIS WILL START.
*     CHOOSE STIME SO THAT TRANSIENTS HAVE DIED-OUT.
*     NPTS DENOTES THE NUMBER OF POINTS IN THE FOURIER TRANSFORM
*     AVG IS THE PARAMETER WHICH DENOTES THE NUMBER OF AVERAGES
*     OF THE FOURIER COEFFICIENTS WHICH WILL BE MADE.
*     IDATA DENOTES THE NUMBER OF FOURIER COEFFICIENTS TO BE PRINTED.
*
PARAM WDTH=0.028
PARAM NPTS=1024
PARAM INCR=0.00005
PARAM IDATA=500
PARAM AVG=6
PARAM STIME=0.01,STIMEI=0.01
PARAM ISIGN=-1.IFORM=1,NDIM=1
*
*     NP DENOTES THE NUMBER OF TEETH ON THE PINION
*     CR DENOTES THE CONTACT RATIO OF THE GEAR PAIR
*
PARAM FAA=9000.
```

```
PARAM PI=3.14159
PARAM NP=41
PARAM GR=1.75
PARAM J1=.010000,J2=.003903,J3=.01441,J4=.0032187,J5=.0467
PARAM B12=6.41,B34=10.88,B45=12.04
PARAM VPDEL=3.95,VGDEL=1.25
PARAM FLTAU=2.5E-05
PARAM K12=8.43E+04,K45=5.0E+05
PARAM R2=1.92635,R3=2.584,R4=1.92635
PARAM FW=0.2
*
*      SSHAFT DENOTES INPUT SHAFT SPEED IN RPM.
*
PARAM SSHAFT=4500.
PARAM KG=0.0633,KT=1.100
PARAM RG=0.1,RL=0.1
PARAM FLTM=.05E-03
PARAM PS1D=-3.9530E-03
PARAM PS2D=-1.7543E-05
PARAM PS3D=-2.1959E-05
PARAM PS4D=-6.5783E-04
PARAM PS1V=2.7387E-01
PARAM PS2V=-5.2871E-01
PARAM PS3V=-3.8600E-01
PARAM PS4V=4.4559E-01
PARAM TH2D=1.2575E+01
PARAM F1=-7.8500E-02
PARAM E2=-1.2263E-05
*
*
*      SET DELT TO INCR OR SUCH THAT INCR IS A MULTIPLE
*      OF DELT.
TIMER DELT=0.000005,FINTIM=0.32,PRDEL=0.001,OUTDEL=0.01
METHOD RKSFX
END
STOP
```

APPENDIX III
GEOMETRY ASSOCIATED WITH STIFFNESS CALCULATIONS

In performance of the computation of the stiffness function for the gears, a set of geometrical relationships between the parameters used in the analytical model must be developed. To conveniently describe these relationships, a new parameter, η, is first introduced.

η = distance from the pitch point of the point of contact between mating teeth along line of action, in.

η is positive for clockwise rotation from the pitch point, zero at the pitch point, and negative for counterclockwise rotation from the pitch point. To begin the analysis, refer to Figure 100 and define the following points:

A = point of initiation of contact
P = pitch point
T = point of tooth contact
B = point of final contact
O_G = gear center
O_P = pinion center
Φ = pressure angle, rad
R_{BG} = radius of base circle of gear, in.
R_{PG} = radius of pitch circle of gear, in.
R_{TG} = radius of contact point of gear, in.
R_{BP} = radius of base circle of pinion, in.
R_{PP} = radius of pitch circle of pinion, in.
R_{TP} = radius to contact point of pinion, in.

The first parameter to be defined is the radius of curvature to be used in the calculation of the Hertzian compliance.

$$\begin{aligned} R_{GP} &= |\overline{AT}| \\ &= |\overline{AP}| + \eta \\ &= R_{BP} \tan \Phi + \eta \end{aligned} \tag{58}$$

$$\begin{aligned} R_G &= |\overline{BT}| \\ &= |\overline{BP}| - \eta \\ &= R_{BG} \tan \Phi - \eta \end{aligned} \tag{59}$$

Right triangle laws allow the determination of the radius to the contact point.

$$\begin{aligned} R_{TP} &= \left\{ \left(|\overline{AO_P}| \right)^2 + \left(|\overline{AT}| \right)^2 \right\}^{1/2} \\ &= \left\{ (R_{BP})^2 + \left(R_{PP} \sin \Phi + \eta \right)^2 \right\}^{1/2} \end{aligned} \tag{60}$$

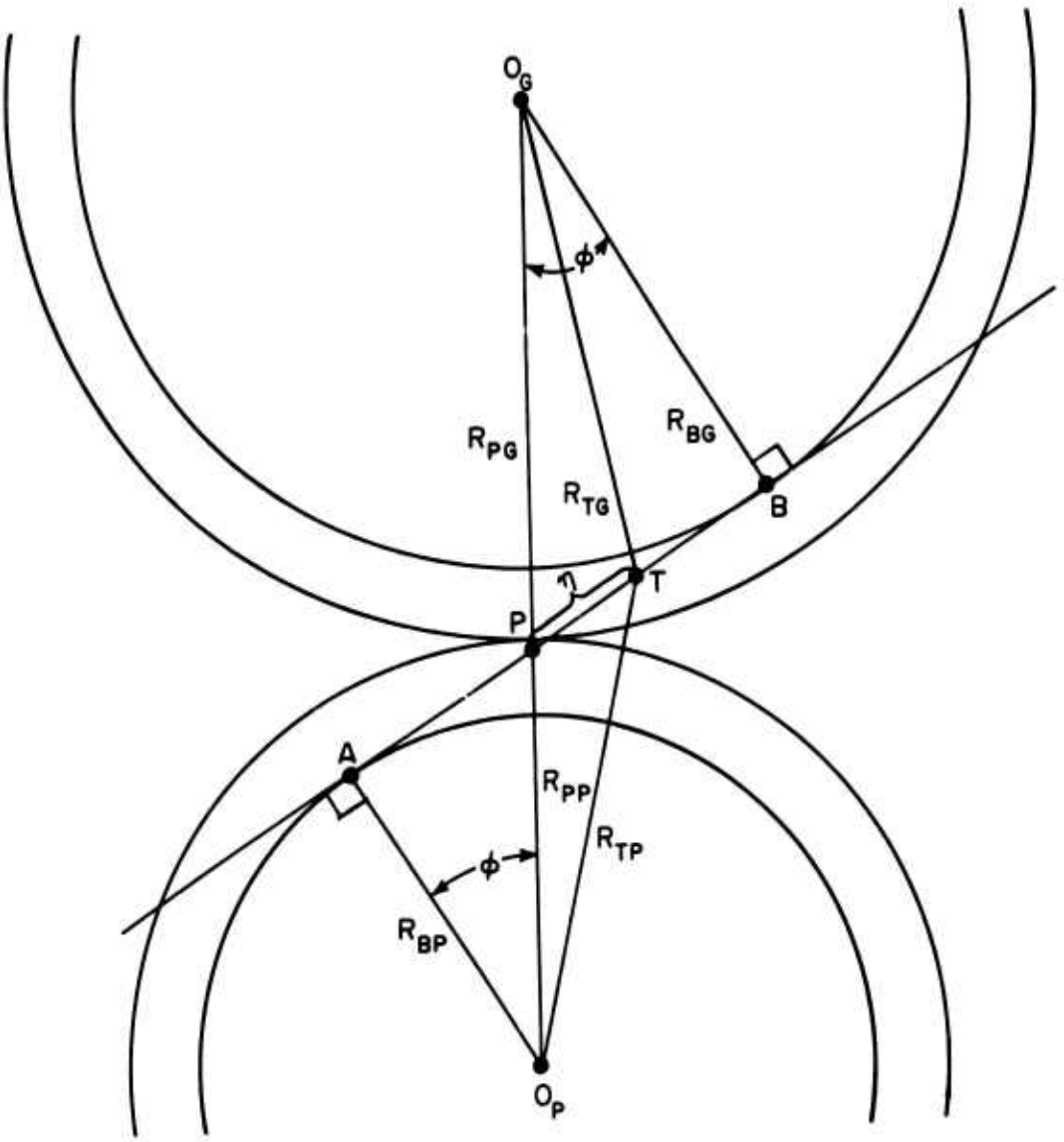

Figure 100. Geometry Associated With Gear Pair.

$$R_{TG} = \left\{ \left(\left| \overline{BO_G} \right| \right)^2 + \left(\left| \overline{BT} \right| \right)^2 \right\}^{1/2}$$
$$= \left\{ \left(R_{BG} \right)^2 + \left(R_{PG} \sin \phi - \eta \right)^2 \right\}^{1/2} \quad (61)$$

An approximation is used in the expression for the gear tooth thickness. At the contact point, by involutometry the following is satisfied:

$$R_P \cos \phi = R_T \cos \xi_T \quad (62)$$

ξ_T = involute angle, rad

Using the following relationships, the tooth thickness at the pitch circle is found:

$$G_S = \frac{R_P \cos \phi}{R_T} \quad (63)$$

$$\xi_T = \tan^{-1} \frac{\sqrt{1 - G_S^2}}{G_S} \quad (64)$$

$$t_T = 2R_T \left(\frac{t_c}{2R_P} + \text{inv } \phi - \text{inv } \xi_T \right) \quad (65)$$

where G_S = defined parameter
t_T = tooth thickness at the contact point, in.
t_c = tooth thickness at the pitch circle, in.
inv = involute function

$$t_c = \frac{P_c}{2} \quad (66)$$

where P_c = circular pitch, in.

$$\text{inv } \phi = \tan \phi - \phi \quad (67)$$

$$\text{inv } \xi_T = \tan \xi_T - \xi_T \quad (68)$$

The tooth thickness at any point other than the contact point is approximated from the previous relationships in the following manner:

$$G_S^* = \frac{R_P \cos \phi}{R_B + Y} \quad (69)$$

$$\xi = \tan^{-1} \frac{\sqrt{1 - G_S^{*2}}}{G_S^*} \tag{70}$$

$$2X = 2(R_B + y)\left(\frac{tc}{2R_P} + \text{inv } \phi - \text{inv } \xi\right) \tag{71}$$

$$\text{inv } \xi = \tan \xi - \xi \tag{72}$$

Figure 101 is used in the description of the angle (θ) which specifies the direction of the gear tooth centerline with respect to the pressure line. From the figure,

C = is the intersection of the line of action with the tooth center
CD = is a perpendicular to the tooth centerline

$$\angle BCD = \theta_G \tag{73}$$

$$\angle ACO_P + \angle OCD + \angle BCD = 180° \tag{74}$$

$$\angle O_P CD = 90° \tag{75}$$

$$\therefore \angle ACO_P = 90° - \theta_G \tag{76}$$

$$\angle BAO_P + \angle AO_P C + \angle ACO_P = 180° \tag{77}$$

$$\angle BAO_P = 90° \tag{78}$$

$$\therefore \angle AO_P C = \theta_G \tag{79}$$

$$\angle AO_P C = \angle AO_P T - \beta \tag{80}$$

From Figure 100,

$$\angle AO_P T = \tan^{-1}\left(\frac{R_{PP} \sin \phi + \eta}{R_{BP}}\right) \tag{81}$$

$$\beta = \frac{t_{TP}}{2R_{TP}} \tag{82}$$

$$\therefore \theta_P = \tan^{-1}\left(\frac{R_{PP} \sin \phi + \eta}{R_{BP}}\right) - \frac{t_{TP}}{2R_{TP}} \tag{83}$$

Figure 102 is now used in the determination of θ_P (for the pinion).

$$\angle O_G C_G B = 90° - \theta_G \tag{84}$$

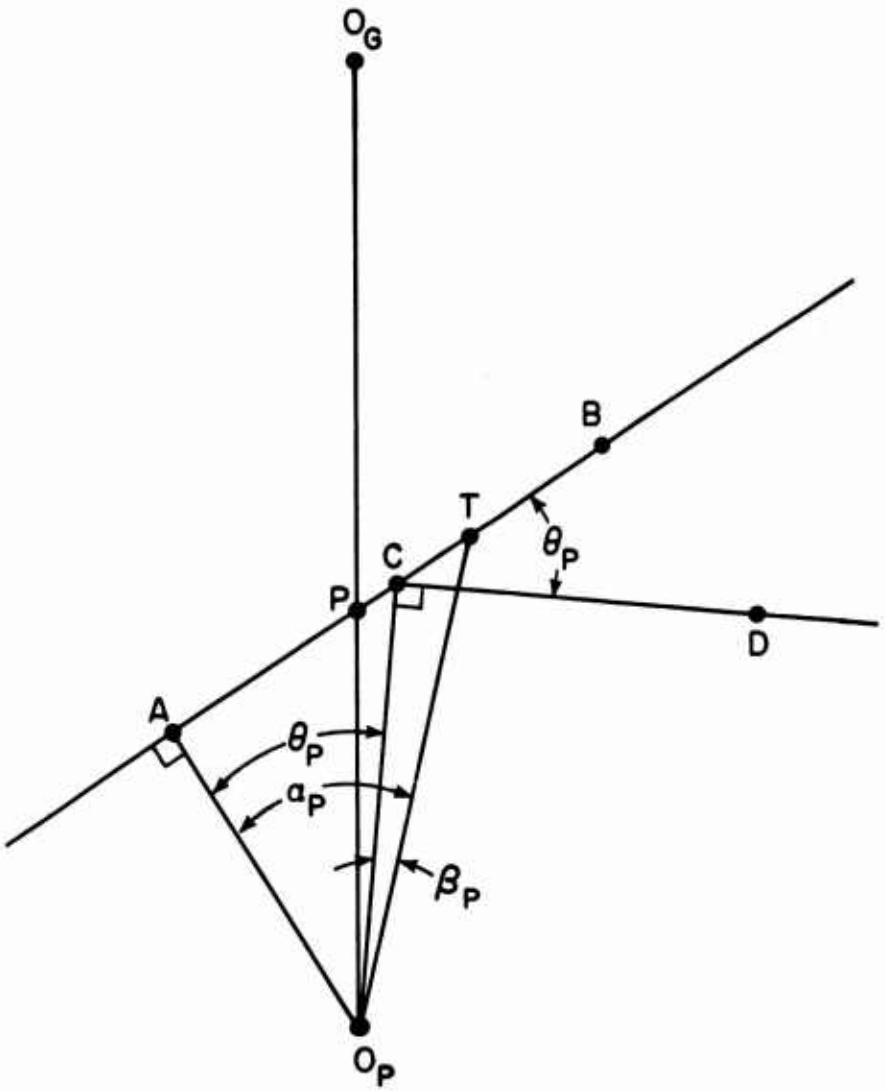

Figure 101. Geometry Associated With Pinion.

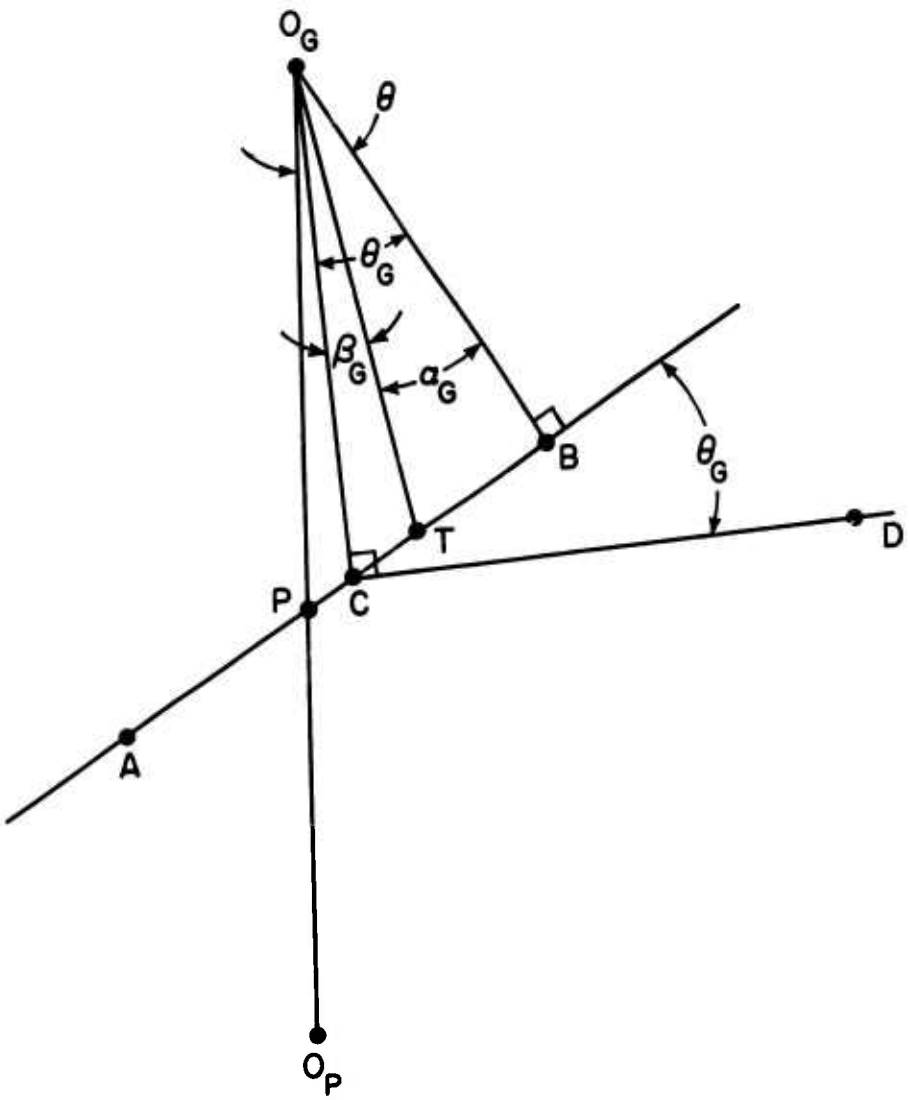

Figure 102. Geometry Associated With Gear.

$$\angle BO_G C_G + \angle O_G C_G B + \angle C_G B O_P = 180° \tag{85}$$

$$\angle C_G B O_G = 90° \tag{86}$$

$$\therefore \angle BO_G C_G = \theta_G \tag{87}$$

From Figure 100,

$$\angle BO_G T = \tan^{-1}\left(\frac{R_{PG} \sin \phi - \eta}{R_{BG}}\right) \tag{88}$$

$$\angle C_G O_G T = \frac{t_{TG}}{2R_{TG}} \tag{89}$$

$$\therefore \theta_G = \tan^{-1}\left(\frac{R_{PG} \sin \phi - \eta}{R_{BG}}\right) - \frac{t_{TG}}{2R_{TG}} \tag{90}$$

From Figure 101,

$$|O_P C| = \frac{|\overline{OA_P}|}{\cos \theta_P}$$

$$= \frac{R_{BP}}{\cos \theta_P} \tag{91}$$

$$Y_{LP} = |\overline{O_P C}| - R_{BP}$$

$$= R_{BP}\left(\frac{1}{\cos \theta_P} - 1\right) \tag{92}$$

From Figure 102,

$$|\overline{O_G C}| = \frac{|\overline{OB_G}|}{\cos \theta_G}$$

$$= \frac{R_{BG}}{\cos \theta_G} \tag{93}$$

$$Y_{LG} = |\overline{O_G C}| - R_{BG}$$

$$= R_{BG}\left(\frac{1}{\cos \theta_G} - 1\right) \tag{94}$$

From Figure 101,

$$|\overline{CT}| = |\overline{AT}| - |\overline{AC}|$$

$$= R_{BP} \tan (\theta_P + \beta_P) - R_{BP}\tan \theta_P \tag{95}$$

$$h_p = |\overline{CT}|$$

$$= R_{BP}\left[\tan (\theta_P + \beta_P) - \tan \theta_P\right] \tag{96}$$

From Figure 102,

$$|\overline{CP}| = |\overline{BT}| - |\overline{TC_G}|$$

$$= R_{BG} \tan(\theta_G + \beta_G) - R_{BG}\tan \theta_G \tag{97}$$

$$h_G = |\overline{CP}|$$

$$= R_{BG}\left[\tan(\theta_G + \beta_G) - \tan \theta_G\right] \tag{98}$$

Two final parameters are needed in the stiffness calculation; i.e., the values of η at the initial point of contact and the final point of contact. From Figure 100,

$$\eta_{\substack{\text{initial}\\ \text{contact}}} = -(R_{OG}^2 - R_{BG}^2)^{1/2} + R_{PG} \sin \phi$$

R_{OP} = outside radius of pinion, in.

R_{OG} = outside radius of gear, in. (99)

$$\eta_{\substack{\text{final}\\ \text{contact}}} = (R_{OP}^2 - R_{BP}^2)^{1/2} - R_{PP} \sin \phi \tag{100}$$

With the geometrical relationships developed in this appendix, the gear mesh stiffness functions may now be expressed as a function of the position η and the physical dimensions of the gears.

APPENDIX IV
COMPUTER PROGRAM: GEAR STIFFNESS CALCULATIONS

Programs were written in FORTRAN to calculate the values of the gear stiffness functions. Separate programs were used for gears in good condition and gears with faults, but the programming differences were slight. The following parameters are required in the operation of either program:

ROG = outside gear radius, in.
ROP = outside pinion radius, in.
RBG = base circle radius of gear, in.
RBP = base circle radius of pinion, in.
RPG = pitch circle radius of gear, in.
RPP = pitch circle radius of pinion, in.
PI = 3.14159
PHI = pressure angle, rad
E = Young's modulus, lb/in^2
G = shear modulus, lb/in^2
NU = Poisson's ratio
PC = circular pitch, in.
RPM = input speed, rpm
PWR = input power, hp
W = face width, in.
PD = diametral pitch
PTS = number of points of stiffness function to be calculated

The program which calculates stiffness for a gear with a fault requires one more parameter; i.e.,

WDTH = width of fault with respect to the line of action, in.

The calculations use a number of subroutines, as follows:

THKNS = calculates tooth thickness at position off contact point
TKPC = calculates tooth thickness at contact point
TRAP = performs a trapezoidal numerical integration on the function:

$$f(y) = \int_0^{y_L} \frac{(y_L - y)^2}{(2x)^3}\, dy \qquad (101)$$

TRAP2 = performs a trapezoidal numerical integration on the function:

$$f(y) = \int_0^{y_L} \frac{dy}{(2x)} \qquad (102)$$

THETA = calculates the angle between the direction of tooth force application and perpendicular to tooth centerline.

The program calculates the stiffness functions based on the equations presented in the section on Theoretical Analysis and Appendix III. Compliance values are calculated as a function of ETA(η) per inch of face width.

COM(J,1) = bending compliance of gear (J refers to η), in./lb
COM(J,2) = bending compliance of pinion, in./lb
CMHZ(J) = Hertzian compliance, in./lb

The total compliance is then calculated.

COMT(J) = tooth pair compliance, in./lb

The program next calculates stiffness functions in the manner described under Theoretical Analysis. The results are then formulated to produce punched cards for use in the torsional dynamic computation.

Listings of the programs with parameters used in sample runs follow.

```
C      PROGRAM FOR CALCULATION OF STIFFNESS FUNCTION(GOOD GEAR)
       DIMENSION POS(100),COMH(100),COM(100,2),COMT(100)
       DIMENSION POSL(101),POSK(101),STFNS2(101),STFNS(101)
       DIMENSION ANG(101),VAL(202)
       DIMENSION ANG2(101)
       REAL NU,IOTA,IOTAG,IOTAP
       COMMON PHI,PC
       ROP=2.15
       ROG=2.85
       RBP=3.8527/2.
       RBG=5.168/2.
       RPP=2.05
       RPG=5.5/2.
       PI=3.14159
       PHI=20.*PI/180.
       E=30.E+06
       G=11.5E+06
       NU=.287
       PC=.3142
       RPM=4500.
       PWR=15./0.7
       W=0.20
       PTS=50.
       ETA1=-SQRT(ROG**2-RBG**2)+RPG*SIN(PHI)
       ETA2=SQRT(ROP**2-RBP**2)-RPP*SIN(PHI)
       PD=10.0
       PN=PI*COS(PHI)/PD
       ETASS=ETA2-PN
       ETASF=ETA1+PN
       TQ=PWR*6.3E+04/RPM
       FL=TQ/RPP
       FO=FL/W
       ETAD=(ETA2-ETA1)/PTS
C      CALCULATES BENDING COMPLIANCE
       I=1
  3    ETA=ETA1
       J=1
  4    CONTINUE
       IF(I-1)5,5,6
  5    RP=RPP
       RB=RBP
       RT=SQRT(RB**2+(RP*SIN(PHI)+ETA)**2)
       GO TO 7
  6    RP=RPG
       RB=RBG
       RT=SQRT(RB**2+(RP*SIN(PHI)-ETA)**2)
  7    CONTINUE
       IOTA=THETA(RB,RP,RT,ETA,I)
       YL=RB*((1./COS(IOTA))-1.)
 88    FORMAT(' ',I6,3X,I6,3X,E14.5,3X,E14.5,3X,E14.5)
       CMMM=(12.*TRAP(YL,RB,RP)*(COS(IOTA))**2)/E
       CMSH=(1.2*TRAP2(YL,RB,RP)*(COS(IOTA))**2)/G
       CMNF=(1.2*TRAP2(YL,RB,RP)*(SIN(IOTA))**2)/E
       COM(J,I)=(CMMM+CMNF+CMSH)/W
       POS(J)=ETA
       ETA=ETA+ETAD
       J=J+1
       D=PTS+2
       IF(J-D)4,29,29
 29    CONTINUE
       IF(I-1)30,30,31
 30    CONTINUE
```

```
      I=I+1
      GO TO 3
C     CALCULATES HERTZIAN COMPLIANCE
 31   ETA=ETA1
      J=1
 34   CONTINUE
      RTP=SQRT(RBP**2+(RPP*SIN(PHI)+ETA)**2)
      RTG=SQRT(RBG**2+(RPG*SIN(PHI)-ETA)**2)
      RCVG=RBG*TAN(PHI)-ETA
      RCVP=RBP*TAN(PHI)+ETA
      BETAG=TKPC(RPG,RTG)/(2.*RTG)
      BETAP=TKPC(RPP,RTP)/(2.*RTP)
      IOTAG=THETA(RBG,RPG,RTG,ETA,2)
      IOTAP=THETA(RBP,RPP,RTP,ETA,1)
      ALPHAG=IOTAG+BETAG
      ALPHAP=IOTAP+BETAP
      HG=RBG*(TAN(ALPHAG)-TAN(IOTAG))
      HP=RBP*(TAN(ALPHAP)-TAN(IOTAP))
      B=SQRT((4.*FO*RCVG*RCVP)*(2.*(1.-NU**2))/(E*PI*(RCVG+RCVP)))
      CMHZ=2.*(1.-NU**2)*(ALOG(4.*HG*HP/B**2)-NU/(1.-NU))/(PI*E)
      COMH(J)=CMHZ/W
      ETA=ETA+ETAD
      J=J+1
      IF(J-D)34,39,39
 39   CONTINUE
      L=PTS+1
      WRITE(6,97)
C     CALCULATES TOTAL TOOTH PAIR COMPLIANCE
      DO 40 J=1,L
      COMT(J)=(COMH(J)+COM(J,1)+COM(J,2))
      WRITE(6,99)J,POS(J),COMT(J),COMH(J),COM(J,1),COM(J,2)
 40   CONTINUE
      WRITE(6,98)ETA1,ETA2,TQ
C     CALCULATES POSITION OF ADJACENT TOOTH PAIR COMPLIANCE WITH
C        RESPECT TO TOOTH PAIR OF INTEREST
      DO 41 I=1,L
      STFNS(I)=1./COMT(I)
      STFNS2(I)=STFNS(I)
      POSL(I)=POS(I)-PN
      POSR(I)=POS(I)+PN
 41   CONTINUE
 42   I=1
 43   J=1
C     CALCULATES EFFECT OF INITIAL TWO TOOTH PAIR CONTACT
 44   K=J+1
      IF(K-L)47,47,51
  47  IF(POS(I).LT.POSL(J))GO TO 49
      IF(POS(I).GT.POSL(K))GO TO 50
      DPOS=POSL(K)-POSL(J)
      POS1=POS(I)-POSL(J)
      POS2=POSL(K)-POS(I)
      STFNS2(I)=STFNS(I)+(POS1*STFNS(J)+POS2*STFNS(K))/DPOS
      IF(POS(I)-ETASS)48,48,51
 48   CONTINUE
 49   I=I+1
      GO TO 43
 50   J=J+1
      GO TO 44
 51   CONTINUE
 52   I=1
C     CALCULATES EFFECT OF SECOND TWO TOOTH PAIR CONTACT
 53   J=1
```

```
 54   K=J+1
      IF(K-L)57,57,61
 57   IF(POS(I).LT.POSR(J))GO TO 59
      IF(POS(I).GT.POSR(K))GO TO 60
      DPOS=POSR(K)-POSR(J)
      POS1=POS(I)-POSR(J)
      POS2=POSR(K)-POS(I)
      STFNS2(I)=STFNS(I)+(POS1*STFNS(J)+POS2*STFNS(K))/DPOS
      IF(POS(I)-ETA2)58,58,61
 58   CONTINUE
 59   I=I+1
      GO TO 53
 60   J=J+1
      GO TO 54
 61   CONTINUE
      DO 70 I=1,L
      WRITE(6,99)I,POS(I),STFNS(I),STFNS2(I),POSL(I),POSR(I)
 70   CONTINUE
C     PREPARES STIFFNESS FUNCTION FOR FUNCTION GENERATOR
      AB=SQRT(ROP**2-RBP**2)
      AAS=AB-(ETA2-ETA1)
      AASOA=ATAN(AAS/RBP)
      ABOA=ATAN(AB/RBP)
      ATRVL=ABOA-AASOA
      DO 71 J=1,51
      ANG(J)=ATAN((AAS-ETA1+POS(J))/RBP)-AASOA
 71   CONTINUE
      DO 72 K=1,51
      ANG2(K)=(ANG(K)-ANG(11))/(ANG(39)-ANG(11))
 72   CONTINUE
      K=11
      I=1
 100  CONTINUE
      VAL(I)=ANG2(K)
      VAL(I+1)=STFNS2(K)/1.0E+06
      IF(I-58)101,102,102
 101  I=I+2
      K=K+1
      GO TO 100
 102  CONTINUE
      PUNCH94,VAL(1),VAL(2),VAL(3),VAL(4),VAL(5),VAL(6)
      I=7
 103  CONTINUE
      PUNCH95,VAL(I),VAL(I+1),VAL(I+2),VAL(I+3),VAL(I+4),VAL(I+5),
     1VAL(I+6),VAL(I+7)
      I=I+8
      IF(I-54)103,104,104
 104  CONTINUE
      PUNCH96,VAL(55),VAL(56),VAL(57),VAL(58)
      DO 105 I=1,57,2
      WRITE(6,1000)VAL(I),VAL(I+1)
 105   CONTINUE
 94   FORMAT('AFGEN STFNS=',F6.4,',',F6.4,',',F6.4,',',F6.4,',',
     1F6.4,',',F6.4,',...')
 95   FORMAT(7X,F6.4,',',F6.4,',',F6.4,',',F6.4,',',F6.4,',',
     1F6.4,',',F6.4,',',F6.4,',...');
 96   FORMAT(7X,F6.4,',',F6.4,',',F6.4,',',F6.4)
 97   FORMAT('1',14X,'ETA',11X,'COMT',9X,'COMHZ',10X,'COMP',10X,'COMG')
 98   FORMAT('0','ETA1=',E14.5,3X,'ETA2=',E14.5,3X,'TORQUE=',E14.5)
 99   FORMAT(' ',I6,3X,5E14.5)
1000  FORMAT(' ',2E14.5)
      STOP
```

```
      END
      FUNCTION  THKNS(RB,RP,Y)
C     CALCULATES TOOTH THICKNESS
          COMMON PHI,PC
          GS=RP*COS(PHI)/(RB+Y)
          ZETA=ATAN(SQRT(1.-GS**2)/GS)
          TC=PC/2.
          INVZET=TAN(ZETA)-ZETA
          INVPHI=TAN(PHI)-PHI
          THKNS=2.*(RB+Y)*(TC/(2.*RP)+INVPHI-INVZET)
          RETURN
       END
      FUNCTION  TKPC(RP,RT)
C     CALCULATES TOOTH THICKNESS AT CONTACT POINT
          COMMON PHI,PC
          TC=PC/2.
          GT=RP*COS(PHI)/RT
          ZETAT=ATAN(SQRT(1.-GT**2)/GT)
          INVPHI=TAN(PHI)-PHI
          INVZET=TAN(ZETAT)-ZETAT
          TKPC=2.*RT*(TC/(2.*RP)+INVPHI-INVZET)
          RETURN
       END
      FUNCTION  TRAP(YL,RB,RP)
C     PERFORMS INTEGRATION FOR COMPLIANCE DUE TO BENDING MOMENT
          COMMON PHI,PC
          F1=0.
         DELT=YL/200.
          Y=DELT
    9     YS=Y
          Y=Y+DELT
          IF(Y-YL)10,10,21
   10     X2=((YL-Y)**2)/(THKNS(RB,RP,Y))**3
          X1=((YL-YS)**2)/(THKNS(RB,RP,YS))**3
          F1=F1+DELT*(X1+X2)/2.
          TRAP=F1
          GO TO 9
   21     CONTINUE
          RETURN
       END
      FUNCTION  TRAP2(YL,RB,RP)
C     PERFORMS INTEGRATION FOR COMPLIANCE DUE TO SHEAR AND NORMAL FORCES
          COMMON PHI,PC
          F2=0.
         DELT=YL/200.
          Y=DELT
   19     YS=Y
          Y=Y+DELT
          IF(Y-YL)20,20,22
   20     X3=1./THKNS(RB,RP,Y)
          X4=1./THKNS(RB,RP,YS)
          F2=F2+DELT*(X3+X4)/2.
          GO TO 19
   22     CONTINUE
          TRAP2=F2
          RETURN
       END
      FUNCTION  THETA(RB,RP,RT,ETA,I)
C     CALCULATES ANGLE THETA OF LOAD FORCE
          COMMON PHI,PC
          BETA=TKPC(RP,RT)/(2.*RT)
          IF(I-1)80,80,82
```

```
80        THETA=ATAN((RP*SIN(PHI)+ETA)/RB)-BETA
          GO TO 84
82        THETA=ATAN((RP*SIN(PHI)-ETA)/RB)-BETA
84        CONTINUE
          RETURN
      END
```

```
C       PROGRAM FOR CALCULATION OF STIFFNESS OF GEAR WITH FAULT.
        DIMENSION POS(100),COMH(100),COM(100,2),COMT(100)
        DIMENSION POSL(101),POSR(101),STFNS2(101),STFNS(101)
        DIMENSION ANG(101),VAL(202)
        DIMENSION ANG2(101)
        REAL NU,IOTA,IOTAG,IOTAP
        COMMON PHI,PC,WDTH
        ROP=2.15
        ROG=2.85
        RBP=3.8527/2.
        RBG=5.168/2.
        RPP=2.05
        RPG=5.5/2.
        PI=3.14159
        PHI=20.*PI/180.
        E=30.E+06
        G=11.5E+06
        NU=.287
        PC=.3142
        RPM=4500.
        PWR=15./0.7
        W=0.20
        PTS=50.
        ETA1=-SQRT(ROG**2-RBG**2)+RPG*SIN(PHI)
        ETA2=SQRT(ROP**2-RBP**2)-RPP*SIN(PHI)
        PD=10.
        PN=PI*COS(PHI)/PD
        ETASS=ETA2-PN
        ETASF=ETA1+PN
        WDTH=0.015
        TO=PWR*6.3E+04/RPM
        FL=TO/RPP
        FO=FL/W
        ETAD=(ETA2-ETA1)/PTS
        YPMIN=0.094-WDTH
        YPPLS=0.094+WDTH
C       CALCULATES BENDING COMPLIANCE
        I=1
  3     ETA=ETA1
        J=1
  4     CONTINUE
        IF(I-1)5,5,6
  5     RP=RPP
        RB=RBP
        RT=SQRT(RB**2+(RP*SIN(PHI)+ETA)**2)
        GO TO 7
  6     RP=RPG
        RB=RBG
        RT=SQRT(RB**2+(RP*SIN(PHI)-ETA)**2)
  7     CONTINUE
        IOTA=THETA(RB,RP,RT,ETA,I)
        YL=RB*((1./COS(IOTA))-1.)
 88     FORMAT(' ',I6,3X,I6,3X,E14.5,3X,F14.5,3X,E14.5)
        CMMM=(12.*TRAP(YL,RB,RP,I)*(COS(IOTA))**2)/E
        CMSH=(1.2*TRAP2(YL,RB,RP,I)*(COS(IOTA))**2)/G
        CMNF=(1.2*TRAP2(YL,RB,RP,I)*(SIN(IOTA))**2)/E
        COM(J,I)=(CMMM+CMNF+CMSH)/W
        POS(J)=ETA
        ETA=ETA+ETAD
        J=J+1
        D=PTS+2
        IF(J-D)4,29,29
```

```
 29   CONTINUE
      IF(I-1)30,30,31
 30   CONTINUE
      I=I+1
      GO TO 3
C     CALCULATES HERTZIAN COMPLIANCE
 31   ETA=ETA1
      J=1
 34   CONTINUE
      RTP=SQRT(RBP**2+(RPP*SIN(PHI)+ETA)**2)
      RTG=SQRT(RBG**2+(RPG*SIN(PHI)-ETA)**2)
      RCVG=RBG*TAN(PHI)-ETA
      RCVP=RBP*TAN(PHI)+ETA
      B=SQRT((4.*FO*RCVG*RCVP)*(2.*(1.-NU**2))/(E*PI*(RCVG+RCVP)))
      BETAG=TKPC(RPG,RTG)/(2.*RTG)
      BETAP=TKPC(RPP,RTP)/(2.*RTP)
      IOTAP=THETA(RBP,RPP,RTP,ETA,1)
      IOTAG=THETA(RBG,RPG,RTG,ETA,2)
      ALPHAG=IOTAG+BETAG
      ALPHAP=IOTAP+BETAP
      COR=0.0
      YLP=RBP*((1./COS(IOTAP))-1.)
      WRITE(6,2000)ETA,RTP,RTG,RCVG,RCVP
      WRITE(6,2000)B,BETAG,BETAP,IOTAG,IOTAP
      IF(YLP-YPMIN)300,300,35
 35   IF(YLP-YPPLS)36,300,300
 36   COR=2.*WDTH
      CORB=YLP-YPMIN
      IF(B-CORB)38,38,37
 37   B=B-CORB
 300  CONTINUE
      HG=RBG*(TAN(ALPHAG)-TAN(IOTAG))-COR
      HP=RBP*(TAN(ALPHAP)-TAN(IOTAP))
      CMHZ=2.*(1.-NU**2)*(ALOG(4.*HG*HP/B**2)-NU/(1.-NU))/(PI*E)
      GO TO 301
 38   CMHZ=1.0E+64
 301  CONTINUE
      COMH(J)=CMHZ/W
      WRITE(6,2000)ALPHAG,ALPHAP,COR,YLG,CORB
      WRITE(6,2000)B,HG,HP,CMHZ,ETA
2000  FORMAT(5E14.5)
      ETA=ETA+ETAD
      J=J+1
      IF(J-D)34,39,39
 39   CONTINUE
      L=PTS+1
      WRITE(6,97)
C     CALCULATES TOTAL TOOTH PAIR COMPLIANCE
      DO 40 J=1,L
      COMT(J)=(COMH(J)+COM(J,1)+COM(J,2))
      WRITE(6,99)J,POS(J),COMT(J),COMH(J),COM(J,1),COM(J,2)
 40   CONTINUE
      WRITE(6,98)ETA1,ETA2,TQ
C     CALCULATES POSITION OF ADJACENT TOOTH PAIR COMPLIANCE WITH
C        RESPECT TO TOOTH PAIR OF INTEREST
      DO 41 I=1,L
      IF(COMT(I)-1.0E+60)73,74,74
 73   STFNS(I)=1./COMT(I)
      GO TO 75
 74   STFNS(I)=0.0
 75   STFNS2(I)=STFNS(I)
      POSL(I)=POS(I)-PN
```

```
      POSR(I)=POS(I)+PN
   41 CONTINUE
   42 I=1
   43 J=1
C     CALCULATES EFFECT OF INITIAL TWO TOOTH PAIR CONTACT
   44 K=J+1
      IF(K-L)47,47,51
   47 IF(POS(I).LT.POSL(J))GO TO 49
      IF(POS(I).GT.POSL(K))GO TO 50
      DPOS=POSL(K)-POSL(J)
      POS1=POS(I)-POSL(J)
      POS2=POSL(K)-POS(I)
      STFNS2(I)=STFNS(I)+(POS1*STFNS(J)+POS2*STFNS(K))/DPOS
      IF(POS(I)-ETASS)48,48,51
   48 CONTINUE
   49 I=I+1
      GO TO 43
   50 J=J+1
      GO TO 44
   51 CONTINUE
   52 I=1
C     CALCULATES EFFECT OF SECOND TWO TOOTH PAIR CONTACT
   53 J=1
   54 K=J+1
      IF(K-L)57,57,61
   57 IF(POS(I).LT.POSR(J))GO TO 59
      IF(POS(I).GT.POSR(K))GO TO 60
      DPOS=POSR(K)-POSR(J)
      POS1=POS(I)-POSR(J)
      POS2=POSR(K)-POS(I)
      STFNS2(I)=STFNS(I)+(POS1*STFNS(J)+POS2*STFNS(K))/DPOS
      IF(POS(I)-ETA2)58,58,61
   58 CONTINUE
   59 I=I+1
      GO TO 53
   60 J=J+1
      GO TO 54
   61 CONTINUE
      DO 70 I=1,L
      WRITE(6,99,I,POS(I),STFNS(I),STFNS2(I),POSL(I),POSR(I)
   70 CONTINUE
C     PREPARES STIFFNESS FUNCTION FOR FUNCTION GENERATOR
      AB=SQRT(ROP**2-RBP**2)
      AAS=AB-(ETA2-ETA1)
      AASOA=ATAN(AAS/RBP)
      ABOA=ATAN(AB/RBP)
      DO 71 J=1,51
      ANG(J)=ATAN((AAS-ETA1+POS(J))/RBP)-AASOA
   71 CONTINUE
      DO 72 K=1,51
      ANG2(K)=(ANG(K)-ANG(11))/(ANG(39)-ANG(11))
   72 CONTINUE
      K=11
      I=1
  100 CONTINUE
      VAL(I)=ANG2(K)
      VAL(I+1)=STFNS2(K)/1.0E+06
      IF(I-58)101,102,102
  101 I=I+2
      K=K+1
      GO TO 100
  102 CONTINUE
```

```
      PUNCH94,VAL(1),VAL(2),VAL(3),VAL(4),VAL(5),VAL(6)
      I=7
  103 CONTINUE
      PUNCH95,VAL(I),VAL(I+1),VAL(I+2),VAL(I+3),VAL(I+4),VAL(I+5),
     1VAL(I+6),VAL(I+7)
      I=I+8
      IF(I-54)103,104,104
  104 CONTINUE
      PUNCH96,VAL(55),VAL(56),VAL(57),VAL(58)
      DO 105 I=1,57,2
      WRITE(6,1000)VAL(I),VAL(I+1)
  105  CONTINUE
   94 FORMAT('AFGEN STFNS2=',F6.4,',',F6.4,',',F6.4,',',F6.4,',',
     1F6.4,',',F6.4,',...')
   95 FORMAT(7X,F6.4,',',F6.4,',',F6.4,',',F6.4,',',F6.4,',',
     1F6.4,',',F6.4,',',F6.4,',...')
   96 FORMAT(7X,F6.4,',',F6.4,',',F6.4,',',F6.4)
   97 FORMAT('1',14X,'ETA',11X,'COMT',9X,'COMHZ',10X,'COMP',10X,'COMG')
   98 FORMAT('0','ETA1=',E14.5,3X,'ETA2=',E14.5,3X,'TORQUE=',E14.5)
   99 FORMAT(' ',I6,3X,5E14.5)
 1000 FORMAT(2E14.5)
      STOP
      END
      FUNCTION  THKNS(RB,RP,Y,I)
C     CALCULATES TOOTH THICKNESS
          COMMON PHI,PC,WDTH
          GS=RP*COS(PHI)/(RB+Y)
          ZETA=ATAN(SQRT(1.-GS**2)/GS)
          TC=PC/2.
          INVZET=TAN(ZETA)-ZETA
          INVPHI=TAN(PHI)-PHI
          COR=0.0
          YMIN=0.094-WDTH
          YPLS=0.094+WDTH
          IF(I-1)110,110,115
  110     IF(Y-YMIN)115,115,111
  111     IF(Y-YPLS)112,115,115
  112     COR=2.*WDTH
  115     CONTINUE
          THKNS=2.*(RB+Y)*(TC/(2.*RP)+INVPHI-INVZET)-COR
          RETURN
       END
      FUNCTION  TKPC(RP,RT)
C     CALCULATES TOOTH THICKNESS AT CONTACT POINT
          COMMON PHI,PC
          TC=PC/2.
          GT=RP*COS(PHI)/RT
          ZETAT=ATAN(SQRT(1.-GT**2)/GT)
          INVPHI=TAN(PHI)-PHI
          INVZET=TAN(ZETAT)-ZETAT
          TKPC=2.*RT*(TC/(2.*RP)+INVPHI-INVZET)
          RETURN
       END
      FUNCTION  TRAP(YL,RB,RP,I)
C     PERFORMS INTEGRATION FOR COMPLIANCE DUE TO BENDING MOMENT
          COMMON PHI,PC,WDTH
          F1=0.
          DELT=YL/200.
          Y=DELT
    9     YS=Y
          Y=Y+DELT
          IF(Y-YL)10,10,21
```

```
 10       X2=((YL-Y)**2)/(THKNS(RB,RP,Y,I))**3
          X1=((YL-YS)**2)/(THKNS(RB,RP,YS,I))**3
          F1=F1+DELT*(X1+X2)/2.
          TRAP=F1
          GO TO 9
 21       CONTINUE
          RETURN
       END
      FUNCTION  TRAP2(YL,RB,RP,I)
C     PERFORMS INTEGRATION FOR COMPLIANCE DUE TO SHEAR AND NORMAL FORCES
          COMMON PHI,PC,WDTH
          F2=0.
          DELT=YL/200.
          Y=DELT
 19       YS=Y
          Y=Y+DELT
          IF(Y-YL)20,20,22
 20       X3=1./THKNS(RB,RP,Y,I)
          X4=1./THKNS(RB,RP,YS,I)
          F2=F2+DELT*(X3+X4)/2.
          GO TO 19
 22       CONTINUE
          TRAP2=F2
          RETURN
       END
      FUNCTION  THETA(RB,RP,RT,ETA,I)
C     CALCULATES ANGLE THETA OF LOAD FORCE
          COMMON PHI,PC
          BETA=TKPC(RP,RT)/(2.*RT)
          IF(I-1)80,80,82
 80       THETA=ATAN((RP*SIN(PHI)+ETA)/RB)-BETA
          GO TO 84
 82       THETA=ATAN((RP*SIN(PHI)-ETA)/RB)-BETA
 84       CONTINUE
          RETURN
      END
```

APPENDIX V
TRANSFER FUNCTION ANALYSIS OF TEST STAND

In order to determine the structural dynamic properties of the test stand system, a number of transfer function tests were performed utilizing the Spectral Dynamics S.D. 1000 E Mechanical Impedance System and an electromagnetic shaker. The driving motor was disconnected from the test stand and excitation was provided at the input to the torquemeter. The system was preloaded by counterweighting the generator.

Figure 103 shows a driving point impedance plot taken for torsional excitation of the test stand system. Evident on the plot are a number of resonances and antiresonances. A test was also performed in the bending mode of excitation; a driving-point plot for this test is shown in Figure 104. Because of the difficulty encountered in providing a purely torsional excitation force, with a single linear stroke, it may be suggested that when peaks (such as those at 305 and 475 Hz) occur in both the torsional and bending modes, they should be ignored, since they are bending rather than torsional resonances. This would thus suggest major torsional resonances at 65, 97, 285, and 660 Hz.

Transfer functions were also obtained for other parameters. Figure 105 shows a plot of torquemeter output to driving point force ratio. Resonances are evident at positions determined as torsional resonances by driving point impedance tests.

Figure 106 shows a plot of acceleration at the gear mesh to the driving force. An accelerometer was mounted on the gear at a meshing tooth for these tests. The accelerometer was positioned to monitor primarily torsional rotation. Figure 107 plots a transfer function between this accelerometer at the mesh to an accelerometer mounted outside the gearbox near the input bearing position. This plot was used to provide a transformation between the rotational accelerations generated by the simulation and acceleration signals which could be monitored experimentally.

One major consideration of validity of results must be realized in using this transfer function information. Since no measurement of the coherence between the two signals was available, there may be unreliable data points. It is rather difficult to determine if this is the case unless more sophisticated testing tools are available.

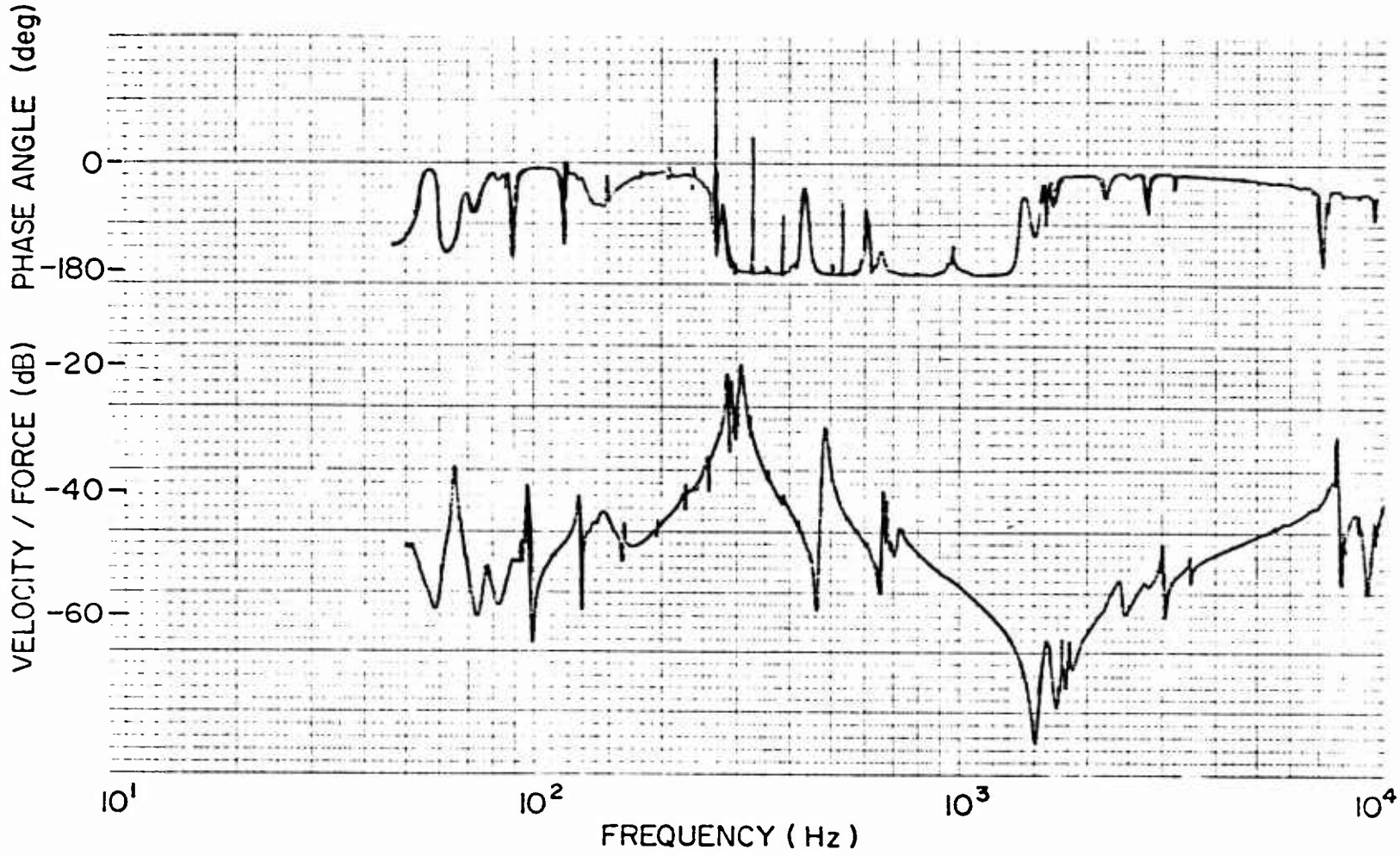

Figure 103. Driving Point Impedance of Test Stand in Torsional Mode.

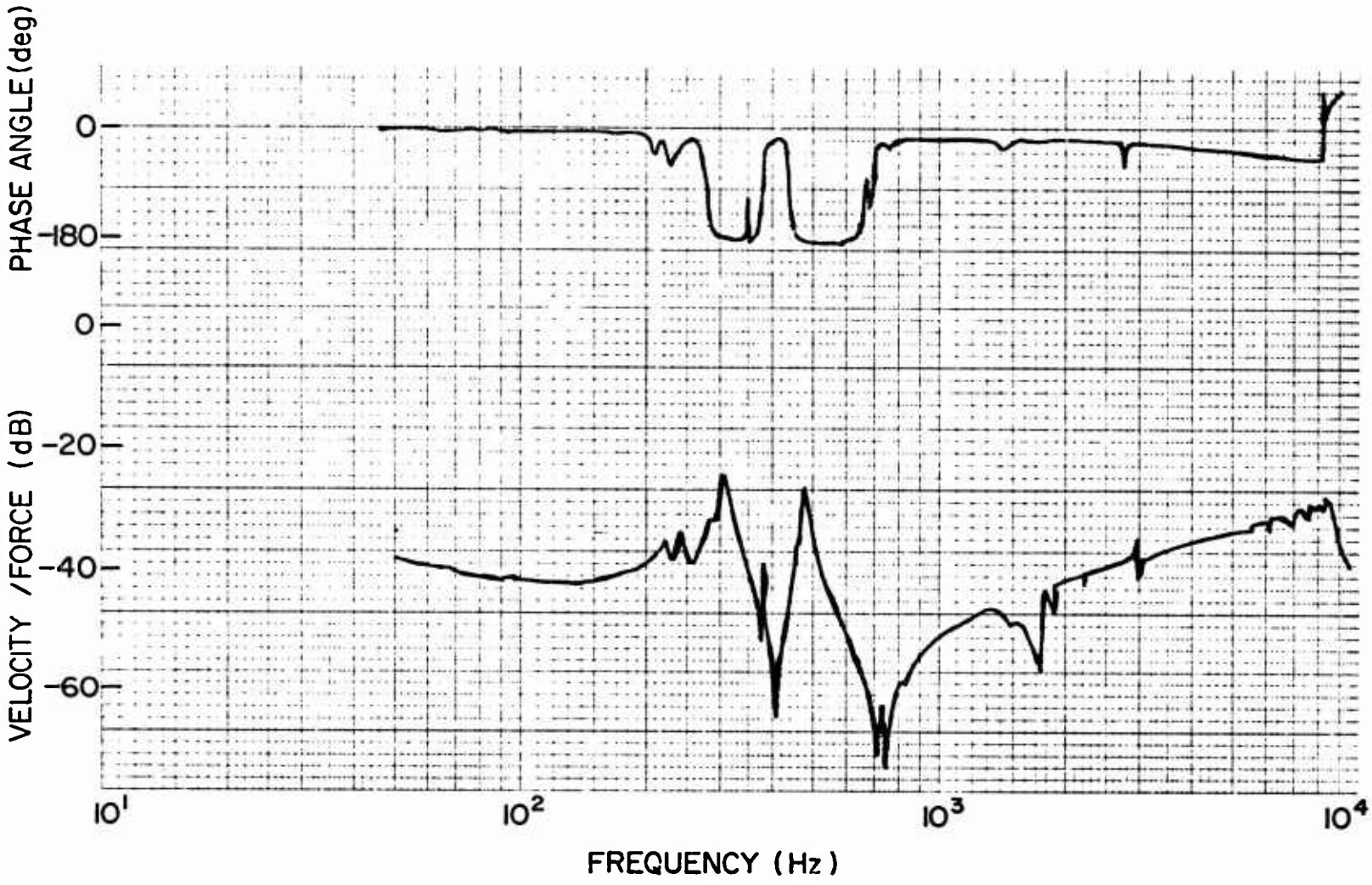

Figure 104. Driving Point Impedance of Test Stand in Bending Mode.

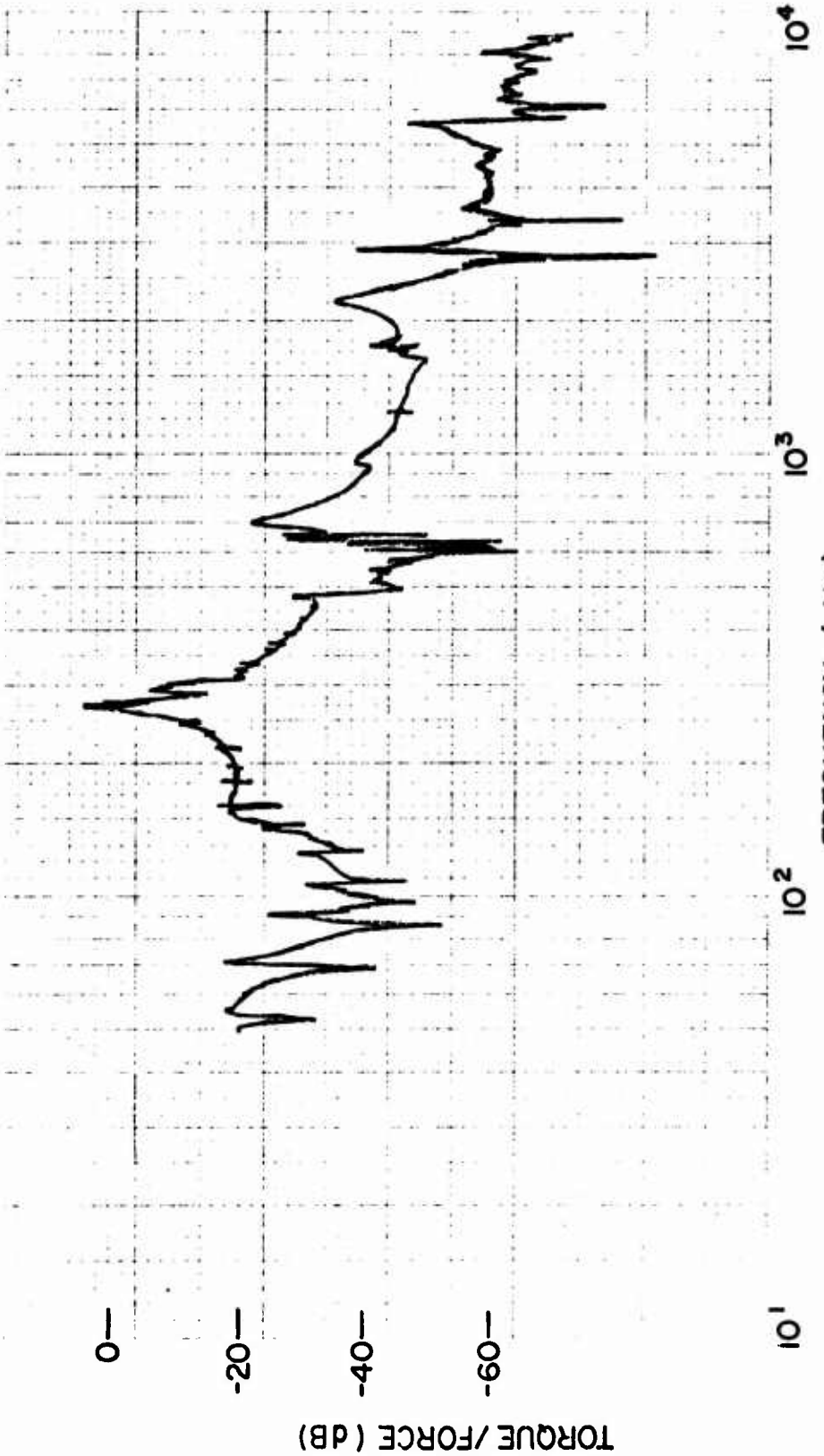

Figure 105. Torque Output Versus Driving Point Force in Torsional Mode.

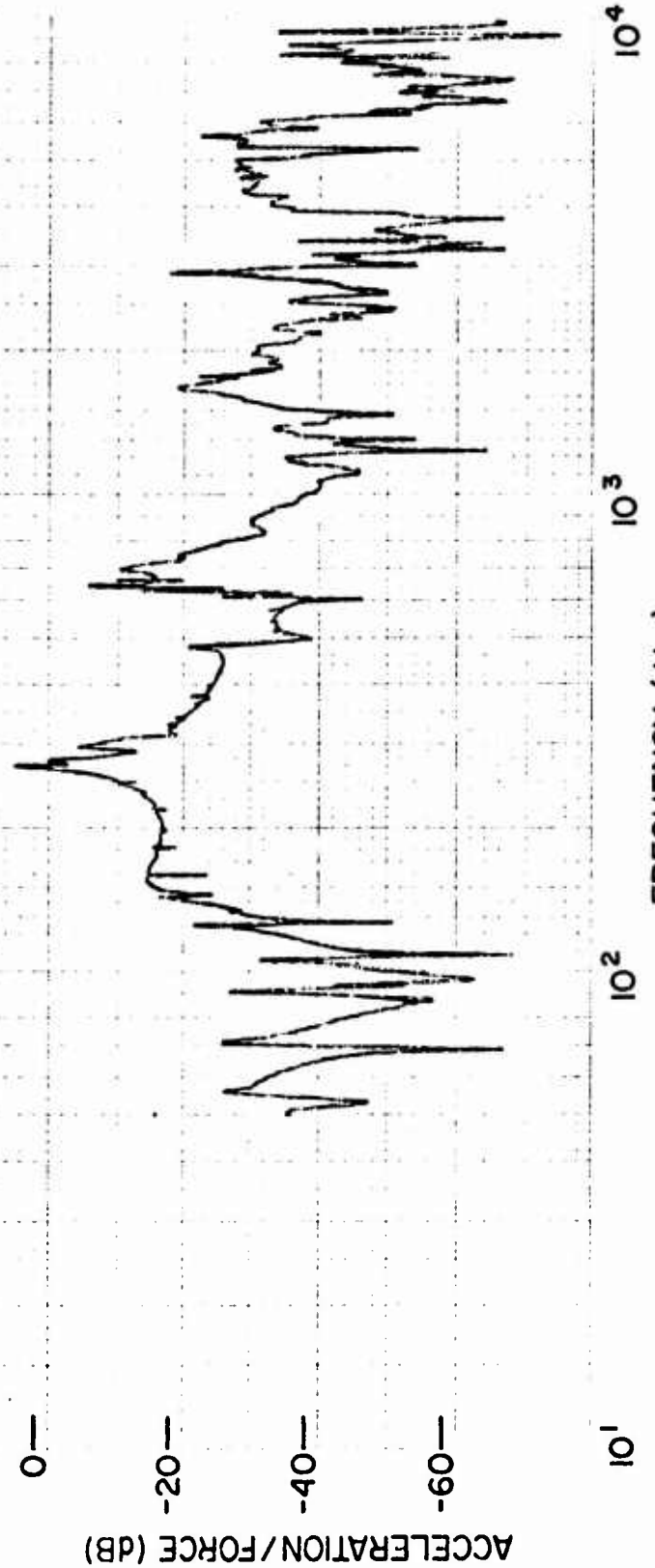

Figure 106. Acceleration at Gear Mesh to Driving Point Force.

Figure 107. Transfer Function Between Accelerometer at Gear Mesh to Accelerometer on Gearbox.

APPENDIX VI
CHARACTERISTIC ROTATIONAL FREQUENCIES OF TEST STAND BEARINGS

A number of rolling element bearings are present in the test stand, both in the gearbox itself and in associated fixtures. Calculations were performed to determine the characteristic rotational frequencies associated with the bearings. Table VI shows the dimensions associated with the bearings. The parameters for the gearbox input roller bearing are starred since all the bearing data was not available and approximations had to be made. The input speed of 4500 rpm was used and the frequencies as shown in Table VII were calculated. It might be noted that no significant amount of signal was seen at these frequencies in the experimental data that was presented. Significant amplitudes at these frequencies are seen when faults are encountered on bearings.

TABLE VI. BEARING DIMENSIONS

	No. Balls	Ball Diameter (in.)	Pitch Diameter (in.)
Gearbox			
A. Output	14	0.75	2.0079
B. Idler	9	0.50	2.106
C. Input			
i. Ball	16	0.3125	2.126
ii. Roller	16*	0.32	2.224*
Pillow Blocks			
A. Main Shaft	9	0.375	1.811
B. Sliprings	9	0.4375	2.1063
Sliprings	12	0.375	2.363
Torquemeter	11	0.3125	1.909

TABLE VII. BEARING CHARACTERISTIC FREQUENCIES (Hz)

	Cage Pass	Ball Pass	Outer Race Pass	Inner Race Pass
Gearbox				
A. Output	23.5	172.8	328.9	721.1
B. Idler	21.3	222.2	191.9	311.3
C. Input				
i. Ball	32.0	499.2	511.8	688.2
ii. Roller	32.2*	523.2*	515.7*	684.3*
Pillow Blocks				
A. Main Shaft	29.7	346.7	267.6	407.4
B. Sliprings	29.7	345.5	267.4	407.6
Sliprings	31.5	460.7	378.6	521.4
Torquemeter	31.4	445.9	345.0	480.0

LIST OF SYMBOLS

B_{23}	linear damping coefficient of pinion-idler gear mesh, lb/in.$\cdot s^{-1}$
B_{34}	linear damping coefficient of idler-gear gear mesh, lb/in.$\cdot s^{-1}$
B_{t12}	torsional damping coefficient of input shafting, in.-lb/rad$\cdot s^{-1}$
B_{t45}	torsional damping coefficient of output shafting, in.-lb/rad$\cdot s^{-1}$
E	Young's modulus, lb/in.^{2}
F_o	tooth force per unit facewidth, lb/in.
g	acceleration due to gravity, in./s^2
G	shear modulus, lb/in.^{2}
h_g	distance from contact point to the gear centerline along the angle of tooth loading, in.
h_p	distance from contact point to the pinion centerline along the angle of tooth loading, in.
J_1	inertia of shafting and input gear, in.-lb$\cdot$s^2
J_2	inertia of spur gear pinion, in.-lb$\cdot$s^2
J_3	inertia of idler spur gear, in.-lb$\cdot$s^2
J_4	inertia of spur gear, in. lb$\cdot$s^2
J_5	inertia of generation, in.-lb$\cdot$s^2
K_{23}	linear spring coefficient of pinion-idler gear mesh, lb/in.
K_{34}	linear spring coefficient of idler-gear gear mesh, lb/in.
K_{t12}	torsional spring coefficient of input shafting, in.-lb/rad
K_{t45}	torsional spring coefficient of output shafting, in.-lb/rad
P_c	circular pitch, in.
P_m	normal pitch, in.
R_{BG}	radius of base circle of gear, in.
R_{PG}	radius of pitch circle of gear, in.
R_{TG}	radius of base circle of pinion, in.

R_{PP}	radius of pitch circle of pinion, in.
R_{TP}	radius of contact point of pinion, in.
X	half-thickness of tooth, in.
Y_L	height above tooth root circle of imposed force, in.
θ_1, θ_2, θ_3, θ_4, θ_5	angular rotations of inertias, rad
ψ_1, ψ_2, ψ_3, ψ_4	relative angular rotations between inertias, rad
δ_B	tooth bending due to deflection, in.
θ	angle between direction of tooth force application and perpendicular to tooth centerline, rad
ν	Poisson's ratio
δ_H	total deflection due to Hertzian force, in.
τ_{FLT}	time gear spends in fault, s
δ_{FLT}	fault width, rad
τ_{IMP}	length of impact, s
Φ	pressure angle, rad
ξ	involute angle, rad
η	distance from the pitch point to the point of contact between mating teeth along line of action, in.